Total–energy models for phase–stability studies in multicomponent oxides

by

Adrián Favio Kohan

Licenciado en Ciencias Físicas
Universidad de Buenos Aires, 1991

Submitted to the Department of Materials Science and Engineering
in partial fulfillment of the requirements for the degree of

Doctor of Philosophy in Materials Science

at the

MASSACHUSETTS INSTITUTE OF TECHNOLOGY

June 1997

Author .....
Department of Materials Science and Engineering
May 2, 1997

Certified by .....
Gerbrand Ceder
Associate Professor of Materials Science
Thesis Supervisor

Accepted by .....
Linn W. Hobbs
John F. Elliott Professor of Materials
Chairman, Departmental Committee on Graduate Students

A “el tate”,
in memoriam

Total–energy models for phase–stability studies in multicomponent oxides

by

Adrián Favio Kohan

Submitted to the Department of Materials Science and Engineering
on May 2, 1997, in partial fulfillment of the
requirements for the degree of
Doctor of Philosophy in Materials Science

Abstract

The computation of thermodynamical properties of oxides from first principles involves the use of both statistical– and quantum–mechanical models. We show that the solution of the former models can be considerably simplified with a low–temperature expansion of the free energy. This overcomes the numerical problems of standard statistical–mechanical techniques at low temperatures or for highly–stoichiometric compounds. We find that with only a few terms in the expansion, an accurate description is obtained up to temperatures where Monte Carlo simulations or cluster variation calculations are practical.

The formation energies of a large number of real or hypothetical compounds are an essential input to compute free energies. These values are usually obtained from sophisticated and time–consuming quantum–mechanical calculations. We show that the same accuracy can be obtained from simpler approaches when all the relevant contributions in the Hamiltonian are properly included. We identify four effects that are necessary to accurately reproduce formation energies in oxides: charge transfer, nonspherical electronic relaxations, ionic breathing, and directional bonding. We successfully integrated these effects into a tight–binding formulation. The Hamiltonian of the model includes explicit parametrizations of these terms. The parameters are fit to pseudopotential bands and equations of state. From this information, formation energies can be obtained with an accuracy comparable to the pseudopotential predictions, but at a fraction of the computational cost. On average, the tight–binding formation energies in the CaO–MgO and CaO–ZrO_2 systems only differ by 10% from the pseudopotential results.

As an example of the applicability of the new tight–binding scheme to complex oxides, we use it to study the dependence of the ionic charge on the atomic environment. We show that the variations in valence state can be important and produce significant errors in the formation energies when they are not properly accounted for.

Thesis Supervisor: Gerbrand Ceder
Title: Associate Professor of Materials Science

Acknowledgments

It would be impossible to acknowledge here all the people that in one way or another shaped my education and consequently this thesis. I will just mention those directly involved.

I would like to express my deepest gratitude to my advisor, Professor "Gerd" Ceder. His guidance, encouragement, and enthusiasm were essential to build this thesis. But, most of all, I am grateful to Gerd for providing me with the freedom to pursue my own ideas with his unconditional support.

I thank the members of my thesis committee, Professor Samuel Allen and Professor John Joannopoulos for their suggestions, confidence, and support.

Leaving Argentina to come to MIT was not an easy decision. I am very thankful to Roberto Perazzo and Alberto Pignotti for their advice and teaching in science and in life. If there had not been for the long talks with Alberto in our way back from work, or with Roberto in a rainy Sunday afternoon I would probably have not been writing this now.

The pseudopotential calculations in this thesis were performed with a code that was generously provided by Professor John Joannopoulos. I am in debt to him and his former student Kyeongjae Cho for teaching me the nuts and bolts of the pseudopotential technique.

Many other people contributed to the research presented here. I thank Mark van Schilfgaarde for providing the LMTO–ASA code. Harold Stockes and Patrick Tepesch are acknowledged for the CaO–MgO SSCAD and pair–potential calculations. The General Utility Lattice Program (GULP), kindly provided by Julian Gale, was used for the pair–potential calculations in calcia–doped zirconias. Chris Wolverton supplied us with the Pd–V ECI's employed in chapter 2. Finally, the vibrational contribution to the CaO–MgO ECI's was computed by Gerardo Garbulsky.

Various financial sources helped support my Ph.D. studies. I would like to acknowledge the fellowships provided by Roberto Rocca, the Starr Foundation, D. V. Ragone, G. Chin, S. Z. Uram, and N. J. Grant. Additional funding from the National Science Foundation (under contract N° DMR9501856) and the National Institute for Health (under contract N° 2-P30-ESO2109-16) is also acknowledged. I thank the Pittsburgh Supercomputer Center for the possibility of using their Cray 90 computer, where most of the pseudopotential calculations were performed.

I was very fortunate to be part of a highly motivating research group. The numerous conversations with Gerd, Patrick, Jerry, Anton, Shuba, Kadri, Axel, Eric, and Nie had an invaluable impact on my work.

It is very difficult to express in words what working with Jerry and Patrick meant to me. I will always miss our long discussions about any possible topic. During this time is where I learned most of what I know. Their friendship is one of the most precious treasures I preserve from these years at MIT.

My frequent trips to Buenos Aires helped mitigate my nostalgia. I always looked forward to meeting my family and my old friends Faby, Pablin, Guadu, and Gaby. And, when I am in Boston, my new friends Patrick, Kate, Felipe, Flor, Juanpi, Sally, Yair, Jackie, Julio, Vicky, Roby, Sandra, Ale, Daniel, Marcela, Pampa, Analia, and Alan make me feel at home.

Jerry, Marce, Luigi, and Adri were both my friends and family during these years. In the good and in the bad times, they always made me laugh. Our camping experiences in the "wild", our "ten minutes" hikes, or our long–weekend trips showed me that there was life beyond my thesis. For all these, I thank them very much.

To my "older" brother Bele, I have to express thanks not only for his love, but also for his encouragement and support. I also enjoyed the visits of my "in laws", Norma, José, and Dari. I am sincerely grateful for their support and help in spite of the fact I *stole* they beloved daughter and sister.

When I was at primary school, I could hardly spell the word *Mamá*. Without the patience and dedication of my mom, I would probably still be struggling with this. To her perseverance and love, I owe most of my career. I do not have words to thank her.

But, if there is one person I have to thank the most, that person is Cari, my wife. Without her caring and love, I could have never finished this thesis. She gave me the strength to face difficult times, the happiness to enjoy what I was doing, and the wisdom on which to build my dreams. After all, she is my *cómplice en la vida.*

The words in this thesis are dedicated to someone that would probably never read them. To someone that taught me the meaning of love, sweetness, ideals, and innocence. To someone that would always give and never ask. To someone that would tirelessly fight against windmills. Yes, it is true that according to the laws of physics, on which this thesis are based, he will not read these words. But he doesn't know that. I am sure my dad will smile at the equations I am about to write...

Contents

List of Figures

List of Tables

Chapter 1

Introduction

Humans have been trying to unravel the secrets of matter since the origins of civilization. Looking for the ideal hunting tools, the deadliest weapons, or the best heart implants, the synthesis and development of new materials have never stopped. The importance of this search is reflected in the fact that many periods of history are named after the materials that were used in them. The Stone Age, the Bronze Age, and the Iron Age were all strongly influenced, both socially and culturally, by the use of stone, bronze, and iron respectively.

The concept of matter is a very elusive one. The first attempts to apply some rationality to the study of materials can probably be tracked down to the origins of *Alchemy* [1]. Although most well known as a search for a way to transmutate the base metals into noble metals in the sixteenth and seventeenth centuries, it produced an enormous amount of information about materials properties, processing, and experimental techniques since the beginnings of the Egyptian era.[1] Even the brightest minds were seduced by the mysteries and powers of the alchemy knowledge. For example, Sir Isaac Newton wrote many alchemical papers in his search for understanding the structure of matter and how it can be transformed [2, 3]. In his *Praxis*, we can read [3]:

> *"....so soon as it beginns to calcine pour upon it 1 part of y^e cold fire extracted out of Lead ore w^{th} salt of Venus & not yet volatized, & so on till you have poured on eleven parts & all be calcined. ffor y^e Saturn will first resolve into water by fusion & then resolve y^e quicksilver of the bodies & promote y^e action of y^e sympatetic fire.....And thus you may understand what the first gate of calcination is & how in the calcination of perfect bodies w^{th} y^e first menstrue nothing unclean enters but y^e green Lyon & how y^e King after his resurrection is fed with the blood of this Lyon...."*

One has to remember that until the chemical elements were identified, the main alchemy theory (usually ascribed to Aristotle, but widely recognized in Egypt and

[1] The Egyptians were expert goldsmiths as far back as the year 3000 B.C. They were also remarkably skilled in metallurgy and enameling. The origin of the word "alchemy" can be tracked down to "Al Khem" that is how the Islamic world called "the art of the dark country" [1]. (Egypt was known as "Khem" or the country of "dark soil".)

India long before his era) was that all bodies were composed of four elements (water, earth, air, and fire) in different proportions. One body could be *transmutted* into another by changing these proportions.[2] Having this theoretical background, most advances had to come from purely empirical approaches!

Profound changes occurred at the end of the XVIII and during the XIX centuries when the concepts of elements, atoms, and molecules were developed or perfected. The use of chemical compositions, rudimentary crystallography, and new technologies (such as better furnaces) dramatically improved the understanding of matter. But still, only a few empirically selected materials were used by the end of last century and only 20 of the 92 naturally found elements formed them [4]. A major revolution took place in the first half of the XX century due to the understanding of the interior of the atom, the introduction of new experimental techniques (such as x–ray diffraction), and the use of accurate mathematical descriptions to formulate the semiempirical relations already known. Completely new materials were synthesized during this period and the role of structure and chemistry on their properties was widely investigated. Plastics, semiconductors, and synthetic fibers, are just a few examples. (See reference [4] for a much more detailed description of the evolution of materials science.)

But how more advanced is our search for new materials now? What different methods would a scientist use at the verge of the XXI century? The *trial and error* procedure evolved from being purely empirical to a very complex relationship between semiempirical laws, mathematical models, and experiments. Current technology provides very advanced tools to characterize and understand materials behavior, making the whole process very efficient. However, the possibilities for combining elements are gigantic. When a material with specific properties is sought, one is sometimes left with just well educated *guesses* on which elements to mix and how to process them.

As a hundred years ago, a revolution is starting to take shape. Advances in computer technology and in the simulation techniques are making possible to just use the guidance of the laws of physics to tailor the properties of materials to our needs [5]. These so–called *computational experiments* are already complementing traditional experiments and are starting to realize a future where novel materials will be predicted and developed before they are synthesized.

This thesis is about some of the methods that are helping this revolution to take place. Our work is focused on how quantum– and statistical–mechanical techniques can be used to study and tailor the properties of oxides. Oxides present a wide variety of properties that make them very useful in many industries, from high–technology companies to refractory brick factories. The goal of this thesis is two–fold: improve the methods to compute phase diagrams *and* the quantum–mechanical inputs to them. For the former, we developed a new approach, based on a low–temperature expansion of the free energy, that circumvents the numerical problems that the standard statistical–mechanical techniques have at low temperatures or for highly stoichiomet-

[2]This theory counted at those times with some "experimental evidence": by using fire and water the *character* of matter could be changed (actually its properties). For example, the properties of steels can be changed by precisely using fire and water. Also, the preparation of *alloys* that resemble gold was already known even by the Egyptians (e.g., golden brass).

ric compounds. For the latter, we studied how the approximations used to compute total energies worked in oxides. From these studies, we propose a new approach to compute total energies in these materials, based on the tight–binding method, that combines the accuracy of the most complex quantum–mechanical techniques with the speed of classical treatments.

We start in this chapter by describing what computer simulations are, what they can do, and how our work relates to this field. In the first sections, we introduce the idea of computer simulations (section 1.1) and phase diagrams (section 1.2). Then, we describe the application of total–energy techniques (section 1.3) to compute oxide's properties and we introduce the problems that the complexity of oxide crystals poses for computer simulations. Finally, we present a brief description of the world of oxides and their applications (section 1.4) followed by a summary of the contributions made in this thesis (section 1.5).

1.1 Computational experiments

Every time we observe a material we can think that *nature* is solving the fundamental equations of physics to see how to move the atoms. In the same way, in a computer experiment, the system under study (atomic nuclei and electrons) is evolved based on the same equations, but this time in the space of the *computer world.*

Nature *has to be* an incredibly fast computer to be able to solve coupled nonlinear equations in more than 10^{23} variables, self–consistently, and in "real time". Real computers are of course much slower and calculating the *exact* state of any relevant system in a reasonable time is basically impossible. However, *approximations* can be introduced to make some of the problems tractable.

Computer experiments have many advantages over real ones. Extreme environmental conditions (e.g., pressure, temperature, toxicity) are usually as easy to study as any other condition. An exact control over all the variables of the *computer experiment* is always possible and thus the interpretation of the results can be made as clear as desired. Moreover, materials can be studied under conditions in which they would not exist in nature. For example, to understand the stability trends of different compounds in a given system *any* metastable structure can be simulated and not only those that can be observed due to sluggish kinetics.

1.1.1 Computer evolution and the limits of simulations

The ability to perform atomistic simulations was slow to emerge because of the extreme complexity of solving the quantum– and statistical–mechanical equations involved. Although most of the currently used approximations were known a long time ago, the calculation power was very limited. In 1965, Gordon Moore, co–founder of Intel, forecasted that the power and complexity of silicon–based integrated circuits would double every 18 to 24 months with proportionate reductions in cost. This is known as Moore's Law and has proven to be remarkably accurate. For example, the first chip introduced by Intel (4004) in 1971 had 2,300 transistors and a speed of 0.06

MIPS (millions of instructions per second). Today, 25 years later, the Pentium Pro processor has 5.5 million transistors and a speed of 428 MIPS. The fast growth in computer power made it possible, in the last decades, to perform the first realistic atomistic simulations. Moore's law is expected to be valid for at least 15 more years using the current technology, and it may hold for even longer if new advances are introduced. Figure 1-1 shows the exponential growth of computer speed since the invention of the first machines.

Correspondingly, computational *materials science* also had an incredible growth. The size of the systems solved is increasing every day and more accurate predictions about macroscopic materials properties can be done. However, even if the rate of growth in computer power is sustained for many more decades, we will not be able to predict properties *exactly*. The most accurate, but still approximate, quantum–mechanical techniques available can only deal with just a few atoms. The computer time they require usually scales at least as N^3 (where N is the number of atoms). If Moore's law is valid for 50 more years we will only be able to solve systems containing of the order of 10^2 atoms, or a cube of material with a side of $\sim$0.1 nanometer. Grain sizes, essential to understand the macroscopic behavior of materials span, according to the processing, length scales from a few tens of nanometers to many centimeters. This means that performing a brute force, *almost exact*, quantum–mechanical calculation to study macroscopic systems is out of the question.[3]

1.1.2 The need for approximations

The introduction of approximations can dramatically increase the size of the systems that can be studied today. Simple classical–potential models can be used to solve problems containing 10^6 atoms [8]. In 50 years, this will be translated into length scales of the order of tens of microns (assuming linear scaling with the size of the system). On the other hand, complex quantum–mechanical methods,[4] can still only handle a few hundreds of atoms. However, they are much more **accurate** than potential models.

There is usually a trade–off between **accuracy** and **speed**. The accuracy and speed that the solution of the problem requires will dictate the necessary approximation level. The optimal balance between these two depends on the number of calculations that needs to be performed and the scale of the physical phenomena we are looking at. For example, the study of phase stability usually requires many quantum–mechanical calculations as input to the statistical models. The accuracy is set by the scale of temperature effects, typically only a few hundreths of an eV. Consequently, only very accurate techniques can be used and long computer runs are needed. On the other hand, the wealth of information that can be obtained from these studies is enormous, and most of this thesis will be devoted to improve the ap-

[3]Even if the methods scaled linearly, the size of the cube of material would be 30 nanometers. This is the scale of the so–called nanophase materials that have been studied since 1985 and whose grains are formed by nanometer–size atomic clusters [7].

[4]Using the local–density approximation to density–functional theory. See section 1.3.

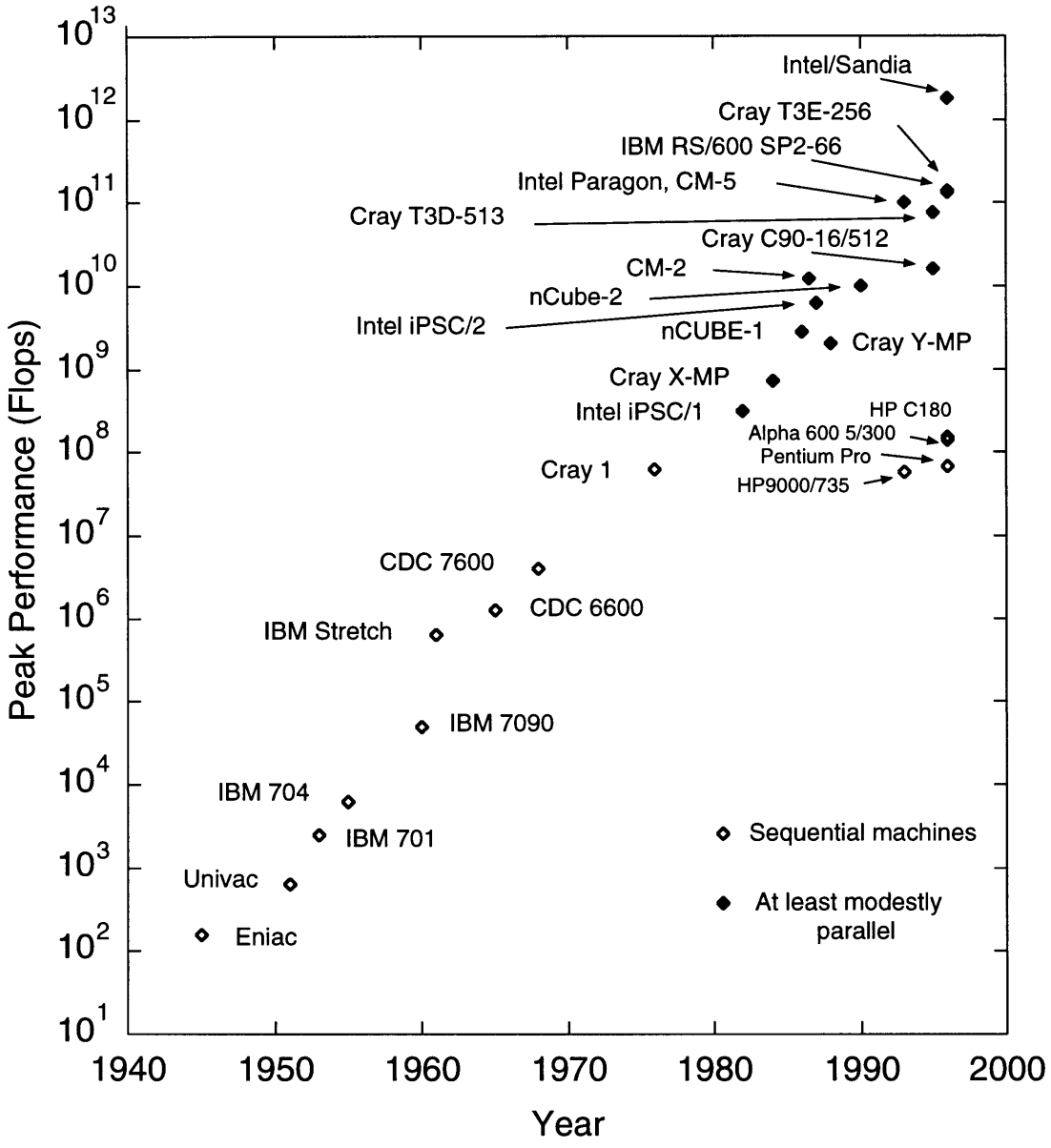

Figure 1-1: Peak performance of the fastest computer models built as a function of time. The performance is written in floating point operations per second (Flops). Also shown are the speeds of the latest workstations. Data from reference [6] and from manufacturers' information sheets.

proximations of current models in order to make them faster and, at the same time, accurate enough.

1.2 Phase diagrams

Most technologically relevant materials make use of more than one element of the periodic table. The ability to tailor materials to our needs depends greatly on the understanding of the relationship between properties, structure, and composition when different elements are mixed. In this sense, phase diagrams are one of the most important tools to design and process materials efficiently. We can think of a phase diagram as a *map* that shows what phases are stable in a temperature–composition space (at constant pressure). This is very valuable information to predict the final microstructure of an alloy[5] after processing.

The experimental determination of phase diagrams is usually a difficult task. Measurements are often hampered by sluggish kinetics or extreme temperatures, among other conditions. On the other hand, by using the laws of physics it is possible, in principle, to compute any phase diagram using as only input the atomic numbers and masses of the elements that are being mixed. This approach to compute materials properties is sometimes called "*ab initio*" or from "*first principles*".

In spite of the advances in computer power, we can not track the movements and interactions of the more than 10^{23} nuclei and their electrons that form a macroscopic solid. All *ab initio* approaches introduce different degrees of approximations. In chapter 2, we show how the alloy problem can be mapped onto lattice models that are specially suited for studying the thermodynamic properties of *substitutional* alloys. From the free energies provided by the model, the phase diagram can be easily computed. In a *substitutional* alloy, the different species arrange themselves on the sites of an underlying parent lattice.[6] We will focus on the stability of *solid* phases and we will not include the liquid or gas portion of the diagrams.

To compute free energies using statistical mechanics, the dependence of the system energy on the substitutional arrangement of the ions on the lattice has to be known. Most of the ionic arrangements are not periodic, making these calculations difficult if not impossible. Even for periodic systems, the solution of the quantum–mechanical problem is very complex and empirical potential models are often used.

The situation changed dramatically with the introduction of the *cluster expansion* by Sanchez and collaborators [9]. They showed that any property of the alloy that depends on the arrangement of the ions on a given lattice can be expanded in "cluster functions". These functions are easily computed from the lattice site occupations. When the property that is being expanded only depends on the local environment, the cluster expansion is rapidly convergent and only a few coefficients need to be

[5] An alloy is a combination of two or more elements. Note that we do not limit this definition to just *metallic* alloys but we will also consider a *ceramic* mixture as an alloy.

[6] This is not a severe assumption. When two phases that are in equilibrium with each other arrange themselves on different lattices, the free energies can be computed in each of the lattices and then compared to determine the stable phases.

determined. The usual procedure is to compute the energy of a few *periodic* arrangements using any total–energy method and from this information find the expansion coefficients [10, 11, 12].

By "total energy", we mean the interaction energy of the whole system of electrons and nuclei that form the solid. Computing this energy from first principles is still one of the most challenging problems in condensed–matter physics and is currently one of the limiting factors in *ab initio* predictions of phase stability. Even for a perfect crystal, calculations are very computer–time intensive, particularly when large unit cells are involved. Consequently, it is very important to understand what approximations can be introduced to make the methods faster but retaining the required accuracy. This will be the main focus of the present thesis.

The methodology we will follow to compute phase diagrams is summarized in figure 1-2. The alloy problem is mapped onto a lattice model. Once a simplified Hamiltonian is built (i.e., once we assumed a given set of approximations), the formation energies of many intermediate compounds are computed. The number of compounds depends on the system being studied. For example, for the CaO–MgO system 21 values were enough to obtain the coefficients used in the cluster expansion. If more than one parent lattice is necessary to describe the full phase diagram, a cluster expansion is needed for each lattice. The next step is to compute the phase boundaries. The regions of phase stability can be obtained by computing free energies for each of the possible competing phases and keeping the ones that have the minimum values (or a combination of them, through the "tangent construction"). Two techniques are widely used in lattice models: the cluster variation method [13] (CVM) and Monte Carlo [14] (MC) simulations. In its most basic formulation, the MC approach generates equilibrium ensembles using a stochastic procedure and the phase boundaries can be found, for example, by looking for discontinuities in concentration vs. temperature instead of computing free energies.[7] Free energies can also be obtained by performing time–consuming path integrations from states where the free energy is known. On the other hand, the CVM is a generalized mean field technique that gives free energies directly.

1.3 Total–energy methods

The computation of total energies requires the determination of the *interaction* energies between *all* the electrons and nuclei that form the material. Even when all the symmetry of the problem is exploited, the calculations are very involved.

Many different techniques have been proposed to compute total energies in the last seventy years. From "classical" approaches to very complex quantum–mechanical models, the whole range of accuracies and speeds has been explored. The reasons for the existence of this wide variety of schemes lie in the extreme difficulties in solving

[7] In many cases, strong hysteresis may prevent the accurate location of phase boundaries from discontinuities in the sampling averages in a reasonable amount of computer time. Under these circumstances, free energies have to be computed.

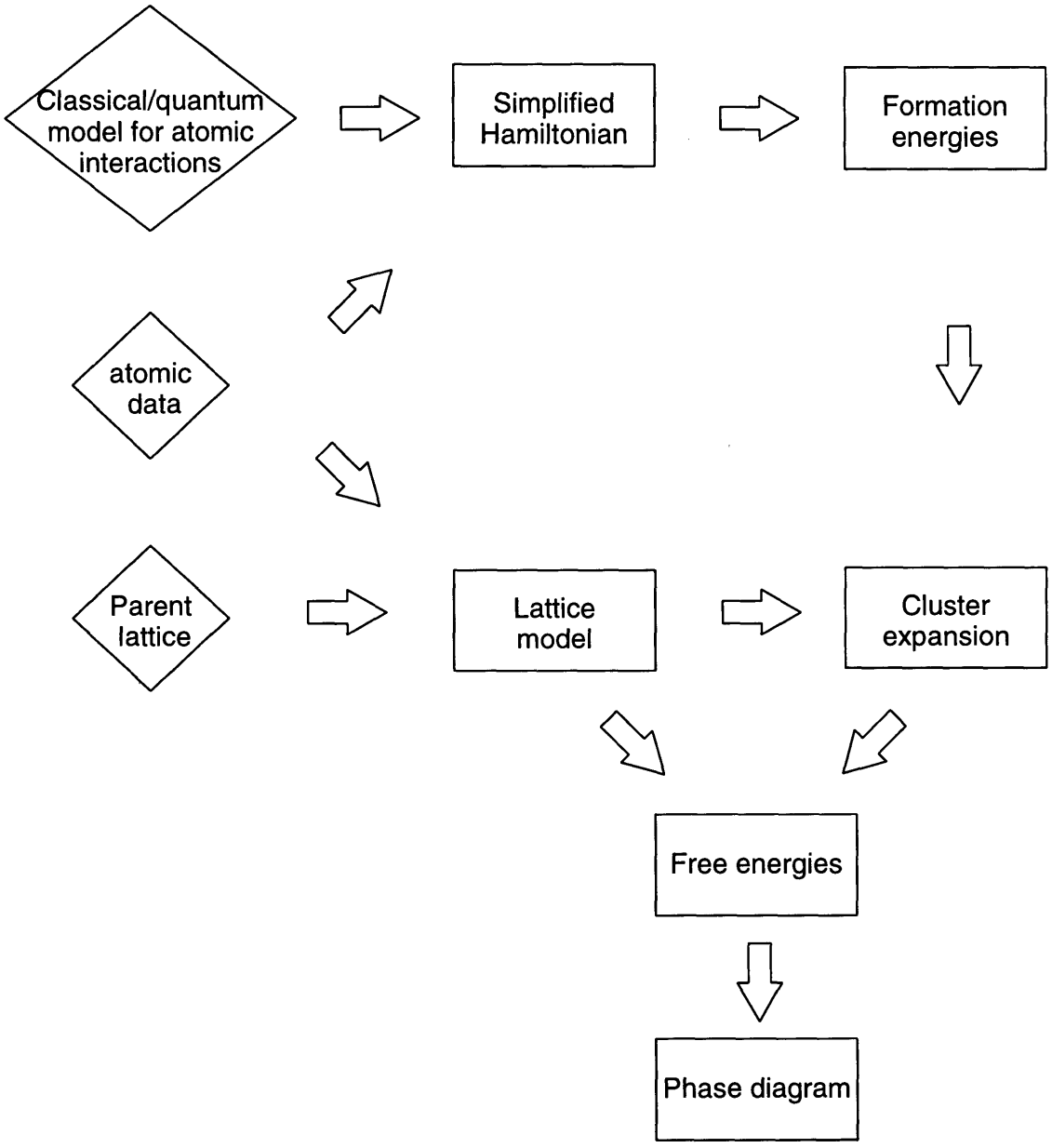

Figure 1-2: General procedure used to compute phase diagrams. The rhombuses represent the input information to the model.

the problem at hand that force the introduction of different approximations. The revolutionizing changes that computational materials science is producing are due not only to the advances in computer technology but also, in a comparable extent, to the improvements in the computational techniques.

In general, two different approaches can be taken to compute total energies: we can assume a model for the electronic density and solve for the energy, or we can directly solve Schrödinger's equation in the solid *self–consistently.* In the first case, quantum–mechanical equations are not necessarily used. For example, in empirical potentials, the electronic density and ionic charges are replaced by point charges centered at the ions. The energy is computed as the sum of the electrostatic interaction and a short–range repulsive term that represents the overlap of the electronic clouds. The parameters of these models are usually fit to reproduce experimental or *ab initio* data. On the other hand, in the self–consistent quantum–mechanical methods the electronic wave function, and therefore the interaction potential between the electrons, is not known before the problem is solved. Different quantum–mechanical methods typically differ in the basis functions they use to expand this electronic wave function. *A priori* assumptions, such as spherical symmetry for the electrostatic potentials, are introduced to speed up the calculations. A more detailed description of the methods and the effects of the approximations used can be found in chapters 3 and 5 respectively.

A major step in the development of total–energy techniques was the introduction of the density–functional theory [15] for the treatment of the many–body electronic problem. Currently, most *ab initio* quantum–mechanical models are based on a local–density approximation [16] (LDA) to this theory or on improvements over the LDA by using gradient corrections [17, 18]. Other methods, based on the Hartree–Fock approximation are also used [19].

Not all quantum–mechanical methods are *ab initio.* One particularly useful technique is the semiempirical tight–binding formalism. Originally proposed by J. C. Slater and G. F. Koster [20] as a way of interpolating bands, it can be reformulated as a very effective total–energy technique [21, 22, 23]. We will use this technique extensively in chapters 6 and 7 since it will allow us to introduce the relevant physical effects for computing total–energy differences in oxides while still retaining the simplicity and speed of the semiempirical approaches.

Within the appropriate model for the system, most of the materials properties can be related to differences between *total energies.* Lattice parameters, elastic constants, pressure–induced transitions, and defect concentrations are just a few examples of materials aspects that can be analyzed using total–energy methods. We will mainly focus on their use to compute phase diagrams. However, other applications, such as the engineering of new cathode materials for batteries, will also be discussed.

We will use total–energy methods to compute *formation energies,* which are important inputs for the statistical–mechanical models. The *formation energy* of a compound is the difference between its total energy and the total energy of its constitutive compounds (or elements). A large number of formation energies are usually required to compute phase diagrams. Oxides present a difficult challenge to total–energy techniques since they have very complex crystal structures with low symmetry

that make accurate methods very computer–time intensive.

1.4 Oxides

Oxide materials are everywhere in our daily life. From glass products and bricks to electronic components, from enamels and clay to computer screens and nuclear fuels, the applications of these materials are countless. As our knowledge of their properties increase, new applications are being found every day. In 1986, J. G. Bednorz and K. A. Muller discovered superconductivities above 30 °K, in oxygen–deficient compounds in the Ba–La–Cu–O system [24]. These temperatures were higher than previously known cases. One year later, the critical temperature was raised again, to 90 °K, in $YBa_2Cu_3O_z$ [25] and even higher values have been observed in recent years. The $YBa_2Cu_3O_z$ case represents an example of the interplay between experiments and simulations we mentioned earlier. D. de Fontaine, G. Ceder, and M. Asta studied the oxygen ordering in this superconductor. They developed a phase diagram that predicted new ordered phases that were later observed experimentally [26].

In the following chapters, we will focus on high–technology applications of oxides such as lithium–transition–metal oxides and doped zirconias for battery cathodes and oxygen sensors respectively. These are usually called *advanced materials* and their use is growing at a fast pace. The world market for high–technology ceramics (not only oxides) in the year 2000 is estimated to be $5 billion [27]. Although it is still small compared to the $500 billion steel market, its growth rate of 20% is ten times larger than for steel [27]. Oxides have many uses not only because oxygen is very abundant[8] but also because they form numerous and complex *crystal structures.* Typical oxide crystals may contain more than four elements of the periodic table, have low symmetry, and large unit cells. This complexity is reflected in the wide range of properties that oxides exhibit making them very attractive to the materials engineer. The insight that computational tools can offer will be fundamental to fully take advantage of the properties of complex oxides.

The simplest metal–oxide structures are based on a close packing of the oxygen ions, with the cations filling the available interstices. For example, figure 1-3 shows the crystal structure of the stable phase of pure zirconia (ZrO_2) at room temperature. This structure is monoclinic, with 12 atoms at symmetry–distinct positions in the unit cell and with 13 degrees of freedom.[9] The computation of the total energy of this structure is already a formidable task and no calculation with *state–of–the–art* methods has been reported so far. To determine the phase diagram of zirconia when it is mixed with CaO or Y_2O_3, the formation energies of many even more complicated compounds would have to be computed, seriously pushing the limits of the methods currently available. Any technique, such as the one presented in chapter 6, that allows

[8] Oxygen accounts for 50% of the elements in the earth crust [28].

[9] These degrees of freedom refer to all the possible displacement of the atoms that do not violate the symmetry of the structure. They include both volume and internal relaxations. To compute formation energies, the total energies of the different structures are minimized with respect to these degrees of freedom.

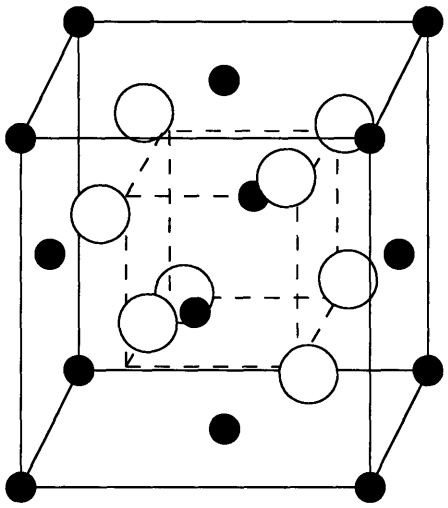

Figure 1-3: Stable structure at room temperature of pure zirconia. It can be obtained as a deformation of the fluorite structure. The black circles represent zirconium ions while the white circles are the oxygen ions. The corners of the dashed cube are the oxygen positions in an ideal fluorite structure.

the accurate interpolation of complex calculations is fundamental if we want to make any progress in predicting this type of phase diagrams *ab initio*.

Any material property is markedly dependent on small deviations from ideal structures. Atomic defects, interfaces, and grain boundaries are examples of such deviations that add a new dimension to the problem of predicting materials properties from first principles. Oxides are no exception and we are far from any rigorous treatment with the techniques currently available. For this reason, the tight–binding formulation presented here can play a fundamental role in the understanding of oxides in the future.

1.5 Thesis outline

New technological advances are imposing stronger demands than ever before on materials performance. To help the materials engineer meet these challenges, new tools are being introduced every day. Among them, there is a particular set of techniques that do not respond to the traditional concept for developing novel materials. Usually called "atomistic simulations" or "computer experiments", they are revolutionizing the way in which materials science and engineering works. Both the increase in computer power and the improvement in the numerical methods are making this revolution possible.

The increase in computer power alone, will not allow us to accurately model complex materials or macroscopic properties in the near future. New and faster numerical techniques have to be developed. In this thesis, we focus on ways of improving the methods to compute phase diagrams in complex oxides. In recent decades, there has been an increased interest in oxides. From simple applications in glasses to high–technology tiles for the aerospace industry, their wide variety of properties has been used in almost any industry. This flexibility correlates with the complexity of the materials. The complexity pushes the limits of the computational methods that are used to understand, and eventually design new oxides. With this work we hope to contribute to a future where these novel materials can be created from purely computational experiments.

Phase diagrams are one of the most important tools to develop new materials. The *ab initio* study of phase stability involves solving complicated quantum– and statistical–mechanical equations. In the statistical–mechanical field, we will introduce a new methodology to compute phase diagrams at low temperatures or for highly–stoichiometric compounds. In chapter 2, we will explain the details of a low–temperature expansion technique of the thermodynamical potentials that overcomes the numerical problems that more traditional methods, such as Monte Carlo simulations or the cluster variation method, have in that temperature regime. The general formalism of lattice models will also be described.

In the quantum–mechanical field, we will focus on how to compute formation energies in a fast and accurate way. Formation energies are the main input to the statistical–mechanical models. The complexity of oxides makes the computation of total energies very computer–time consuming. In chapters 3, 4, and 5, we will show

that although it is possible to accurately compute formation energies in oxides, only the very complex quantum–mechanical techniques can accomplish the task. These methods are very slow and many approximations need to be introduced.

In chapter 5, we will also analyze the effects of the approximations used in different total–energy methods and we will determine the relevant terms that should be included in a simplified Hamiltonian in order to reproduce formation energies accurately. This simplified Hamiltonian will be then formalized within a self–consistent tight–binding model in chapters 6 and 7. We will demonstrate that within the tight–binding framework, formation energies can be computed very accurately and without an excessive computational burden.

Most oxides are highly ionic. The majority of the simple total–energy models assume *fixed* point charges to compute the inter–atomic Coulomb interaction. In chapter 8, we will use the self–consistent tight–binding technique to demonstrate that large charge variations between the same ionic species can exist. The actual charge will depend on the particular atomic arrangement around the ion (e.g., different structures, different site symmetries within a given unit cell, etc.). We will show that assuming constant charges can introduce large errors in the total energy. Simple ways of modeling the charge transfer will be evaluated.

Finally, we will summarize the conclusions of this work and future research in the field of computational materials science in chapters 9 and 10 respectively.

Along the process, we will also discuss applications of these techniques to specific materials systems. The low–temperature expansion will be tested in the Pd–V phase diagram. Although this particular alloy is not an oxide, it offers a remarkable illustration of the difficulties occurring at low temperatures. The CaO–MgO system will be also extensively analyzed from different perspectives not only because of its technological applications (refractory ceramics) but also because of its relative simplicity. In chapters 2, 5, and 7, its phase diagram and energetics will be discussed. We will also study doped zirconias, that are widely used as oxygen sensors, fuel cells, and coatings. Their intricate structures and behavior will be an ultimate test for our simplified tight–binding Hamiltonian (chapter 7). Finally, the power of the *ab initio* approach and total–energy techniques will also be illustrated in the design of cathode materials for lithium–transition–metal oxide batteries (Appendix C).

Chapter 2

The computation of phase diagrams

The stability regions of the different phases (or their coexistence regions) in a phase diagram can be computed by minimizing (tangent construction) the free energies of all the possible phases in the system. A brief review of the methods to implement this procedure will be done in section 2.1. In some of these approaches, the free energies are not even evaluated and the stable phases are obtained by simply "observing" the arrangement of the atoms during a simulation.

At low temperatures, equilibration times become unaffordably long in some of the simulations. These problems are aggravated in systems with highly ordered stoichiometric phases since most of the standard statistical–mechanical techniques, such as Monte Carlo or the cluster variation method, are only practical if at least a minimum amount of disorder is present. In section 2.2, we develop a low–temperature expansion (LTE) of the thermodynamic potentials that overcomes the above problems. Our work is an extension to complex alloy Hamiltonians of the formalism previously developed for the Ising model with pair interactions [29].

The LTE complements MC simulations and the CVM extremely well as it provides analytical expressions for the free energy in the situations where the latter methods become inefficient: highly stoichiometric phases with little disorder. In section 2.3, we apply this "combined" approach to compute the phase diagrams of the CaO–MgO and the Pd–V systems. The former presents a simple miscibility gap, as shown in figure 2-1. Although any technique can be used in this case, we are including this system as a simple example to illustrate the formalism. On the other hand, the Pd–V alloy is very complex at low temperatures. The experimental phase diagram is shown in figure 2-2. Bellow 400 °C, measurements are hampered by sluggish kinetics. However, Cheng and Ardell were able to detect a new ordered phase, Pt_8Ti (with stoichiometry Pd_8V), in this region [32]. Note that some of the compounds present in the phase diagram stay stoichiometric up to very high temperatures.

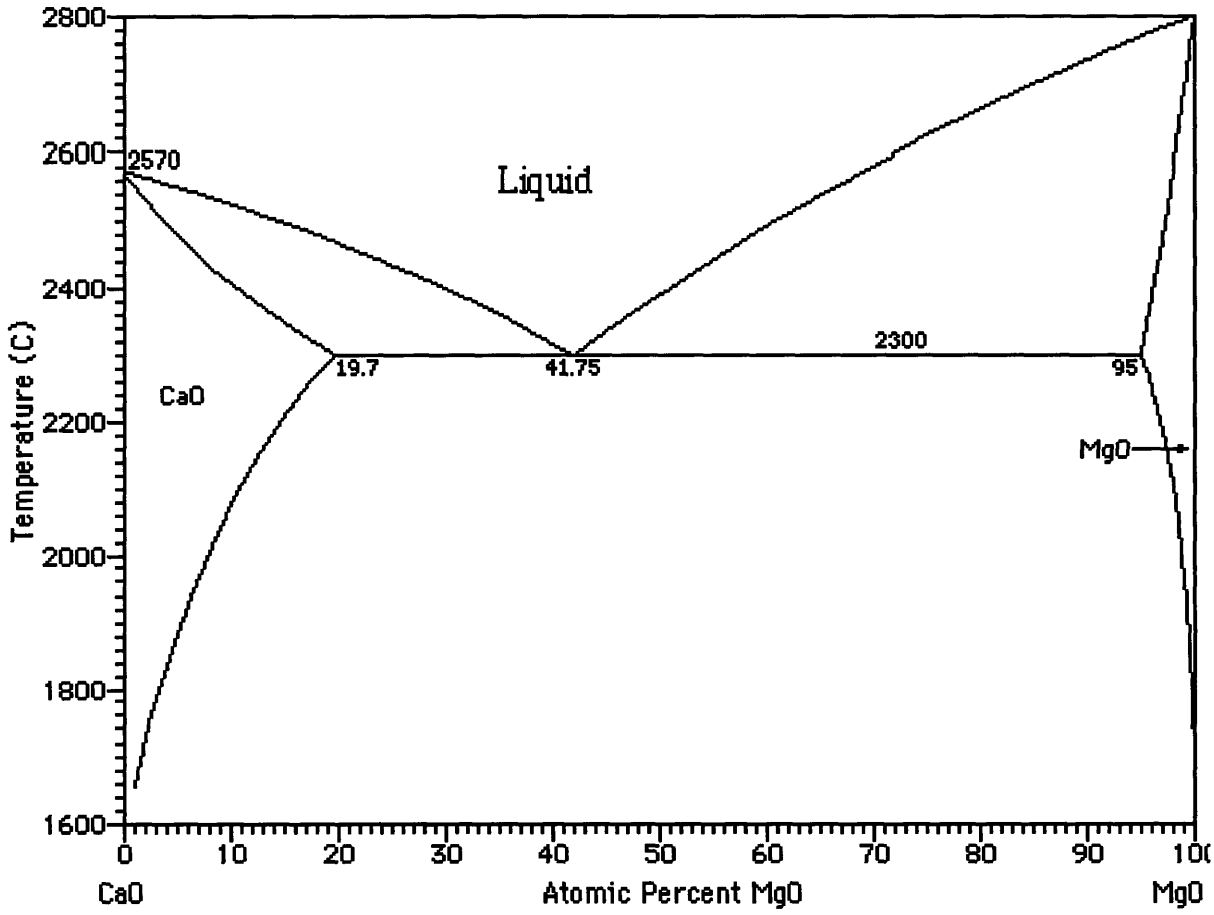

Figure 2-1: Experimental phase diagram for the CaO–MgO system. There are no stable compounds in the solid phase, just a miscibility gap. See for example reference [30] for more details.

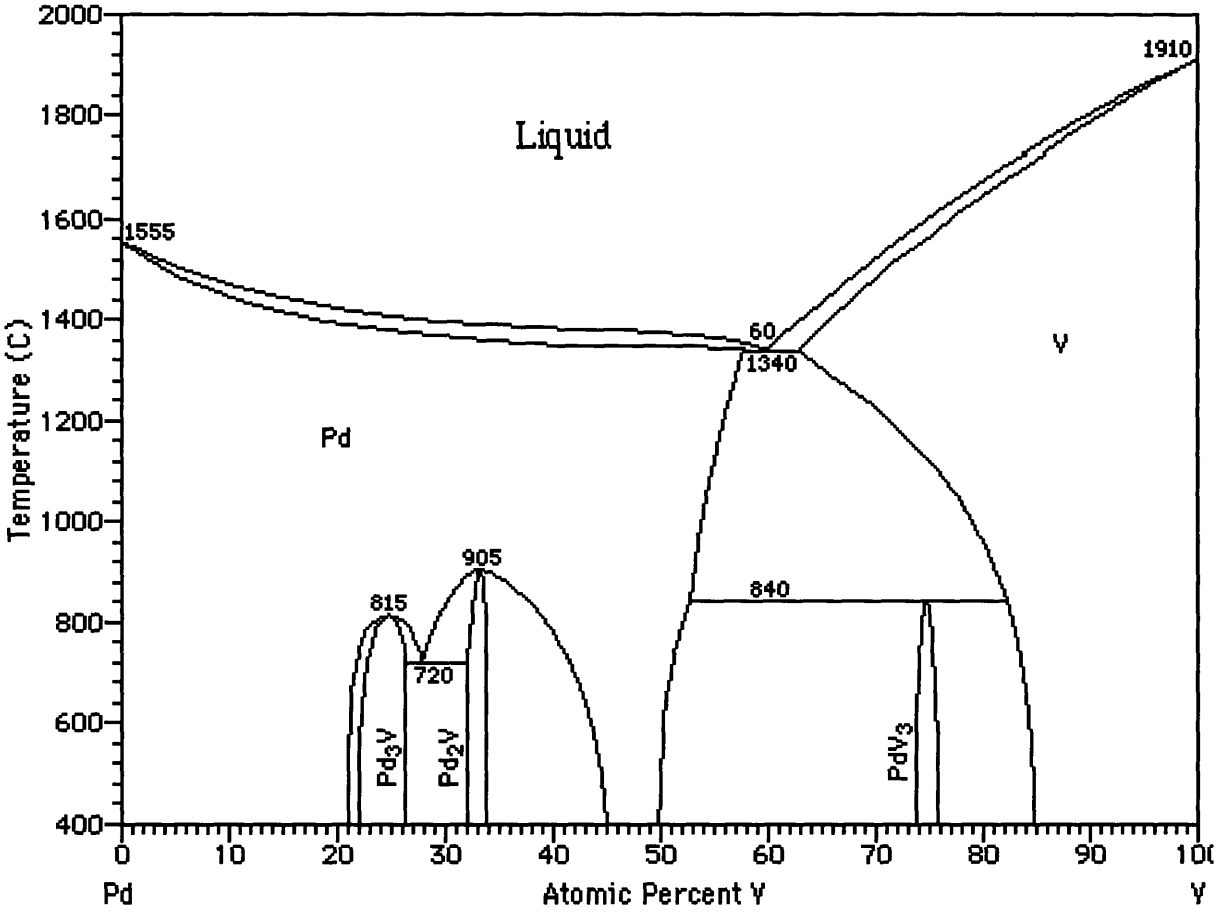

Figure 2-2: Experimental phase diagram for the Pd–V system. The Pd_8V phase is not shown since it is very difficult to measure its boundaries experimentally. Note that Pd_2V and PdV_3 have a very narrow stability region which makes traditional simulations difficult to perform. See reference [31] for experimental information.

2.1 General formalism

A direct simulation of the equilibrium *solid* phases with a single technique is not possible since the phenomena being observed spans many different time scales. The energy and entropy contributions to the free energy involve, for example, electronic excitations, atomic vibrations, and configurational disorder. While atomic vibrations have typical periods of $\sim 10^{-13}$ seconds, the changes in configuration (related to atomic jumps) have time scales that are many orders–of–magnitude longer. A combination of different techniques, such as molecular dynamics [33], for treating the atomic vibrations, and Monte Carlo simulations, for dealing with the configurational disorder, is one option to study dissimilar time scales.

In this thesis, we follow a different approach. We integrate out the faster degrees of freedom and only retain the *substitutional* degrees of freedom, which can then be mapped onto a lattice Hamiltonian. The cluster expansion mentioned in chapter 1 can be thought of as a *generalized* Ising Hamiltonian within this model. Finally, we use standard statistical–mechanical lattice–model techniques to study the system configuration space.

2.1.1 The alloy problem

The free energy of any alloy can be computed from the partition function, Z,

$$Z(T,P) = \sum_j e^{-\beta E_j}. \tag{2.1}$$

The sum is over all possible quantum–mechanical eigenstates j of the Hamiltonian of the system, T is the absolute temperature, E_j is the eigenvalue corresponding to j, and $\beta = \frac{1}{K_B T}$, where K_B is the Boltzmann constant. We assume the pressure, P, to be constant and equal to zero.[1] We will not explicitly write the pressure in the rest of this work.

For the temperatures at which the solid phases are stable, the contribution of the noncrystalline states to the partition function is negligible. We can then only considered the crystalline states in the sum in equation 2.1. These states can be grouped according to the parent lattice "L" (e.g., fcc) on which the atoms order. Different atomic arrangements on a given lattice will be labeled by σ. We will assume that there is a unique mapping from the microstates j of equation 2.1 onto σ.[2] Note that these microstates not only correspond to states with the atoms at the ideal lattice positions, but also states with small deviations from them and in general, any excited state, such as atomic vibrations or electronic excitations, that can be mapped onto σ. This procedure is illustrated in figure 2-3.

The sum in equation 2.1 can be arranged so that it is written as an explicit function of the different arrangements of the atoms at the sites of all the possible

[1] In this thesis, we will not address pressure–induced transitions.

[2] This is true for most systems of interest.

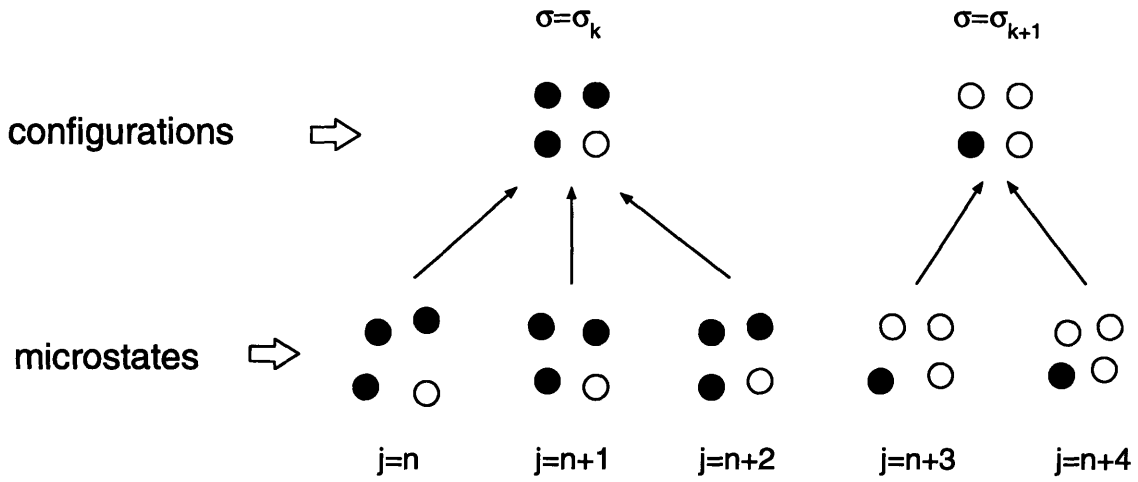

Figure 2-3: Mapping of different microstates j into configuration space. The arrangement of the atoms on the parent lattice is labeled with σ. It is assumed that there is a unique mapping from j onto σ.

parent lattices of the system.

$$Z(T) = \sum_{L} \sum_{\sigma \in L} \sum_{j \in \sigma} e^{-\beta E_j}. \tag{2.2}$$

The last sum is now over all quantum–mechanical eigenstates that correspond to a given distribution σ of atoms on the lattice L.[3] Many phase diagrams can be described as arrangements of atoms on a *single* underlying lattice. In this case, the first sum in equation 2.2 has only one term. For simplicity, we will assume that this is the case. If more than one lattice is present, the procedure has to be repeated for each lattice.

Since the time scales of the atomic jumps are orders–of–magnitude larger than the time scales of the other excitations, we can assume that at each configuration, the system will *ergodically* sample all the possible j microstates. In this way, it is possible to define a free energy, $F(\sigma, T)$, for every configuration on the lattice.[4] Thus, equation 2.2 can be expressed in the following way,

$$Z(T) = \sum_{\sigma} e^{-\beta F(\sigma, T)}, \tag{2.3}$$

where

$$F(\sigma, T) = -\frac{1}{\beta} \ln \left(\sum_{j \in \sigma} e^{-\beta E_j} \right). \tag{2.4}$$

[3]Note that the only condition for equation 2.2 to be exact is that there is a *unique* mapping from j onto σ.

[4]This assumption is not always correct but, for most systems of interest, the error it introduces in the phase boundaries is negligible. See reference [34] for a detailed discussion on this problem.

Note that in equation 2.3, only the configuration dependence appears *explicitly*, all the other degrees of freedom have been "integrated out". This procedure is usually referred to as the "coarse–graining" of the partition function and it allows us to compute the free energy with a single simulation technique.

Equation 2.3 can be thought of as the partition function of a system with Hamiltonian $F(\sigma, T)$. This Hamiltonian accounts for all the nonsubstitutional degrees of freedom. It can be explicitly written as

$$F(\sigma, T) = E_o(\sigma) + F^{exc}(\sigma, T), \tag{2.5}$$

where $E_o(\sigma)$ corresponds to the eigenstate with the lowest energy for a given σ and $F^{exc}(\sigma, T)$ represents the free energy of the different excitations available to the system for that σ. The lowest energy state does not necessarily correspond to the atoms sitting at their ideal lattice sites.[5] It is common practice to use $E_o(\sigma)$ as an approximation to $F(\sigma, T)$, effectively neglecting $F^{exc}(\sigma, T)$. In this case, the Hamiltonian is temperature independent. However, in recent years, an argument has been made for the importance of the different nonsubstitutional excitations for the determination of phase diagrams. For some systems, changes in transition temperatures of the order of 30% can be expected if they are not included. (See for example references [34, 35, 36, 37] and references therein.)

Different contributions to $F^{exc}(\sigma, T)$ should be considered. Among them, atomic vibrations and electronic excitations are the most relevant [34, 37]. However, Garbulsky argued that the former are the most important for determining alloy phase stability [34]. For insulators, as many oxides are, it can safely be assumed that this is the case. Consequently, we will only take into account the effect of atomic vibrations. Equation 2.5, is then reduced to,

$$F(\sigma, T) = E_o(\sigma) + F^{vibr}(\sigma, T). \tag{2.6}$$

In the following chapters, we will focus on different ways of computing $E_o(\sigma)$. Since most of the configurations σ are not periodic, a cluster expansion is used. Before introducing this concept, it is convenient to map the alloy problem onto an Ising lattice model.

2.1.2 The Ising model

The Ising model was introduced in 1925 by Lenz and Ising.[6] It was developed to study magnetic ordering and consists of a fixed lattice with a spin variable σ_i defined at each site i. They also defined a simple nearest–neighbor coupling interaction between the spins.

In alloy theory, the value of the spin variables is not associated with a particular magnetic moment but with the identity of an atom. For example, for a binary alloy A–B, σ_i takes the value +1(-1) when site i is occupied by an A(B) atom. In this

[5] For a given σ, the atoms will *relax* to their lowest energy position at T= 0 °K.

[6] The history of the model can be found in reference [38].

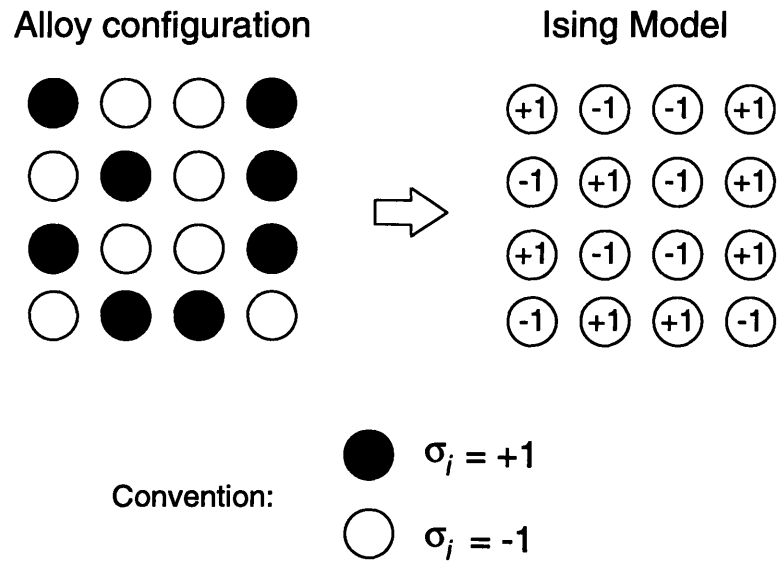

Figure 2-4: Mapping of a binary alloy configuration onto an Ising model. If site i is occupied by the black(white) atomic species, the spinlike variable $\sigma_i = +1(-1)$ is assigned to that site.

way, any arrangement σ of the atoms on a lattice can be labeled with the set formed by the σ_i at each lattice site.[7] This mapping is illustrated in figure 2-4 for a binary system on a two dimensional lattice.

In this chapter, we have been using σ to denote a specific arrangement of the ions on a lattice. In terms of the Ising model, σ is the set of all the spinlike variables σ_i. In other words,

$$\sigma = (\sigma_1, \sigma_2, \sigma_3, ..., \sigma_N), \tag{2.7}$$

where N is the total number of lattice sites. The Ising model is a convenient way to label the possible atomic arrangements on a lattice. It should not be confused with atoms actually sitting at *fixed* atomic positions. As we mentioned earlier, a complete ensemble of microstates is associated with a given configuration and most of them correspond to atoms displaced from their ideal lattice sites.

In the following section, we will generalize the simple Ising nearest–neighbor *pair* Hamiltonian by expanding $F(\sigma, T)$ in *cluster functions.*

[7] Contrary to the crystallographic definition, it is customary in the field of lattice models, to refer to a "lattice" as any periodic structure of sites instead of just one site per unit cell.

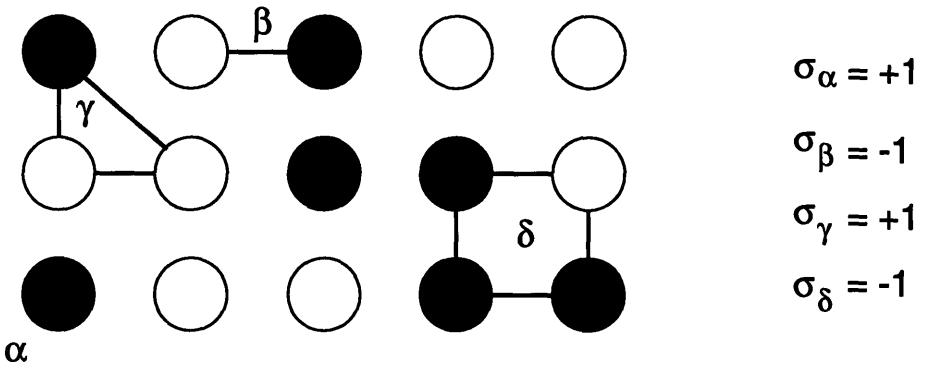

Figure 2-5: Two dimensional binary alloy lattice, where 4 different clusters are shown: α, β, γ, and δ. They represent a point, a pair, a triplet, and a quadruplet cluster respectively. The value of the cluster functions for these clusters is also indicated, following the convention that "black atoms"("white atoms") correspond to spinlike variables $\sigma_i = +1(-1)$.

2.1.3 The cluster expansion

A *cluster*, α, is a set of sites on a lattice. A cluster *function*, σ_α, on the other hand, corresponds to the product of all the spin variables σ_i at each site of the cluster,

$$\sigma_\alpha(\sigma) = \prod_{i \in \alpha} \sigma_i(\sigma), \tag{2.8}$$

where we have used the convention of naming the clusters with Greek subindices and the sites with Roman subindices. In figure 2-5, we show different clusters and their associated cluster functions for a two dimensional lattice.

Given an appropriate definition of an internal product, it can be shown that the cluster functions form an *orthonormal basis* of functions in configuration space [9, 34]. For two arbitrary scalar functions, $f(\sigma)$ and $g(\sigma)$, the scalar product can be defined as,

$$\langle f, g \rangle \equiv \frac{1}{\mathcal{N}} \sum_\sigma f(\sigma) g(\sigma). \tag{2.9}$$

The sum is over all possible $\mathcal{N}$ configurations of the lattice. Note that for a binary alloy, $\mathcal{N} = 2^N$, where N is the number of sites on the lattice.

Consequently, any function $f(\sigma)$ of the configuration of the lattice can be expressed as a linear combination of cluster functions:

$$f(\sigma) = \sum_\alpha C_\alpha \sigma_\alpha(\sigma), \tag{2.10}$$

where

$$C_\alpha = \langle f, \sigma_\alpha \rangle. \tag{2.11}$$

Equation 2.10 is usually called the *cluster expansion* of $f(\sigma)$. The energy and the elastic or lattice constants are a few examples of the properties that can be cluster expanded. In particular, since $F(\sigma, T)$ is a function of the configuration it can also be cluster expanded,

$$F(\sigma, T) = \sum_\alpha V_\alpha(T)\sigma_\alpha(\sigma), \tag{2.12}$$

where the expansion coefficients, $V_\alpha(T)$, are generally referred to as the *effective cluster interactions* (ECI's).

Expansion 2.12, can be thought of as a generalization of the Ising Hamiltonian, where not only are nearest–neighbor pair interactions used but also more distant pair, triplet, quadruplet, and larger cluster interactions.[8] Not all the ECI's are independent, but they can be related by the symmetry of the lattice. Equation 2.12 can be written as,

$$F(\sigma, T) = N\sum_\alpha{}' m_\alpha V_\alpha(T)\langle\sigma_\alpha\rangle(\sigma). \tag{2.13}$$

The prime in the sum indicates that the addition is over the non symmetry–equivalent clusters α. The coefficient m_α is the number of clusters equivalent to cluster α per site, and $\langle\sigma_\alpha\rangle(\sigma)$ is the average of the cluster functions over the equivalent clusters. These averages are often called *correlation functions.*

Even with the transformation used in the last equation, the number of ECI's diverges in the thermodynamic limit.[9] This implies that in order to compute phase diagrams an infinite number of coefficients should be computed. This is similar to the original situation since in any simulation an infinite number of total–energy calculations should, in principle, be done. However, the benefits of performing a cluster expansion of the lattice Hamiltonian become clear when one notes that in general, the ECI's decay very fast with respect to the cluster size. In metallic alloys, for example, the energy of the system depends mostly on the local atomic arrangements. When this is the case, a few clusters, with sites close together are enough to accurately describe the dependence of the Hamiltonian on σ. Even in systems in which the exact ECI's are long–range, as is the case of oxides (due to the Coulombic interactions), it can be shown that short–range ECI's can be used as an accurate approximation [39]. Consequently, expression 2.12 can be truncated after a maximal cluster α_{max},

$$F(\sigma, T) = \sum_{\alpha \leq \alpha_{max}} V_\alpha(T)\sigma_\alpha(\sigma). \tag{2.14}$$

The number and type of clusters that are actually needed in expansion 2.14 depend on the system. Convergence of the cluster expansion should always be carefully

[8]The ECI's should not be confused with "real" interactions. For example, a pair $V_\alpha(T)$ is not the actual interaction between two atoms but it is just a *coefficient* in an expansion.

[9]Finite–size simulations are used to approximate the thermodynamic limit.

checked. There are different techniques to accelerate this convergence.[10]

The application of the cluster formalism we just described is computationally cumbersome when more than two different species are present [9, 42]. However, there are some cases where the problem can be reduced to two binary problems that are coupled through the ECI's. For example, in oxides, the cation and anion sublattices do not interchange ions.[11] When there are at most two different species on each sublattice, the problem can be treated as two binary systems that interact through coupling ECI's [43].

2.1.4 The computation of ECI's

The temperature dependence of the ECI's arises from the nonconfigurational excitations in equation 2.5. As we already mentioned, we will just consider atomic vibrations since they are the largest contributions in most oxide systems. In the harmonic approximation, the temperature dependence can be linearized above the Debye temperature [36],

$$V_\alpha = V_\alpha^{chem} + k_b T V_\alpha^{vibr}. \tag{2.15}$$

The first term in the right–hand side of equation 2.15 represents the *chemical* contribution to the ECI coming from $E_o(\sigma)$ in equation 2.6. The second term is the contribution from the *vibrational* free energy. When only configurational excitations are considered, the last term is zero. In the rest of the thesis, we will focus on efficient ways for computing the chemical ECI's.[12] There are three well established approaches to compute these ECI's: the **Connolly–Williams** method, the **direct configurational averaging** technique, and the **coherent–potential approximation** with the **generalized–perturbation** method.

The **Connolly–Williams** method (CWM) takes advantage of the fact that the cluster expansion can be truncated at some maximal cluster. By computing total energies for a finite set of ordered structures, for which the σ_α's are easily computed, a set of linear equations on the ECI's is formed based on equation 2.14. In the original formulation [10], the *same* number of structures and ECI's were used. However, working with more structures than unknown ECI's usually gives more stable ECI's through a least–square fit.[13]

In the **direct configurational average technique**, equation 2.11 is followed as close as possible [44] . For example, for a pair interaction in a binary alloy A–B, this

[10]See for example reference [40], where the cluster expansion is recast in reciprocal space, or reference [41] where the composition–dependent, but configuration–independent, long–range elastic energy is analyzed separately from the remaining *local* contributions.

[11]In most systems, the size mismatch and a large increase in the electrostatic energy prevent these interchanges from happening.

[12]For the vibrational ECI, we use the method recently developed by Garbulsky [34]. The ECI's are fit to the vibrational free energy of a few structures. These free energies are computed within the harmonic approximation by diagonalizing the dynamical matrix.

[13]Since the cluster expansion is truncated, a direct inversion does not provide the *exact* ECI's. Contributions from clusters larger than the maximal cluster are *folded–back* into the smaller clusters. Using more structures than ECI's tends to minimize these errors.

equation is equivalent to

$$V_{pair} = \frac{1}{4}(\langle E_{AA}\rangle + \langle E_{BB}\rangle - \langle E_{AB}\rangle - \langle E_{BA}\rangle), \tag{2.16}$$

where $\langle E_{ij}\rangle$ corresponds to the energy when the pair cluster is occupied by atoms i and j, averaged over all possible occupations of the other sites. In practice, a finite crystal is built around the pair whose ECI we want to compute, and the occupation of that cluster is held fixed. Then, the energy is averaged over all possible configurations of the other sites.[14] This average has to be repeated for the different configurations of the pair. Tight–binding and recursion techniques are used in the calculations.

The **coherent–potential approximation** [45] is a mean field theory to compute the electronic structure of the disordered alloy. This state is then considered as a *reference* state for the **generalized–perturbation** [45] method to produce concentration dependent ECI's.

The last two techniques have the advantage that the ECI's are not fit but the *exact* definition is used. On the other hand, up to date, no atomic relaxations away from the ideal lattice sites have been included in their formalism. The effect of relaxations is very important in oxides since size mismatch of the ions is a common feature of these materials. The Connolly–Williams method can naturally incorporate these effects since the structural energies used as inputs (usually called *direct energies*) can always be the ones from relaxed structures. Furthermore, *any* total–energy technique, from very simple classical approaches to very complex quantum–mechanical methods, can be used to compute the direct energies.[15] Consequently, the Connolly–Williams method seems to be the best choice in oxides.

The Connolly–Williams procedure is illustrated in figure 2-6. The direct energies usually correspond to formation energies of periodic structures with *small* unit cells. The number of ECI's required to obtain a converged cluster expansion depends on the system and determines the number of total–energy calculations that are needed. Due to the characteristic long range of the interactions in oxides, many more ECI's than in metallic systems have to be computed.

None of these procedures indicates what clusters should be used to obtain a convergent cluster expansion. Since the degree of convergence is not known, the cluster–expanded energies should always be checked against the direct energies. Some of these direct energies can be left out of the fit to be later compared with the predictions of the cluster expansion. More complex schemes can also be used to check the clusters chosen and their ECI's, by carefully watching the effect of adding or taking out them during the fit [46].

It is important to realize that the Connolly–Williams method is a fit to the *absolute* value of the formation energies, while most of the phase diagram features depend on *subtle differences* of these values. Furthermore, it can not guarantee that the *direct* ground states[16] be predicted by the computed ECI's. Whenever there are close

[14] Usually, 30 different configurations are enough to obtain a good convergence [44].

[15] This is also true for the DCA, though for complex methods it is very computer intensive.

[16] Ground states are arrangements of atoms on the lattice that minimize the energy of the system.

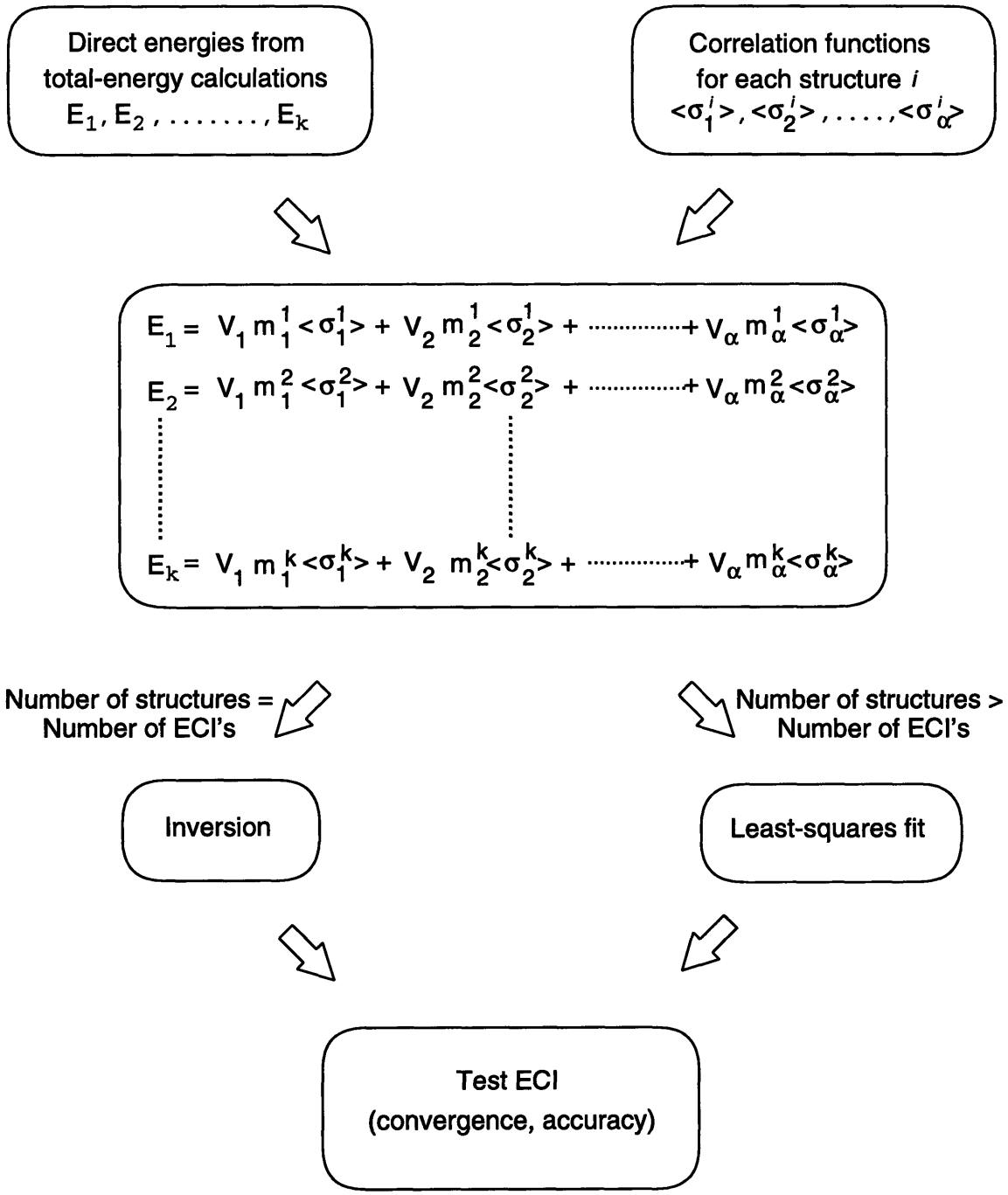

Figure 2-6: Procedure for computing effective cluster interactions using the Connolly–Williams method. The system of equations is either solved by matrix inversion, if the number of direct energies and ECI's is the same, or by fitting the ECI's, if they are less than the number of structural energies.

metastable structures, they can became stable during the fit. Finally, as we already mentioned, there is no systematic way of truncating the expansion. These difficulties can be overcome by a linear programming technique recently developed [12], in which not only are the direct energies fit to, but also the ground–state line[17] and the relative values of the formation energies.

2.1.5 Thermodynamic properties

Once the lattice Hamiltonian has been determined, thermodynamic properties of the system, such as phase diagrams, can be obtained. Two traditional approaches in lattice models have been used in the past years: **Monte Carlo** (MC) simulations and the **cluster variation method** (CVM).

For any large lattice model, the total number of possible configurations is astronomically large and sampling these states is not straightforward. The **Monte Carlo** method is a way of generating statistical trajectories, so that averages over these states correspond to the equilibrium ensemble averages. Many good articles have been written about the method (see [48] and references therein) and is not our intention to review them here. We would just like to point out to a few limitations of the method when applied to phase diagrams.

As we mentioned, MC simulations provide a way of obtaining thermodynamically–averaged properties, such as the internal energy. Free energies can be computed in MC by performing a time–consuming integration from states where their value is known (i.e., ordered state at absolute zero or disordered state at infinite temperature). This procedure is not trivial and in general, a simpler approach is adopted to compute phase boundaries. One can, for example, look for discontinuities in the temperature dependence of the concentration (at constant chemical potential) or even simply "inspect" the structures during the simulation.

Even when free energies are not computed, MC simulations present problems, specially at low temperatures or for highly stoichiometric compounds. Under these conditions, averaging times become very large and complex phase boundary features might be impossible to determine (hysteresis effects become important).

The **cluster variation method** is a generalized mean field technique that treats correlations exactly between sites within a maximal cluster, with all other correlations implicitly approximated by a superposition over smaller clusters. The CVM has the advantage that it gives a precise value for the free energies. These free energies are written in a variational form with respect to the probabilities of all possible occupations on all the clusters within the maximal cluster.

They correspond to the stable phases at 0 ^{o}K. If the right ground states are not reproduced by the cluster expansion, the topology of the phase diagram at low temperature will be wrong. The problem of finding *all* the ground–state structures for a general Ising–like Hamiltonian is nontrivial. Many approaches have been developed to find the ground–state structures [45, 47] and their predictions are limited by the current computer power. For a review of all these techniques, see reference [34] and [45].

[17]The ground–state line is the line formed by the ground–state structures in an energy vs. composition plot.

At low temperatures or near stoichiometric phases, some of these variational parameters are very close to zero and numerical instabilities appear in the minimization process. Another disadvantage of the method is that only a limited range of ECI's can be used. In the CVM, the maximal cluster should contain at least one cluster that corresponds to each non–zero ECI. Having a large maximal cluster increases the computational burden considerably[18] and MC simulations are preferred over the CVM when long–range interactions are necessary to model the system. The CVM, though widely applied to metallic alloys, is not usually used in oxides since the electrostatic contributions to the lattice Hamiltonian make the ECI's long–ranged. More details on the CVM can be obtained in references [13, 45, 49, 50].

2.2 Low–temperature expansion of a thermodynamic potential

Low–temperature expansions for the free energy of the Ising model have been used for a long time [51]. Systematic methods for deriving the expansion coefficients have been studied for the Ising Hamiltonian with pair interactions [29, 51, 52, 53, 54]. Here, we apply the LTE to the generalized Ising Hamiltonian we developed in section 2.1.3 expressing the energy in cluster functions (not necessarily pairs). By expanding the grand potential around different ground states, the low–temperature region of any phase diagram can be computed regardless of its complexity.

The coefficients of the expansion are computed by a direct counting scheme, taking advantage of the symmetry of each structure. This is very similar to the standard procedures used to compute the input data for the CVM [50]. As we will show, only a few terms need to be considered in the LTE, making the construction of the expansion relatively straightforward. The low–temperature expansion is well behaved for highly stoichiometric phases with little disorder. This condition naturally arises for all nondegenerate ground states as the temperature is lowered.

2.2.1 Formalism

For a binary A–B alloy, the grand potential per mole, ϕ, can be written as:[19]

$$\phi(T,\mu) = u - Ts - \frac{\mu}{2}(x_{\mathrm{A}} - x_{\mathrm{B}}), \tag{2.17}$$

where u, s, and x are the molar energy, entropy, and atomic fraction respectively and T is the temperature. The chemical potential μ is defined as the difference in

[18]The computational requirements of the CVM increase rapidly as the symmetry is lowered or the number of different species is more than two. For example, the number of variational parameters increases from 742 on the fcc lattice to 2679 in the simple $L1_2$ ordering when the 13–14 point cluster combination (see figure 2-11) is used as the maximal cluster.

[19]See reference [55]. Also, recall that we assume the pressure to be equal to zero.

chemical potentials between species A and B:

$$\mu = \mu_{\mathrm{A}} - \mu_{\mathrm{B}}. \tag{2.18}$$

Equation 2.17 can be rewritten as

$$\phi(T,\mu) = u - Ts + \mu x_{\mathrm{B}} - \frac{\mu}{2}. \tag{2.19}$$

The last term in the right–hand side of equation 2.19 can be omitted when computing phase diagrams as it only contributes a constant amount to ϕ. The grand potential can then be obtained from the grand partition function, $Z(T,\mu)$, in the following way:[20]

$$\phi(T,\mu) = -\frac{1}{\beta N}\ln\left(Z(T,\mu)\right) = -\frac{1}{\beta N}\ln\left(\sum_{\sigma} e^{-\beta(E(\sigma)+\mu N_B(\sigma))}\right). \tag{2.20}$$

Here, N is the total number of lattice sites and $N_B(\sigma)$ is the number of sites occupied by species B for configuration σ.[21]

For a given ground state, the energy, E_o, can be factored out from equation 2.20,

$$\phi(T,\mu) = \frac{E_o}{N} + \mu x_{\mathrm{B}}^{o} - \frac{1}{\beta N}\ln\left(1 + \sum_{\sigma}{}' e^{-\beta(\Delta E(\sigma)+\mu n(\sigma))}\right). \tag{2.21}$$

In this equation, x_{B}^{o} is the atomic fraction of species B in the ground state, $n(\sigma)$ is the number of spins in configuration σ that are overturned with respect to the ground–state arrangement, and the prime in the sum indicates that we sum over all possible configurations except for the ground state. We also define the excitation energy $\Delta E(\sigma)$ as,

$$\Delta E(\sigma) = E(\sigma) - E_o. \tag{2.22}$$

In equation 2.21, the logarithm can be expanded in a Taylor series,

$$\phi(T,\mu) = \frac{E_o}{N} + \mu x_{\mathrm{B}}^{o} - \frac{1}{\beta N}\sum_{j=1}^{\infty}\left[\frac{(-1)^{(j+1)}}{j}\left(\sum_{\sigma}{}' e^{-\beta(\Delta E(\sigma)+\mu n(\sigma))}\right)^{j}\right]. \tag{2.23}$$

Using the linked cluster theorem,[22] equation 2.23 can be rewritten in a simpler form,

[20] For simplicity, we will assume that $F^{exc}(\sigma,T) = 0$ in equation 2.5.

[21] One should note that μ plays the role of an external magnetic field in the Ising spin language. This chemical potential selects the different ground states so that ϕ can be expanded, at low temperatures, around any of them.

[22] This theorem states that it is sufficient to keep the terms proportional to N in the expansion of $\ln Z$. The other contributions cancel out. This can be seen from the fact that $\phi(T,\mu)$ is an *intensive* property. The theorem applies to various types of expansions, and a formal proof can be found in reference [56]. See also reference [57].

$$\phi(T,\mu) = \frac{E_o}{N} + \mu x_B^o - \frac{1}{\beta N}\sum_{\sigma}'' e^{-\beta(\Delta E(\sigma)+\mu n(\sigma))}, \tag{2.24}$$

in which the sum is performed by grouping all the terms with the same number of overturned spins and the same excitation energy. The double prime means that only the resulting terms with coefficients linear in N are summed over. At low enough temperatures, usually only a few terms need to be considered in the sum. We will show that these *low* temperatures are *high* enough to get reliable free energies up to values where Monte Carlo simulations become practical.

In the present form, the LTE requires that a finite number of ground states be present in the system except for a trivial degeneracy[23] (i.e., different ground–state configurations that transform into each other through trivial symmetry operations of the lattice). For the system and range of interactions used in this work, it is possible to find all the fcc ground–state structures in the Pd–V alloy [58]. In the CaO–MgO system, the only stable structures are the *pure* oxides.

2.2.2 Implementation

The practical implementation of equation 2.24 involves two main tasks: the computation of $\Delta E(\sigma)$ and the determination of the different configurations that should be summed over. The excitation energy of overturning spins from the ground–state configuration can be computed using the cluster expansion. When just one spin, at site i, is overturned,

$$\begin{aligned}
\Delta E(\sigma^i) &= \sum_{\alpha} V_\alpha \sigma_\alpha(\sigma^i) - V_\alpha \sigma_\alpha(\sigma^o) \\
&= -2\sum_{\alpha \supset i} V_\alpha \sigma_\alpha(\sigma^o) \\
&= -2\sum_{\Omega_\alpha \supset i} a_{i\alpha} V_\alpha \sigma_\alpha(\sigma^o).
\end{aligned} \tag{2.25}$$

σ^i is the configuration of the lattice when the spin at site i is flipped, σ^o is the configuration of the ground state, and $a_{i\alpha}$ is the number of α clusters that contain the site i. This last quantity can be computed as[24]

$$a_{i\alpha} = \frac{m_\alpha}{m_i} m_{i\alpha}, \tag{2.26}$$

where m_α and m_i are the multiplicities of the cluster α and the site i respectively, and $m_{i\alpha}$ is the number of sites of the same type as i in cluster α. Note that in

[23] If n_{gs} is the number of trivially degenerate structures of a given ground state, a term of the form $-\frac{1}{\beta N}\ln(n_{gs})$ should be added to the grand potential. However, since $N \to \infty$ this term goes to zero in the thermodynamic limit and consequently, can be safely ignored.

[24] Note that "$m_\alpha m_{i\alpha}$" *overcounts* the number of i–type sites ("m_i") because each i–type site belongs to "$a_{i\alpha}$" α clusters. Consequently, $a_{i\alpha} m_i = m_\alpha m_{i\alpha}$.

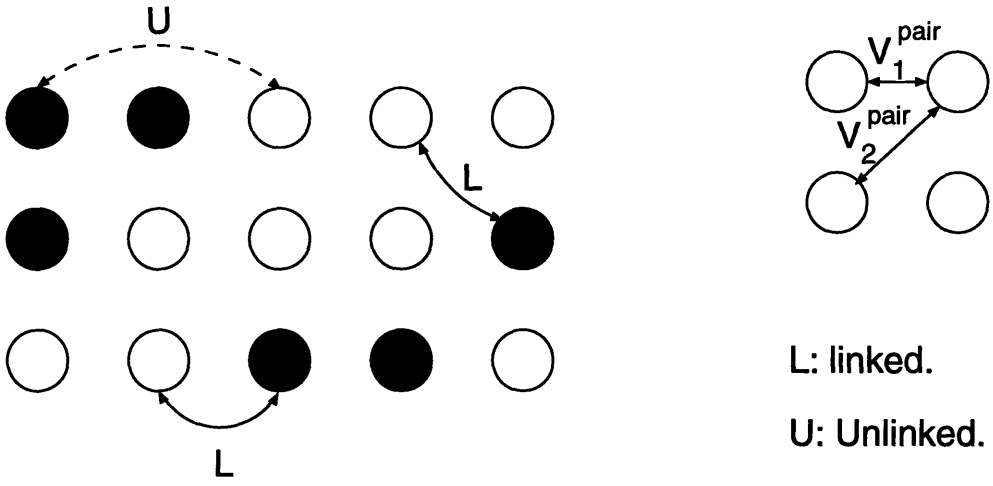

Figure 2-7: Examples of linked and unlinked pair clusters on a two dimensional lattice. The only ECI's different from zero are V_1^{pair} and V_2^{pair}.

equation 2.25, the sum is over all the different *sets* of clusters, Ω_α. Each of these sets is formed by all the clusters α that are related by symmetry operations of the lattice. Equation 2.25 can be used iteratively to compute the energy of overturning more than one spin by replacing σ^o with σ^i and so on.

The different configurations that should be summed over in equation 2.24 are grouped together according to their excitation energy. This is a trivial operation to do when flipping just one spin. The different excitation energies correspond to overturning spins on the symmetry–distinct sites of the ground state. Consequently, the coefficients of the terms in the sum are the multiplicity of each site.

In configurations with multiple spins overturned, the excited spins can form a *linked* or an *unlinked* cluster. A *linked* cluster is one in which the overturned spins are interconnected through the interactions of the cluster expansion. All the linked clusters related by symmetry have the same excitation energy. The number of these clusters on the lattice scales linearly with N. On the other hand, an *unlinked* cluster has one or more spins that are not connected with *any* of the other overturned spins through *any* of the ECI's (see figure 2-7). From the unlinked terms, only those contributions coming from "excluded volume effects" (the same spin can not be flipped twice) and "counterterms" from linked clusters (the linked clusters are "not available" as unlinked excitations) need to be retained.[25] See examples in section 2.3.

The LTE can be built simply from the information that is already required for the

[25]For example, if two spins are being overturned on a cubic lattice with N sites, there are $\binom{N}{2} = \frac{N(N-1)}{2}$ ways of picking them. If only nearest neighbor interactions are defined in the Hamiltonian, there are $3N$ linked pair clusters. Consequently, the number of unlinked clusters is $\frac{N(N-1)}{2} - 3N$. Since only terms linear in N should be kept, the coefficient in the expansion corresponding to the unlinked clusters is $-\frac{N}{2} - 3N$ ("$-\frac{N}{2}$" comes from the excluded volume effect and "$-3N$" is the "counterterm" from the linked clusters).

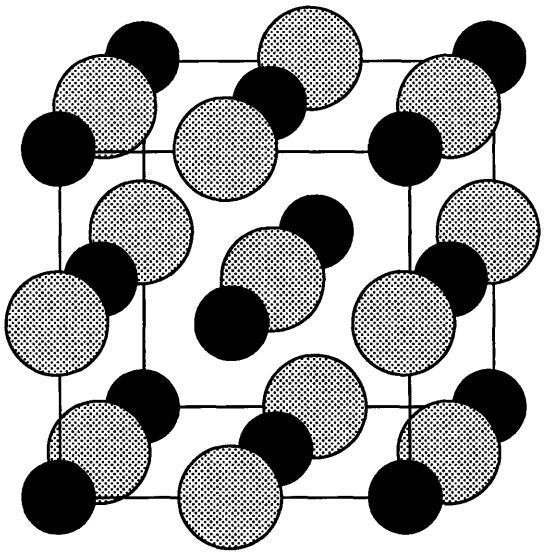

Figure 2-8: The rocksalt crystal structure. The black spheres represent magnesium or calcium atoms, while the grey ones are the oxygen atoms.

construction of the CVM functional. The linked clusters, their multiplicity, and the $m_{i\alpha}$ are automatically found for each ground state with a computer code that uses a direct enumeration procedure combined with simple group–theoretical concepts [50]. The same code is used for computing the CVM free energy expressions. From these data, the LTE coefficients are generated. This procedure is very fast and needs to be performed once for a given ground state and set of cluster interactions.[26]

2.3 Applications of the low–temperature expansion

2.3.1 The MgO-CaO phase diagram

MgO and CaO crystallize in the rocksalt structure shown in figure 2-8. This structure can be thought of as two interpenetrating fcc lattices. When they are mixed, the calcium and magnesium ions distribute themselves on the fcc cation sublattice while the oxygen sublattice remains *fully* occupied. Consequently, we can regard this system as a substitutional *binary* alloy with occupation variables σ_i only defined on the sites of the cation sublattice. We do not assume that the ions occupy the ideal positions on the lattice but only that there is a one–to–one correspondence between ions and lattice sites. Note that, although the anion sublattice is fully occupied, the oxygen ions are still allowed to move away from their ideal lattice sites.

[26]Note that we assumed temperature–independent ECI's. The use of temperature–dependent ECI's (through the incorporation of nonconfigurational excitations) is straightforward.

The substitutional species (Mg and Ca), have the same valence charge (isovalent system) and consequently, no charge–compensating defects need to be introduced. This considerably simplifies the calculations. Moreover, the above assumption that the oxygen sublattice remains fully occupied is likely to be valid. Furthermore, the fact that both Ca and Mg ions have the same valence charge, implies that the dependence of the long–range interactions on configuration is very small, resulting in a rapidly convergent cluster expansion.

The CaO–MgO phase diagram is very simple, and *any* of the methods already mentioned can be used to compute its boundaries. The only purpose of introducing it here is to clarify the concepts of the previous section before dealing with the complex Pd–V phase diagram.

We will use expression 2.24 to compute the grand potential around the CaO and MgO ground states. We will start with the terms corresponding to overturning one spin. This is equivalent to the exchange of one Ca (Mg) with one Mg (Ca) on an otherwise pure Ca (Mg) sublattice. The energy of this exchange corresponds to the formation energy of a single substitutional defect. Since all the sites on the cation sublattice are equivalent for the CaO and MgO ground states, equation 2.24 reduces to:[27]

$$\phi_{\mathrm{CaO}}(T,\mu) = -\frac{1}{\beta}e^{-\beta(\Delta E_{\mathrm{CaO}}+\mu)}, \tag{2.27}$$

$$\phi_{\mathrm{MgO}}(T,\mu) = \mu - \frac{1}{\beta N}e^{-\beta(\Delta E_{\mathrm{MgO}}-\mu)}, \tag{2.28}$$

where ΔE_{CaO} (ΔE_{MgO}) is the energy of replacing a Ca (Mg) by a Mg (Ca) in pure CaO (MgO), and ϕ_{CaO} and ϕ_{MgO} are the "one flip" low–temperature expansions for the CaO and MgO phases respectively.

The phase boundaries can be obtained by requiring $\phi_{\mathrm{CaO}}(T,\mu) = \phi_{\mathrm{MgO}}(T,\mu)$ and solving for μ at each desired temperature [55]. The concentration of the phase boundaries is given by,

$$x_{\mathrm{CaO}} = \frac{\partial \phi_{\mathrm{CaO}}}{\partial \mu} = e^{-\beta(\Delta E_{\mathrm{CaO}}+\mu)}, \tag{2.29}$$

$$x_{\mathrm{MgO}} = \frac{\partial \phi_{\mathrm{MgO}}}{\partial \mu} = 1 - e^{-\beta(\Delta E_{\mathrm{MgO}}-\mu)}. \tag{2.30}$$

Since $\mu \to 0$ when $T \to 0$, if $\Delta E_{\mathrm{CaO}} < \Delta E_{\mathrm{MgO}}$ the miscibility gap will be "tilted" towards the MgO–rich side, with a larger solubility of MgO in CaO than vice versa.[28] In section 5.2.1, we compute these energies and find $\Delta E_{\mathrm{CaO}} < \Delta E_{\mathrm{MgO}}$, in agreement with the experimental phase diagram of figure 2-1. Using these values, we computed

[27] In what follows, we identify CaO with the "A" species and MgO with the "B" species of equation 2.24. Consequently, x_B^o is equal to 0(1) for the CaO (MgO) phase. Since the energy is defined except for a constant, we can safely assume that E_o is zero for both CaO and MgO. Once this choice is made, the zero of any mixture is fixed.

[28] This is in agreement with the fact that if $\Delta E_{\mathrm{CaO}} < \Delta E_{\mathrm{MgO}}$ it "costs" more, at the same temperature, to add a Ca on the cation sublattice of MgO than vice versa.

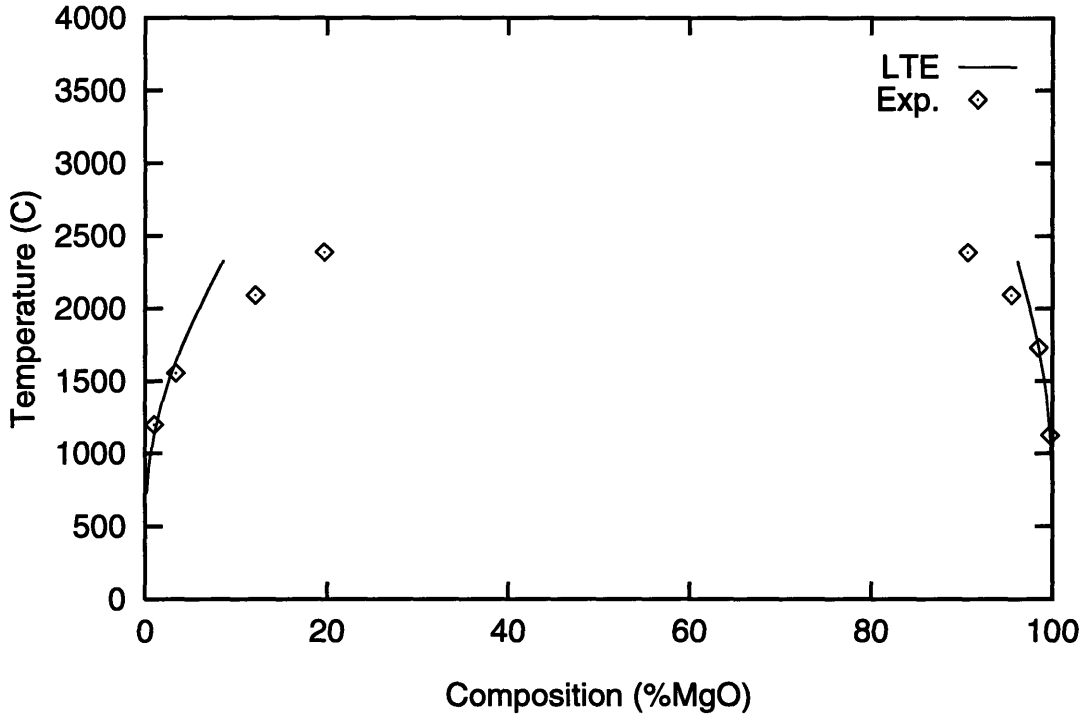

Figure 2-9: Solubility limits predicted by the low–temperature expansion using just the single–defect energies. The experimental points are from reference [30].

the solubility limits (see figure 2-9). The low–temperature expansion correctly predicts the asymmetry of the miscibility gap. Also, the agreement with the experimental points is good up to relatively high temperatures.[29]

If the energy of overturning spins were independent of the atomic configuration, equations 2.27 and 2.28 would be exact. However, this is not true, and a *correction* due to the fact that the spins are actually "linked" has to be introduced. These correction terms are the remaining contributions in expansion 2.24. We will show how to incorporate their effect in the next section.

2.3.2 The Pd–V phase diagram

To illustrate the application of the LTE and demonstrate how it can be combined with the CVM and MC simulations, we computed the phase diagram of a system that models the Pd–V substitutional alloy. The Pd–V system has been extensively studied both theoretically [12, 58, 59, 60, 61, 62, 63, 64] and experimentally (see reference [31] and references therein). In the Pd–rich side of the phase diagram, the stable phases are based on the fcc lattice while on the V–rich side PdV_3 is stable in the

[29]In chapter 5, we compute the phase diagram using Monte Carlo simulations. For this case, the prediction of the simulation and the experiments coincide. This is why it is fair to compare the LTE prediction with the experiments, and not to a Monte Carlo calculation, to assess the accuracy of the method.

cluster	ECI (meV/atom)
V_1^{Pair}	30.48
V_2^{Pair}	-3.40
V_3^{Pair}	6.90
V_4^{Pair}	8.33
$V_1^{Triplet}$	8.01
$V_2^{Triplet}$	-1.68
$V_3^{Triplet}$	-1.36
$V_4^{Triplet}$	10.97
$V_1^{Quadr.}$	-2.15

Table 2.1: Effective cluster interactions (ECI's) used to model the Pd–V system. The clusters are named according to the convention followed in figure 2-10.

A15 structure (which is not an fcc superstructure, see reference [45] for a description of the structure). Pure vanadium is bcc. To test the LTE, we computed the fcc phase diagram of the Pd–rich side.

In order to compute the ECI, total–energy calculations for different structures in the Pd–V system need to be performed. We used the so–called linear muffin–tin–orbital method in the atomic–sphere approximation [65] (LMTO–ASA). Details of this technique are given in chapter 3. For this system, the accuracy of the method is comparable to the most accurate quantum–mechanical approach. In each calculation, the total energy was minimized with respect to a hydrostatic volume deformation. Internal relaxations were neglected, in accord with other calculations which found them to be negligible [64]. Details of these computations and the resulting formation energies were reported in reference [64].

We performed a Connolly–Williams fit to the energy of these structures. The resulting ECI's are shown in table 2.1. We used 9 different ECI's: pairs up to fourth nearest neighbors, 4 triplets, and the nearest–neighbor quadruplet as shown in figure 2-10. Going beyond this range of interactions implies using a prohibitively large CVM maximal cluster. We used the 13–14 point cluster combination shown in figure 2-11 as the maximal cluster.

By minimizing equation 2.14 under the constraints that the probabilities on the 13– and 14–point clusters be between zero and one [58], we computed the ground states predicted by these ECI's. They are shown in figure 2-12. A description of the different ground–state structures can be found in references [45] and [66]. To clarify the relation with the experimental Pd–V phase diagram, we also show the calculated energy of the A15 structure in figure 2-12. At stoichiometry, PdV_3 is so stable, that its tie–line with the $MoPt_2$ structure on the Pd–rich side, makes the $L1_0$ structure metastable, in accordance with experimental information [31]. Consequently, although it is not an fcc superstructure, we decided to include the A15 structure in the calculations since it clearly affects the fcc Pd–rich side of the phase diagram.

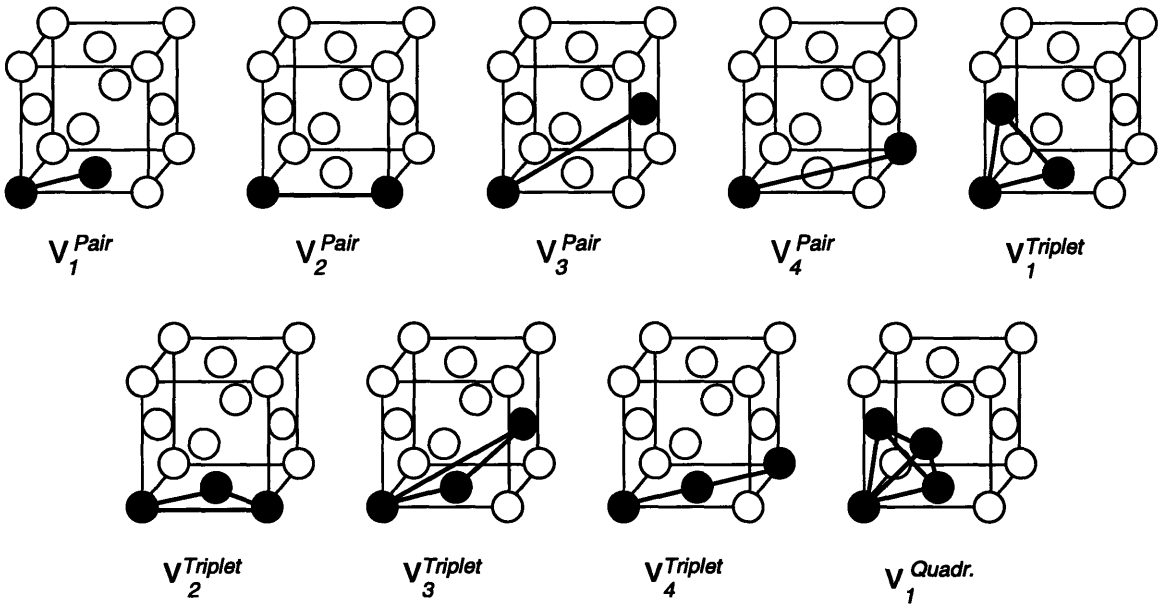

Figure 2-10: Clusters used in the Pd–V cluster expansion. The pairs are identified according to their length, and the triplets according to the length of their longest side, the other two sides being nearest neighbors.

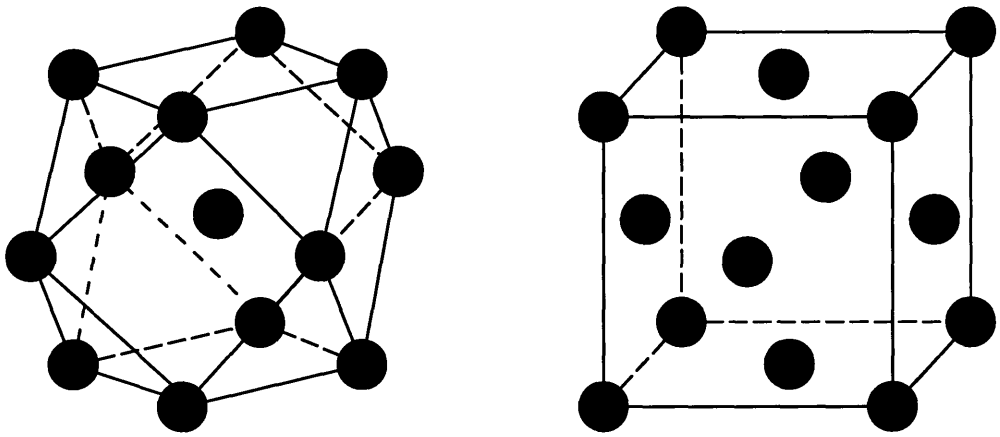

Figure 2-11: Maximal clusters used in the CVM. The 13–point cluster is obtained by taking a point and all its nearest neighbors on the fcc lattice, and the 14–point cluster corresponds to the conventional fcc unit cell.

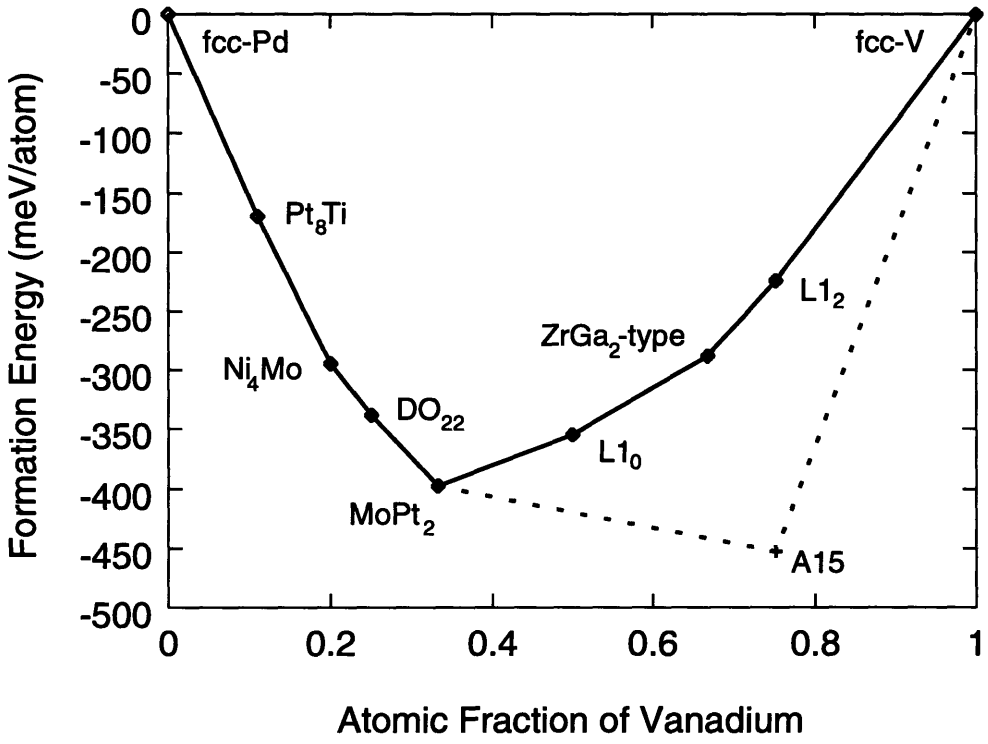

Figure 2-12: Ground states of the Pd–V system predicted by the fcc ECI's shown in table 2.1. The solid line represents the fcc ground–state line. The dashed line corresponds to the change in the ground–state line when the A15–type phase is included. The A15 structure is not an fcc superstructure. Its formation energy was computed by the LMTO–ASA method.

For simplicity, we treated the A15 phase as a line compound with no configurational disorder. The only phase boundary this approximation will affect is the $MoPt_2$–A15 two–phase region.

The $MoPt_2$, DO_{22}, and Pt_8Ti structures have all been observed experimentally [31, 32]. It is a remarkable success of this *ab initio* method that they are all correctly predicted, given the strong ground–state competition in this system [12]. The Ni_4Mo structure, predicted by the cluster expansion in table 2.1, has never been reported. This structure is metastable if one uses the direct LMTO–ASA energies (to which the cluster expansion was fit). The appearance of the Ni_4Mo as a ground state is therefore a direct consequence of truncating the cluster expansion at the 4th nearest–neighbor distance. Using the linear programming techniques mentioned in section 2.1.4, it can be demonstrated that a cluster expansion with only pairs and multiplet interactions up to the 4th nearest–neighbor distance always makes Ni_4Mo a ground state when Pt_8Ti, $MoPt_2$, and DO_{22} are ground states [12]. Although this problem can be resolved by including the 7th or 8th nearest–neighbor pair interactions, we limited ourselves here to the interactions in table 2.1. Longer–ranged interactions would make the CVM intractable and deprive us of a tool to benchmark the LTE, which is the primary purpose of this section.

In figure 2-13, we show the computed phase diagram. The high–temperature part (dashed line) was obtained using a Monte Carlo simulation on a 20x20x20 lattice with periodic boundary conditions. Sampling was done in the grand canonical ensemble over typically 5000 MC passes, after 5000 MC equilibration passes. To speed up calculations, a divided local environment sampling approach [46, 63] was used to tabulate excitation energies from overturning spins. The phase boundaries were found by observing discontinuities in concentration vs. temperature (at constant chemical potential). At these high temperatures little or no hysteresis is observed. At temperatures around 1000 °K the equilibration times become larger and problems with metastable states start to appear during the simulation.

Some phases, such as DO_{22}, remain stoichiometric up to very high temperatures resulting in very poor sampling in a MC simulation. However, this persistent stoichiometry also allows the LTE (solid line in figure 2-13) to be used with only a few terms in the expansion. For example, the LTE with two spin–flip excitations converges well up to at least 1100 °K for the DO_{22} phase and up to 1300 °K for the $MoPt_2$ phase. The convergence of the LTE was tested by recomputing the phase boundaries with terms in the expansion corresponding to up to three spin flips. No significant changes occurred for temperatures bellow the ones previously mentioned. As can be seen from figure 2-13, the results of the MC simulation and the LTE expansion join smoothly. The use of the LTE was indispensable for determining the shape of the phase diagram around 1000 °K and for finding the peritectoid reaction of the Pt_8Ti–type phase.

Only for the disordered fcc phase is the LTE problematic. Large solubility limits are present at very low temperatures and consequently, many terms need to be kept in the free energy expansion of equation 2.24. On the other hand, the free energy of this phase can be most easily computed with the CVM as it has a higher symmetry than the ordered phases. Consequently, for temperatures higher than 100 °K we replaced

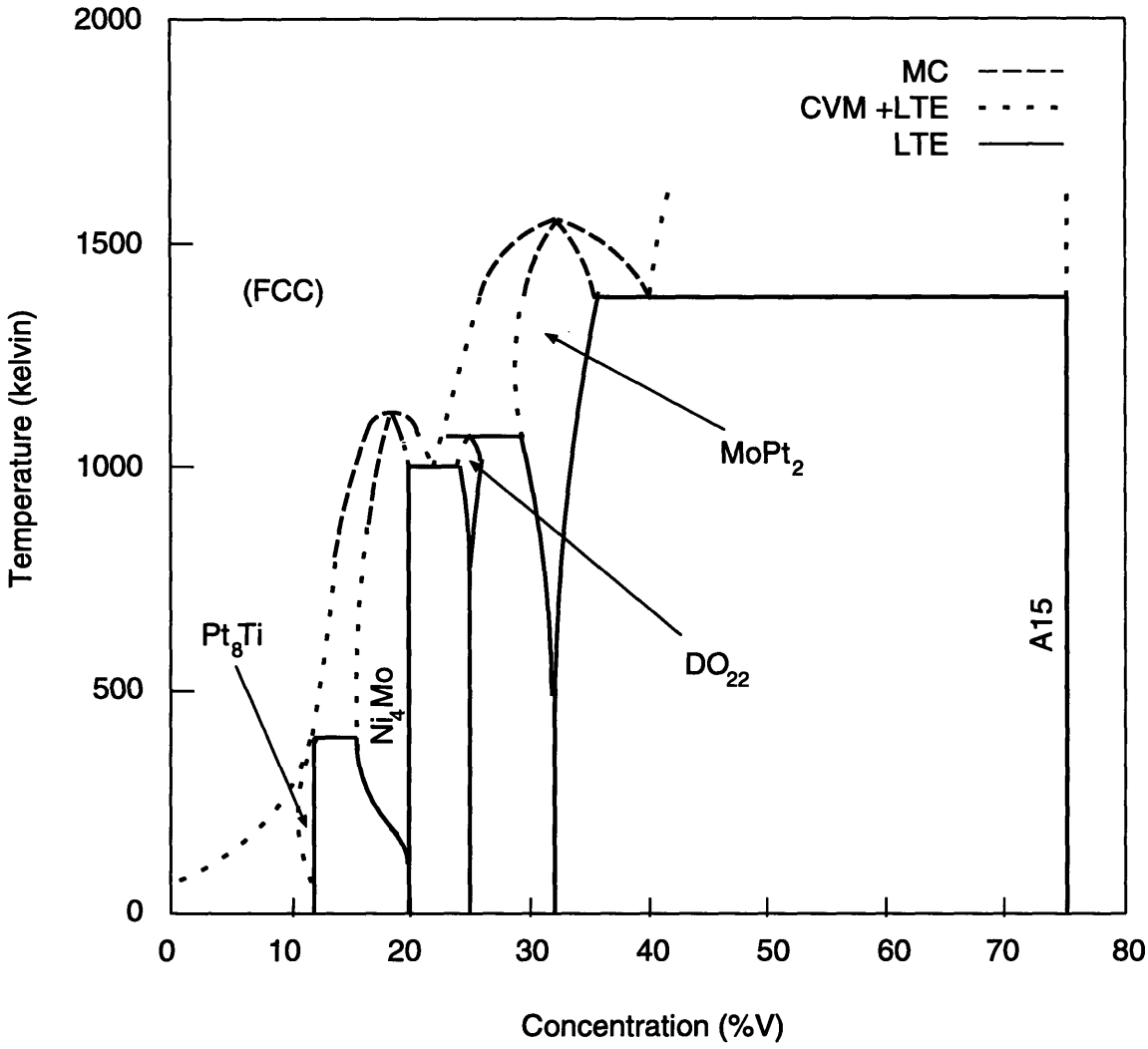

Figure 2-13: Phase diagram for an alloy that models the Pd–V system obtained with the combination of three different methods: cluster variation method (CVM), Monte Carlo (MC) simulations, and the low–temperature expansion (LTE). The solid lines represent low–temperature expansion predictions and the dashed lines are the results of a Monte Carlo simulation. The dotted lines correspond to phase boundaries computed using the CVM and the LTE free energies together. Monte Carlo simulations were performed for temperatures above 700 °K. The overlap between the methods is not shown for clarity.

the LTE free energy of the fcc phase by the CVM free energy. The phase boundaries computed with this combination of free energies are shown in figure 2-13 as dotted lines.

Although different approximations are involved in the LTE, CVM, and MC simulations, all phase boundaries in the Pd–V system join very smoothly.

2.4 Conclusions

In this chapter, we showed how we can map the alloy problem onto a lattice model. By coarse–graining the system partition function to the partition function of a lattice model, an effective Hamiltonian for the space of substitutional excitations was constructed. This Hamiltonian can account for other entropic effects such as vibrations and electronic excitations. We do not assume that the ions occupy the ideal positions on the lattice, but only that there is a one–to–one correspondence between ions and lattice sites.

The generalized Ising Hamiltonian was explicitly constructed by expanding it in an orthonormal basis set of cluster functions. In practice, this expansion is truncated at some maximal cluster and its coefficients (ECI's) are obtained from total–energy calculations. In principle, one only needs as many ordered arrangements as there are nonzero ECI's. However, many more are used to obtain a stable least–squares fit. Finding these energies is the computing–intensive part of *ab initio* models for obtaining phase diagrams. Especially in oxides, that have large and complex unit cells, current accurate methods are not fast enough. Solving this problem will be the focus of the following chapters.

Monte Carlo simulations or the cluster variation method are usually used to compute phase boundaries from the lattice Hamiltonian we defined. However, both methods present numerical problems at low temperature. We overcame these difficulties by extending the low–temperature expansion formalism of the grand potential energy to the alloy Hamiltonian with multi–site interactions. With this expanded free energy, we were able to determine complex temperature–composition phase diagrams under conditions in which the use of MC or the CVM is nontrivial or even impossible to complete in a reasonable amount of computer time. We showed that with just a few terms in the expansion, the LTE is an accurate and simple tool to compute the free energies up to temperatures where the other more traditional methods can be used.

As an illustration, we computed the solubility limits of CaO in MgO and vice versa and the phase diagram of a system that models the fcc Pd–rich side of the Pd–V alloy. We demonstrated that the LTE, MC simulation, and CVM predictions join smoothly and can be used as complimentary techniques. Furthermore, the coefficients of the LTE can be obtained from the same information used to build the CVM free energies which makes this approach very easy to implement.

Chapter 3

Total–energy methods

As described in chapter 2, the formation energies of many compounds in a system are one of the key inputs to the models for computing phase diagrams. The formation energies are obtained from differences in the total energies of the compounds and of the "end members".[1] These total energies are determined by the interactions between the electrons and nuclei that form the solid.

The equations that govern these interactions have been well known for almost 70 years, but their *exact* solution for a solid is far beyond the current or foreseeable computer power. Starting from Dirac's equation, a hierarchy of approximations needs to be introduced.[2] In this chapter, we will describe the different techniques that can be used to compute total energies. We start in section 3.1 by summarizing the approximations that lie at the core of most modern quantum–mechanical and classical methods.

Section 3.2 deals with the classical techniques. The word "classical" can be misleading. Here, it will be used to identify those total–energy methods in which no explicit calculation of the electron wave function is performed. However, they usually account approximately for *some* quantum–mechanical effects. For example, the largest contribution to the total energy in an ionic solid is the inter–ionic Coulomb interaction. This interaction is balanced by a short–range core–core repulsion that prevents the crystal from collapsing. The repulsion originates in the Pauli exclusion principle. Consequently, even the simplest classical model for an ionic solid has to account for this quantum–mechanical effect in order to provide meaningful results.

In section 3.3, we introduce the quantum–mechanical approaches and their most relevant approximations. Different materials have different types of bonding between the constituent atoms. In general, some of the approximations are better suited for one type of bonding leading to total–energy models applicable to specific materials. In all of them, there is a balance between accuracy and simplicity or computational speed. From this point of view, oxides present a specially difficult case since they

[1] The "end members" are the elements or compounds that are mixed, and whose phase diagram we want to determine.

[2] Quantum mechanics is essential to study the electrons in a solid since the scale of the periodicity of the ionic potential (~1Å) is comparable to the size of the typical de Broglie wavelength for these particles.

usually have a mixed type of ionic and covalent bonding. In general, *approximate* techniques can accurately deal with one type of bonding but not with both. The methods that will be described here seem to offer the best compromise between speed and accuracy in oxides.

The time scaling of the methods with the number of atoms (size of the system) is also a concern. Most of the accurate formulations scale at least as $N^2 \ln N$, where N is the total number of atoms. Since the final goal is to be able to predict macroscopic properties, considerable work is being done to develop techniques that would scale linearly with N. In section 3.4, we compare the time performance of different total–energy techniques and briefly summarize the advances in the area of order–N methods (i.e., linear time scaling).

3.1 The computation of total energies

Dirac's equation can be approximated by Schrödinger's equation plus "perturbation" terms that account for relativistic effects such as the variation of the electron mass, the spin–orbit coupling, the coupling between the proton and the electron spin,[3] etc. [67, 68]. The corrections to the total energy introduced by these terms are usually small[4] and, for simplicity, we will neglect them. Most of the systems studied here are nonmagnetic.[5] For a review on how to incorporate magnetic effects, see reference [71] and references therein.

Due to the large difference in masses between the electrons and nuclei, it is common practice to assume that the nuclei are frozen. In this way, the electronic and nuclear coordinates can be treated separately in the solid wave function. This is the so–called **Born–Oppenheimer approximation** and is equivalent to consider that the electronic wave functions respond "instantaneously" to the positions of the nuclei. These nuclei are treated as classical particles. The dependence of the total energy on their positions plays the role of a *potential energy* of interaction between the nuclei.

Under these assumptions, the total energy of the system can be regarded as a function of the position $\vec{R}_I$ of the nuclei so that

$$E = E(\vec{R}_1, \vec{R}_2, ..., \vec{R}_N), \tag{3.1}$$

where N is the number of atoms in the material. Classical and quantum–mechanical methods differ on how to determine this function. The latter techniques will compute it explicitly by solving the Schrödinger equation. On the other hand, classical approaches will assume some functional form whose parameters are fit to reproduce experimental or *ab initio* results.

[3]The electronic spin appears naturally when both the postulates of quantum mechanics and special relativity are imposed.

[4]The order of magnitude of these corrections is typically of a few meV/atom ($\frac{1}{2000}$meV/atom for terms that depend on the proton spin) [67].

[5]Even for magnetic systems, the differences in total energies between a magnetic and a nonmagnetic treatment are usually small [69, 70].

In the following sections, we will describe both formulations.

3.2 Classical models

As mentioned in the previous section, the Born–Oppenheimer approximation allows us to write the interaction energy of the atoms in a solid as a function of only the atomic coordinates. Classical models suggest different expressions for this dependence [72]. The simplest and most commonly used one is the *pair potential*, in which the total energy is a sum of pair–interaction terms between the atoms. An improvement over the pair–potential approximation is obtained if terms that depend on the position of more than two atoms are also included (*cluster potential*). Finally, *pair* and *cluster functionals* can also be used to work with a more accurate representation of the atomic interaction. In this case, nonlinear functions are applied to pair and cluster interaction terms respectively. Here, we will discuss pair–potentials and pair–functional models.

Ionic crystals are good examples of systems that can be modeled with pair potentials. The solid is regarded as an arrangement of charged spheres (ions). They are assumed to be classical particles placed at the equilibrium crystal lattice positions. These positions are determined by the competition between the attraction of the positively and negatively charged spheres (simple Coulombic electrostatic force) and the repulsion caused by the Pauli exclusion principle.[6] The repulsion interaction is represented as an effective pair potential that acts between the ions. The coefficients and sometimes the ionic charges of these potential functions are fit to *ab initio* or experimental results.[7]

Since a large contribution to the differences in total energies comes from purely electrostatic effects, pair–potential models are sometimes good enough to study the structural stability of highly ionic crystals. However, they can not be used in metals. A pair potential assumes that the total energy of a solid is a sum over *independent* bonds (i.e., the strength of the bond does not depend on the existence of other bonds). This is only correct if the nature of the bond is purely ionic. In metals, the cohesive energy of a series of crystal structures that only differ on the atomic coordination z scales more as $-z^{\frac{1}{2}}$ than as $-z$ (which is the result one expects for independent bonds) [73].

In order to correct for this problem, a pair–functional method is generally used (see for example reference [74]). The total energy of the crystal is regarded as a sum of an "embedding energy" for the atoms and a pair–potential term that accounts for electrostatic contributions. The "embedding energy" is the energy associated with placing an atom in the electronic environment of the solid. It not only incorporates some many–body effects but also the dependence of bonding with coordination. Here,

[6] Due to this principle, the electrons are prevented from occupying the same energy levels when they overlap and since the ions in these crystals usually have closed shells, they need to occupy higher orbitals. As a result, it costs too much energy to overlap the ions and they effectively repel each other.

[7] Most frequently, however, the ionic charge is not fit but the corresponding chemical oxidation state is used instead.

we will discuss a particular implementation of this approach, called the embedded–atom method (EAM) since it has recently been applied to oxides [75, 76].

Both the pair–functional and the pair–potential models lack a good description of *directional* bonds. This is specially important in semiconductors and covalent materials in general. Cluster potential and functionals should be used in this case. We will come back to this point later, in section 3.2.4.

3.2.1 Approximations of classical models

The major approximation of the classical methods is to assume a given functional form for the energy in equation 3.1. Although sometimes inspired in the actual physics of bonding, only a self–consistent formulation of Schröedinger's equation is capable of capturing all the details of the problem.

But even when the potential or functional form for the energy is adequate, most popular versions of these models introduce other approximations that can be particularly important in oxides. For example, it is common practice to assume constant charges for the ions, independently of the environment. We will show in chapter 5 that this can produce large errors in the formation energies. Also, it is important in oxides to account for the oxygen breathing.[8] Recently, some schemes to correct for these problems have been introduced, and will be described in section 3.2.2.

The transferability of the parameters of classical models depends on the accuracy of the function chosen to describe the energy. These parameters are usually fit to *ab initio* or experimental information for a few structures. When applied to other structures with different atomic arrangements large errors can be introduced. Mixing studies of multicomponent systems may suffer from a similar problem. When the fit is only done to the end members, the properties of mixtures are not necessary well reproduced.

3.2.2 Pair–potential models

Due to the complexity of oxides, modeling in these materials has been mainly done with simple empirical potential models. To date, most potentials for oxides have been based on Coulomb and pairwise short–range interactions, with ionic polarizability treated by the shell model of Dick and Overhauser [77]. See [78, 79, 80, 81] and references therein for a review. These models have been successful in predicting defect energies, lattice constants, and some elastic properties [82, 83]. However, they are inadequate to make *quantitative* predictions when computing phase diagrams [84] as we will show in chapter 5.

With these potentials, the total energy is expressed as the sum of the short–range interactions, Coulomb terms, and the polarization of the ions. The electronic cloud of the i ion is simulated by a massless shell of charge Y_i and the nucleus by a core of

[8] Oxygen breathing is the change in the size of the oxygen due to changes in the Madelung field (see section 3.3.1).

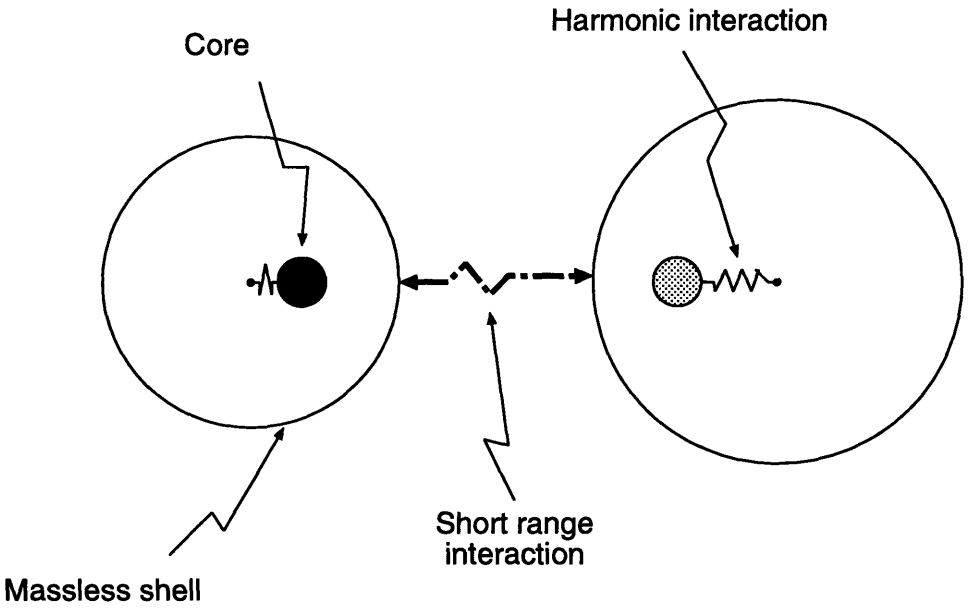

Figure 3-1: Illustration of the interaction between two ions in the pair–potential model. Each ion is represented by a massless shell, on which a short–range pairwise interaction acts, and a core (here represented by the shaded and black circles) coupled by a harmonic force to the shell. A Coulombic, long–range interaction, is also assumed to exist between the ions.

charge X_i. The total charge, q_i, is

$$q_i = X_i + Y_i. \tag{3.2}$$

The core and the shell of the ion are coupled by a harmonic force, with spring constant k_i. The polarization energy is given by

$$V_i = \frac{1}{2} k_i d_i^2. \tag{3.3}$$

The distance d_i is the relative displacement of the core and the shell.[9] The short–range interaction is assumed to act between the shells. The situation is illustrated in figure 3-1.

Different functional forms have been proposed to model the short–range pair interactions. The simplest one is represented by hard spheres,

$$V(r_{ij}) = \begin{cases} \infty & r_{ij} \leq a \\ 0 & r_{ij} > a \end{cases}. \tag{3.4}$$

[9]Within this model, the free–ion electronic polarizability α_i is equal to $\frac{Y_i^2}{k_i}$.

Here, a is the ionic radius and r_{ij} is the distance between ions i and j. The two–body potential used in this work has the following functional form:

$$V(r_{ij}) = A_{ij}e^{\left(-\frac{r_{ij}}{\rho_{ij}}\right)} - \frac{C_{ij}}{r_{ij}^6}, \tag{3.5}$$

where A_{ij}, ρ_{ij}, and C_{ij} are parameters that depend on the identity of the ions.[10] The functional form in equation 3.5 is known as the Buckingham potential. The exponential term represents the repulsion due to the electronic cloud overlap and the r^{-6} term is related to induced dipole–induced dipole interactions. These potentials are usually truncated beyond a distance corresponding to a few lattice constants.

The Ewald summation method [85] is used to compute the electrostatic energy of the point charges q_i. The value of the charges is fixed and does not depend on the environment.[11] For simplicity, *formal charges* equal to the valence of the atom are usually assumed. *Partial charges*, that correspond to nonintegral values, have been used to study some systems such as alumina [86]. Unless they are used in conjunction with a charge transfer model, their transferability to structures other than the ones used in the fit is questionable.

The parameters of the potential, A_{ij}, ρ_{ij}, C_{ij}, Y_i, and K_i, are typically obtained from fitting to lattice parameters, elastic and dielectric constants, phonon frequencies, etc. All these properties sample a system close to equilibrium. To enhance the transferability of the potential to different environments (e.g., different crystal structures), where they are not necessarily evaluated at the same distance range, fits to defect properties, *ab initio* equations of state, and different structures should also be included.

Pair–potential models present serious limitations. They can neither account for multibody effects (angular–dependent interactions, oxygen breathing, charge transfer, etc.) nor for the fact that the strength of the bond may depend on the actual number of bonds. Their parameters are environment independent. Furthermore, for cubic materials at zero pressure, they predict relationships between elastic constants that are not necessarily valid (for example, $c_{12} = c_{44}$, see reference [87]).

Some of these issues have been addressed by pair functionals or by models that include breathing and variation of charge. We will discuss some of these models in the next sections.

Charge transfer

Recently, Streitz and Mintmire have proposed a method to model the charge transfer between the ions [75]. It can be used within a potential or functional formalism. The charges are obtained by minimizing the electrostatic energy E_{es}.[12]

The electrostatic energy is written as a sum of atomic energies $E_i(q_i)$ and inter-

[10]Typical values for these parameters are: $A_{ij} = 10^3$ eV, $\rho_{ij} = 0.3$ Å, and $C_{ij} = 30eV$ Å^6.

[11]This is a strong assumption and it is often not valid as we will show in chapter 8.

[12]Note that there is no variational principle that justify this procedure.

action energies between all pairs of atoms. Using their notation:

$$E_{es} = \sum_i E_i(q_i) + \frac{1}{2}\sum_{i \neq j} V_{ij}(\vec{r}_{ij}, q_i, q_j), \tag{3.6}$$

where $V_{ij}(\vec{r}_{ij}, q_i, q_j)$ is the Coulomb pair interaction between ions i and j and q_i are the charges to be computed.

The atomic energy represents the intra–electrostatic interaction between electrons on the same atom. It is written as a Taylor expansion on the ionic charge q_i. The coefficients of this expansion are determined during the fit of the potential or the functional form.[13] The $V_{ij}(\vec{r}_{ij}, q_i, q_j)$ can be computed by simply assuming point charges or an atomic charge–density distribution.

Finally, the values q_i are obtained by minimizing E_{es} subject to the constraint that the sum of all the charges in the solid should be zero (charge neutrality). This model was used to study metal–oxide interfaces (aluminum α–alumina) [75].

Compressible–ion model

The effect of the change in size of the ions with the Madelung field can be modeled by computing the energy to create the ionic charge density appropriate to a given set of lattice parameters. Different ways of implementing this procedure exist. Here, we will briefly describe the scheme by Wilson and coworkers since they integrated their formalism within a pair–potential method [88]. Other approaches will be presented in section 3.3.1.

The electronic charge density of the ion is computed by solving for the self–consistent wave function within a potential that simulates the crystal. This potential is the sum of two contributions: a long–range Madelung field (assuming the ions to be point charges) and an electrostatic repulsion from the neighboring charge densities. The energy to obtain a given charge distribution (or its difference with respect to isolated ions) is then incorporated into a potential as a function of *generalized ionic coordinates.*

The generalized coordinates include not only the positions of the ions but also a description of their "state". The "state" is specified by assigning a radius to the ions that would depend on the environment. A term is then added to the short–range potential, that depends on this radius and represents the energy to rearrange the ionic charge density. For a fixed set of ionic positions, the total energy should be minimized with respect to the radius coordinates *before* evaluating the energy.

The term that represents the charge rearrangement at the ions is given the form:

$$F(\delta) = c(e^{-\gamma\delta} + e^{\gamma\delta}), \tag{3.7}$$

where δ represents the change in the ionic radius with respect to a reference value and γ and c are coefficients to be fit to *ab initio* results.

[13] The fit is performed as explained in the previous section.

Note that the overlap within the ionic wave functions also depend on δ. Consequently, within this model, the pair potential short–range repulsion is a function of the ionic radius. For more details about the method, see reference [88]. The compressible–ion model has recently been used to study MgO, CaO, Al_2O_3, and ZrO_2 [88, 89, 90].

3.2.3 The embedded–atom method

Up to now we have assumed that the total energy of the solid was given by a sum over independent bonds. As already mentioned, this is only true for a perfectly ionic crystal. A solution for this problem can be found by using pair functionals such as it is done in the embedded–atom method (EAM).

The basis of the EAM consists in expressing the energy of a solid in terms of "embedding" energies and electrostatic interactions. Each atom is assumed to be "embedded" into the electron gas created by the other atoms. The cohesive energy E_{coh} is then written as,

$$E_{coh} = \sum_i \mathcal{F}_i \left(\sum_{j \neq i} \rho_j(R_{ij}) \right) + \frac{1}{2} \sum_{\substack{\mathrm{i,j} \\ i \neq j}} V_{ij}(R_{ij}). \tag{3.8}$$

Here, $\mathcal{F}_i$ is the embedding energy for atom i and is applied to the superposition of the spherically averaged electron atomic–density tails ($\rho_j(R_{ij})$) from other atoms evaluated at the position of atom i. $V_{ij}(R_{ij})$ represents electrostatic, two–atom interactions.

Equation 3.8, and correspondingly $\mathcal{F}_i$ and $V_{ij}(R_{ij})$, can be derived from density–functional theory.[14] However, they are generally fit to bulk properties such as lattice and elastic constants and vacancy formation energies. The embedding energy is non-linear (convex), reflecting the saturation of the bonds with the number of neighbors.

Analytic functions or tables are used to express $\mathcal{F}_i$. The $V_{ij}(R_{ij})$ are represented as decaying exponentials (due to electrostatic screening). The spherical electron densities can also be parametrized with simple decaying exponentials. For more details on the EAM, see reference [73].

The embedded–atom method has been recently applied to oxides, yielding reasonable results for alumina [75]. To appropriately account for the long–range Coulomb interaction, Streitz and Mintmire added E_{es} (see equation 3.6) to the cohesive energy in equation 3.8 [75]. They did not eliminate the $V_{ij}(R_{ij})$ terms in equation 3.8 but kept them so that their coefficients could be used as free parameters. Baskes also reported EAM calculations in oxides [76].

[14] Two assumptions should be made. One is that the electron density of the solid can be computed as a linear superposition of the atomic electronic densities. The other one is that the kinetic, exchange, and correlation energies (see section 3.3.1) can be written in terms of *local* electron densities and its derivatives. See reference [91] for more details.

3.2.4 Cluster functions for the energy

Both the pair–potential and the embedded–atom methods do not work well for systems with directional bonding. *Cluster* potentials and functionals should be used instead.

It is common practice to add 3– and 4–body interactions to potential models when semiconductors are modeled. These new terms allow for the inclusion of bond–bending and torsion effects. For example, computational simulations in silicon are usually performed with multibody potentials such as the Stillinger–Weber one [92].

The EAM can also be modified to accommodate directional bonding effects. The modified embedded–atom method (MEAM) is similar to the EAM except that now the electronic density contributions from the neighbor atoms can include angular dependencies. See reference [93, 94] for more details.

3.3 Quantum–mechanical approaches

Quantum mechanics can be used to explicitly find the dependence of the total energy on the nuclear coordinates in equation 3.1. In the remainder of this chapter, we will study different techniques to perform this operation.

The methods differ on the different approximations used to solve the Schrödinger equation. Within the assumptions made in section 3.1, this equation can be written as[15]

$$\begin{aligned} H\Psi \;=\; & \left(-\sum_{i=1}^{N_e} \frac{\hbar^2}{2m_e}\nabla_i^2 - \sum_{I=1}^{N}\sum_{i=1}^{N_e} \frac{Z_I e^2}{\left|\vec{r}_i - \vec{R}_I\right|} + \frac{1}{2}\sum_{I}^{N}\sum_{J\neq I}^{N} \frac{Z_I Z_J e^2}{\left|\vec{R}_I - \vec{R}_J\right|} \right. \\ & \left. + \frac{1}{2}\sum_{i}^{N_e}\sum_{j\neq i}^{N_e} \frac{e^2}{|\vec{r}_i - \vec{r}_j|} \right) \Psi = E\Psi. \end{aligned} \tag{3.9}$$

Here, Ψ is the solid wave function, E is its eigenvalue, N_e is the number of electrons, N is the number of atomic nuclei, Z is the atomic number, e is the electron charge, and $\vec{R}$ and $\vec{r}$ are the nuclear and electron coordinates respectively.

The different terms in the Hamiltonian of equation 3.9 represent the kinetic energy and the electron–ion, ion–ion, and electron–electron electrostatic interaction operators respectively. The solid wave function Ψ, is a function of the electronic and ionic coordinates.

Even after decoupling the nuclear and electronic coordinates, solving equation 3.9 is unfeasible since there are practically an infinite number of electrons that interact with each other. We will show that this problem can be surmounted by using the periodicity of the crystal and assuming that equation 3.9 can be transformed into a set of single–electron equations coupled through the electronic interactions. (Thus, the solution of Schrödinger's equations has to be found self–consistently.)

The interaction of a single electron with the nuclei and the other electrons has

[15] We use capital and small letters to denote nuclear and electron coordinates respectively.

the periodicity of the crystal. This allows the use of Bloch's theorem to express the electron wave function ψ as[16]

$$\psi_{n\vec{k}}(\vec{r}) = e^{i\vec{k}.\vec{r}} u_{n\vec{k}}(\vec{r}), \tag{3.10}$$

where $u_{n\vec{k}}$ is a function with the periodicity of the Bravais lattice, $\vec{k}$ is a wave vector, and n is known as the band index. Not all the possible $\vec{k}$ points are allowed but they are restricted by imposing appropriate boundary conditions to the bulk solid, namely that [95]:

$$\psi(\vec{r} + \sum_{i=1}^{3} N_i \vec{a}_i) = \psi(\vec{r}). \tag{3.11}$$

The $\vec{a}_i$ are the three primitive vectors of the unit cell and N_i are positive integer numbers such that the total number of primitive cells in the solid be $N_1 N_2 N_3$.[17] In this way, the problem of finding the wave functions of an *infinite* number of electrons is transformed into finding the wave functions of a *finite* number of electrons at an *infinite* number of $\vec{k}$ points. At each $\vec{k}$ point, only a finite number of levels are occupied.

The advantage of this procedure becomes clear when we realize that solutions at $\vec{k}$ points that are close together are very similar. Consequently, we can represent different regions in $\vec{k}$ space by a *finite* number of $\vec{k}$ points. Thus, the electronic potential and total energies can be obtained from computing the electronic states at this limited set of points. See appendix B on how the $\vec{k}$ points are chosen.

Defects and atomic vibrations usually break the periodicity. In what follows, we will always assume crystals that have a *perfect* periodicity. Nonperiodic configurations can be dealt with by using a *supercell approximation.* In a supercell approximation, a particular unit cell containing the "defect" in the arrangement of atoms is repeated periodically throughout space so that a perfect regular configuration is recovered. The defect in question is thus also artificially repeated throughout space and the further apart its images are (i.e., the larger the unit cell), the more accurate the approximation becomes. It is common practice to evaluate how the defect properties vary with the size of the supercell in order to assess the importance of the errors introduced by the "interaction" of the images.

Although the original problem seems to have been greatly simplified by the above approximations, more work needs to be done to deal with the many–body electron–electron interactions and to make the computational burden more affordable. These new approximations are more specific to the particular methods and are dealt with in the next sections. In table 3.1, we summarize the methods we use in this work and their most common approximations. We have chosen these techniques since they provide the best compromise between computational speed and accuracy in oxides.

[16]See for example reference [95].

[17]We are using a generalization of the Born–von Karman periodic boundary condition [95]. The surface of the solid is eliminated by replicating the solid throughout space. An electron coming to a surface simultaneously reenters the solid on the opposite surface. An infinite solid has an infinite number of $\vec{k}$ vectors. We will assume the size of the solids to be infinite.

	LDA[a]	Spherical symmetry	Frozen core
FLAPW	•		
LMTO–ASA	•	•	
Pseudopotentials	•		•
SSCAD	•	•	
Tight binding	•		•

Table 3.1: Total–energy methods and their approximations. The bullets indicate the most common approximations used by each technique. A detailed description of the methods and approximations can be found in section 3.3.

[a]Local–density approximation to density–functional theory

In section 3.3.1, we will describe the different approximations mentioned in table 3.1. The details of the particular implementation of the techniques will be discussed starting in section 3.3.1. The major difference between them is the basis functions used to expand the solutions of the quantum–mechanical equations. Some functions are more suited than others for solving certain problems (such as the calculation of forces) or work with specific types of bonds.

3.3.1 Common approximations in quantum–mechanical approaches

Different choices exist for breaking equation 3.9 into single–electron equations and expressing the interaction between the electrons. In this work, we will apply the density–functional theory (DFT) which is an *exact* transformation of equation 3.9 into single–electron equations, but valid only for computing *ground–state* properties. Unfortunately, DFT does not offer a recipe to determine the potential felt by a single electron. Extrapolations from limiting cases where the solution is known have to be taken. Another commonly used approach is the Hartree–Fock method. This method will not be described here since its implementation is very computer intensive and does not provide significant benefits over DFT. (A detailed explanation of this method can be found in reference [19].)

Once the problem is described by one–electron equations, other approximations are still introduced to reduce the computational burden of the methods. They range from assuming special geometries or symmetries for the electronic potential, to "freezing" the core electrons.

Density–functional theory and its approximations

Many reviews have been written about DFT (see for example references [96] and [97]). Here, we will only describe its main features. The focus of this theory is more on the electronic density rather than on the wave functions. Hohenberg and Kohn [15]

proved that the total energy of a system is a unique functional of the electron density and that the minimum value of the functional corresponds to the actual ground–state energy and the corresponding electronic density to its actual density. The next step was taken by Kohn and Sham [16] who showed that equation 3.9 can be replaced by a set of noninteracting single–electron equations such that the ground–state total electronic density is the sum of the single–electron ground–state densities. Thus, DFT provides a general method for calculating the energy and the electronic density of the *lowest energy state* (and all the properties that can be obtained from them).

The Kohn–Sham equations are written as,[18]

$$H_{KS}\psi_i = \left(-\frac{\hbar^2}{2m_e}\nabla^2 - \sum_{I=1}^{N} \frac{Z_I e^2}{\left|\vec{r} - \vec{R}_I\right|} + e\int \frac{n(\vec{r'})}{\left|\vec{r'} - \vec{r}\right|} d\vec{r'} + V_{xc} \right) \psi_i = \varepsilon_i \psi_i. \qquad (3.12)$$

H_{KS} is the Kohn–Sham Hamiltonian, V_{xc} is the exchange and correlation potential,[19] ψ_i is the single–electron wave function, and ε_i its eigenvalue. The total electronic density n is given by

$$n = e\sum_{i}^{N_e} |\psi_i|^2 . \qquad (3.13)$$

Although the Kohn–Sham equations are an *exact* mapping of the many–electron problem onto a single–electron one, the ε_i are not the real single–particle eigenvalues [98].

The exchange and correlation potential that the electrons face is not known and different approximations are used to determine it. The most popular one is the local–density approximation (LDA) [16]. In the LDA, the exchange–correlation energy per electron at point $\vec{r}$, ϵ_{xc}, is replaced by the exchange–correlation energy of an homogeneous electron gas with the same density as the electron gas at point $\vec{r}$. The LDA assumes that ϵ_{xc} is local and ignores all the effects of inhomogeneities around $\vec{r}$.

Several parameterizations exist for the exchange–correlation energy in a uniform electron gas. They are frequently expressed as interpolations between the high and low electron–density limits. See for example references [99] and [100]. Most of them lead to very similar total–energy results.

In recent years, the generalized–gradient approximation (GGA) [17, 18] has been developed as a way to improve over the LDA. In this approach, the ϵ_{xc} is expressed as a local function of not only the density, but also its gradient. In this way, one tries to capture the effects of inhomogeneities in the electronic density.

Spherical approximations for crystal potentials

Shape approximations are introduced to accelerate the solution of Schrödinger's equation. The most widely used approximation was first applied by Slater [101], and is

[18]For simplicity, the electrostatic interaction between the ionic cores is not written. It will be directly added to the total energy.

[19]The V_{xc} potential captures all the electronic exchange and correlation effects. It is computed from the exchange–correlation energy per electron, ϵ_{xc}, as $V_{xc} = \frac{\partial[n\epsilon_{xc}]}{n}$, where n is the electronic density.

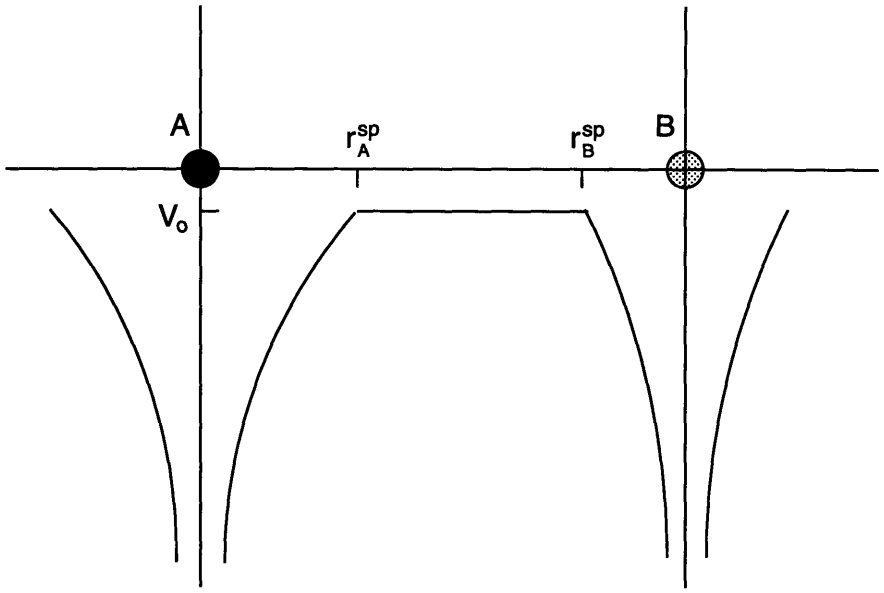

Figure 3-2: Muffin–tin potential often used to approximate the actual crystal potential. The sphere radii r_A^{sp} and r_B^{sp} (for atoms A and B respectively) are arbitrary, except for the fact that the spheres should not overlap.

called the **muffin–tin approximation** (MTA).

In the MTA, the crystal potential[20] is assumed to be spherically symmetric inside spheres centered at each atomic site, and constant outside these spheres. If we place a sphere of radius r_i^{sp} at site R_i, the muffin–tin potential $U(\vec{r})$ is:

$$\begin{aligned} U(\vec{r}) &= V(\left|\vec{r}-\vec{R}_i\right|) \quad \text{when } \left|\vec{r}-\vec{R}_i\right| < r_i^{sp}, \\ &= V_o(r_i^{sp}) \quad \text{when } \left|\vec{r}-\vec{R}_i\right| \geq r_i^{sp}. \end{aligned} \tag{3.14}$$

The shape of this potential is shown in figure 3-2. Since $U(\vec{r})$ is spherically symmetric, only the radial components need to be specified. The only constraint to fix the radii of the spherical regions is that the spheres do not overlap. The nonspherical contributions to the crystal potential and the effect of assuming a constant value in the interstitials can frequently be included using some sort of perturbation or correction. As we will mention in the next sections, these effects can be taken into account very accurately.

The spherical–symmetry approximation is generally correct as long as the spheres are centered at high–symmetry sites. Consequently, the MTA gives accurate results for closed packed materials (for example, fcc or ideal hcp) and is increasingly less reliably as the site symmetry decreases and the coordination number lowers.

[20]The crystal potential is usually defined as the potential experienced by an electron that originates in the electrostatic interactions with the atomic nuclei and the other electrons.

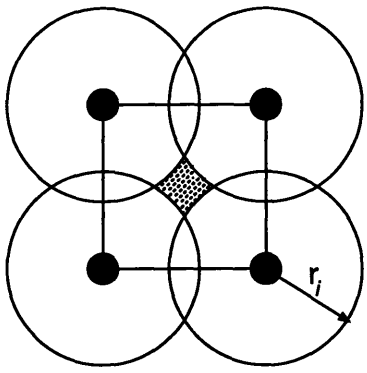

$$\text{Unit cell volume} = \frac{4}{3}\Pi \sum_i r_i^{\,3}$$

Figure 3-3: Cubic unit cell showing the Wigner–Seitz overlapping spheres in the ASA. The interstitial region (shaded area in the figure) is usually neglected. The sum in the equation is over the spheres in the unit cell.

In some cases, an even simpler approximation than the MTA, called the **atomic–sphere approximation** (ASA), is taken [65, 102]. In the ASA, the unit cell is mapped onto the space of Wigner–Seitz overlapping spheres generally centered at atoms. All integrals over the cell are substituted by integrals over these spheres and the electronic density is spherically averaged within each of them. The potential is then a superposition of spherical contributions from each sphere. The situation is described in figure 3-3.

Note that in the ASA case, the errors would come not only from nonspherical contributions but also from the overlap and the neglect of the interstitial regions for the integrals.[21] In open structures, some of the overlap errors can be alleviated by the use of *empty spheres* to reduce the degree of overlap.

Frozen–core approximation

In any material, there is often a clear distinction between *core* and *valence* electrons. Core electrons are usually strongly bound to the atomic nucleus and do not respond significantly to the motion of the valence electrons. Consequently, when atoms are brought together to form a solid, the changes in the core electron wave functions are very small. They can be regarded as essentially *frozen*. This is known as the **frozen–core approximation**.

To take advantage of this behavior, some total–energy methods compute only the valence wave functions. The effect of the core electrons on them is taken into account as a potential added on top of the nuclear potential. Considerable savings in computational time may be obtained when this approximation is used.

The contribution of the core electrons to the total energy is very large and cancels

[21] Corrections for the overlap regions and nonspherical contributions can be used. (See section 3.3.3.)

out when formation energies are taken. When the frozen–core approximation is used, this contribution is not computed and the formation energies can be determined as differences between *small* total–energy numbers requiring a *smaller* relative accuracy.

The frozen–core approximation is very accurate as long as the valence and the core electron wave functions do not overlap significantly. If this is not the case, some core electrons have to be treated as part of the valence electrons. As we discuss in the following chapters, some total–energy methods incorporate special treatments that correct these problems while still retaining the so–called *semicore* states as part of the core.

3.3.2 The spherical self–consistent atomic deformation model

The spherical self–consistent atomic deformation (SSCAD) model [103] is a first–principles method for computing total energies in *ionic* crystalline solids. It is based on density–functional theory in the local–density approximation. The SSCAD takes advantage of the characteristics of the ionic materials to make simplifying approximations that allow fast calculations without sacrificing too much accuracy.

The electronic density is assumed to be localized about each ion and the *total* electron density n to be the sum of these individual densities,

$$n(\vec{r}) = \sum_{i}^{N} n_i(r_i). \tag{3.15}$$

In equation 3.15, n_i is the density corresponding to the ith ion and r_i the distance from $\vec{r}$ to that ion. The total energy of the crystal can be written as a functional of this total electron density as

$$\begin{aligned} E(n) &= T + \frac{1}{2}\sum_{I}^{N}\sum_{J\neq I}^{N}\frac{Z_I Z_J e^2}{\left|\vec{R}_I - \vec{R}_J\right|} - \sum_{I=1}^{N}\frac{Z_I e^2 \int n(\vec{r})}{\left|\vec{r} - \vec{R}_I\right|}d^3r \\ &\quad + \frac{1}{2}e^2\int\int\frac{n(\vec{r'})n(\vec{r})}{\left|\vec{r'} - \vec{r}\right|}d^3r'd^3r + \int \epsilon_{XC}(\vec{r})n(\vec{r})d^3r, \end{aligned} \tag{3.16}$$

where T is the kinetic energy of the electrons (the ions are assumed to be fixed). The kinetic energy is approximated as a sum of an *intra–ionic* term plus a correction coming from the overlap of the electronic clouds (computed from the Fermi–Thomas energy for a gas of interacting electrons with uniform density) [103].

Applying density–functional theory to the energy, as in reference [16], a one–particle Schrödinger–like equation is obtained for each ion,

$$-\frac{1}{2}\nabla^2\psi + V_i\psi = \epsilon\psi. \tag{3.17}$$

Here, V_i and ψ are the Kohn–Sham potential and eigenfunctions for ion i respectively.

As in reference [16], the potential V_i depends on the total density, and the equation

is solved self–consistently starting from the densities of isolated ions. To reduce the computational time, V_i is spherically averaged about ion i. After imposing spherical symmetry, equation 3.17 becomes an ordinary "radial" Schrödinger equation and can be solved either by finite differences or by expanding the solution in a set of basis functions. Usually, the Slater basis–set expansions of the Roothaan–Hartree–Fock wave functions are used in this expansion [104, 105]. Once equation 3.17 is solved, the total–electron density is computed and the total energy is obtained from equation 3.16.

The SSCAD has many similarities with the Gordon–Kim electron–gas model [106] for calculating the interaction energy in closed–shell ions. However, two major improvements have been introduced in the former: ionic breathing and self–consistency. In the Gordon–Kim scheme, free–ion electron densities were used. This can introduce large errors since these densities can change considerable when the solid is formed. This phenomena is commonly known as the *breathing* of the ions.[22] In the SSCAD, the dependence of the ionic electron density on the Madelung field is incorporated through the potential V_i in equation 3.17. The self–consistency in the SSCAD model allows the effect of the nearest–neighbor electronic cloud to be taken into account when computing the electronic density in the ion.

The major limitation for the use of the SSCAD in oxides is the imposed spherical symmetry and the approximated treatment of the electron kinetic energy. The electronic density in these materials is not necessarily spherically symmetric and a large error in the total energy can be introduced as we will show in chapter 5. Nonspherical versions of the SSCAD are currently under development.

3.3.3 The linear muffin–tin–orbital method

It is not our intention to review here all the complex details of the linear muffin–tin–orbital (LMTO) method in the atomic–sphere approximation (ASA). The reader is referred to the many review articles and books that have been published on this topic [65, 102, 110]. Instead, we will briefly mention the main approximations that are incorporated into the LMTO. Due to these approximations, the solution of the Kohn–Sham equations can be performed much faster than with other less approximate methods.

In the LMTO–ASA, space is divided into overlapping Wigner–Seitz spheres, generally centered at the atomic positions. The solutions are computed in the atomic–sphere approximation (see section 3.3.1). The basis functions used to expand the solution of the Kohn–Sham equations in an ASA potential are computed as the solutions of the Laplace equation (i.e., Schrödinger's equation with zero kinetic energy) outside each sphere which are augmented by the solutions for the spherically–symmetric

[22] For example, O^{-2} is *unstable* as a free ion. It can only exist in a solid due to the stabilization effect of the Madelung field. Since the Gordon–Kim scheme could not be applied to this ion, Boyer and coworkers developed the potential–induced breathing (PIB) model [107, 108]. PIB uses a spherical shell of charge (Watson sphere [109]) to simulate the effect of the solid environment on the ion. Thus the O^{-2} ion is made stable and its electronic density can be computed.

potential within each sphere. These functions are usually called muffin–tin orbitals (in the ASA). Both the wave functions and their spatial derivatives are required to be continuous at the sphere boundary.[23]

The muffin–tin orbitals have a complicated energy dependence that can be eliminated by expanding around a fixed energy E_ν to first order in $(E - E_\nu)$.[24] The basis functions thus obtained are called *linear* muffin–tin orbitals and are used to solve the eigenvalue problem. Only a reduced number of basis orbitals are needed to obtain converged results.[25] For example, most atoms require only nine orbitals (corresponding to the s, p, and d quantum–angular momenta). The small number of basis orbitals increases the computational efficiency of the method considerably. Other methods, such as the plane–wave pseudopotential technique (see section 3.3.5), may require orders–of–magnitude more basis functions.

There is no unique way to choose the radii of the atomic spheres. The only condition is that the sum of the volumes of all the spheres in the unit cell be equal to the volume of the cell itself. This is enough to determine the radii only when one atom per cell is present in the solid. For all other cases, a criterion for choosing the radii is needed. Four different criteria are usually used. The first criterion is to take equal–size spheres for all the atoms in the crystal. The second one is to make the atomic spheres charge neutral (in this way, the Madelung energy error in the ASA vanishes). The third one is to minimize the total energy of the compound with respect to the radii of the spheres, though there is no variational principle that justifies this procedure. Finally, the last criterion, proposed by Andersen [112], gives an explicit formula for the sphere radii in terms of Wigner–Seitz radii, bulk moduli, and elemental volumes.

For close–packed solids, the LMTO–ASA method is very accurate. Corrections are sometimes used to compensate for the sphere overlap (usually called "combined corrections" [102, 112, 113]) and the symmetrization of the potential (usually called "muffin–tin corrections" [114]). In more open structures, the method gives less accurate energies and empty spheres (not centered at atoms) are used to reduce the overlap. A *full–potential* version of the LMTO, where no shape approximations are made, has been developed [115] but it will not be discussed here.

Formation energies in oxides are poorly predicted by the LMTO–ASA even in close–packed solids. As we will show in the next section, total energies are very sensitive to the sphere radii chosen, and the consistent use of any of the mentioned four criteria along many compounds in the same system does not provide accurate formation energies.[26]

---

[23] The muffin–tin orbitals we just defined decay slowly in space (specially for low quantum–angular momentum). Short–range basis functions can be defined by combining linearly independent solutions of Laplace equation through what is usually known as a *screening transformation* [111].

[24] E_ν is usually the value corresponding to the center of the occupied part of the band. See reference [65] for more details.

[25] The linear muffin–tin orbitals in the ASA form a complete basis set for the wave functions of an electron in a crystalline ASA potential and provide a very good description of them.

[26] In metallic alloys, these four criteria usually coincide and LMTO–ASA formation energies are comparable to the values of the most accurate methods. In oxides, on the other hand, some of the

Effect of the ASA in oxides

We performed numerous LMTO–ASA calculations in CaO–MgO, ZrO_2, Na_2O, and Li–transition–metal oxides. In all cases, we found an important dependence of the total energies on the size of the atomic spheres even when the "combined" and the "muffin–tin" corrections were used. We will illustrate this behavior in the CaO–MgO system.

An *s–p–d* basis was used for the calculations in CaO–MgO. The number of self–consistent iterations and $\vec{k}$ points were selected so that the variation of the total energy was less than 1meV/cell. This resulted in a 17^3 $\vec{k}$ space uniform grid (we considered crystal symmetry). The von Barth–Hedin form for the exchange–correlation potential was used [116].

In figure 3-4, we show the total energy versus sphere radius for the CaO structure. The variation of the total energy is almost 1 eV/cell.[27] Since formation energies are of the order of tens of meV, their value can be switched from positive to negative by choosing different points on this curve.

There is a clear need for a criterion to determine the sphere sizes. Unfortunately, our results show that it is not possible to use the same criteria in oxides as in other materials. Here, it does not make sense to make the spheres charge neutral. In general, we also found that even the consistent use of any of the criteria for all compounds in the same system does not provide accurate formation energies when compared to FLAPW or pseudopotentials. For example, we found that both the Ca– and Mg–rich $L1_2$ structures in the CaO–MgO system have negative formation energies when using equal–size spheres while all the other total–energy methods predict them to be positive. Using a smaller radii for the cations than for the anions makes the formation energies of the $L1_2$ structures positive but we could not find a consistent way of setting the sphere sizes that provided reasonable results for all compounds. We observed the same behavior in the other oxide systems we studied (ZrO_2–CaO, Na_2O, and Li–transition metal oxides). In metals, the error introduced by the ASA is less critical and it is usually very small when using neutral spheres.

The dependence of the lattice constants and the shape of the band structures on the sphere radii is much smaller. For example, the lattice constant for a cubic cell, such as the rocksalt structure, may only change by a few percent.

The LMTO–ASA method on the other hand, is orders–of–magnitude faster than more accurate total–energy techniques. However, the errors introduced by an incorrect treatment of the overlap region and the spherical approximation can be very large in oxides. Consequently, we will not make use of the LMTO–ASA formalism. A full–potential non–ASA LMTO method can overcome these difficulties but at the expense of computational speed.[28]

---

criteria can not even be applied. For example, it does not make sense to make the spheres charge neutral.

[27]The sphere radii range in figure 3-4, was chosen taking into account that Ca ions are usually smaller than O ones and that very dissimilar radii will considerably increase the overlap between the atomic spheres.

[28]For example, the formation energy of the $CaMg_3O_4$ compound in the $L1_2$ structure was predicted

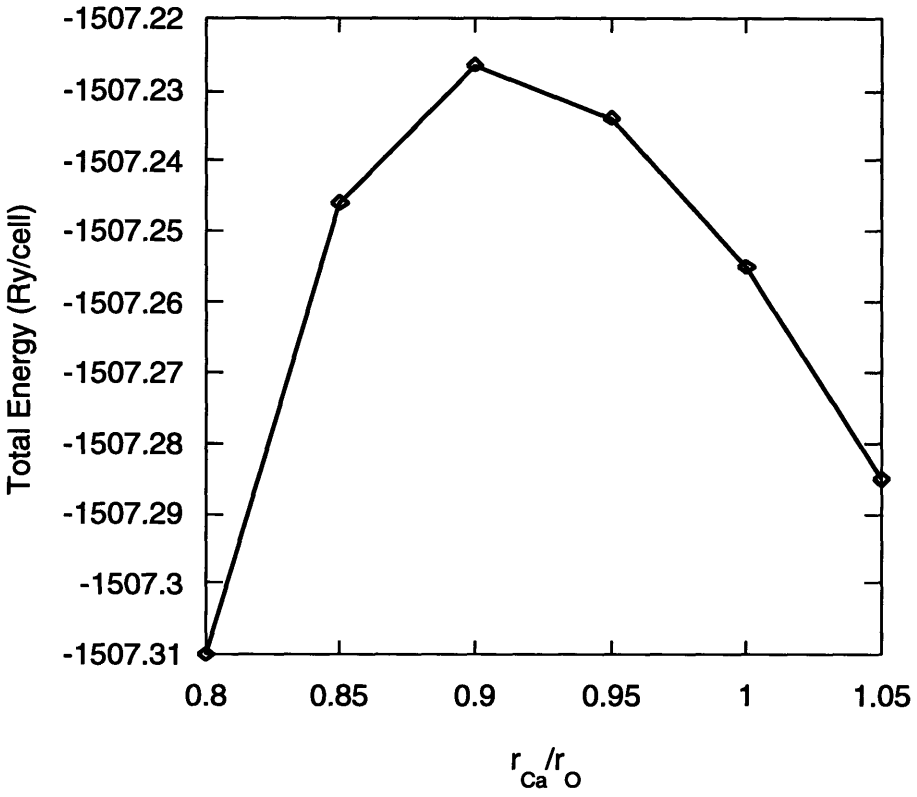

Figure 3-4: Total energy for pure CaO as a function of the ratio between the Ca and the O sphere radius in the LMTO–ASA. The volume of the cell was kept constant and corresponds to the experimental value. Empty spheres, and muffin–tin and combined corrections were used to reduce the errors introduced by the ASA. The total energy changes in a scale much larger than the scale of the temperature effects and a criterion is needed to choose the sphere size.

3.3.4 The full–potential linearized augmented–plane–wave method

The full–potential linearized augmented–plane–wave (FLAPW) method has its origins in the augmented–plane–wave (APW) technique introduced by Slater [101]. The basis functions on this approach are quite similar to those of the LMTO. Again, space is divided using spheres.[29] Plane waves are used in the interstitials which are then augmented by the solutions for the spherical radial equation (multiplied by spherical harmonics) within the spheres. These basis functions are also made energy independent in a similar fashion to the LMTO.

The FLAPW method is one of the most accurate techniques that are currently available. The only major approximation influencing the results is the LDA. The FLAPW method will not be used here. However, we will take results from the literature as benchmarks for some of our calculations. More details of this technique can be found in references [118, 119, 120, 121].

3.3.5 The pseudopotential method

The pseudopotential approach will be described in detail in chapter 4. Contrary to the previous methods, plane waves are used to describe the solid wave functions everywhere in space (and not only in an *interstitial* region). Only the solutions for the valence electrons are computed (frozen–core approximation). The effect of the core electrons on the valence states is taken into account by a potential that is added to the nuclear potential. This *pseudopotential* is chosen so that its valence *pseudo* wave functions are equal to the actual all–electron wave functions beyond a given core radius and so that they do not have nodes in the core region. Since only the outer electrons participate in bonding, using pseudopotentials is an excellent approximation in most cases.

The use of the pseudopotential approximation reduces not only the number of plane–wave basis functions but also the number of orbitals to be determined. The core–electron wave functions are not computed. All–electron techniques, on the other hand, need to accurately treat these core electrons that constitute a large portion of the total energy, while generally their effects are canceled out when energy differences are taken. Consequently, the pseudopotential energy is much smaller and requires a smaller relative accuracy than all–electron methods when computing formation energies.

Plane waves greatly simplify the solution of the Kohn–Sham equation: shape approximations are not necessary and Pulay forces are zero [122]. Furthermore, very efficient fast Fourier transforms are available.

The computational speed of the method depends on the chemical identity of the

---

to be 0.147 meV/ion with a full–potential version of the LMTO [117]. This is within 10% of the values shown in table 5.1 which were computed with the most accurate techniques that are available.

[29] As in the LMTO–ASA case, spheres centered at atomic positions are used. However, in the APW these spheres do not overlap.

elements that form the material. Sharply peaked valence states, as in first row non-metals such as oxygen, or in transition metals, require a large number of plane waves to be expanded. However, in the last years, new developments such as Car–Parrinello molecular dynamics [123], conjugate–gradients [124], and optimized [125] and ultra-soft [126] pseudopotentials have shown that plane–wave pseudopotential calculations can be efficiently performed for any element in the periodic table [124].

For a review on the pseudopotential method, see references [124, 127, 128, 129] and references therein.

3.3.6 The tight–binding method

Descriptions of the tight–binding method can be found in references [130, 131] and references therein. In this technique, the one–electron wave functions are expanded in a set of atomiclike local wave functions. This choice of basis makes the computation of the Hamiltonian matrix very involved. Consequently, two popular ways of thinking about this technique were developed: as an *ab initio* method or as a semiempirical approach. In the early days,[30] the latter was the only way to avoid the calculation of very time–consuming interaction integrals.[31] The basis functions remained unspecified and the Hamiltonian matrix elements were fit to reproduce physical properties obtained from other methods or from experiments (e.g., electronic band structure).

Due to the increase in computer power, the first–principles tight–binding (TB) approach has been gaining popularity in recent years, specially to compute electronic properties of ceramic materials (particularly oxides) [133]. In this work, we will use the semiempirical tight–binding (SETB) method [20] in the self–consistent form suggested in references [23] and [134]. Contrary to empirical potential models, an explicit treatment of the electronic structure is made and all the relevant terms for computing total–energy differences in systems with charge transfer (such as oxides) are incorporated. A detailed description of the method will be given in chapter 6.

The SETB model is not limited to a given type of bonding and no shape approximations for the ionic potentials need to be made. Furthermore, it is particularly fast since the interaction integrals are fit to *ab initio* results. In this sense, the SETB represents a much more sophisticated and accurate interpolation tool than potential models and is still orders–of–magnitude faster than *ab initio* quantum–mechanical techniques.

3.4 Time scaling

The time it takes for the different total–energy methods to perform a certain calculation is assumed to be given by cN^i where N is the number of atoms in the unit cell,

[30] The use of a linear combination of atomic orbitals to solve the quantum–mechanical equations in a solid was originally proposed by Bloch in 1928 [132].

[31] These integrals correspond to the "hopping" and "overlap" terms we will describe in chapter 6.

Method	Time scaling
Potentials	N (N^2)
SSCAD	N (N^2)
Tight binding	N (N^3)
Pseudopotentials	$N^2 \ln(N)$ (N^3)
LMTO–ASA[a]	N^3
FLAPW	N^3
Hartree–Fock	$N^{3.5}$–N^7

Table 3.2: Time scaling of some total–energy methods with respect to the size of the system N (number of atoms in the unit cell). The values in parenthesis represent upper limits according to different implementations.

[a]It can be order–N in TB form.

c is a prefactor, and i is a number that corresponds to the *order* of the algorithm.[32] It is generally the case that a low order corresponds to a large prefactor, so whenever two techniques with different orders are compared, the crossover point (where both take the same computational time) corresponds to systems with large unit cells.

Ideally, if we are interested in exploring larger and larger systems, the order of the time scaling should be as small as possible. Most traditional electronic structure calculation methods have a cubic scaling. This cubic scaling reflects the need to keep the wave functions orthonormal. Recently, several propositions have been made to provide methods that scale with N (the so–called order–N methods). This is a very active field of research [135, 136, 137, 138, 139]. The crossover point varies from method to method and goes from just a few atoms to a few hundred atoms.

The scaling of the methods mentioned in this chapter are shown in table 3.2. The techniques with the smallest number of approximations have at least a cubic or $N^2 \ln(N)$ scaling.[33] Potential models can be of order–N or N^2 according to how they deal with the Coulomb interaction. The same applies to the SSCAD.[34] The traditional tight–binding method scales as N^3, but order–N algorithms have recently been developed [138, 140].

From this point of view, the tight–binding technique is very promising since it can

[32]Actually, this is the leading term in the expression. The "time" equation is usually much more complex since different parts of the algorithm scale with different i and c. It is conventional to characterize the method by the *leading* power i.

[33]This reflects the fact that an orthogonalization step is required in these methods. Although this step scales as N^3 its prefactor can be made very small and many people call them order $N^2 \ln(N)$ methods.

[34]The calculation of the Ewald sum is of order–N^2, but the prefactor is very small compared with the total calculation time, specially in the SSCAD. Furthermore, this part of the calculation only needs to be done once.

be framed as an order–N method, with a relatively small prefactor. As we will show in chapter 7, it is also very accurate.

The prefactors of the methods shown in table 3.2 have different values. A typical calculation for a two–atom cell may take a few milliseconds with Potentials, a few seconds with the SSCAD or the SETB, close to a minute with the LMTO–ASA, and a few minutes with pseudopotentials.

3.5 Conclusions

We used many different approximations to transform Dirac's original equation into a tractable Schrödinger's equation. The wide variety of paths taken reflects the complexity of the problem at hand. There is no hope, at least in the near future, to solve this problem *exactly*.

In this chapter, we reviewed the different total–energy methods that can be used to compute formation energies. Only those that are relevant in oxides were mentioned. We extensively described the different approximations commonly introduced by these techniques. In the following chapters, they will play a fundamental role in understanding the failure of some methods to produce accurate results.

We already showed that the ASA can introduce large errors when computing formation energies in oxides. Consequently, we will not further pursue this approach. We expect that all shape approximations will in general cause large errors since they are only suited for closed packed materials. Oxides, on the other hand, usually have low symmetry.

Another important characteristic of oxides is that they present a combination of an ionic and a covalent type of bonding. Classical models will need to incorporate terms to deal with directional bonding, nonspherical electron–density relaxations, and charge transfer. Furthermore, the SSCAD was designed to be used in ionic materials. Its performance will have to be carefully tested when this condition is not fully met.

The pseudopotential method seems to be the best suited technique to compute formation energies in oxides. In the next chapter, we will evaluate its performance.

When choosing a method, both the accuracy and speed should be taken into account. If our final goal is to simulate macroscopic behavior from the atomistic point of view, order–N methods are going to prevail. In the next chapters, we will show that the semiempirical tight–binding method is a very good approach not only because it can be formulated as an order–N method with a low prefactor, but also because it is a very accurate technique for oxides.

Chapter 4

The effect of approximations in total–energy methods: pseudopotentials as a benchmark

At this point, after so many approximations have been introduced in both the quantum– and the statistical–mechanical treatment of the solid, the skeptical reader may justifiably have some doubts about the applicability of our models. It is the purpose of the next sections to clarify these points and illustrate the power of the *ab initio* approach to predict and give insight on the behavior of materials.

We will study the effects of approximations in total–energy methods in two stages. In this chapter, we will show that the plane–wave pseudopotential technique can be used to accurately compute oxide properties. In the next chapter, we will use these results as a benchmark to evaluate the other, more approximate, methods.

To properly test the performance of the different total–energy techniques, it is essential to investigate materials systems that exhibit different types of bonding and behavior. We will mainly focus on three cases: CaO–MgO, ZrO_2, and CaO–ZrO_2. The first one, is one of the simplest oxide systems. Its properties are very well known and is an excellent case to test the accuracy of the methods against experimental results. It is also a typical example of a highly ionic material.

Zirconia (ZrO_2) and calcia–doped zirconia (CaO–ZrO_2), on the other hand, present a mixture of a covalent and an ionic bonding. Pure zirconia undergoes structural transformations from a low–symmetry monoclinic into a tetragonal and a cubic phase. They are an excellent case to test shape approximations of the crystal potentials.

Finally, since Ca and Zr are aliovalent,[1] the doping of zirconia by calcia is accompanied by the presence of charge–compensating vacancies. It is expected that in this situation, the cation and the anion will exhibit a variation in their charge that depends on the particular atomic arrangements [141, 142]. Consequently, it will be an ideal test case for those formalisms in which fixed charges are assumed.

Apart from the FLAPW method, the pseudopotential technique makes the least number of simplifying assumptions. The simplicity of the plane–wave basis and the

[1] Aliovalent means that the two cations have different valence.

ability of easily controlling the convergence and accuracy of the results have made the pseudopotential approach one of the most popular choices for performing *ab initio* calculations. Furthermore, as we mentioned in chapter 3, the use of the frozen–core approximation considerably simplifies the computation of formation energies (which is one of our main goals).

In the following sections, we will describe the use of pseudopotentials and lattice models for predicting materials properties. We will also study the effects of the approximations introduced by the former, and how they may affect its predictions. Applications of these techniques to different oxide systems will be discussed. We will show that they provide very reliable results. This will demonstrate that we are approaching a situation where computer experiments are becoming a reality.

We will start in section 4.1 by introducing the main features of the pseudopotential method. In section 4.2.1, we will apply this approach to the CaO–MgO system. Finally, in section 4.2.2 calcia–doped zirconia and the polymorphic transformations of zirconia will be studied.

Some of these applications *push the limits* of what can be computed in a reasonable time. The need for faster, but still accurate methods should be clear by the end of this chapter. Fulfilling this need is the objective of the rest of this work.

4.1 The pseudopotential method

The pseudopotential theory was introduced in 1959 by Phillips and Kleinman [143]. Very useful reviews can be found in references [124, 127, 128, 129, 144] and in the book by Singh [121].

In the pseudopotential method, the solution of the Kohn–Sham equation 3.12 is obtained by expanding the one–electron wave functions in plane waves. This is one of the easiest choices for a basis, which is reflected in the simplicity of the underlying ideas and in the implementation of the method. The valence wave functions are expanded poorly with a truncated plane–wave basis. Even by using the frozen–core approximation they have rapid oscillations near the core.[2] A pseudopotential is defined so that the valence wave functions have no nodes and consequently, are easier to expand. These *pseudo* wave functions are identical to the actual wave functions beyond a given core radius.

In the next sections, these different approximations and the actual implementation of the plane–wave technique are discussed.

[2]The origin of this behavior can be understood from the fact that the core and valence electron wave functions are orthogonal.

4.1.1 The plane–wave basis

The cell–periodic part, $u_{n\vec{k}}(\vec{r})$, of the electron wave function in equation 3.10 can be expanded in terms of a *discrete* plane–wave basis set,

$$u_{n\vec{k}}(\vec{r}) = \sum_{\vec{G}} c_{n\vec{k}\vec{G}} e^{i\vec{G}.\vec{r}}. \tag{4.1}$$

The sum is over all reciprocal lattice vectors $\vec{G}$. Equation 3.10 thus transforms into,

$$\psi_{n\vec{k}}(\vec{r}) = \sum_{\vec{G}} c_{n\vec{k}\vec{G}} e^{i(\vec{k}+\vec{G}).\vec{r}}. \tag{4.2}$$

Even though the plane–wave basis set is discrete, an infinite number of reciprocal lattice vectors is needed, in principle, to expand the valence wave functions in great detail. However, the coefficients $c_{n\vec{k}\vec{G}}$ corresponding to the large kinetic energy plane–wave contributions are small and the expansion is truncated beyond some particular cutoff energy E_{cut}.[3]

Plane waves form a *complete* set of basis functions. However, this is not true for a truncated expansion, leading to an error in the description of the valence wave functions. The magnitude of the error can be controlled by adjusting the value of the cutoff energy.

In principle, E_{cut} should be increased until the total energy has converged within the desire error. However, *differences* in energy converge faster than total energies with respect to E_{cut}. The high kinetic energy components of the expansion are used to reproduce the details of the rapidly varying parts of the valence wave functions. These parts are located close to the core and they usually remain unchanged when the atom is placed under different environments. Consequently, quantities that depend on *differences* of this electron–density distribution, such as the formation energy, converge faster with respect to E_{cut} than the total energy.

To avoid large cutoff energies with unmanageable large basis sets, the *pseudopotential approximation* needs to be used.

4.1.2 Pseudopotential approximation

The physical properties of a material are mostly determined by the behavior of the wave functions beyond the core region. The pseudopotential approximation takes advantage of this fact by replacing the actual valence orbitals by pseudo wave functions. The core orbitals, on the other hand, are assumed to be frozen (frozen–core approximation). Their effect on the valence electrons is taken into account as a potential added to the nuclear potential. The idea is then to replace these two contributions by a *pseudopotential* with the same scattering properties as the original potential but

[3]The kinetic energy corresponds to $\frac{\hbar^2}{2m}\left|\vec{k}+\vec{G}\right|^2$. The reciprocal vectors that are used in the expansion are determine by the relationship $\frac{\hbar^2}{2m}\left|\vec{k}+\vec{G}\right|^2 \leq E_{cut}$.

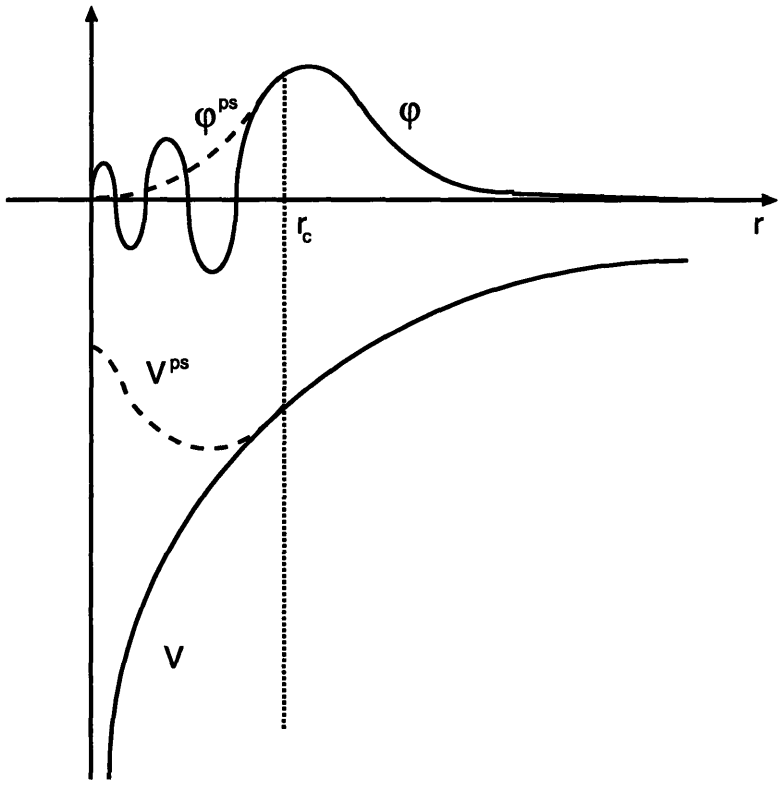

Figure 4-1: Representation of the pseudo wave function and its corresponding pseudopotential (dashed line). The actual wave function and potential from which they are derived are also shown (solid line). The point at which the real and pseudo values are matched is called r_c.

chosen so that the pseudo–valence wave functions do not have nodes inside the core region.

The situation is illustrated in figure 4-1. Outside the core, the pseudo and actual potentials are identical. The strong potential near the core is replaced by a much weaker pseudopotential. The resulting valence pseudo wave function is smoother than the real one in the core region. Consequently, a much lower E_{cut} is needed to expand this orbital.

The all–electron valence wave functions have different number of nodes according to their angular momentum. The pseudopotential should be able to introduce different phase shifts for the different angular components of the pseudo wave functions. A pseudopotential that depends on the angular momentum is called a *nonlocal pseudopotential* (and *local* otherwise).[4]

[4]Though it is possible to introduce arbitrary shifts for each angular momentum with a local potential, there is not a very good control over its smoothness.

4.1.3 Pseudopotential properties

Usually three properties are required of a pseudopotential: **norm conservation**, **transferability**, and **smoothness**.

It is very important that the pseudopotential reproduce the valence electron density outside the core regions since the total energy critically depends on its value. This is guaranteed by requiring not only that the spatial dependence of the real and the pseudo wave function be equal beyond the core but also that the charge within the core be identical. This last condition corresponds to

$$\int \psi^{ps}\psi^{ps*}dv = \int \psi\psi^{*}dv. \tag{4.3}$$

The integrals in this equation are over the core volume. A pseudopotential whose wave functions satisfy equation 4.3 is said to be **norm conserving**. The idea was originally introduced by Topp and Hopfield [145] and Startkloff and Joannopoulos [146].

A pseudopotential should produce accurate results for different valence–electron configurations. This property is known as **transferability**. Hamman and coworkers showed that, by imposing norm conservation, the first order energy dependence of the scattering properties of the core and its pseudo counterpart are the same [147]. This guarantees that the phase shifts of the pseudopotential are accurate over a wide range of energies. Also, it has to be noted that the smaller the value of r_c (where the pseudo– and all–electron values match), the more transferable the potential. However, in this last case the potential will become stronger.

Finally, since the only two conditions imposed on the pseudo wave function inside the core are to be nodeless and norm–conserving, there is still some freedom to choose its actual shape. In order to speed up the calculations, the shape should be **smooth** so that a minimum number of plane waves is needed. For example, Rappe and collaborators optimized the convergence with basis size by minimizing the kinetic energy of the high Fourier components of the pseudo wave function [125]. The corresponding pseudopotentials are called *optimized pseudopotentials.*

Various research groups introduced different variants for these nonlocal, norm–conserving pseudopotentials. They are described in references [147, 148, 149].

It is not necessary to impose norm conservation to make the all–electron and the pseudo wave functions equal outside the core. This condition can be imposed while letting the pseudo wave function be as "smooth" (or "soft") as possible. Consequently, while the actual and pseudo density outside the core still coincide, the same is not true inside the core regions. The pseudopotentials that are used to generate these wave functions are called *ultrasoft* and were recently introduced by Vanderbilt [126]. The idea is illustrated in figure 4-2. The high kinetic energy plane waves serve to expand the pseudo wave function mainly within the core. If the normalization requirement is relaxed, strongly peaked functions can be "softened" and considerably smaller cutoff energies can be used.

The use of ultrasoft pseudopotentials results in considerable time savings due to the reduction in the size of the basis set. On the other hand, since the pseudo wave function is no longer normalized, there is no correct change of the phase shift with

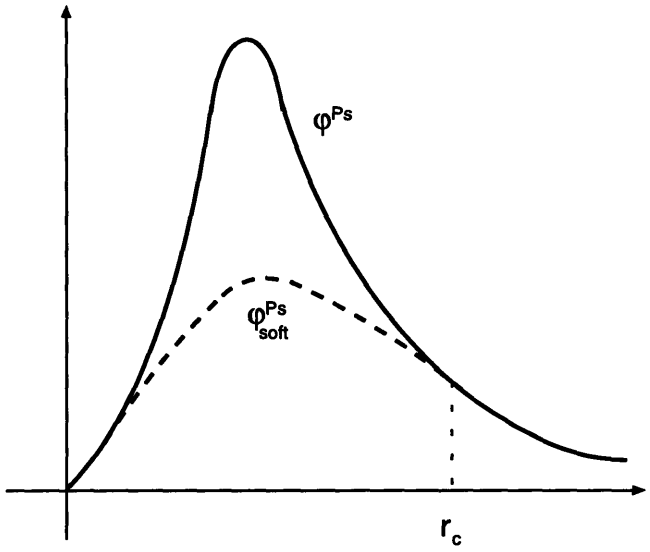

Figure 4-2: Comparison between wave functions obtained by using a norm conserving and an ultrasoft pseudopotential. The solid line is the pseudo wave function corresponding to a regular norm–conserving pseudopotential and the dashed line to an ultrasoft one.

energy and extra time is required to correct for this. Also, new terms need to be added when computing electron densities [126].

4.1.4 Pseudopotential generation

Originally, the pseudopotential method was a semiempirical approach. The pseudopotential was represented by some simple function (e.g., a few terms in a Fourier expansion) whose coefficients were adjusted to fit experimental results, such as some features of the band structure [150].

Here, we use a completely *ab initio* approach to find the pseudopotential. An all–electron calculation is performed on an atom, and a parametrized form of the pseudopotential is adjusted so that it reproduces the eigenvalues and eigenfunctions beyond the core radius r_c.[5] A strict lower limit for r_c is the position of the outermost node in the actual wave function. In general, r_c is chosen so that it lies between this lower value and the position of the outermost peak of the all–electron wave function.

Note that different pseudopotentials are computed from different atomic configurations. Though the transferability properties of a norm–conserving pseudopotential are very good, a configuration close to the one present in the solid should be used (e.g., instead of using a neutral atomic configuration, ionized or excited configurations are taken to avoid "bumpy" pseudo wave functions [148]).

[5]It is common practice to use different r_c for different angular momenta (i.e., r_{cl}, where l specifies the angular momentum).

The procedure just outlined provides a pseudopotential whose predictions are equivalent to those from all–electron calculations for the reference atom, but that represent a linearization of the exchange–correlation energy when the valence electron configuration is changed.[6] When the valence and core densities are well separated, the errors introduced are small. On the other hand, when there is a significant overlap between them, the transferability is greatly reduced and the errors in the total energy can be important. This problem can be avoided by using the so–called *core corrections* that explicitly treat the nonlinear exchange and correlation interaction between the core and the valence electrons [151].

The Kleinman–Bylander transformation

The computational speed is significantly improved by using local pseudopotentials. However, there are certain cases in which nonlocal pseudopotentials have to be used to obtain accurate results. To make this as efficient as possible, only a *partial* projection of the nonlocal components of the wave functions is usually performed. Kleinman and Bylander suggested using a single basis state ϕ_{lm}^{ps} (the wave functions of the pseudoatom) for each angular momentum component [152]. The Kleinman–Bylander pseudopotential is then written as

$$V_{KB} = V_{loc} + \sum_{lm} \frac{|\phi_{lm}^{ps} \delta V_l >< \delta V_l \phi_{lm}^{ps}|}{< \phi_{lm}^{ps} |\delta V_l| \phi_{lm}^{ps} >}, \tag{4.4}$$

where V_{loc} is an arbitrary local potential used to produce an accurate and transferable pseudopotential and $\delta V_l = V_{NL,l} - V_{loc}$, $V_{NL,l}$ being the real l component of the nonlocal pseudopotential. For the reference atomic state, both V_{KB} and the real nonlocal potential produce the same result. By carefully choosing V_{loc},[7] a high–quality pseudopotential can be obtained.[8]

4.1.5 Computational procedure

The general procedure for computing the total energy of a solid using the pseudopotential approach is summarized in figure 4-3. It starts by computing the pseudopotentials for the elements that form the solid and by defining the size of the basis by means of the cutoff energy. A starting electronic density (or the coefficients of the electron wave functions) is guessed to build the potential in the Hamiltonian. Its eigenvalues and eigenfunctions can be computed using methods such as **conventional diagonalization**, **molecular–dynamics**, or **conjugate gradient minimization**. From

[6] The interaction between the valence and core electrons is transferred to the pseudopotential and consequently, linearized. This is a source of error since the kinetic and exchange–correlation energy are explicitly nonlinear. The contribution of these terms is only important when there is a significant overlap between the core and valence orbitals.

[7] Usually the $l = 0$ component is taken as the local potential.

[8] The application of the Kleinman–Bylander transformation can introduce problems, such as the existence of "ghost" states that can be avoided by a proper choice of the local potential or by changing the core radius [153].

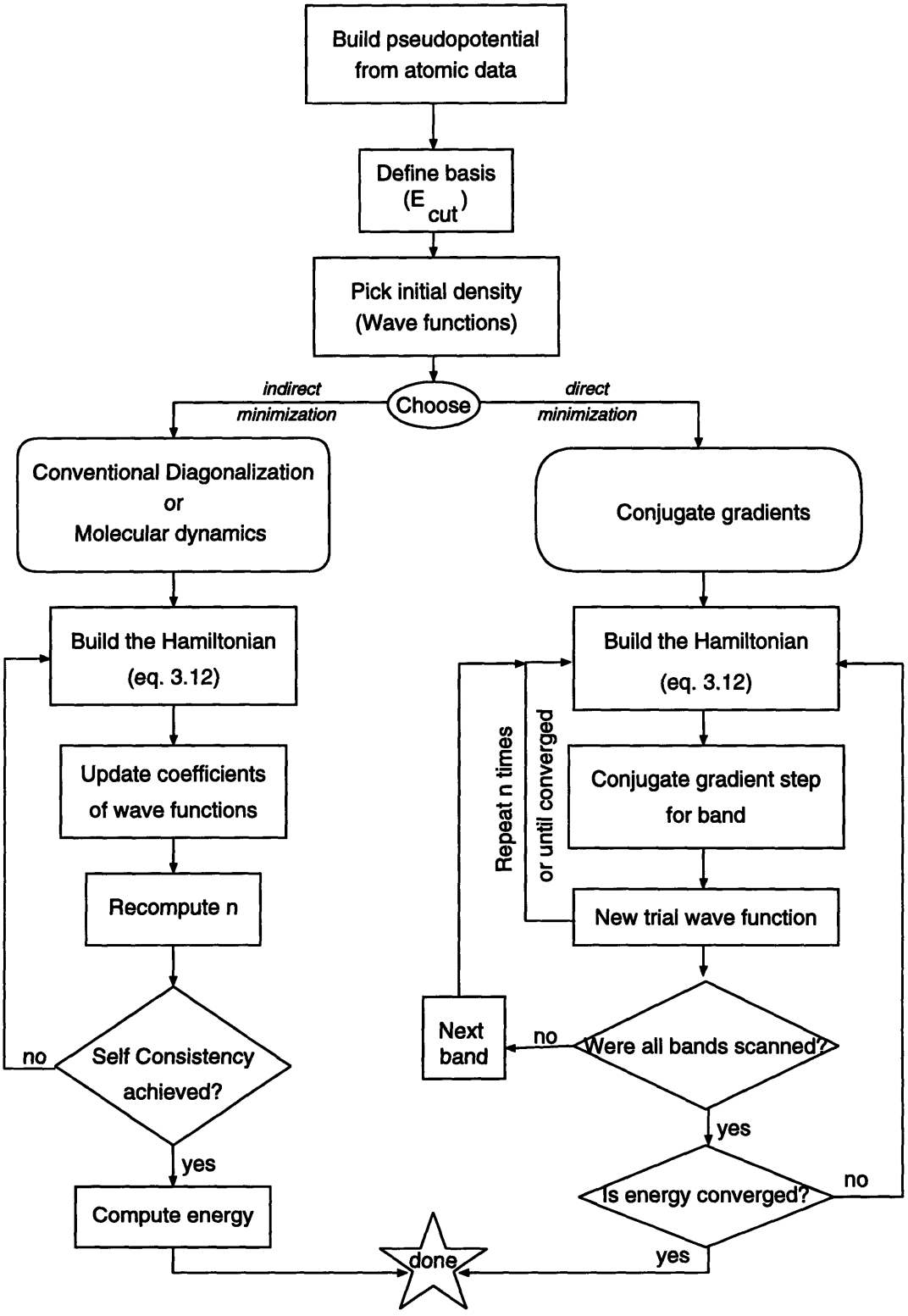

Figure 4-3: Steps for computing total energies using the *ab initio* pseudopotential approach.

the resulting eigenfunctions, the density is recomputed and the process repeated until self–consistency is achieved. At each iteration, a linear combination of the "new" and "old" electronic density is used to speed up convergence.

Conventional diagonalization procedures are straightforward to use but they can only handle Hamiltonian matrices of limited size in a reasonable time. The Hamiltonian matrix can be very large (of the order of thousands or more basis functions) and increases with the number of atoms in the unit cell. Consequently, this method is limited to those cases where only a few atoms are present. The time scaling is also a problem since the computational cost of diagonalization increases as the third power of the number of plane waves used.

Alternative approaches to minimize the Kohn–Sham energy have been suggested. For example, the Car–Parrinello method to perform **molecular dynamics** on the electronic degrees of freedom can be used [123, 124]. The Kohn-Sham energy functional is a function of the coefficients of the plane–wave basis set. These coefficients are regarded as the "coordinates of classical particles". Starting from a set of trial wave functions, these classical particles are given an initial kinetic energy and the system is cooled down until the set of coordinates reaches the minimum.[9] After each molecular–dynamics step the Hamiltonian is recomputed. The positions of the ions and the electronic degrees of freedom can be optimized at the same time. This procedure scales as $N_b N_{pw} \ln N_{pw}$ where N_{pw} is the number of plane waves and N_b is the number of bands (generally orders of magnitude less than N_{pw}). This method is usually much faster than the conventional diagonalization.

The two techniques just described constitute an *indirect* way of minimizing the energy functional by finding the self–consistent Kohn–Sham Hamiltonian. This indirect procedure can lead to instabilities when performing calculations on large systems with large energy cutoffs [124]. This problem is avoided with the **conjugate gradient** procedure that allows for a *direct* minimization of the Kohn–Sham energy functional. To avoid using large amounts of computer memory, the conjugate gradient steps are usually performed one band at a time. Each conjugate gradient iteration requires twice as many operations than a molecular–dynamics step does for a single band, but usually less iterations are needed. More details of this approach can be found in reference [124].

4.1.6 Further developments

The use of plane waves to expand the solutions of the Kohn–Sham equation has many advantages. They are very simple to implement, efficient fast Fourier transforms can be used, and an excellent control of convergence is obtained by changing the energy cutoff. Furthermore, plane waves provide a uniform and unbiased resolution in space. Physical quantities can thus be computed accurately and with little complication. For example, forces are determined using the Hellmann–Feynman theorem [154] without

[9]The Kohn–Sham energy functional takes the place of the potential energy of a conventional molecular dynamics procedure and a fictitious mass, μ, is introduced so that the kinetic energy is defined as $\mu < \dot{\psi}|\dot{\psi} >$. The electronic wave functions are constrained by orthonormality requirements.

corrections from Pulay forces [122] since plane waves do not depend on the ionic positions.

On the other hand, these same characteristics make their use in all–electron calculations, or for elements with hard pseudopotentials, very difficult. Solutions of the Kohn–Sham equations vary rapidly close to the ions and decay smoothly in the space between them. Increasing the cutoff energy increases the resolution not only in the core regions but in all space. Thus, a large part of the computational effort is spent in describing the interstitial regions with unnecessary precision. In order to reduce these efforts, a nonuniform resolution can be used.[10]

Recently, some schemes have been proposed to modify the plane–wave approach so that the simplicity of the basis is maintained but its size greatly reduced. Gigy generalized the use of plane waves to a non–Euclidean curvilinear space [155, 156, 157]. As a result, an effective energy cutoff that varies in the unit cell in an unbiased way is obtained. Other approaches have been developed to go beyond the use of plane waves while retaining their advantages. They employ a wavelet formalism that provides a systematically improvable basis and a nonuniform resolution [158].

In Gigy's approach, the curvilinear coordinates themselves are treated as a variational parameters. The coordinate system is thus allowed to adapt to the variations in the potential, effectively increasing the plane–wave resolution in those regions where the inhomogeneities are larger (for the same cutoff). Consequently, a much smaller energy cutoff is required,[11] considerably increasing the speed of the method. The resulting basis set does not depend explicitly on the ionic positions, therefore Pulay corrections are not needed [156].

The use of plane waves in adaptative curvilinear coordinates do not necessarily require the use of pseudopotentials. Due to the considerable reduction in the cutoff energy, all–electron calculations can be carried out, as shown by Devenyi and collaborators [159].

The wavelet basis functions on the other hand, are localized both in real and reciprocal space. This allows the description of functions with spatially variable resolution. These bases do not depend on the positions of the ions and thus Pulay corrections are not necessary. More details can be found in reference [158].

4.2 Applications

The plane–wave pseudopotential method will be applied to three cases: CaO–MgO, ZrO_2, and CaO–ZrO_2. Various properties such as formation energies, lattice constants, and electron densities will be computed. From this information, we will be able to show that reliable predictions can be obtained from the pseudopotential method. Furthermore, in the next chapter, these properties will be used as a benchmark to assess the accuracy of different approximations in the total–energy methods shown

[10] Localized wave functions, such as atomic orbitals, can be used to obtain nonuniform resolution in space. However, it is usually difficult to systematically improve the basis. Furthermore, they depend on the ionic positions so that Pulay forces need to be computed.

[11] Usually four times smaller [156].

in table 3.1. Whenever possible, we will also use the results to gain insight in the behavior of these oxides.

In appendix C, we describe another application of pseudopotentials. We show that this method can be used to compute voltages of lithium batteries. The voltage is directly related to the formation energy of a lithium–transition–metal oxide from a metallic lithium and a transition–metal oxide. The insight pseudopotential provides in understanding the factors that determine the voltage will lead to the design of better batteries.

Some characteristics of the pseudopotential calculations are common to the three cases. We will use norm–conserving Kleinman–Bylander–type pseudopotentials. They will be optimized to reduce the energy cutoff. This is very important since all the compounds have oxygen atoms (and some of them even transition metals). We will minimize the Kohn–Sham energy functional using the conjugate–gradients technique.

In all cases, we will use the same oxygen pseudopotential. Its core radius is 0.42 Å for the $2s$ and $2p$ valence orbitals. The s component is taken to be the local one in the Kleinman–Bylander transformation. The Perdew–Zunger parametrization of the exchange and correlation energy [99] will be used in all the calculations.

4.2.1 The CaO–MgO system

The CaO–MgO system was described in section 2.3.1. It can be thought of as two interpenetrating fcc sublattices. One of them is fully occupied by oxygen atoms while the other one is occupied by different arrangements of calcium and magnesium atoms. Since one of the main goals is to compute the phase diagram, the formation energies of many different structures (or arrangements of Ca and Mg in one of the sublattices) have to be computed. At least 20 structures are required to obtain a converged cluster expansion, pushing the limits of what can be done with pseudopotentials in a reasonable time.

Instead of computing the phase diagram, we constructed ten of the smallest possible structures in the system and we computed their formation energies and cell parameters. This information was then used to evaluate faster, more approximate total–energy methods. We will also use a subset of these results in the next chapters to fit pair–potential models and a tight–binding Hamiltonian. The "end members" of the phase diagram, CaO and MgO, were also studied extensively.

We identified each ordered structure according to its cation arrangement on the fcc sublattice. The assigned names correspond to either their Strukturbericht notation, their prototype structure, or a conventional name. A description of each of the atomic arrangements can be found in references [45] and [66].

Pseudopotential generation

Both the Ca and the Mg pseudopotentials were generated for a neutral atom with a [Ar]$4s^2$ and a [Ne]$3s^2$ configuration respectively (the core is marked between brackets). The core radius was 1.32 Å and 0.84 Å for Ca and Mg respectively.

There is a slight overlap between the core $2p$ and the valence $3s$ orbitals in

	CaO	MgO
Lattice constant (Å)	4.8 (4.81[a])	4.21 (4.211[b])
Bulk Modulus (Mbar)	1.19 (1.15[a])	1.55 (1.55[c]–1.62[d])

Table 4.1: Calculated lattice constants and bulk modulus for pure CaO and MgO. The values in parenthesis correspond to experimental measurements.

[a]Reference [162].
[b]Reference [163].
[c]Neutron scattering data [164].
[d]Ultrasonic interferometry [165].

Mg [160]. Core corrections can be used to compensate for nonlinearities in the exchange–correlation functional. We did not include these corrections since their effect is only important at very high pressures as shown in the FLAPW calculations of reference [120]. (See also reference [161].)

Details of the calculation

We used 10 special Chadi–Cohen $\vec{k}$ points (see appendix B) for Brillouin zone integrations for the rocksalt structure, resulting in a total–energy convergence better than 1 meV per atom. We also added extra points when computing bands (with zero weight for the integrations). For all the other superstructures, we took a set of $\vec{k}$ points *equivalent* to these Chadi–Cohen points.[12]

Convergence of formation energies with respect to basis size (number of plane waves) was carefully verified within 1meV per atom. A 900 eV energy cutoff was used for all the superstructures.[13]

All the structures were fully relaxed with respect to their symmetry–allowed degrees of freedom. This means that the total energies were minimized by letting the atoms move in the directions compatible with the symmetry of the structure.

Results for pure CaO and MgO

Both CaO and MgO have the rocksalt structure shown in figure 2-8. The side of the cubic unit cell is the only degree of freedom than can be relaxed according to the symmetry. In table 4.1, we compare the experimental and the computed lattice constants and bulk moduli for these structures.

The electronic band structures are shown in figure 4-4. We find CaO and MgO to

[12]The equivalent Chadi–Cohen $\vec{k}$ points in the Brillouin zone were determined by applying all the fcc symmetry operations. These points were then reduced back to a smaller set by applying the symmetry operations of the corresponding superstructures. See appendix B.

[13]This is an extremely high cutoff value. By increasing the accepted error in the energy to a few meV, the cutoff energy can be reduced to 700 eV.

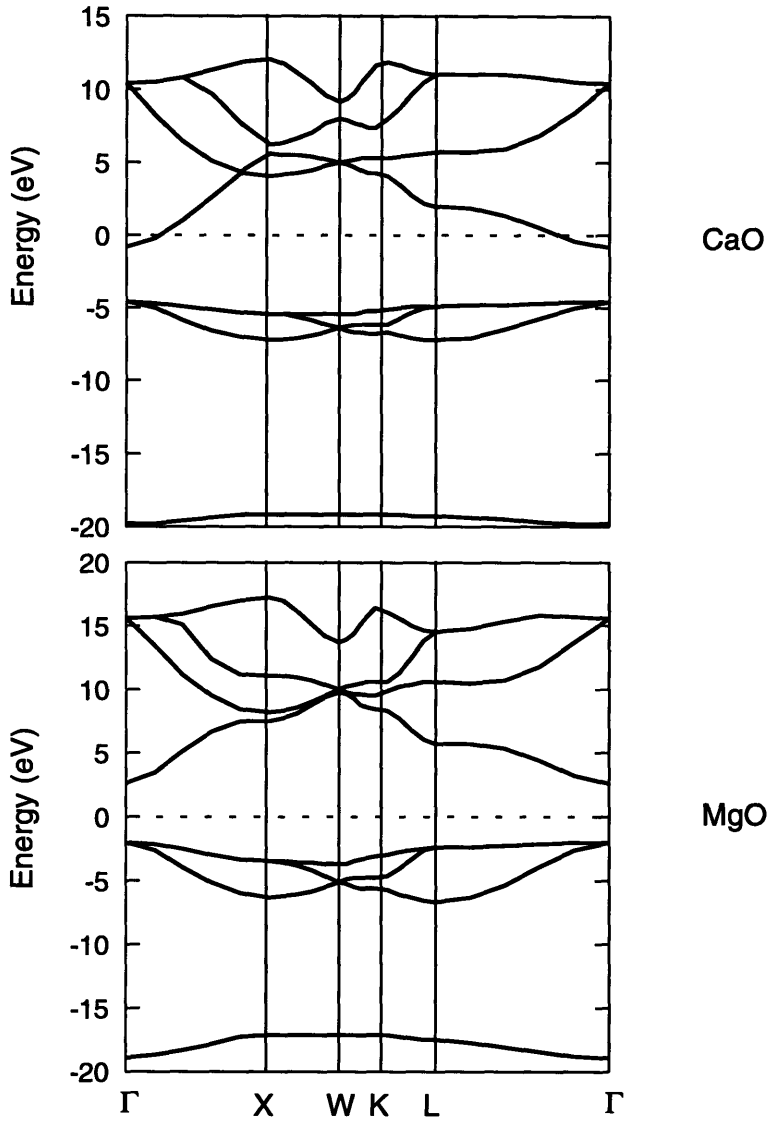

Figure 4-4: Electronic band structures for pure CaO and MgO in the rocksalt structure computed with the pseudopotential method.

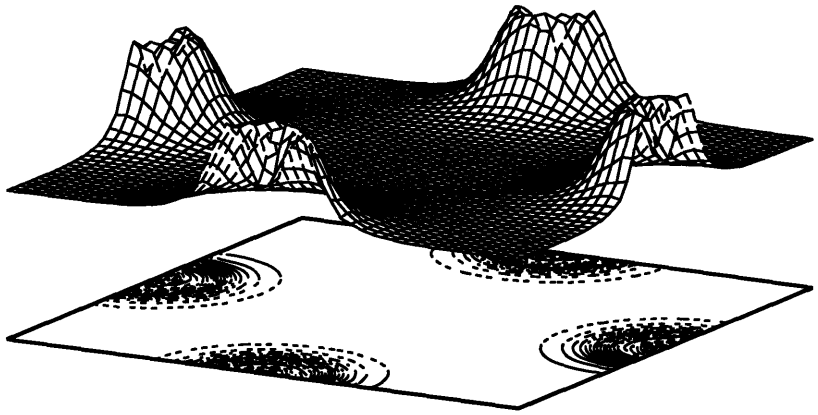

Figure 4-5: Valence electronic density and its contour plot for the (001) plane of MgO. The Mg ions sit at the corners and center of the region of the plane shown in the picture while the oxygen ions sit at the middle of the edges. It is clear from the figure that almost no valence electrons are close to the Mg ions.

be insulators with a direct Γ–Γ gap of 3.74 eV and 4.57 eV respectively. The experimentally measured band gaps are 7.09 eV for CaO [166] and 7.77 eV for MgO [167].

The total electron valence density for MgO is shown in figure 4-5. The density for CaO (not shown) is very similar.

Results for CaO–MgO compounds

The lattice constants and formation energies of all the computed structures are shown in table 4.2.

Discussion

The lattice constants calculated for CaO and for MgO are predicted within less than 0.2% of the experimental values. One has to remember that the only inputs to the method were the atomic numbers and the structure.[14] In general, the experimental and computed lattice constants coincide within a few percent for LDA methods. The LDA consistently overestimates the stability of the bonds leading to lattice constants smaller than the experimental ones [97]. The errors in the bulk modulus predicted by the LDA are usually larger. The difference can be as large as 30% with respect to experimentally measured values. For CaO and MgO, they were within 4%.

[14]The structural information is not required but when used, it considerably speeds up the calculations.

Structure	Composition	Cell Parameters	ΔE_{pseudo}
1- $L1_0$	$CaMgO_2$	a=b=3.240; c=4.558	0.141
2- $L1_1$	$CaMgO_2$	a=b=3.215; c=15.643	0.094
3- A_2B_2	$CaMgO_2$	a=b=4.608; c=8.900; $x_1 = 0.235$	0.093
4- $L1_2$	Ca_3MgO_4	a=b=c=4.698	0.092
5- $L1_2$	$CaMg_3O_4$	a=b=c=4.423	0.131
6- DO_{22}	Ca_3MgO_4	a=b=4.715; c=9.279; $x_1 = 0.235$	0.073
7- DO_{22}	$CaMg_3O_4$	a=b=4.448; c=8.665; $x_1 = 0.264$	0.100
8- $MoPt_2$	Ca_2MgO_3	a=4.673; b=3.266; c=9.832; $x_1 = 0.335$; $x_2 = 0.345$	0.087
9- $MoPt_2$	$CaMg_2O_3$	a=4.487; b=3.118; c=9.409; $x_1 = 0.330$; $x_2 = 0.319$	0.091
10- Ni_4Mo	Ca_4MgO_5	a=b=7.446; c=4.755; $x_1 = 0.600$; $y_1 = 0.204$; $x_2 = 0.288$; $y_2 = 0.093$	0.060

Table 4.2: Formation energies and cell parameters of different ordered structures in the CaO–MgO system obtained by using the plane–wave pseudopotential method. All cell parameters were fully relaxed, including the internal positions, x_i, that are shown here according to the Wyckoff notation in reference [168]. Lattice constants are expressed in Å and formation energies are in eV/ion. A description of each structure can be found in reference [45] or [66].

The errors in the band structure are larger. The LDA usually underpredicts the band gaps by 50% (as in our case). However, we have to be careful with the interpretation of the computed bands. The bands shown in figure 4-4 are a plot of the Kohn-Sham single electron eigenvalues for different $\vec{k}$ points. These are not the quasi–particle energies although they represent a good approximation of them, particularly for the occupied states. Strictly speaking, these energies are the derivatives of the total energy with respect to the occupation numbers of the corresponding states [98].[15]

The electronic density in figure 4-5 shows no evidence of any concentration of valence charge between the ions. The great majority of the charge resides in the oxygen atom, the valence orbitals of the magnesium atoms being almost empty. These characteristics agree well with the picture of ionic bonding (with almost perfect formal charges) that is used to describe CaO and MgO. However, the charge does not have a perfect spherical symmetry around the oxygen atoms and their size changes with the environment. This will be carefully analyzed in chapter 5.

All the formation energies of intermediate compounds in the CaO–MgO system were found to be positive. This agrees well with the fact that no stable ordered structure has been observed in the system except for the pure end members. The number of computed formation energies is not enough to obtain a converged cluster expansion. However, if the SSCAD ECI's are rescaled according to the difference between the pseudopotential and the SSCAD formation energies the solid part of the CaO–MgO phase diagram can be estimated. The resulting phase boundaries are very close to the experimental ones. We will come to this point later in chapter 5.

Though not rigorous, the above process shows the power of the first–principles approach to study phase stability if an accurate *and* fast total–energy technique is developed. The rest of this work is dedicated towards that goal.

4.2.2 The CaO–ZrO_2 system

Zirconia is stable at room temperature in a monoclinic structure (baddeleyite) and transforms into a tetragonal phase (space group $P4_2/nmc$) at approximately 1180 °C [170]. Before melting, it transforms again, but now into a cubic phase (fluorite–type structure) at approximately 2350 °C [171]. In figure 4-6, we describe these three phases. The addition of impurities such as CaO, MgO, or Y_2O_3, can stabilize the cubic and tetragonal phases to room temperatures. In figure 4-7, we show the zirconia rich part of the CaO–ZrO_2 phase diagram. Apart from the pure zirconia structures, three other structures have been detected in this portion of the diagram with compositions: $CaZr_4O_9$, $Ca_6Zr_{19}O_{44}$, and $CaZrO_3$. They correspond to space groups $C2/c$, $R\bar{3}c$, and $Pcmn$ respectively. Note that $CaZr_4O_9$ and $Ca_6Zr_{19}O_{44}$ are not stable at low temperatures. For a detailed description of these structures, see references [173] and [174].

[15]The highest occupied eigenvalue gives the ionization energy of the system (work function in metals) if the *exact* density–functional formalism is used. For most approximate functionals, it is common practice to keep that interpretation though it is not completely correct [169].

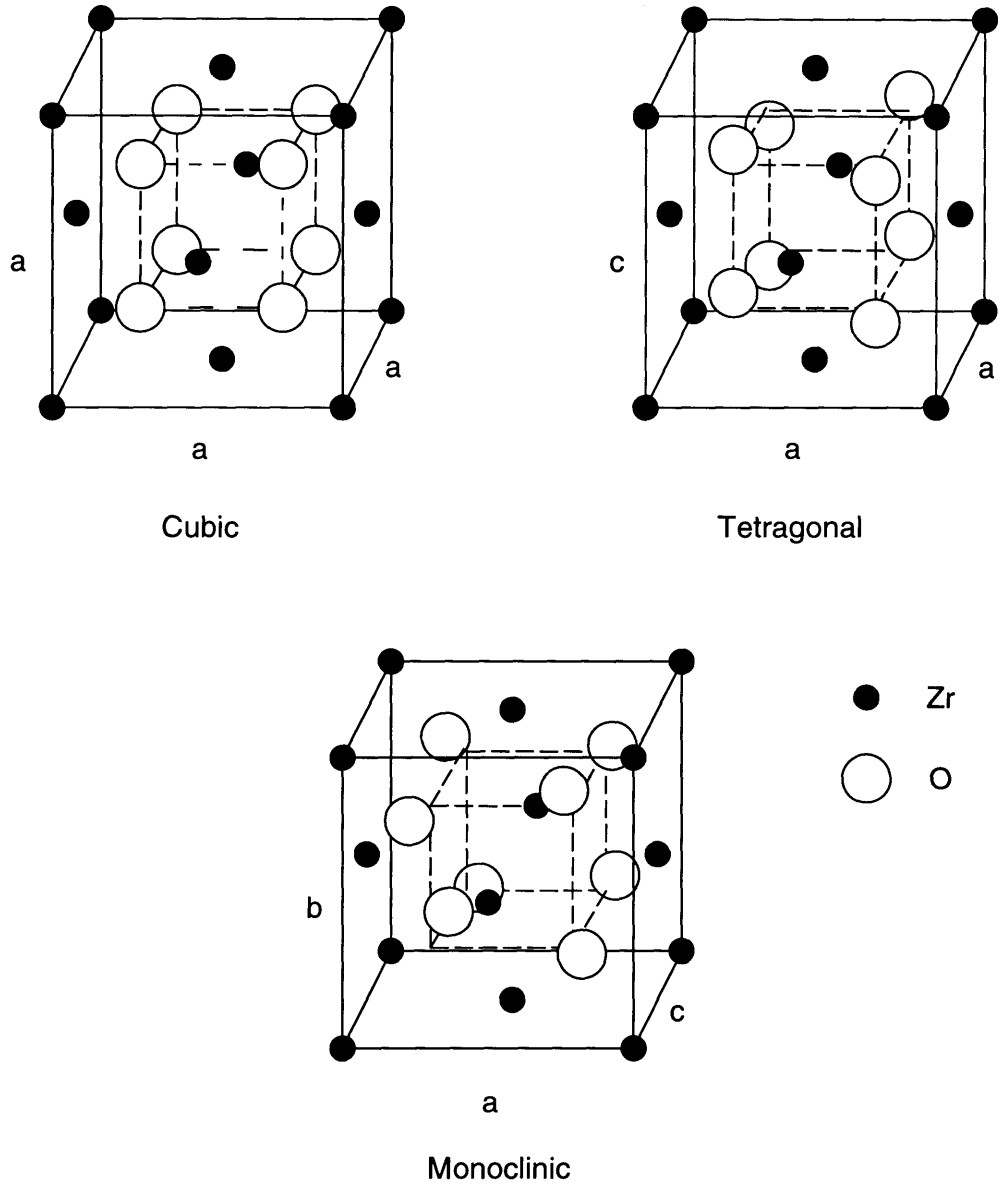

Figure 4-6: Polymorphic structures of zirconia.

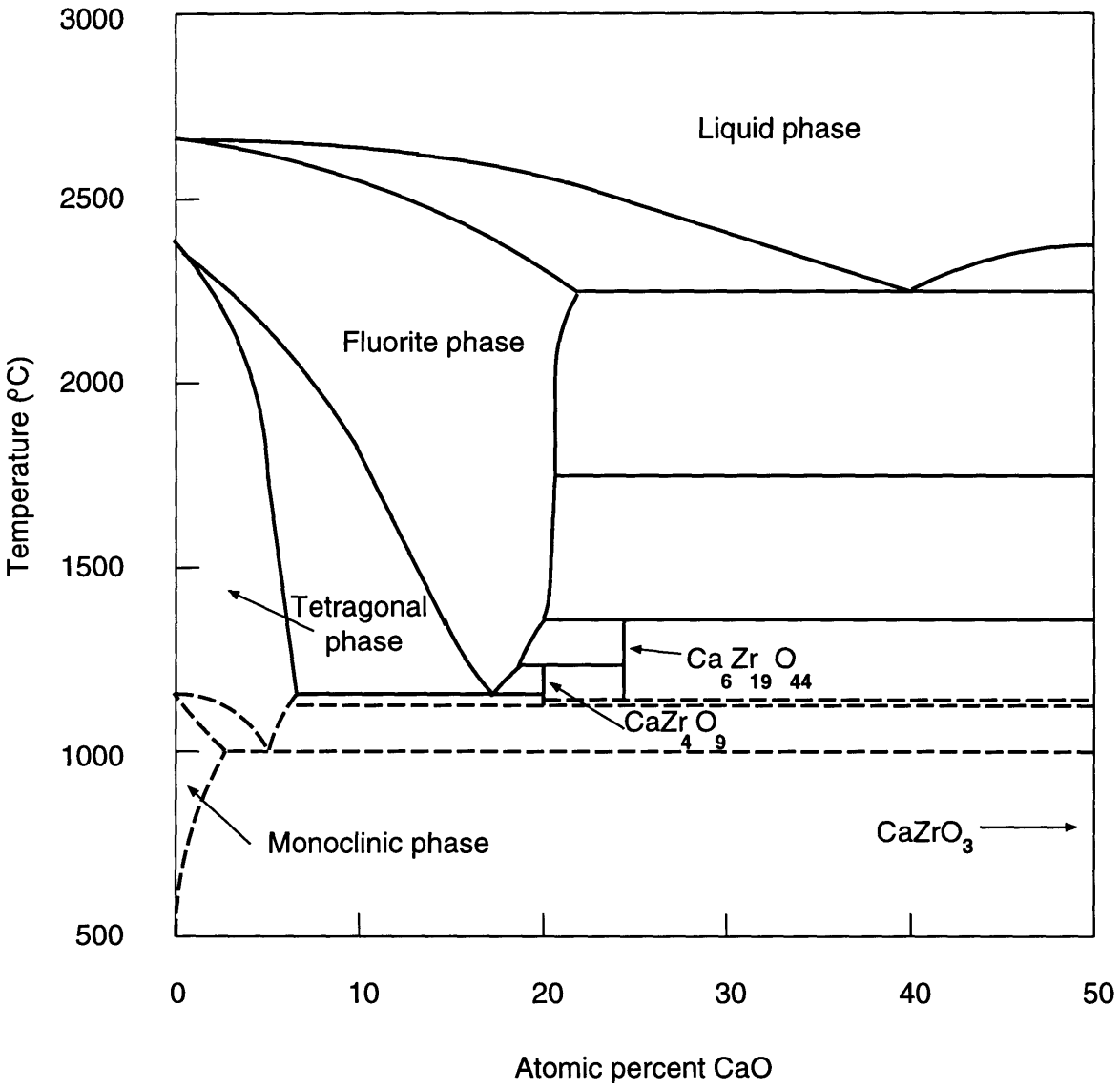

Figure 4-7: Experimental $CaO–ZrO_2$ phase diagram. See reference [172].

The stabilized zirconias present excellent ionic conductivity[16] and thermomechanical properties.[17] Consequently, zirconia has many applications from refractory or structural materials to oxygen sensors, solid state electrolytes, high–temperature fuel cells, and resistance heating elements.

Ceramics are ideal to be used in environments with extremely high temperatures since their melting point is above the one for most common structural metals. However, their brittleness sometimes prevents this kind of applications. The low fracture toughness implies little resistance to crack propagation. Consequently, there is a considerably interest in understanding the toughening mechanisms in doped zirconia and specially the stabilization effects that lead to them. The toughening process has its origins in the stress–induced martensitic transformation of tetragonal particles to the monoclinic phase. This transformation causes a 4% increase in particle volume whose residual strain field tends to limit the crack opening [176].

Many experimental and theoretical studies have been conducted to understand the stabilization mechanisms in zirconia [89, 141, 142, 171, 177]. Measurements are difficult to perform since they must be done at extremely high temperatures. The quality of the samples is also a concern (defects and impurities). This seems to be the ideal scenario for the use of computational experiments. However, the extremely complex crystal structure of monoclinic zirconia prevents the use of accurate total–energy methods. Most quantum–mechanical calculations have been performed on the tetragonal and cubic phases.

Even potential models are problematic in this system, not because of the complexity or size of the cell but because oxygen breathing, electron polarizability, and covalency play an important role in determining the formation energies (as we explain in the next chapter). These effects are not well represented in such simple energy models. However, very useful information has been obtained about the defect structure [175] and the identification of possible stabilization mechanisms [141]. Recently, Wilson and collaborators went beyond the standard potential and shell model [89]. They introduced a breathing mechanism for the oxygen atoms (see section 3.2.2) and included the dipolar and quadrupolar induction effects. Although they adopted formal ionic charges in their model, the right ordering of the energies of the different possible structures in pure zirconia was predicted.[18]

Many *ab initio* calculations have been reported for the tetragonal and cubic phases. Almost every total–energy technique has been used in zirconia: FLAPW [178, 179], *ab initio* Hartree–Fock [141, 177], full potential LMTO [89], linear combination of atomic orbitals (LCAO) [142, 180], and PIB [181]. However, to our knowledge, this is the first time pseudopotential studies were performed.

Our goal is to use the pseudopotential calculations as both an input and a test

[16]The ionic conductivity is produced by the numerous charge–compensating vacancies originated in the replacement of Zr^{+4} by Ca^{+2}, Mg^{+2}, Y^{+3}, etc. See references [171] and [175].

[17]Stabilized zirconia presents extremely high strength, toughness, and thermal–shock resistance.

[18]Partial charges are not physically well defined. However, we will show in chapter 8 that there is a strong dependence of the ionic charge on the environment when we adopt a consistent definition for the charge. This effect needs to be taken into account.

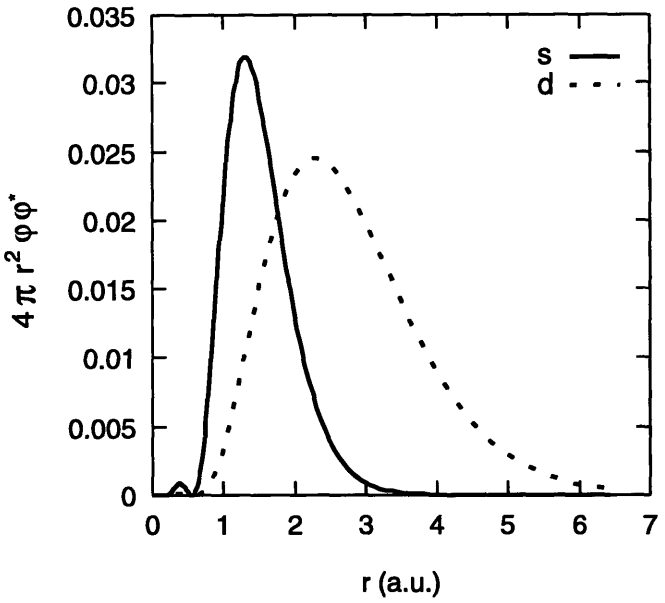

Figure 4-8: Computed electronic density for the 4p and 4d orbitals of the Zr^{+2} ion. The wave functions have been normalized to one. The overlap between the densities can clearly be seen.

to our tight–binding Hamiltonian. We will compute the structural energy difference for the cubic–tetragonal transition and the formation energies of several CaO–ZrO_2 ordered structures. We will also analyze the electronic charge densities to understand the approximations of simpler methods.

Pseudopotential generation

The electronic configuration of zirconium is [Kr]$4d^2 5s^2$. One would like to treat [Kr] as the atomic core. However, we detected a significant overlap between the $4d$ and the $4p$ orbitals. This is illustrated in figure 4-8. Furthermore, zirconium atoms are usually highly ionized in oxide environments. Consequently, we generated the pseudopotential for the valence configuration $4s^2 4p^6 4d^2 5s^0$ corresponding to Zr^{+2}.

We generated an optimized pseudopotential, with the Kleinman–Bylander transformation. The s angular component was taken as the local potential, with the p and d components as the nonlocal ones. The core radii were 0.687 Å, 0.74 Å, and 0.84 Å for the s, p, and d orbitals respectively.

Results for pure ZrO_2

We calculated the energy difference between cubic and tetragonal zirconia. The monoclinic phase was not computed since it is very complex, with 12 atoms in the unit cell and 13 variables to optimize. Performing these calculations with pseudopotentials requires a large number of supercomputer hours. A single point calculation may

	Experiments[a]	Pseudopotentials
Cell Parameter		
Cubic ZrO_2		
a=b=c	5.092	5.050
Tetragonal ZrO_2		
a=b	3.571	3.575
c	5.20	5.153
z(O)	0.303	0.295
Energy differences:		
E_{cubic}-$E_{tetragonal}$	0.058	0.045

Table 4.3: Cell parameters and structural energy differences for the tetragonal and cubic phases of zirconia at zero pressure. The energies are in eV per ZrO_2 formula unit and the lattice constants are in Å. All cell parameters were fully relaxed, including the internal position z_i (shown here according to the Wyckoff notation in reference [168]). The experimental z value for the tetragonal structure was measured at 1295 °C. All the other experimental values were interpolated to 0 °K as explained in the text.

[a]See references [182], [171], and [183].

take about 20 Cray90 cpu hours (see figure 1-1). On the other hand, a single–point calculation of the tetragonal phase takes about 40 minutes and has 3 relaxation parameters. The cubic phase has just one relaxation parameter and takes about 15 minutes.

Ten special Chadi–Cohen $\vec{k}$ points were chosen for the cubic phase and an equivalent set for the tetragonal phase (12 $\vec{k}$ points). The energy cutoff was 700 eV. The two structures were fully relaxed.

The results are presented in table 4.3. The tetragonal phase is predicted to have a lower energy than the cubic one, as one would expect from the experimental information. The difference in energy between these two phases agrees well with the estimated enthalpy of the transition measured at 2377 °C in reference [182]. The cell parameters for the cubic and tetragonal phases also agree well with experiment. The reported experimental values for the tetragonal a and c, and the cubic a parameter are linear extrapolations to 0 °K using the data from reference [171] (since the two phases are very similar we assumed the same temperature dependence in both cases).

In figure 4-9, we show the charge density along the (110) plane of cubic zirconia. Contrary to the CaO–MgO case, it is not clear from the *total* valence density if the orbitals $4d$ and $5s$ are fully ionized. Consequently, we also plot in the figure, the contributions coming from these orbitals. They show a significant presence of charge in them. The value of the integrated electronic charge density within a sphere of

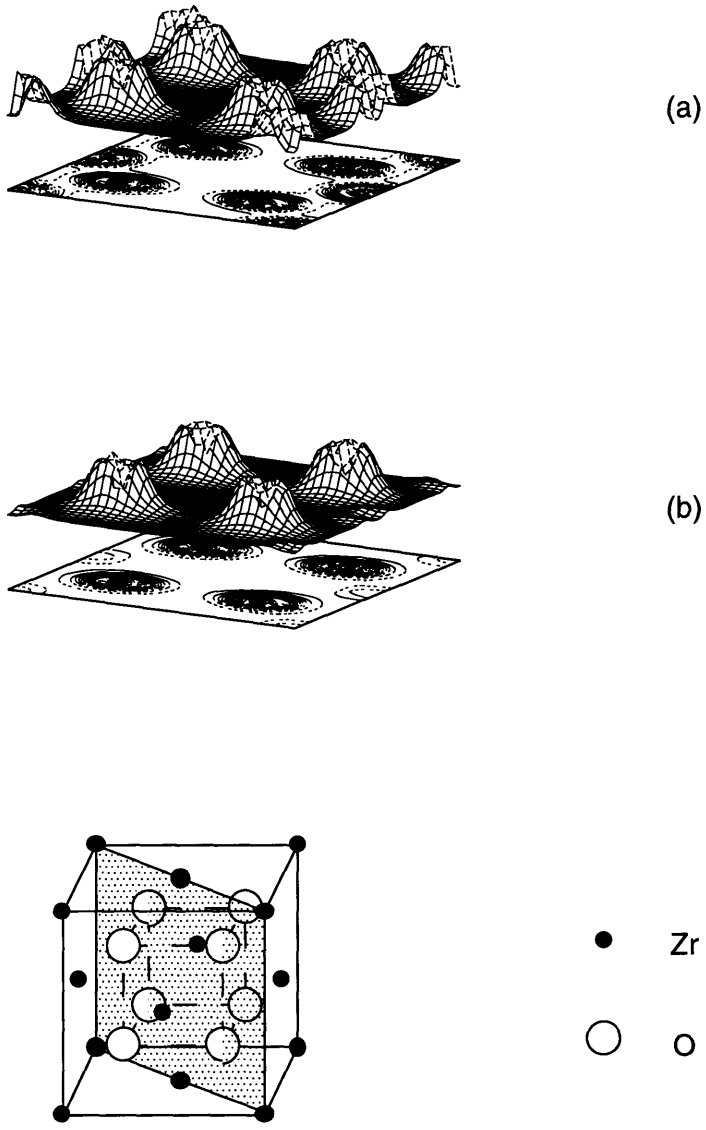

Figure 4-9: Valence electronic density and its contour plot for the (110) plane of cubic zirconia (shaded plane in the figure). (a) Full valence density. (b) Contribution from the $4d$ and $5s$ bands. (The density coming from the oxygen orbitals is also shown as a reference.)

radius[19] 1.1 Å centered at the zirconium ion is ~8 electrons[20] (i.e., 4 electrons were removed from the valence). When the contribution from the bands with $4s$ and $4p$ character is left out of the integration, the number of electrons in the sphere was reduced to ~1.5. This indicates that part of the 4 electrons that are being transferred to the oxygen ions come from the $4s$– and $4p$–type bands.[21]

Results for CaO–ZrO_2

The ordering of oxygen vacancies and the cations in CaO–ZrO_2 produce very complex structures. Except for the high–temperature phases of pure zirconia, the *ab initio* treatment of these compounds requires computer runs beyond any reasonable time. The computation of the phase diagram is out of the question. Using a simpler approach, such as the tight–binding technique presented in this thesis, is the only feasible alternative for studying phase stability in this system from first principles.

However, fitting and testing the tight–binding Hamiltonian will require more information about the observed compounds than what is available experimentally. Consequently, we generated new compounds, simpler than the experimentally observed ones, by replacing some zirconium atoms in the fluorite structure by calcium atoms and adding the right number of vacancies to preserve charge balance.[22] In figure 4-10, we show the five structures (S1 to S5) with the smallest unit cells that were generated using this procedure.

The pseudopotential formation energies and lattice parameters of these structures are shown in table 4.4. For simplicity, only volume relaxations were allowed. The energy cutoff was 700 eV. We used a uniform mesh in the Brillouin zone for the $\vec{k}$–space integrations. Only the symmetry independent $\vec{k}$ points were kept. A 4x4x4 and a 3x3x3 mesh were used for structures S1 to S3 and S4 to S5 respectively. With these parameters, the formation energies were converged within a few meV/atom.

In figure 4-11, we show the valence electron density corresponding to the S2 structure. As in CaO–MgO, the Ca atoms are fully ionized. We found the same situation in all the five structures.

The charge of an ion is not a well–defined quantity. However, we have seen that classical models make an extensive use of this concept. One of the approximations of these formulations is that the charge is fixed (i.e., independent of the particular arrangements of the ions in the lattice). To test these assumptions, we integrated the charge density within spheres centered at the ions of structures S1 to S5. The *same* radius was taken for all the ions of the *same* species. The results detected differences

[19]The nearest neighbor distance between zirconium and oxygen is 2.18 Å. The 1.1 Å value corresponds to the minimum of the spherically–averaged density along the axis that joins a zirconium and an oxygen ion.

[20]Recall that the we took $4s^2 4p^6 4d^2 5s^2$ as the valence of zirconium.

[21]If we had taken the $4s$ and $4p$ orbitals as part of the pseudopotential core, this effect would have not been properly accounted for. The large overlap between these and the $4d$ orbitals is a clear indication that the semicore states had to be included in the valence.

[22]For this, we assumed the ions to have the integral formal charges. (i.e., +4, +2, and -2 for Zr, Ca, and O respectively.)

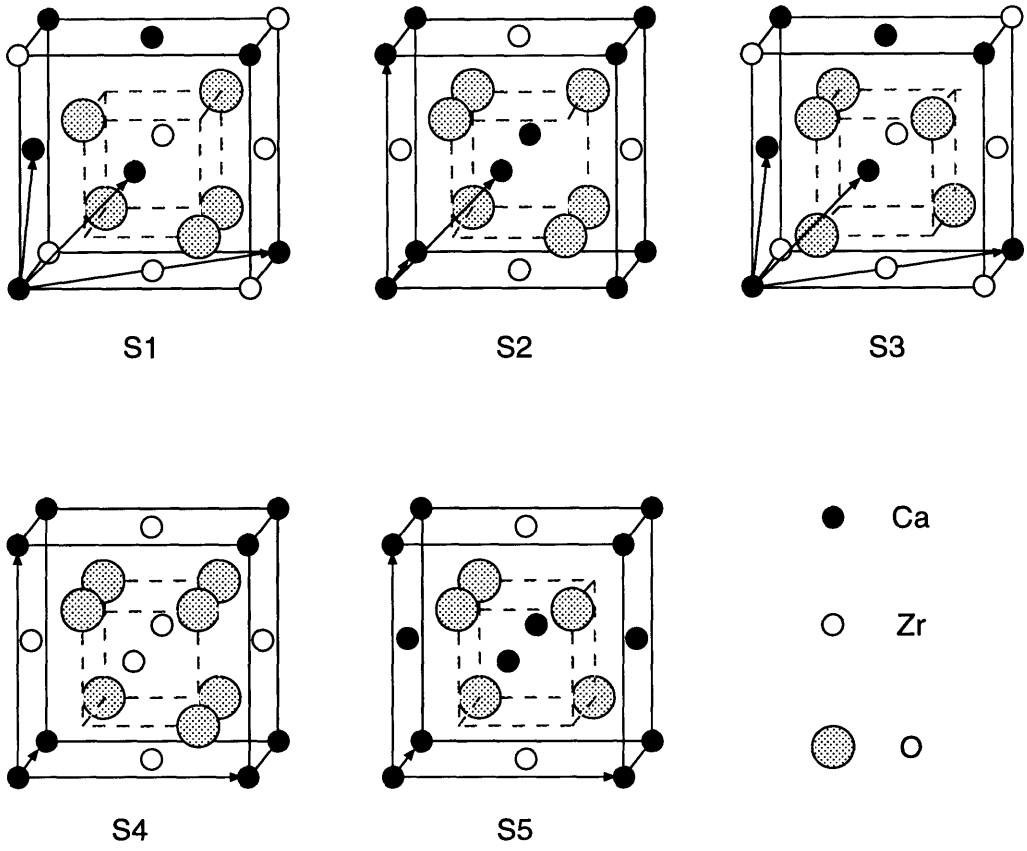

Figure 4-10: Smallest volume Zr–Ca–O structures in the fluorite lattice that preserve charge neutrality. The arrows indicate one possible set of primitive basis vectors.

Structure	Composition	Cell Parameter (Å)	ΔE (meV/atom)
S1	$ZrCaO_3$	a=5.13	380
S2	$ZrCaO_3$	a=5.13	626
S3	$ZrCaO_3$	a=5.136	884
S4	Zr_3CaO_7	a=5.08	367
S5	$ZrCa_3O_5$	a=5.22	860

Table 4.4: Formation energies and cell parameters of different ordered structures in the CaO–ZrO_2 system obtained by using the plane–wave pseudopotential method. Only cubic volume relaxations were allowed. The structures are described in figure 4-10.

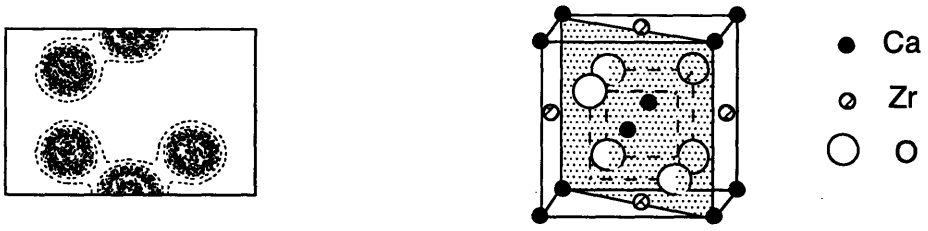

Figure 4-11: Valence electron density for the S2 structure. Note that Ca atoms are fully ionized.

as large as 0.3 electrons between Zr (or O) spheres. This is an *indication* that the charge associated with the ions of the same species may change considerably within and along the 5 structures.[23]

Discussion

The computed structural energy difference between the cubic and the tetragonal phases, 45 meV/ZrO_2, is in very good agreement with the estimated enthalpy of the transition measured at 2377 °C (58meV/ZrO_2).

As in the CaO–MgO case, the comparison between the pseudopotential and the experimental cell parameters is excellent. The calculated lattice constants of the cubic and tetragonal phases and the experimentally measured values extrapolated to 0 °K agree within less than 1%.

The charge–density plots consistently show that zirconium is not fully ionized. Not all the 4d and 5s electrons are transferred to the oxygen atoms. A small amount of charge lies in between the ions indicating some degree of covalency.

Although the charge of the ions is not a well–defined physical quantity, our results indicate that there seems to be an important dependence of its value on the atomic environment. This dependence can introduce large errors when computing formation energies with potential models. The situation will be further analyzed in chapter 8.

[23]Note that other effects, such as ionic breathing, may be responsible for this variation in the integrated electron densities. We regard these results as an *indication*, and we will come back to this point later, in chapter 8, where the uniquely defined tight–binding charges will be used to study these claims.

4.3 Conclusions

In this chapter, we showed that in spite of its approximations, the pseudopotential method can be used to compute useful materials properties. Many technologically relevant questions can be answered faster and at a smaller cost by performing computational rather than real experiments.

However, only simple systems can be studied with accurate first–principles approaches. Calcium stabilized zirconias, more complex arrangements of the Li and metal ions in the batteries, or even the phase diagram of one of the simplest oxide systems (CaO–MgO) can not be analyzed by using the pseudopotential approach. It is clear that a faster method is necessary if we want to study more complex systems.

Faster methods make use of many simplifying assumptions at a risk of reducing accuracy. Thus, it is essential to analyze the effect of the approximations employed to speed up the calculations. In the next chapter, the pseudopotential results will be used to assess the accuracy of these simpler methods. At the same time, we will be able to determine the relevant physical effects that should be accounted for in any total–energy calculation for oxides.

Chapter 5

The effect of approximations in total–energy methods: relevant terms in the Hamiltonian

With the currently available total–energy methods, the study of even relatively simple oxides is beyond the computational capability of today's fastest computers. When studying other materials, many approximations are introduced to obtain the desired speeds. Unfortunately, these same approximations produce large errors in oxides.

In the following sections, we will study the effects on oxides of the approximations introduced in chapter 3. The goal is to analyze their performance and determine the causes of their failure to predict accurate formation energies. There is a widespread belief that *only* the state–of–the–art methods should be able to accurately[1] compute those values. Here, we will follow a different path. By studying the effects of the different approximations, we will identify the relevant terms in the Hamiltonian needed to compute formation energies. This information will then be used in chapter 6 to build a tight–binding Hamiltonian that will allow us to compute energy differences fast and accurately.

Our plan consists of two stages. In the first one, we showed that pseudopotentials, within the LDA, produce reliable results in a wide variety of oxides. Now, in the second stage, we will use these calculations as a benchmark to test other methods, and at the same time, identify the important contributions to the Hamiltonian. In figure 5-1, we summarize both the main approximations used by the different total–energy methods and the systems where their effects will be tested. The techniques chosen represent the most popular methods currently used in oxides. On the other hand, the oxides were selected for their dissimilar characteristics. As previously explained, CaO–MgO is the prototype system for an ionic material with highly symmetric structures and completely ionized cations. These aspects make it an ideal candidate for shape and non–self–consistent approximations. Pure and doped zirconias have low–symmetry

[1]Recall that the accuracy of a calculation depends on the sensitivity to changes in the total–energy value of the physical property we want to compute. Since we look at energies of the order of thermal effects, the energy differences have to be computed within a few meV/atom.

	LDA	Frozen core	Spherical symmetry	Non self-consistency	Semiempirical $E=E(R_1,.....,R_N)$
FLAPW	●				
PP	●	●			
SSCAD	●		●		
Pair Potentials		●	●	●	●

Compatible with:

● Applies

◎ Approximately applies

High Symmetry	Fixed Charge	
●	●	CaO-MgO
	◎	ZrO_2
		$CaO\text{-}ZrO_2$

Figure 5-1: Total–energy methods and their most commonly used approximations. Also shown are the oxide systems where the effect of these approximations on the formation energies will be tested.

	Ca_3MgO_4	$CaMg_3O_4$	CaO	MgO
PP Formation energy	0.092	0.131	–	–
FLAPW Formation energy	0.101[a]	0.137[a]	–	–
PP Lattice constant	4.698	4.423	4.8	4.21
FLAPW Lattice constant	4.620[b]	4.350[b]	4.714[c]	4.167[c]

Table 5.1: Formation energies and cell parameters for the $L1_2$ structure in the CaO–MgO system computed with the pseudopotential (PP) and the full–potential linearized augmented–plane–wave (FLAPW) methods. The ions in the CaO–MgO system are arranged on two interpenetrating fcc lattices. The $L1_2$ nomenclature identifies the distribution of the Ca and Mg ions on the fcc cation sublattice (that corresponds to the minority species at the corners of the conventional fcc cell) while the oxygen fcc sublattice remains fully occupied. Energy values are expressed in eV/ion and the cell parameters are in Å. The values correspond to fully relaxed structures.

[a]From reference [84].
[b]From reference [184].
[c]From reference [120].

phases and a combination of a covalent– and an ionic–type of bonding. Consequently, they represent a major challenge for *approximate* total–energy methods.

We will start by studying the effects of the frozen–core approximation by comparing plane–wave pseudopotential calculations with all–electron FLAPW results (section 5.1). Although the frozen–core approximation is used in many other methods, this will be a last test of the results we intend to use as a benchmark. We will then proceed to *relax* the accuracy of the calculations by allowing shape approximations to the potential (section 5.2) and non–self–consistency including a classical[2] representation of the dependency of the total energy on the ionic coordinates (section 5.3). Finally, we will analyze which contributions should be included in the Hamiltonian to accurately compute formation energies in oxides (section 5.4).[3]

5.1 Effect of the frozen–core approximation

We analyze the effect of the frozen–core approximation by comparing the pseudopotential and the all–electron FLAPW results. The differences between them are very small in the CaO–MgO system, as shown in table 5.1. The formation energies agree well within the convergence errors of the calculation. These errors were 2 meV/atom

[2]Recall that we use the word "classical" to denote those techniques that do not explicitly solve the Schrödinger equation to find the dependence of the total energy on the coordinates of the ions.

[3]In this chapter, we will not test the accuracy of the local–density approximation. The only proof of the accuracy of the LDA is the excellent agreement with experiments of the FLAPW and pseudopotential results shown in chapter 4.

and 5meV/atom in our calculations and in reference [184] respectively. The lattice constants are slightly different. Part of this difference can be attributed to the use of a different exchange and correlation potential (Hedin–Lundqvist [100] in reference [120] and Perdew–Zunger [99] in our case). Other possible source of error is the overlap of the valence orbitals with the core. However, the predicted MgO lattice constant in reference [160] coincides within less than 0.2% with our values although they included core corrections. This seems to indicate that the disagreement is due to different LDA formulations and different convergence criteria rather than the frozen–core approximation.

On the other hand, for the predictions of the energy differences between the tetragonal and cubic phases of zirconia, the agreement is not good (see table 5.2). However, we do not think this difference comes from the pseudopotential approximations. The pseudopotential predictions are not only much closer to the experimental values but also the FLAPW calculations [178] were not fully converged. In reference [178], a limited number of basis functions was used, which introduced relative errors of the order of 15meV/cell, compared to 2meV/cell in our case, and the relaxation of the tetragonal phase was not thoroughly performed.

When there is an appreciable overlap between the valence and core orbitals the frozen–core approximation can become an important source for error.[4] When this is the case, some of the core orbitals should be taken as valence orbitals reducing the size of the core or a correction term should be introduced. If a pseudopotential is being used, a smaller core results in a deeper potential, considerably increasing the number of plane waves and the computational demands of the method. Consequently, core corrections are usually implemented.

5.2 Effect of the spherical–symmetry approximation for crystal potentials: the SSCAD case

The SSCAD method was specially designed for systems with interacting closed–shell ions and highly–symmetric structures. A highly–ionic system, such as CaO–MgO, meets all these requirements and should be an ideal case for the method to work well. The major approximation of the SSCAD is the spherical symmetrization of the ionic potentials.

We will extensively study the CaO–MgO system, in particular its phase diagram. Computed phase diagrams are very sensitive to small changes in the formation energies. Consequently, a comparison between the measured and the predicted phase boundaries is an excellent test of the accuracy of the SSCAD. We will also directly compare the SSCAD and the pseudopotential formation energies.

On the other hand, more open structures can present an important challenge

[4]For example, in reference [185], the lattice constant of bcc lithium is computed with and without core corrections using the pseudopotential method. The reported values were 3.534 Å and 3.269 Å respectively. Note that there is more than a 7% difference between them. Furthermore, the experimental result (3.491 Å) is closer to the former values.

	Expt.[a]	Pot.[b]	PIB[c]	PP	FLAPW[d]
Cell Parameter					
Cubic ZrO_2					
a=b=c	5.092	5.075	5.10	5.050	5.050
Tetragonal ZrO_2					
a=b	3.571	3.588		3.575	3.568
c	5.20	5.216	Not	5.153	5.084
z(O)	0.303	0.31	stable	0.295	0.279
Monoclinic ZrO_2					
a	5.1505	5.241			
b	5.2116	4.898			
c	5.3173	5.578			
β	99.230	90.0			
x_1(Zr)	0.2754	0.25			
y_1(Zr)	0.0395	0.0	Not		
z_1(Zr)	0.2083	0.1899	stable		
x_2(O)	0.0700	0.0753			
y_2(O)	0.3317	0.2818			
z_2(O)	0.3447	0.3958			
x_3(O)	0.4496	0.4247			
y_3(O)	0.7569	0.7182			
z_3(O)	0.4792	0.3958			
Energy differences:					
E_{cubic}-$E_{tetragonal}$	0.058	0.019		0.045	0.009
$E_{tetragonal}$-$E_{monoclinic}$	0.061	0.166			

Table 5.2: Cell parameters and structural energy differences for the experimentally observed phases in zirconia at zero pressure. The energies are in eV per ZrO_2 formula unit and the lattice constants are in Å. All cell parameters were fully relaxed, including the internal positions, x_i, y_i, and z_i, that are shown here according to the Wyckoff notation in reference [168]. The experimental z value for the tetragonal structure was measured at 1295 °C and the cell parameters are extrapolations to 0 °K (see chapter 4). PIB calculations for the tetragonal and monoclinic phases of zirconia are not reported in the table since these structures are not predicted to be stable by this method.

[a] See references [171, 182, 183].
[b] See references [141, 175].
[c] See reference [181].
[d] See reference [178].

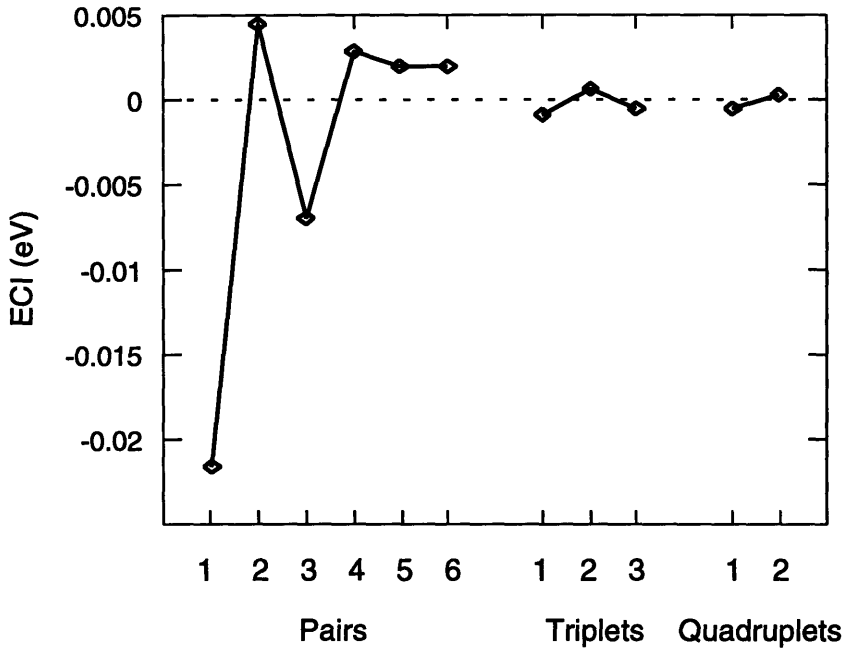

Figure 5-2: Effective cluster interactions for the CaO–MgO system computed with the SSCAD. The pairs are identified according to their length and the triplets and quadruplets according to their longest side, the other sides being nearest neighbors.

to the spherical–symmetry approximation. We will analyze its effects on the total energy by studying the polymorphic transformations of zirconia. Specifically, we will test if the SSCAD predicts the correct energy differences between the different ZrO_2 structures.

5.2.1 The SSCAD CaO–MgO phase diagram

The formation energy of 21 compounds was computed to determine the effective cluster interactions of the system. Their values can be found in appendix A. The ECI's are shown in figure 5-2. Convergence of the cluster expansion was verified by eliminating the six structures with the largest unit cells from the fit. The ECI's were fit again and were used to predict the energy of these six structures. The RMS difference between the *direct* and the *predicted* values was only 1 meV/atom. These results clearly show the predictive power of the expansion.

A further test involved predicting the defect energies of inserting a molecule of CaO (MgO) in an otherwise pure host material. As explained in section 2.3.1, these energies correspond to the single atom spin flip and are directly related to the solubility limits in the end–member phases. In table 5.3, we show the defect energies predicted by the cluster expansion and by the SSCAD. The agreement is excellent, indicating a well converged cluster expansion.

For the CaO–MgO system, we also took into account the effect of atomic vibra-

	Cluster expansion	SCPIB
MgO *rich*	0.720	0.704
CaO *rich*	0.560	0.544
Difference:		
MgO *rich* - CaO *rich*	0.160	0.160

Table 5.3: Defect formation energies, in eV, of a single MgO (CaO) in an otherwise pure CaO (MgO) lattice. The SSCAD values were computed using a 3x3x3 fcc supercell. The term "rich" denotes the host lattice.

	Nearest neighbor pair	Nearest neighbor triplet
V_α^{vibr}	0.006327	0.005073

Table 5.4: Vibrational ECI's for the CaO–MgO system (dimensionless).

tions by using two vibrational ECI's (V_α^{vibr} in equation 2.15). They were fit to the vibrational free energies of CaO, MgO, and the two $L1_2$ structures. The vibrational free energies were computed within the harmonic approximation [84]. The vibrational ECI's are shown in table 5.4.

The phase diagram was computed using a combination of Monte Carlo simulations and the CVM. The CVM entropy expression was used in the 13– and 14–point maximal–cluster approximation (see figure 2-11). The probabilities of the different arrangements in that cluster, the energy, and the composition were obtained from a grand canonical Monte Carlo simulation in a 12x12x12 fcc supercell. These values were averaged for 5000 steps, after another 5000 equilibration passes. The solubility limits can then be found by looking at the intersections of the grand canonical free energy. More details of this hybrid technique can be found in reference [46].

The computed phase diagram is shown in figure 5-3. Note that no experimental input has been used except for the atomic numbers and the lattice.

Discussion

The agreement between the experimental and predicted solubility limits in figure 5-3 is very good. Errors of more than 100% in transition temperatures are not uncommon for first–principles techniques. This is an indication of the good performance of the SSCAD to compute formation energies.

However, since we are including all the relevant contributions to the free energy, the differences between the predicted and experimental solubility limits are likely to come from errors in the SSCAD formation energies. In figure 5-4, we compare the pseudopotential formation energies of the 10 compounds in table 4.2 against the SSCAD predictions. The latter are systematically lower than the pseudopotential

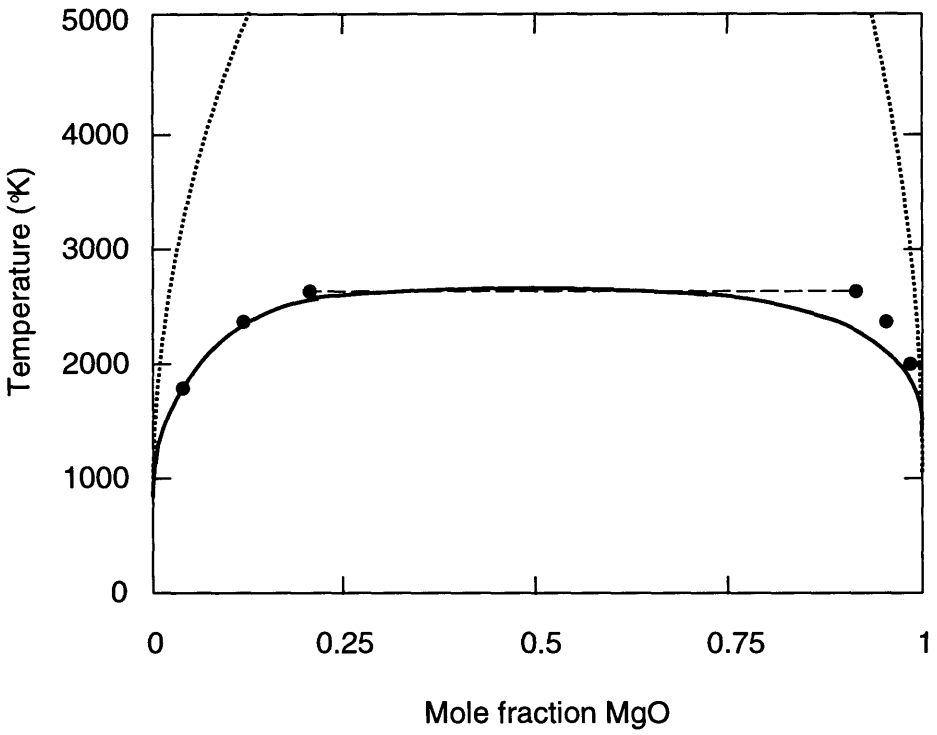

Figure 5-3: CaO–MgO phase diagram. Only the solid solubility limits, computed by a combination of Monte Carlo simulations and the CVM, are shown. The solid and dotted lines were determined with the ECI's derived from SSCAD and from empirical potential models respectively. The circles represent experimental values [30] and the dashed line indicates the experimental eutectic temperature.

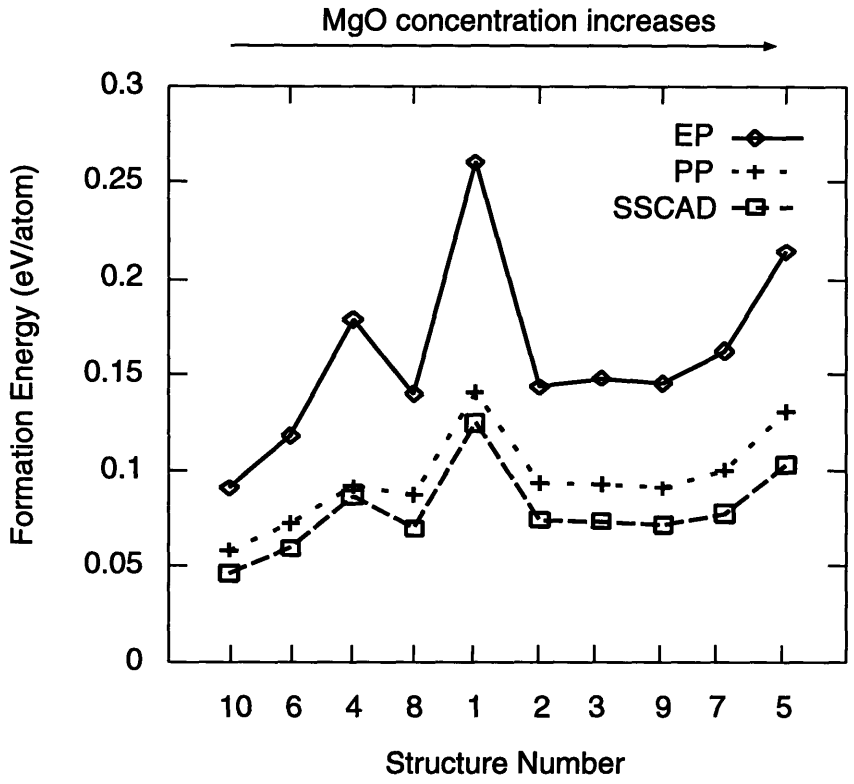

Figure 5-4: Formation energies for different ordered structures in the CaO–MgO system obtained with pseudopotentials (PP), the SSCAD, and empirical potentials (EP). The number that identifies each structure corresponds to the one used in table 4.2.

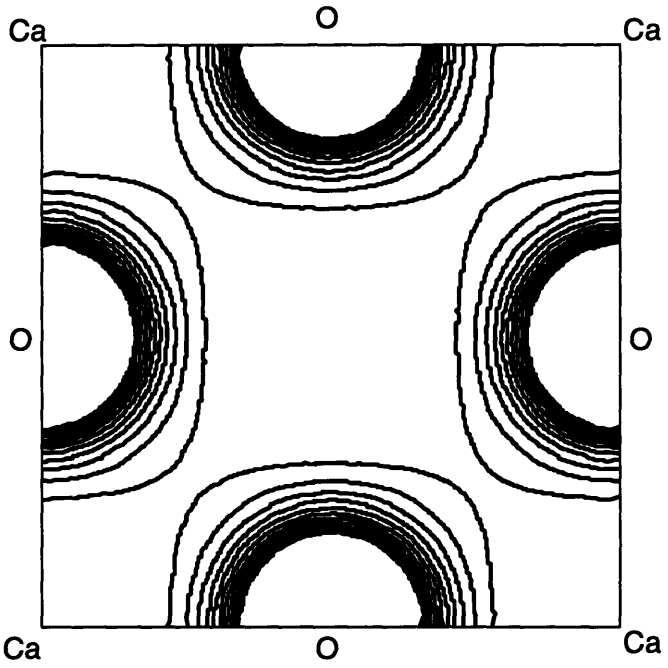

Figure 5-5: Valence electron density for the (001) plane of CaO as computed with the pseudopotential method. Note that the oxygen ions are not perfectly spherical.

results. The average error is of the order of 17%.

Note that the differences between the methods are larger in the MgO–rich than in the CaO–rich side of figure 5-4. This indicates that the SSCAD will underpredict, in particular, the defect energy of introducing a CaO in an otherwise pure MgO host. As we previously explained this will result in an excessively large solubility limit in the MgO–rich side of the phase diagram.

Figure 5-3 clearly shows this behavior, with a much larger overprediction of the solubility limits in the MgO–rich than in the CaO–rich side. Furthermore, if the SSCAD formation energies were to be rescaled to be close to the pseudopotential predictions, the resulting *ab initio* phase diagram will lie on top of the experimental points. Unfortunately, computing the pseudopotential phase diagram is beyond the current computer power.

The main source of errors in the SSCAD is the spherical symmetry imposed on the density. Even for these highly ionic oxides the assumption is not correct. In figure 5-5, we show the contour plot of the valence electron density for the (001) plane of CaO. The oxygen atoms are clearly not spherical. The SSCAD will fail to reproduce these nonspherical relaxations of the valence charge, introducing an error in the energy.

In order to assess the accuracy of the SSCAD in oxides, systems in which nonspherical relaxations are important should be tested. This is the objective of the next section.

5.2.2 Polymorphic transformations in pure zirconia

At low temperature, the stable zirconia structure is monoclinic, which has a low symmetry. The structural transitions in the system were studied by Cohen, Mehl, and Boyer [181] using a non–self–consistent version of the SSCAD (called the potential–induced breathing (PIB) method [107]). Their results are reproduced in table 5.2. The tetragonal and monoclinic phases were found to be unstable at zero pressure. Cubic zirconia was predicted to have the lowest energy when compared to the rutile, the orthorhombic, and the cotunnite structures.[5]

The approximations introduced in the method clearly break down for the zirconia system. The non–self–consistent SSCAD predicts the cubic structure to be the stable phase in contradiction with the experimental findings. Furthermore, the method fails to reproduce the stable low–symmetry phases. Cohen *et al.* [181] suggested that these discrepancies were related to nonspherical charge relaxations not included in the model.

Since many oxides have covalent bonding, significant errors can be expected due to this approximation. It is possible to avoid the spherical approximation in the SSCAD but at the expense of an increase in the computational burden. Consequently, the SSCAD can only be used to compute formation energies in systems with high symmetry. But even in this case, some error should be expected as shown in the CaO–MgO system.

5.3 Effect of the pair–potential approximations

In this section, we will analyze the two remaining approximations in figure 5-1: the use of non–self–consistent formulations and the use of semiempirical functions to model the dependence of the energy on the ionic coordinates. To perform these tasks, we will use a simple pair–potential formulation. Actually, this model also assumes spherical symmetry for the crystal potential and the frozen–core approximation.[6] However, in the previous sections, we showed that although the last two approximations can introduce significant errors, they are very small in CaO–MgO. Thus, we will start investigating the phase diagram of this system and analyzing any additional errors that non–self–consistency and the use of semiempirical functions introduce.

We will complete the analysis by performing calculations in pure and calcia–doped zirconias.

5.3.1 The pair–potential CaO–MgO phase diagram

We computed the CaO–MgO phase diagram using an empirical pair–potential model. It consisted of a Buckingham potential (see equation 3.5) combined with a shell

[5] It is unlikely that a self–consistent treatment will change the results *qualitatively.*

[6] Actually, no explicit mention to the electrons is made within a pair–potential model. We can assume that the core electrons are frozen and that the valence ones are only allowed to deform within the polarization model described in section 3.2.2.

	O^{-2}–O^{-2}	Ca^{+2}–O^{-2}	Mg^{+2}–O^{-2}
A_{ij} (eV)	22764	1090.4	1428.5
ρ_{ij} (Å)	0.149	0.3437	0.2945
C_{ij} (eVÅ^6)	27.88	0.0	0.0
	O	Ca	Mg
Y_i (e)	-3.0	3.135	1.585
X_i (e)	1.00	-1.135	0.415
k_i ($\frac{\text{eV}}{\text{Å}^2}$)	51.4	110.2	361.6

Table 5.5: Potential parameters derived in reference [79]. The parameters are named following the same convention as in section 3.2.2.

model (see section 3.2.2). The parameters were obtained from reference [79] and are reproduced in table 5.5. They were fit to experimental structural information (cell parameters), elastic and dielectric constants, and cohesive energies.

The same cluster as in section 5.2.1 were used here for the cluster expansion. Their coefficients were fit to formation energies of the potential model. The predicted solubility limits are shown in figure 5-3. There is a clear underestimation of their values.

In figure 5-4, we show the formation energies for some compounds in the CaO–MgO system. The potential model predicts almost twice as large formation energies than the pseudopotential method. Consequently, the effect on the phase diagram will be to raise the transition temperature, in agreement with figure 5-3.

5.3.2 Pair–potential predictions for pure and doped zirconias

Here, we will also use a Buckingham potential combined with a shell model. Its parameters were fit to reproduce structural and dielectric constants of the tetragonal zirconia phase [175] (the O–O and Ca–O parameters were taken from reference [79]) and are reproduced in table 5.6.

The potential model incorrectly predicts the energy differences for the polymorphic transformations in zirconia (see table 5.2). The monoclinic phase is stable when compared to the tetragonal and cubic phases.

Problems are also present in calcia–doped zirconias. In figure 5-6, we compare the pseudopotential and the empirical potential predictions for the formation energies of the structures S1 to S5 of section 4.2.2. Again, the latter model overestimates the formation energies.

	O^{-2}–O^{-2}	Ca^{+2}–O^{-2}	Zr^{+2}–O^{-2}
A_{ij} (eV)	22764	1090.4	985.869
ρ_{ij} (Å)	0.149	0.3437	0.376
C_{ij} (eVÅ^6)	27.88	0.0	0.0
	O	Ca	Zr
Y_i (e)	-2.077	0.0	1.35
X_i (e)	0.077	2.0	0.65
k_i ($\frac{\text{eV}}{\text{Å}^2}$)	27.29	∞	169.617

Table 5.6: Potential parameters derived in references [79, 175]. The parameters are named as in section 3.2.2. The "∞" corresponds to the rigid–ion approximation.

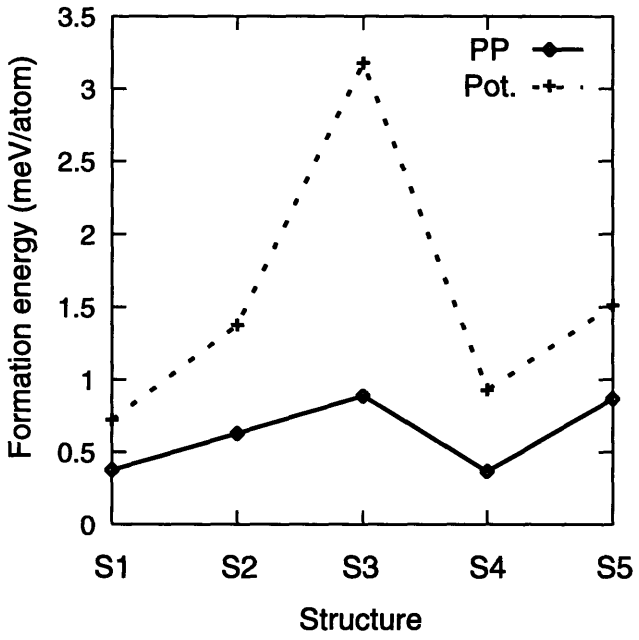

Figure 5-6: Formation energies in the CaO–ZrO_2 system predicted by pseudopotentials (PP) and empirical potentials (Pot.). The structures are identified following the convention in figure 4-10.

	O^{-2}–O^{-2}	Ca^{+2}–O^{-2}	Mg^{+2}–O^{-2}
A_{ij} (eVÅ^5)	0.5054	109.123	68.71
	O	Ca	Mg
Y_i (e)	0.0	0.0	0.0
X_i (e)	-2.00	2.0	2.0
k_i ($\frac{\text{eV}}{\text{Å}^2}$)	∞	∞	∞

Table 5.7: Potential parameters fit to the pseudopotential formation energy of the $L1_0$ structure, its cell parameters, and the CaO and MgO cell parameters. The "∞" corresponds to the rigid–ion approximation.

5.3.3 Discussion

The use of potential models is widespread since they combine simplicity with computational speed. Although they have been successfully used to study many oxide properties [82, 83], they only render *qualitative* agreement for phase diagrams. In the CaO–MgO system, the pair–potential model predicts a miscibility gap with the right asymmetry. Also the correct energy ordering of the zirconia polymorphs is reproduced. However, their *quantitative* predictions can be off by more than 100%.

Most published potentials have been fit to energies on the scale of eV, while temperature effects are determined in the scale of several meV. This can be improved by actually fitting to formation energies and lattice parameters of different structures in the system. For example, we studied the CaO–MgO system using a potential with a simple repulsive term of the form:[7]

$$V(r_{ij}) = \frac{A_{ij}}{r_{ij}^5}, \tag{5.1}$$

fit to the pseudopotential formation energy of the $L1_0$ structure and the lattice parameters of the rocksalt MgO and CaO, and the $L1_0$ structure.[8] No polarization terms were included. The parameters used are shown in table 5.7. The resulting formation energies are compared to pseudopotential and SSCAD predictions in figure 5-7. A complete list of formation energy values can be found in appendix A. It is clear from the results that the agreement has improved, and the potential formation energies are closer to the SSCAD predictions. However, other properties such as the elastic and dielectric constants, or the vibrational properties are much more poorly reproduced

[7]The distance dependence is derived from a very popular formulation of the semiempirical tight–binding Hamiltonian. Its value is different from zero only for the first nearest–neighbor O–Ca and O–Mg interactions, and for the second nearest–neighbor O–O interaction. See appendix A for more details.

[8]Note that since the system presents a miscibility gap, this fit can not be done to *experimental* results. The $L1_0$ structure is not thermodynamically stable. This is an important advantage of fitting potentials to *ab initio* values.

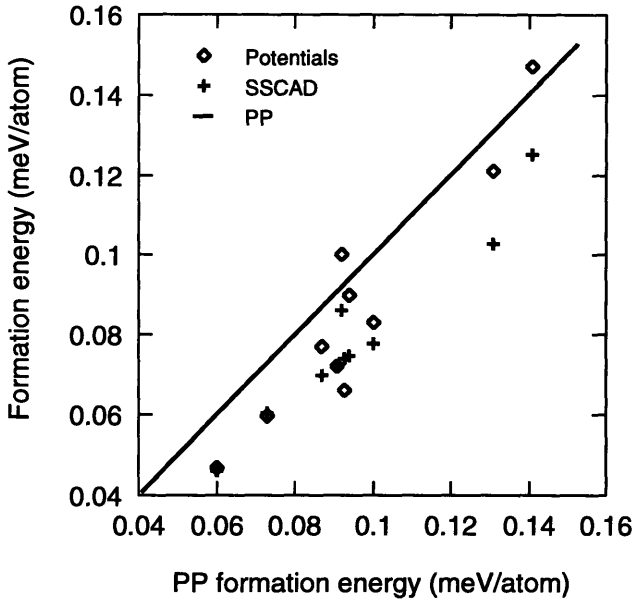

Figure 5-7: SSCAD and pair–potential formation energies for the CaO–MgO system as a function of the pseudopotential predictions. The parameters used in the pair potential are shown in table 5.7. The closer the points to the solid line the better the performance of the potential or the SSCAD method is.

than when using the potentials in reference [79].[9]

A potential model can thus be regarded as an interpolation tool with not much physical content. The mapping of the many physical effects that determine the energy onto a simple pair–potential form is not accurate. This is supported by the fact that when formation energies are well reproduced other properties are worsen. Furthermore, pair–potential values do not agree with the SSCAD or pseudopotential predictions. It seems unlikely that a single set of parameters will be able to reproduce all the properties.

Most of the energy effects that cause problems in pair–potential models have a many–body nature. For example, the size of the oxygen ion is very dependent on the nature of the ionic environment. The free O^{2-} ion is unstable with respect to decomposition to O^{-} (plus one electron). In a crystal, it is only stabilized by the effect of the Madelung field [109]. Consequently, its size and polarizability can change considerably from one structure to the other. As we already explained in section 3.2.2, this effect is known as the breathing of the oxygen ion. In figure 5-8, we show the integrated valence electron charge within an sphere centered around the oxygen ion as a function of the sphere radius and for two different compounds: CaO and MgO. It is clear from the picture that the size of the oxygen atoms is quite different in both cases. The result indicates that the oxygen volume will be variable in different

[9]Even by using a shell model the results do not improve [84].

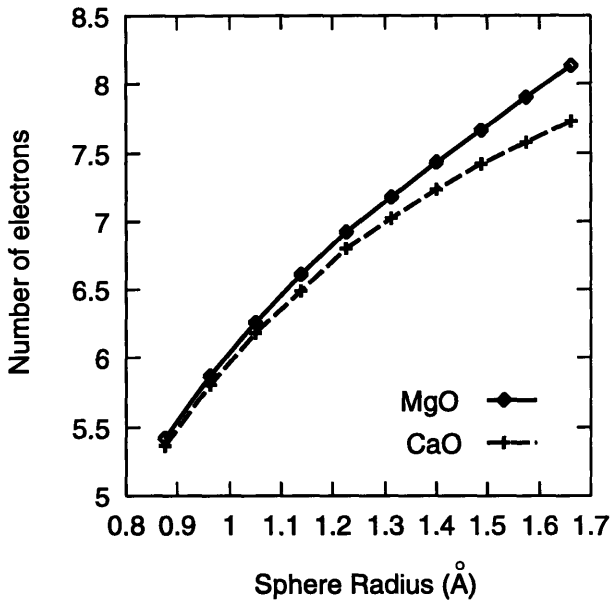

Figure 5-8: Integrated valence charge density within a sphere centered around oxygen, as a function of the sphere radius. The data was computed from pseudopotential calculations.

mixtures of CaO and MgO.

We estimated the effect of the oxygen volume change on the formation energies by freezing the oxygen wave functions to their SSCAD values for CaO and MgO respectively [84]. When the formation energies predicted in the two cases were compared, the use of the different wave functions accounted for changes of the order of 15%.

The nonspherical deformation of the oxygen shape can account for at least another 15% difference in the formation energy values. This can be seen by comparing the pseudopotential and the SSCAD formation values. The major difference between the methods is precisely the nonspherical electronic relaxations.

A potential model that accounts for both the volume change and the polarizability effects introduced by the breathing of the oxygen ion has recently been applied to the energetics of zirconia [89]. However, even when these effects can properly be accounted for (either mapping them into a potential of the form shown in equation 5.1 or by the approach in reference [89]), potentials can not be always used. Charge transfer mechanisms have to be considered.

In the case of the CaO–MgO system, the ionic charge does not change considerably from one structure to the other and a potential could be found that reproduces the formation energies relatively well. However, the same does not apply to calcia–doped zirconias. The charge will change when dopants and vacancies are introduced in the system as shown in section 4.2.2 (see also references [141, 142]). This seriously limits the use of potentials in these materials.

It is clear from figures 5-4 and 5-6 that the potential predictions are worse in

$CaO–ZrO_2$ than in CaO–MgO. Relative errors of more than 250% in the prediction of formation energies are present in the former system. The larger errors correlate well with those structures where the variation of the charge in the Zr and O ions is larger. We will come back to this point later, in chapter 7.

5.4 Relevant contributions to the total energy of oxides

Four mechanisms seem to seriously limit the applicability of the current total–energy methods in oxides: **breathing**, **nonspherical electronic relaxations**, **charge transfer**, and **directional bonding** . For some simple systems, such as CaO–MgO, some of these effects do not play an important role. However, if one wants to accurately describe the energetics of many oxides, a proper treatment of *all* them is desirable.

There are significant computer–time benefits of using simple methods such as potential models. However, it is not straightforward to include all the above effects in their formalism.

Of the four mechanisms, **directional bonding** is probably the simplest to incorporate to a potential model. Although there is always the problem of finding the right functional dependence, many–body potentials have been widely used (see section 3.2.4).

The **breathing** of the ions (specially the oxygen ions) can be approximately accounted for by the compressible–ion model developed by Wilson and collaborators [88]. They represented this many–body effect in a pairwise form. The nearest–neighbor interaction between the ions is considered as the sum of a rearrangement energy (breathing) and an overlap between the ion wave functions (see section 3.2.2 for more details).

Nonspherical electronic relaxations can be incorporated through the shell model explained in section 3.2.2. A quadrupole polarizability of the ions has been recently developed [89].

Still, all potential models assume ionic charges that are *independent* of the environment (either partial– or full–valence charges). There is no systematic way to deal with the **charge transfer** mechanisms. Magri *et al.* and lately Wolverton *et al.* suggested that the charge on a given ion is a linear function of the number of *unlike* close neighbors [186, 187]. This model has proven to be very accurate for metallic alloys. However, its use in highly–ionic materials is questionable since long–range contributions are expected. We will come back to this point later in chapter 8. Another possibility of including charge transfer is the model developed by Streitz and Mintmire [75] (see section 3.2.2).

Up to now, there has not been a simple way of including *all* these four mechanisms in a potential model. Also, note that part of the simplicity of the model is lost, not only because more complex terms need to be included but also because *ab initio* calculations are needed to fit some of the parametrizations. The incorporation of

charge transfer and breathing may also imply performing additional minimizations with respect to the ionic radius or charge.

In chapter 6, we will show that a self–consistent tight–binding formulation can incorporate all these mechanisms in a very accurate and simple way. Furthermore, since it provides a *quantum–mechanical* description of the system, a more realistic representation of bonding in the crystal is obtained. Within this framework, there is no need to *map* physical effects onto simple functional forms. The fact that a tight–binding Hamiltonian can account for all the relevant physical mechanisms provides excellent *transferability* properties.

The fitting of a potential model that incorporates all these mechanisms is becoming as complex and demanding as the determination of the tight–binding parameters. However, potential models are still faster than any semiempirical tight–binding method. Still, the latter is many orders of magnitude faster than any *ab initio* method with comparable accuracy.

5.5 Conclusions

We showed that full–potential quantum–mechanical methods are reliable tools to compute total–energy differences on a scale relevant to the study of phase transitions. When taken to their full capabilities, their predictions compare well with experiments. For example, the agreement between the computed and measured CaO–MgO phase diagrams is excellent. Unfortunately, these techniques are also the most computer–time demanding of all (specially when needed as input to the statistical–mechanical models).

Approximations such as spherical averages of potentials, non–self–consistency, or replacing complex ion-ion interactions by simple pair potentials can dramatically speed up total–energy calculations. However, we showed that, even for the relatively simple CaO–MgO system, most of these approximations break down.

We have identified four mechanisms that are necessary to accurately reproduce formation energies in oxides: charge transfer, nonspherical electronic relaxations, ionic breathing, and directional bonding. These effects should be incorporated into any energy model to capture the relevant physics of the problem. Unfortunately, all the methods that are currently used either do not take into account all these effects or are slow.

In the next chapter, we propose the use of a self–consistent tight–binding model that is capable of capturing the relevant physics of the problem while retaining a low computational cost.

Chapter 6

The tight–binding method

The sophistication of total–energy methods has reached a level in which it is now possible to accurately predict materials properties with no experimental input. In the previous chapters, we showed that the use of density–functional theory in the local–density approximation combined with lattice models is a very powerful tool to design new materials. Unfortunately, the methods are very time demanding and simpler approaches are necessary.

LDA techniques, such as pseudopotentials or FLAPW, do not provide a simple basis to develop an understanding of the relation between *physical intuition*, such as charge, electronegativities, or atomic sizes, and *structural properties*. This intuition is hidden in their complex formulation. However, understanding this relationship is fundamental if we would like to develop simple methods to account for the relevant contributions in the Hamiltonian for oxides. These physical effects were identified in chapter 5. We also illustrated how their incorporation in potential models is far from being trivial. In general, detailed *quantum–mechanical* information is needed to properly deal with them.

In this chapter, we will demonstrate that the semiempirical tight–binding (SETB) method[1] is ideal to incorporate all the relevant physics to compute total energies in oxides. The SETB provides a simplified framework in which a clear identification between physical concepts and the resulting materials behavior can be achieved. This allows all the effects found in chapter 5 to be easily included.

The concept of the tight–binding approach was introduced by Bloch in 1928 [132]. It is based on the use of combinations of atomic orbitals to express the electronic wave functions in a solid. This is appropriate when there is a relatively small overlap between neighboring atoms as in the case of the d–transition metals or the alkali halides. Originally, the tight–binding method was regarded as an *empirical* approach to *qualitatively* interpret the electronic structure of a solid. Later, Slater and Koster proposed to use it as an *interpolation tool* to be combined with other methods such

[1]The use of the *tight–binding* name is sometimes limited *only* to its empirical formulation. The *ab initio* approach is then called *linear combination of atomic orbitals* (LCAO) [130]. In this thesis, we will not make a distinction between the two, and *tight binding* and LCAO will be used interchangeable.

as APW [20]. This was the origin of what we have called the *semiempirical* tight–binding technique, where the various interaction integrals are parametrized according to the results of these other techniques . However, in recent years, there has been a renaissance in the use of the *ab initio* tight–binding method due to the growth in the computing capabilities and the improvement in the numerical techniques.

The use of the SETB approach in oxides requires that one carefully incorporates the important physical effects identified in the previous chapter into the Hamiltonian. The ionic breathing and the charge transfer mechanisms force the introduction of *self–consistency* into the tight–binding framework. Only when all these terms are properly accounted for, will a good description of the energetics be obtained. Furthermore, under these conditions, the parameters of the model will be transferable under changes in the atomic environment.

The transferability of the tight–binding parameters is essential if we want to use the method to calculate formation energies of different compounds. For example, when computing temperature–composition phase diagrams we will fit the SETB parameters to *ab initio* calculations for a few simple ordered structures. From this information the formation energies of many more complex ordered structures will be computed to determine the ECI. Thus, the tight–binding method will replace the time–consuming *ab initio* approaches when dealing with compounds that have large unit cells.

There exists an extensive literature about the tight–binding method. A general review of the different formulations can be found in references [130, 188, 189] and the combination with recursion techniques in references [190, 191]. The semiempirical approach was introduced in great detail in references [20, 22, 131, 192]. Applications in ceramic materials of the first–principles tight–binding technique are described in reference [133] and references therein.

We start in sections 6.1 and 6.2 by briefly describing the first–principles and the semiempirical formulation of the tight–binding approach. Section 6.2.2 is mainly concerned with the self–consistent tight–binding model used in this thesis. In section 6.4, we deal with the computation of the parameters of this method from first–principles calculations. Finally, in section 6.4.2, we discuss the computer implementation of the latter technique.

6.1 Formulation of the method

Solutions of the Kohn–Sham equation 3.12 are sought by expanding the one–electron wave functions, ψ_n, in a basis of atomiclike orbitals, $\phi_{i\alpha}$, centered at site i,

$$\psi_n = \sum_{i,\alpha} c^n_{i\alpha} \phi_{i\alpha}. \tag{6.1}$$

The indices n and α identify the band and the orbital type respectively. Thus, equation 3.12 becomes equivalent to a set of linear equations,[2]

$$\sum_{j,\beta} \left(H_{i\alpha,j\beta} - \varepsilon_n S_{i\alpha,j\beta}\right) c^n_{j\beta} = 0, \tag{6.2}$$

where

$$H_{i\alpha,j\beta} = \int \phi^*_{i\alpha} H \phi_{j\beta} d^3r, \tag{6.3}$$

and

$$S_{i\alpha,j\beta} = \int \phi^*_{i\alpha} \phi_{j\beta} d^3r. \tag{6.4}$$

$H_{i\alpha,j\beta}$ and $S_{i\alpha,j\beta}$ define the elements of the Hamiltonian and overlap matrices respectively (for the atomic basis functions we are using). The integrals are over all space. The quantity $H_{i\alpha,j\beta}$ is sometimes called a *hopping* integral. The eigenvalues ε_n are the solutions of the *secular equation*,[3]

$$\det |\mathbf{H} - \varepsilon \mathbf{S}| = 0. \tag{6.5}$$

The translational symmetry of a crystal can be exploited by using Bloch's theorem (see section 3.3). The basis functions are redefined as a combination of atomic orbitals centered at different sites. The new basis functions, $\chi_{\vec{k},\alpha,\vec{\tau}}$, are:

$$\chi_{\vec{k},\alpha,\vec{\tau}}(\vec{r}) = \frac{1}{\sqrt{N}} \sum_{\vec{R}'} e^{i\vec{k}(\vec{R}'+\vec{\tau})} \phi_\alpha(\vec{r} - \vec{R}' - \vec{\tau}), \tag{6.6}$$

where $\vec{R}'$ denotes the location of the origin of the unit cell and $\vec{\tau}$ is the position of a particular atom within that unit cell.[4] Note that the sum is over atoms on equivalent positions (i.e., same $\vec{\tau}$) on the N different unit cells (i.e., different $\vec{R}'$) and for a given orbital α. If we replace $\phi_{i\alpha}$ in equation 6.4 by $\chi_{\vec{k},\alpha,\vec{\tau}}$,

$$\begin{aligned} S_{\alpha\vec{\tau},\beta\vec{\tau}'}(\vec{k}) &= \int \chi^*_{\vec{k},\alpha,\tau}(\vec{r}) \chi_{\vec{k},\beta,\vec{\tau}'} d^3r \\ &= \frac{1}{N} \sum_{\vec{R}',\vec{R}''} e^{i\vec{k}(\vec{R}''-\vec{R}'-\vec{\tau}+\vec{\tau}')} \int \phi^*_\alpha(\vec{r} - \vec{R}' - \vec{\tau}) \phi_\beta(\vec{r} - \vec{R}'' - \vec{\tau}') d^3r. \end{aligned} \tag{6.7}$$

We can define $\vec{R} = \vec{R}'' - \vec{R}'$ (see figure 6-1) so that equation 6.7 can be written as

$$S_{\alpha\vec{\tau},\beta\vec{\tau}'}(\vec{k}) = \frac{1}{N} \sum_{\vec{R}} e^{i\vec{k}(\vec{R}+\vec{\tau}'-\vec{\tau})} \int \phi^*_\alpha(\vec{r} - \vec{\tau}) \phi_\beta(\vec{r} - \vec{R} - \vec{\tau}') d^3r. \tag{6.8}$$

---

[2]This set of equations is obtained by multiplying each $\phi^*_{i\alpha}$ to the left of $H_{KS}\psi_n$ and integrating over all space. In what follows, H_{KS} will be simply called H.

[3]This equation is the mathematical condition under which equation 6.2 has nontrivial answers.

[4]For clarity, we do not use the i index in ϕ since we are implicitly indicating the location of the basis functions with $\vec{R}'$ and $\vec{\tau}$.

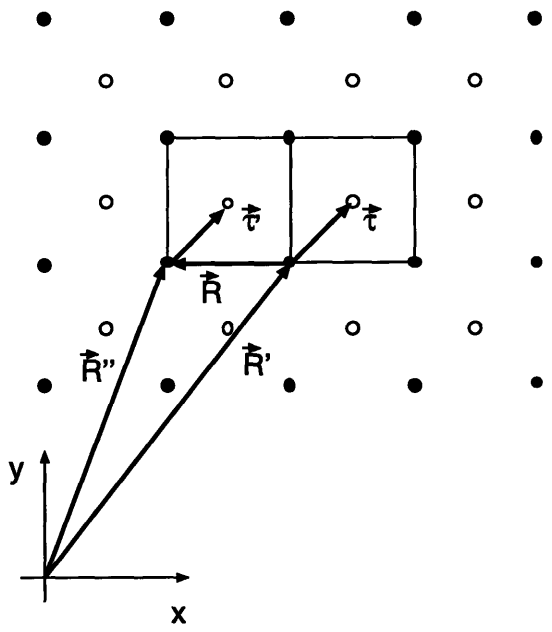

Figure 6-1: Nomenclature used to identify the unit cells and atomic positions. $\vec{R}'$ and $\vec{R}''$ point to the origin of the unit cell (two unit cells are marked in the picture with two squares). $\vec{\tau}$ and $\vec{\tau}''$ indicates the position of the atoms within the unit cell.

Similarly,

$$H_{\alpha\vec{\tau},\beta\vec{\tau}'}(\vec{k}) = \frac{1}{N}\sum_{\vec{R}} e^{i\vec{k}(\vec{R}+\vec{\tau}'-\vec{\tau})} \int \phi^*_\alpha(\vec{r}-\vec{\tau}) H \phi_\beta(\vec{r}-\vec{R}-\vec{\tau}') d^3r. \tag{6.9}$$

Note that the use of Bloch's condition reduced the dimension of the secular equation to the number of basis functions in a single unit cell.[5]

If the atomiclike basis functions ϕ_α are sufficiently localized, the integrals in equations 6.8 and 6.9 are negligible for atoms that are far apart. The sum over the direct lattice vectors $\vec{R}$ is thus limited to those terms that involve atoms that are close neighbors (for a given $\vec{\tau}$ and $\vec{\tau}'$). Consequently, the sum only has a few terms. However, the computation of the overlap and Hamiltonian matrices is very time consuming since these terms involve the calculation of two– and three–center integrals.[6]

Up to now, we have not specified the basis functions ϕ_α. Atomic orbitals were proposed in the original formulation [132]. This basis is *incomplete* unless the continuum of unbound states is included. However, as long as the neighboring potentials do not overlap strongly, the low–valence states form an adequate expansion. (When the potentials overlap significantly, the bound states can be expected to liberate the

[5]However, we will now have an infinite number of secular equations, one for each $\vec{k}$ point.

[6]For example, the integrals can involve the product of an atomic function centered at one atom, another atomic function centered at a second atom, and a potential centered on a third atom.

electrons into free–electron–like states.)

The atomic orbital basis is not orthogonal and problems of *overcompletness* can arise.[7] These problems can make the overlap matrices ill conditioned. They are usually solved by using orthonormalized orbitals.

Modern formulations of the tight–binding method replace the atomic wave functions by Gaussian–type orbitals and spherical harmonics for the radial and angular parts respectively [193]. These orbitals have the advantage that the three–center integrals can be easily computed by the Gaussian transformation technique [194]. On the other hand, the use of several Gaussian–type functions per orbital can make the secular determinant very large. This can be improved by using a *fixed* linear combination of Gaussians, chosen to mimic the orbitals of the free atoms, as basis functions.[8]

It is common practice to use the term *minimal basis* for one in which only the core orbitals[9] and all orbitals in the valence shell are used. Correspondingly, a *full basis* is formed by the minimal basis plus excited orbitals.

The secular equation has to be solved self–consistently since the Kohn–Sham Hamiltonian depends on the electronic density. The computation of multicenter integrals takes a large percentage of the calculation time and only in recent years has the method started to be used from first principles [133]. In the next section, we will describe the semiempirical approach, which replaces these costly calculations by simple parametrizations of the matrix elements.

6.2 The semiempirical tight–binding method

The use of Gaussians as basis functions considerably improves the efficiency of the tight–binding method and the speed of evaluating the various integrals. However, this is achieved at the expense of an increase in computer storage requirements. As systems get larger, more of these terms need to be computed. Consequently, significant time savings can be obtained from evaluating the integrals in equations 6.8 and 6.9 *approximately.*

The computation of these integrals requires the knowledge of both the basis functions and the potential in the Hamiltonian. However, they always appear together in the formalism outlined in section 6.1. The semiempirical tight–binding method takes advantage of this fact by developing parametrizations of the elements of the hopping and overlap matrices without specifying an explicit form for the basis functions or the Hamiltonian potential *separately.* This is the basis of the SETB formulation. It is particularly fast since the time–consuming hopping and overlap integrals are fit to *ab initio* results. In this sense, this method represents a much more sophisticated

[7] As we already mentioned, the atomic orbitals centered at a *single* site are *already* complete when unbounded states are included. Our basis functions are formed from orbitals at *many* sites which causes the overcompletness problem.

[8] In self–consistent calculations, the basis can be *reoptimized* at each step. Also, it is often convenient to eliminate the core states by using the frozen–core approximation, particularly when we are dealing with heavy atoms.

[9] No frozen–core approximation is used.

and accurate interpolation tool than potential models and is still orders of magnitude faster than *ab initio* quantum–mechanical techniques.

Although it has often been used to interpret results from *ab initio* quantum–mechanical calculations, the SETB has also provided semiquantitative answers in studies of structural stability in a wide variety of systems such as *sp*–bonded non-metals [134], semiconductors [195], *pd*–bonded transition metals [196], etc. Recently, a general tight–binding total–energy formalism that accurately reproduces total–energy differences, defect energies, and elastic constants for transition and noble metals has also been introduced [21, 22, 197].

6.2.1 The Slater–Koster formulation

Slater and Koster proposed the use of the tight–binding method as an *interpolation procedure* by treating the various integrals as constants chosen to fit first–principles calculations [20]. Note that the integrals are $\vec{k}$ independent, thus by fitting to *ab initio* results at a few high–symmetry $\vec{k}$ points, they were able to extend their calculations throughout the Brillouin zone. The values of the integrals are not independent but are interrelated by the symmetry of the crystal and the basis orbitals.

In the original formulation, the basis functions were assumed to be orthogonal. In this way, the number of parameters to fit was reduced in half as no overlap integrals need to be determined. However, atomic orbitals centered at different sites are not orthogonal. Lowdin showed that it is always possible to perform an orthogonalization procedure that preserves the original symmetry properties of the atomic orbitals [198]. Slater and Koster assumed that they always worked with this orthogonalized basis. The resulting functions are not necessary localized, producing non–zero hopping integrals between very distant atoms (and thus requiring more parameters). Many authors investigated the construction of *highly localized*, but yet small, basis sets.[10] See references [111, 189].

Another approximation usually made is to neglect the three–center integrals. The potential energy in the Hamiltonian is approximated as the sum of spherical potentials centered at the atomic sites. The only part of the potential energy that is retained is the one coming from the sum of the spherical potentials at the sites of the two atoms where the basis orbitals are located. Thus, the Hamiltonian integrals have the same angular dependence as those in a diatomic molecule. The basis functions can then be expressed as sums of space quantized functions with respect to the axis that join the center of the atoms. For example, a p–type basis orbital is a linear combination of a $p\sigma$ and a $p\pi$ function with respect to that axis.[11]

[10] The idea of these theories is to be able to *exactly* represent the solid single–electron wave function as a combination of localized orbitals that do not need to be recalculated for each system. In this way, they can still provide a simple chemical picture of bonding. The orthogonality constraint is generally removed. However, the overlap matrix does not appear in the formalism at the expense of having a nonhermitian secular matrix.

[11] A $p\sigma$ and a $p\pi$ orbital are oriented along, and perpendicular to, the axis joining the two atoms respectively.

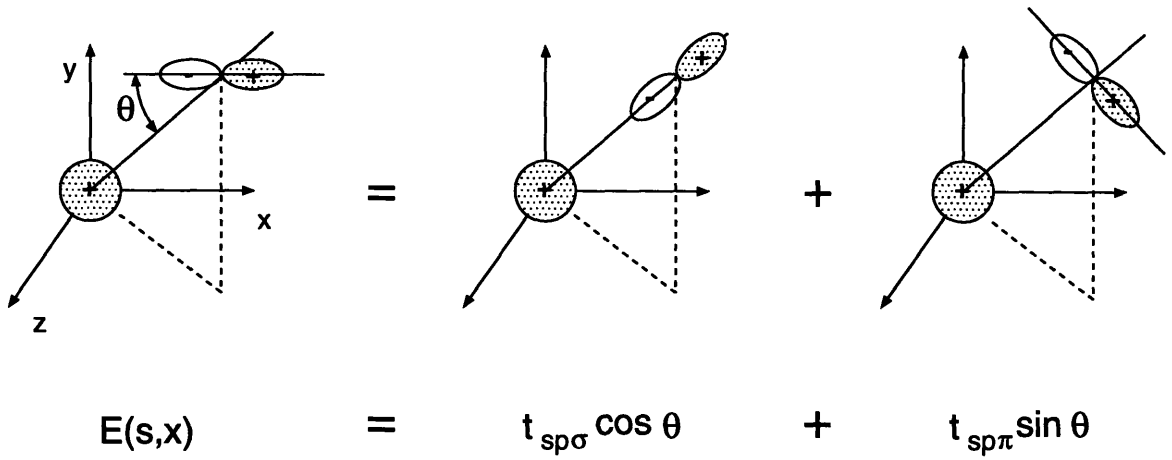

Figure 6-2: Illustration of the representation of the Hamiltonian integral for a s and a p_x orbital ($E_{s,x}$) as a function of two center integrals ($t_{ll'm}$). Note that $t_{sp\pi}$ is zero by symmetry.

The different Hamiltonian integrals can then be expressed in terms of the two–center integrals between these quantized functions usually called $t_{ll'm}$ (e.g., $t_{sp\sigma}$). This is illustrated in figure 6-2, for the Hamiltonian integral between a s and a p_x orbital, $E_{s,x}$. Note that some two center $t_{ll'm}$ integrals, such us $t_{sp\pi}$ in the figure, are zero by symmetry. Tables for different energy integrals can be found in reference [20] for s, p, and d orbitals, and reference [199] for f and g orbitals.[12]

The neglected three–center contributions are not necessary small as already pointed out by Slater and Koster. For some structures, the number of $t_{ll'm}$ integrals is the same as the E integrals. In this case, no savings are made regarding the number of parameters when using the two–center approximation.

The values of the two–center integrals $t_{ll'm}$ depend on the actual distance between the atoms. By relating the tight–binding bands to free electron bands, Harrison and collaborators predicted not only what this distance dependence should be for s–p materials, but also *universal* inter–atomic coefficients for this parametrization [201]. They later obtained general expressions for other bonding types [130, 202, 203]. Their findings are summarized in table 6.1. It should be noted that these universal parameters and distance dependencies are valid for nearest–neighbors integrals. For larger distances, the basis functions decay exponentially. This effect is not taken into account in table 6.1.

Other authors have proposed different distance expressions, whose parameters are

[12]There are some typographical errors in both references. See references [199, 200] for the corrections. Reference [199] presents a general formalism to express the hopping integrals as a function of two–center integrals valid for any angular–momentum quantum numbers.

s-s, p-p	p–d	d–d
$t_{ll'm} = \eta_{ll'm}\frac{\hbar^2}{m_e d^2}$	$t_{ldm} = \eta_{ldm}\frac{\hbar^2 r_d^{\frac{3}{2}}}{m_e d^{\frac{7}{2}}}$	$t_{ddm} = \eta_{ddm}\frac{\hbar^2 r_d^3}{m_e d^5}$
$\eta_{ss\sigma} = -1.40$	$\eta_{sd\sigma} = -3.16$	$\eta_{dd\sigma} = -16.2$
$\eta_{sp\sigma} = +1.84$	$\eta_{pd\sigma} = -2.95$	$\eta_{dd\pi} = +8.75$
$\eta_{pp\sigma} = +3.24$	$\eta_{pd\pi} = +1.36$	$\eta_{dd\delta} = +0.00$
$\eta_{pp\pi} = -0.81$		

Table 6.1: Interatomic matrix elements as proposed by Harrison. The value of the r_d constants can be found in reference [130] and d is the distance between the atoms.

fit to the particular systems. For example, Mehl and coworkers have used

$$t_{ll'm}(d) = \frac{(c_{1,ll'm} + c_{2,ll'm}d + c_{3,ll'm}d^2)}{(1 + e^{\frac{(d-d_o)}{l_o}})} e^{-c_{4,ll'm}^2 d}, \tag{6.10}$$

where d is the distance between atoms, $c_{i,ll'm}$ are the coefficients to be fit to *ab initio* results and l_o and d_o are taken as 0.5 a.u. and 14 a.u. respectively [197]. On the other hand, Mercer and Chou [204] proposed using

$$t_{ll'm} = \frac{c_{1,ll'm}}{d^{c_{2,ll'm}}} e^{c_{3,ll'm}d}. \tag{6.11}$$

The same expressions are usually used for the overlap integrals if the basis is nonorthogonal.

The diagonal elements of the Hamiltonian matrix are usually called on–site terms. These terms correspond to the hopping integrals computed for identical orbitals. If atomic orbitals were used as basis functions, the on–site terms would represent their free–atom eigenvalues changed by the solid environment. Since in most cases of interest the tight–binding model is applied to a different environment than the one in which it was fit, it is necessary to incorporate this environmental dependence. Different functional forms have been proposed to relate the on–site terms to the distance to, and the number of, nearest neighbors. See for example references [197, 204]. We will come back to this point in section 6.2.2.

It is common practice to fit the hopping and overlap terms to the bands produced by *ab initio* methods.

6.2.2 Tight–binding total–energy model

The tight–binding formalism explained in section 6.2.1 is sometimes referred to as a *band* model. No *total–energy* expression has been presented. Thus, the Slater–Koster model can be regarded as a procedure to interpolate the bands to all points in the Brillouin zone from calculations for a few high–symmetry $\vec{k}$ points. Since our aim

is to compute formation energies, it is essential to develop a way of extracting total energies from this technique.

We start from the density–functional expression in the LDA for the total energy [16].[13] For simplicity, we disregard any reference to $\vec{k}$–space,

$$\begin{aligned} E(n(\vec{r})) &= \sum_{i}^{occ} \varepsilon_i - \frac{1}{2}\int\int n(\vec{r})n(\vec{r}')d^3r d^3r' + \int n(\vec{r})\left[\varepsilon_{xc}(n(\vec{r}) - V_{xc}(n(\vec{r}))\right] d^3r \\ &\quad + \frac{1}{2}\sum_{I}^{N}\sum_{J\neq I}^{N} \frac{Z_I Z_J e^2}{\left|\vec{R}_I - \vec{R}_J\right|} \\ &= E_{bs} + F(n(\vec{r})). \end{aligned} \tag{6.12}$$

Here, ε_i are the Kohn–Sham eigenvalues and $E_{bs} = \sum_i^{occ} \varepsilon_i$ is the so–called band–structure energy (the sum is over occupied electronic states). $F(n(\vec{r}))$ represents the overcounting of the electron–electron interaction in the E_{bs} term, the parts of the exchange and correlation not included in the eigenvalue sum, and the core–core electrostatic energy.

The $F(n(\vec{r}))$ term is essentially a *short–range* repulsive interaction if there is no significant charge transfer between the atoms. In this case, the core–core interaction tends to cancel out with the electron–electron interaction.[14] Furthermore, the exchange and correlation part is usually small [188, 205].

Many tight–binding total–energy methods compute total energies by using the Slater–Koster band model to obtain the band–structure energy and a sum of pair potentials to evaluate $F(n(\vec{r}))$.[15] Consequently, the tight–binding total energy is given by

$$E = E_{bs} + E_{pp}. \tag{6.13}$$

The pair potential, E_{pp}, is repulsive and is a function of the bond length r_{ij}. For example, Sigalas and Papaconstantopoulos suggested using [21]

$$E_{pp} = \frac{1}{2}\sum_{\substack{i,j \\ j\neq i}} \left\{ \sum_n \frac{A_n}{r_{ij}^n} \right\} e^{\lambda r_{ij}}. \tag{6.14}$$

The second sum represents a polynomial in $\frac{1}{r_{ij}}$. A_n and λ are coefficients that are fit, together with the hopping and overlap terms, to first–principles band and total–energy vs. volume curves for different structures. Instead, other authors chose to fit to phonon frequencies, bulk modulus, or other experimental measurements. However, the Sigalas–Papaconstantopoulos approach provides more accurate results for computing formation energies since we are directly fitting to the quantities of interest.

There are severe approximations in going from the LDA equation 6.12 to the

[13]The procedure we will follow varies according to the treatment of the many–body electron problem. However, the final form of the result, equation 6.13, is always the same.

[14]If charge transfer is allowed, there can be a long–range contribution in the form of a Madelung sum.

[15]See for example references [21, 188, 206] and references therein.

tight–binding expression 6.13. In the latter, ε_i is not the result of a *self–consistent* approximation. There is also the question of whether it is possible to replace $F(n(\vec{r}))$ by a *pairwise* short–range interaction. These issues are discussed in detail in reference [205].[16] See also reference [188].

There are also practical problems in the implementation of equation 6.13 as pointed out by Cohen and coworkers [22]. The Kohn–Sham eigenvalues can be shifted by an arbitrary constant without changing the results, since its contribution to the total energy is canceled out by $F(n(\vec{r}))$ in a self–consistent calculation. If the two terms in equation 6.13 are parametrized *independently*, extra care should be taken to handle this constant.

On the other hand, the introduction of a shift in the potential can be used to eliminate the E_{pp} term altogether [22]. The shift, S_o, can be defined to be

$$S_o = \frac{F(n(\vec{r}))}{N_e}, \tag{6.15}$$

where N_e is the total number of electrons. Thus, equation 6.12 is transformed into,

$$E(n(\vec{r})) = \sum_{i}^{occ} \left(\varepsilon_i + \frac{F(n(\vec{r}))}{N_e} \right). \tag{6.16}$$

A set of Slater–Koster parameters that simultaneously fits the band–structure and the total–energy vs. volume curves will solve the total–energy problem without the need of a pair–potential term. This model has been successfully applied to compute elastic constants, vacancy formation energies, and other physical properties for many alkaline–earth, transition, and noble metals [22, 197].

Unfortunately, these simple models can not be applied in oxides. As it was already mentioned, when there is a significant charge transfer between the atoms in the solid, E_{pp} is no longer short–ranged. Furthermore, the transfer of charge between atoms will considerably shift the on–site terms. This transfer can not be accurately captured with the standard environment dependence of the diagonal Hamiltonian terms. This long–range effect can only be represented by a proper description of the charge transfer mechanisms.

The explicit use of the atomic charge in the tight–binding Hamiltonian, forces the reinstatement of self–consistency into the calculations. We are now ready to incorporate into the formalism all the relevant physical contributions to the total energy we mentioned in chapter 5. This will be accomplished in the next section.

6.3 Self–consistent tight–binding total–energy model

The tight–binding formalism and its localized basis provide an intuitive picture of

[16] The procedure is justified by showing that the tight–binding model can be understood as a stationary approximation to self–consistent density–functional theory.

how the solid can be viewed as a set of interacting atoms. We will take advantage of this to build an appropriate Hamiltonian model for oxides.

When the atoms are brought together to form a solid, the electrons are attracted not only to their own cores but also to the neighboring ones. The total energy is reduced by this electronic *sharing* between the ions. In a tight–binding formulation, the presence of nonzero hopping integrals reproduces this effect. The hopping integrals have a fundamental role in determining the shape of the bands.

A second effect of bringing the atoms together is the compression of the atomic clouds that causes a repulsive interaction due to an increase in the kinetic energy. It is identified with the overlap of the basis functions and is taken into account through the overlap matrix [198, 207]. This was also pointed out by Gordon and Kim [106] and is an integral part of the SSCAD formalism, as mentioned in section 3.3.1.

It should be clear then that of the four mechanisms identified in chapter 5, only the ionic breathing and the charge transfer effects are missing in the total–energy model of section 6.2.2. The displacement of charge between the atoms is accompanied by the appearance of a long–range electrostatic interaction. The effect of this field (the crystal field) is to shift the on–site terms. For example, in CaO or MgO, this shift moves the oxygen p levels downward, stabilizing the O^{-2} state. The electrostatic interaction between the cores should also be taken into account. It is usually lumped together with the electron–electron interatomic interactions.

Given a certain charge distribution between the ions, the effect of the ionic breathing can be taken into account by adding the crystal field to the on–site terms. The field is easily computed in the form of a Madelung sum.[17]

The occupation of the atomic orbitals is changed by the rearrangements of charge when the atoms are compressed to form the solid. The changes in the intra–atomic interactions between the electrons also modify the electronic levels and should be taken into account.

Both the effect of the crystal field and the change in the intra–atomic interactions require the knowledge of the charge density which, in turn, depends on the Hamiltonian matrix (since it determines the one–electron wave function from which the density is computed). Consequently, the charge density has to be determined *iteratively*. This is the origin of the required self–consistency of the method.

It should be noted that the last two contributions only affect the diagonal terms. In the following, sections we will give details of how these different contributions can be computed and incorporated into the tight–binding Hamiltonian. We will follow reference [192] closely.

[17]The procedure can be compared to the PIB model where the isolated oxygen density is computed within Watson spheres. These spheres reproduce the crystal field that the atom feels when placed in the solid.

6.3.1 Nonorthogonality contributions

As it was already mentioned, the atomiclike basis, $|\phi_{i\alpha}>$ is usually not orthogonal.[18] However, it is more convenient to work with localized orthogonal functions. The original basis can be transformed into an orthogonal one, $|\varphi_{i\alpha}>$, in the following way

$$|\varphi_{i\alpha}>=|\phi_{i\alpha}>-\frac{1}{2}\sum_{j\neq i,\beta\neq\alpha} S_{j\beta,i\alpha}|\phi_{j\beta}>. \tag{6.17}$$

The sum is over all the elements in the basis (except for $|\phi_{i\alpha}>$).

In the new basis, the overlap matrix **S** is zero to first order in the old overlap matrix, except for the diagonal terms (that are equal to one). Furthermore, the new Hamiltonian matrix elements are now

$$\begin{aligned} t_{i\alpha,j\beta} &= <\varphi_{i\alpha}|H|\varphi_{j\beta}> \\ &= <\phi_{i\alpha}|H|\phi_{j\beta}>-\frac{1}{2}\sum_{i'\neq j,\alpha'\neq\beta} S_{i'\alpha',j\beta}<\phi_{i\alpha}|H|\phi_{i'\alpha'}>- \\ &\quad \frac{1}{2}\sum_{j'\neq i,\beta'\neq\alpha} S_{j'\beta',i\alpha}<\phi_{j'\beta'}|H|\phi_{j\beta}>+\vartheta(\mathbf{S}^2). \end{aligned} \tag{6.18}$$

Since the nondiagonal terms are directly fit to *ab initio* results, there is no need to incorporate **S** terms in them. They are implicitly taken into account during the fit. On the other hand, the on–site terms are formed by different contributions which will be fit independently. Consequently, we need to write the effects of nonorthogonalities explicitly,

$$\begin{aligned} t_{i\alpha,i\alpha} &= <\phi_{i\alpha}|H|\phi_{i\alpha}>-\sum_{\beta\neq\alpha,j\neq i} S_{i\alpha,j\beta}<\phi_{i\alpha}|H|\phi_{j\beta}>+\vartheta(\mathbf{S}^2) \\ &= <\phi_{i\alpha}|H|\phi_{i\alpha}>+\mathcal{F}_{i\alpha}. \end{aligned} \tag{6.19}$$

In what follows, we will assume that the unspecified basis we use is orthogonal. Furthermore we will *correct* the on–site terms by $\mathcal{F}_{i\alpha}$. Thus, for example, if we assume that our starting, nonorthogonal basis functions are the free atomic orbitals, equation 6.19 will translate into,

$$t_{i\alpha,i\alpha}=\varepsilon_{i\alpha}+\mathcal{F}_{i\alpha}, \tag{6.20}$$

where $\varepsilon_{i\alpha}$ are the atomic eigenvalues.[19]

[18] In what follows, we will adopt Dirac's bra–ket notation to make the mathematical manipulations more clear. (See for example reference [67].) Recall that we use the symbol i and α to identify the ionic site and angular momentum respectively.

[19] Note that to compute $\mathcal{F}_{i\alpha}$, we need the hopping integrals in the *nonorthogonal* basis. However, the fitting process will provide these matrix elements in the *orthogonal* basis. We can safely replace one by the other to first order in **S** [192].

6.3.2 Intra–atomic electron–electron interactions

An Anderson Hamiltonian [208] model is used to describe the effect on the orbital energies of the Coulomb repulsion between electrons on the same atom. The levels in a *free* atom, $\varepsilon_{i\alpha}$, are described as a function of the orbitals occupation, $Q_{i\alpha}$, in the following way

$$\varepsilon_{i\alpha} = \varepsilon^o_{i\alpha} + \sum_{\beta} Q_{i\beta} U_{i\alpha,i\beta}. \tag{6.21}$$

Here, α are the set of quantum numbers that identify the orbitals and $U_{i\alpha,i\beta}$ are the intra–atomic repulsion parameters computed as,

$$U_{i\alpha,i\beta} = e^2 \int \frac{\phi^*_{i\alpha}(\vec{r})\phi_{i\alpha}(\vec{r})\phi^*_{i\beta}(\vec{r'})\phi_{i\beta}(\vec{r'})d^3r d^3r}{|\vec{r} - \vec{r'}|}. \tag{6.22}$$

This model assumes that the atomic energies are linear functions of the occupation of the orbitals. As shown in reference [209], this approximation is a very reasonable one.

The formulation of the electron–electron interaction in equation 6.21 corresponds to a Hartree–type approximation.[20] These *direct* contributions are usually much larger than the exchange terms [210]. For the case of open d–shells, it may be necessary to include the *exchange* energy explicitly within a Hartree–Fock–type approximation [211]. For simplicity, we treat equation 6.21 as a phenomenological model, whose parameters are fit to *ab initio* LDA results or Hartree–Fock calculations.[21]

Hartree–Fock calculations usually provide a more accurate representation of an *isolated* atom. Consequently, it is common practice to obtain the parameters of the model, $U_{i\alpha,i\beta}$ and ε^o_α from them [209]. Differences between the *experimental* ionization energy and the electron affinity, or between the first and second ionization energies are also used [212]. In this last case, a single $U_{i\alpha,i\beta}$ is generally employed independently of the orbitals α and β. In reference [212], a table is provided for *sp*–configuration atoms.

The change in the atomic eigenvalues with respect to the occupation of the orbitals can also be obtained from the so–called chemical hardness matrix [213]. Assuming $Q_{i\alpha}$ to be continuous, the total energy is expanded in a Taylor series, and the eigenvalues are obtained as the derivative of the total energy with respect to the orbital occupations. The coefficients of the expansion are the elements of the chemical hardness matrix and can be computed from *ab initio* atomic calculations. This can be considered as a generalization of our simple model to any order on the variation of orbital occupancy. For more details, see reference [213].

[20] $U_{i\alpha,i\alpha}$ is formally the exchange *self–energy* of the state $\phi_{i\alpha}$ as well as the Hartree–type Coulomb interaction [208].

[21] Harrison has argued that the principal effect of the Coulomb interactions is to add a correction proportional to the occupation of the orbital, with the proportionality constant depending on the element [212].

6.3.3 The self–consistent tight–binding Hamiltonian

We are now ready to write the one–electron tight–binding Hamiltonian (H_{TB}) by adding the charge transfer effects to the Slater–Koster formalism. In the orthogonalized basis of section 6.3.1, H_{TB} can be written as,

$$H_{TB} = \sum_{i,\alpha} |\varphi_{i\alpha} > \varepsilon_{i\alpha} < \varphi_{i\alpha}| + \sum_{\substack{i,\alpha,j,\beta \\ i \neq j}} |\varphi_{i\alpha} > t_{\alpha\beta} < \varphi_{j\beta}|. \tag{6.23}$$

The first term in the equation corresponds to the on–site or diagonal Hamiltonian matrix elements, while the second term represents the nondiagonal or hopping terms. $t_{\alpha\beta}$ will be fit to *ab initio* results as explained in section 6.4.1.

The extra contributions to the Slater–Koster Hamiltonian can be incorporated into $\varepsilon_{i\alpha}$,

$$\varepsilon_{i\alpha} = \varepsilon^o_{i\alpha} + \mathcal{F}_{i\alpha} + \sum_{\beta} U^{intra}_{i\alpha,i\beta} Q_{i\beta} + \sum_{j \neq i,\beta} U^{inter}_{i\alpha,j\beta} Q_{j\beta} + V_{i\alpha}. \tag{6.24}$$

$\varepsilon^o_{i\alpha}$ represents the kinetic energy and the interaction with its own ionic core (at site i) of an electron at orbital α. $\mathcal{F}_{i\alpha}$ is the shift in the eigenvalues due to the orthogonalization process (see section 6.3.1). The first sum represents the electron–electron interaction within atom i, while the other sum is between electrons at different atoms. Finally, $V_{i\alpha}$ represents the crystal field at site i.

Similarly to $U^{intra}_{i\alpha,i\beta}$, $U^{inter}_{i\alpha,j\beta}$ is computed as

$$U^{inter}_{i\alpha,j\beta} = \int \frac{\phi^*_{i\alpha}(\vec{r})\phi_{i\alpha}(\vec{r})\phi^*_{j\beta}(\vec{r'})\phi_{j\beta}(\vec{r'})d^3r d^3r}{|\vec{r} - \vec{r'}|}. \tag{6.25}$$

The electron–electron interatomic interactions can be computed as Madelung sums over *point* charges.[22] Note that this is an important approximation since the Coulomb interaction can not be meaningfully divided into strictly inter– and intra–atomic terms for overlapping charges. A simple way of solving this is to interpolate the electron–electron interaction between a "e^2/d" potential for large distances and a constant "U" for short distances. See reference [192] for more details.

The eigenvalues, $\varepsilon_n(\vec{k})$, and eigenvectors, $| n\vec{k} >$,[23] of the Hamiltonian matrix H_{TB} at each $\vec{k}$ have to be computed *self–consistently* since its diagonal elements depend on $Q_{i\alpha}$ which is obtained as

$$Q_{i\alpha} = \sum_{n,\vec{k}}^{occ} |< \varphi_{i\alpha} \mid n\vec{k} >|^2 . \tag{6.26}$$

This sum is over all occupied states.

Variants of the Hamiltonian in equation 6.23 have been successfully used by Rob-

[22] Combined with the core charges.

[23] Note that $| n\vec{k} >$ is written as a function of Bloch's sums of the orthogonalized basis functions $|\varphi_{i\alpha} >$. See section 6.1 for more details.

bins and Falicov [214], Schilfgaarde and coworkers [215], Harrison [212], and Majewski and Vogl [216] among others. Within this model, atomic forces can be computed very simply as shown in reference [217].

6.3.4 Total energies within the self–consistent formulation

In section 6.2.2, we showed that the total energy can be written as (see equation 6.12):

$$E(n(\vec{r})) = E_{bs} + F(n(\vec{r})). \tag{6.27}$$

The band–structure contribution is easily computed by finding the eigenvalues of H_{TB},

$$E_{bs} = \sum_{n,\vec{k}}^{occ} \varepsilon_n(\vec{k}), \tag{6.28}$$

where the sum is over the single–particle energies of the occupied states with band index n and wave vector $\vec{k}$.

The second contribution to the total energy in equation 6.27, $F(n(\vec{r}))$, can be explicitly computed within the self–consistent formalism. There is neither a need to add extra parameters in a pair–potential form nor a concern about artificial shifts in the eigenvalues.[24] $F(n(\vec{r}))$ incorporates the effect of the core–core repulsion and corrects for the double–counted electron–electron interactions. Thus, it can be computed as:

$$\begin{aligned} F(n(\vec{r})) &= -\frac{1}{2}\sum_{i\alpha}\left(\sum_{\beta} U^{intra}_{i\alpha,i\beta}Q_{i\beta} + \sum_{j\neq i,\beta} U^{inter}_{i\alpha,j\beta}Q_{j\beta}\right)Q_{i\alpha} \\ &\quad + \frac{1}{2}\sum_{I}^{N}\sum_{J\neq I}^{N}\frac{Z_I Z_J e^2}{\left|\vec{R}_I - \vec{R}_J\right|}. \end{aligned} \tag{6.29}$$

Note that this contribution is not an electrostatic interaction between the atoms. The electron–electron contribution (first term in equation 6.29) has a minus sign.

6.3.5 Implementation

The model Hamiltonian in equation 6.23 describes all the physical effects we found to be important to compute formation energies in oxides. By solving for its eigenvalues and eigenvectors self–consistently, total energies can be computed using expression 6.27. Significant time savings are obtained compared to *ab initio* methods since the various complex integrals have been replaced by adequate parametrizations, and the intra–atomic electron–electron interactions by a phenomenological model.

Before the tight–binding model can be used, its numerous parameters have to be determined. It is common practice to fit the hopping and overlap integrals to *ab initio* or experimental results. Since charge–transfer mechanisms were included in

[24] The electron–electron parameters that are used to compute $F(n(\vec{r}))$ should be the *same* ones used to determine E_{bs}.

the formalism, we also need to compute the intra–atomic electron–electron interaction coefficients.

Different approximations can be used to reduce the number of unknown parameters of the model. For example, some authors (see references [134, 213]) make use of the extended Hückel theory [218] to relate the overlap and hopping integrals,

$$t_{i\alpha,j\beta} = K_{i\alpha,j\beta}(\varepsilon_{i\alpha} + \varepsilon_{j\beta})S_{i\alpha,j\beta}. \tag{6.30}$$

In the simplest approximation, $K_{i\alpha,j\beta}$ is regarded as a constant for each row of the periodic table (or a geometric average for cases that involve atoms from different rows) [219]. We did not find this approximation accurate in oxides. Consequently, we fit to both types of integrals independently but with the same distance dependence.

If Hückel's theory is combined with the set of universal parameters in table 6.1, no fitting is necessary within the Slater–Koster formalism. Furthermore, the electron–electron intra–atomic interaction parameters can be obtained from ionization energies and electron affinities, and the atomic levels from published Hartree–Fock calculations [104, 105]. This opens the possibility for the self–consistent formulation to also be a "fitting–free" model. The results thus obtained are usually *qualitatively* correct. As already mentioned, the values and distance dependence of the parameters in table 6.1 are not known exactly. They are usually fit to results for many different systems. Moreover, the computation of the intra–atomic interaction coefficients also involves many approximations.

Many authors have been successful in predicting general trends in materials properties by performing fits to different systems [130, 134, 216]. However, our aim will be to reproduce very accurately the properties of a *specific* system. For example, we will fit the overlap and hopping integrals to *ab initio* calculations for pure CaO, MgO, and $CaMgO_2$ ($L1_0$ structure), and then predict formation energies for many mixtures of the end members. The values of the intra–atomic interactions and the electronic levels will be taken from the tables.[25] The distance dependence of the integrals will be assumed to be the ones in table 6.1.[26]

We expect the fit parameters to be transferable within different structures in a given oxide system since our tight–binding Hamiltonian incorporates all the relevant effects to compute total energies. Of course, the transferability of the parameters can be reduced by the approximate treatment of some of these terms or by other effects not accounted for that can be mapped onto them. However, we will show in chapter 7 that the formulation used here is an adequate representation of the energetics of oxides and that no significant transferability problems arise.

[25]When the intra–atomic parameters were taken as fitting coefficients they stayed very close to the values in the tables.

[26]Note that there are tremendous savings in the number of parameters to be fit when simple distance dependencies such as the ones in table 6.1 are used. Polynomial dependencies will require at least twice as many parameters.

6.4 Computation of the tight–binding parameters

As already mentioned at the beginning of this chapter, the computation of the hopping and overlap integrals is very time–consuming. Consequently, semiempirical formulations fit those parameters to *ab initio* calculations or experimental properties. The fitting process is generally very involved. A large number of parameters should be determined and the optimization space is nonlinear, with many local minima.

The number of parameters to fit varies with the size of the basis set. For a typical oxide, with 3 different species in the unit cell and a *s-p-d* basis, it is around 70. This number can be 4 times larger if a more complex distance dependence of the parameters are used. The parameters are adjusted so that the tight–binding model reproduces a set of different physical properties. A "distance" or *merit function*, usually proportional to the square of the difference between the predicted and the "direct" values, is defined. The parameters are evolved to minimized this "distance" by using a nonlinear least–squares algorithm such as the Marquardt procedure [220].

However, a different approach in which the coefficients are directly computed from a first–principles method can be taken. Andersen and Jepsen showed that there exists an *exact* transformation of the muffin–tin–orbital basis into a tight–binding basis [111].[27] Within the ASA, they were able to cast their Hamiltonian into a Slater–Koster tight–binding Hamiltonian in a two–center form. See references [111, 221] for more details.

Unfortunately, as it was shown in chapter 3, the LMTO–ASA approximations in oxides do not yield accurate results. The choice of sphere radii was critical and no criterion to properly set the size could be found. Consequently, in this work we will fit the parameters to results from pseudopotential calculations.

Significant time savings would be achieved if all the necessary parameters of the model could be obtained from fits to the end members. These compounds are usually simpler than any of their mixtures. A fast optimization procedure can then be performed. We will come back to this point at the end of the chapter.

6.4.1 Fitting procedure

We will use the tight–binding model mainly to reproduce structural energy differences. Consequently, following reference [21], the fitting will consist in computing bands *and* equations of state for a given set of parameters, compare these predictions to LDA calculations, and change the parameters to improve the matching. This is a very difficult procedure since the function to be optimized is nonlinear in a large multidimensional space. Many "local" minima exist, and a straightforward fit frequently does not find the absolute minimum.

The starting point in parameter space is very important to converge to the "right" minimum. Many *universal* values exist based on the LMTO-TB transformation or

[27] Since the transformation is exact, all the results obtained with muffin–tin orbitals can be reproduced by the tight–binding method.

on plain fitting to many elements across the periodic table. However, they are not always close to the optimum values. Many different results for the parameters can still be obtained from the process. A more restrictive criteria during the optimization is necessary.

We imposed constraints during the fitting so that many local minima are removed. By analyzing the physics of the problem, it is possible to identify properties that are relevant and that should be reproduced correctly. For example, in the CaO–MgO system, the pseudopotential results clearly show that Ca and Mg are fully ionized. By using this information we "penalized" any significant departure from this condition, effectively reducing the size of the space where the optimization search is performed. This allowed us to easily obtain the parameters used in chapter 7.

In other cases, the situation is less clear. For example, although Ca is fully ionized in CaO–ZrO_2, neither Zr nor O has its formal charge. Still, an estimation of their charge can be made so that it can then be used during the fit.[28]

For all the systems studied, we found that imposing these extra constraints allows the optimization process to select the "right" minimum. As in any minimization technique, it is never sure that the resulting parameter set is not a local minimum. Checking new structures, not included in the fit, is always a good idea.

It is important that the equation of state scan all the relevant relaxations. A correct distance dependence of the integrals can only be captured if the volume of the cell and internal position of the ions used in the fit are varied over a wide range of values.

The more species involved in the fit the more difficult it becomes. The optimization space is not only larger but also the structures are bigger, which makes the calculation slower. We are usually interested in formation energies resulting from a combination of two oxides. Fitting them independently is simpler than fitting to a mixture of them. However, the end members do not provide all the required parameters. Some cation–cation integrals will be missing. In the next section, we will explore the possibilities of computing these missing values by just using the information provided by the end members. If successful, not only will the fitting process be simpler but once the parameters for several oxides are obtained, total–energy calculations can be performed for any mixture of them.

6.4.2 Tight–binding parameters for oxide mixtures from end–member information

The CaO–MgO is the simplest oxide system we will deal with. Even in this case, fitting to the end members does not provide enough information to compute all the overlap and hopping integral parameters. It is clear that the Ca–Mg interaction parameters can only be obtained from fits to properties of the mixtures.

[28] From equation 6.27, $F(n(\vec{r})) = E(n(\vec{r})) - E_{bs}$. If the intra–atomic repulsion parameters are known, $F(n(\vec{r}))$ only depends on the values of the charges. These values can be assigned so that the tight–binding representation of $F(n(\vec{r}))$ best matches the *ab initio* predictions for the $E(n(\vec{r})) - E_{bs}$ difference as a function of the distance between the ions.

Many attempts have been made to "guess" these coefficients. Most of them were applied to binary alloys with elements of similar electronic structure [222]. A simple geometric average of the *self* cation–cation interactions of the type,

$$t^2_{i\alpha,j\beta} = t_{j\beta,j\beta} t_{i\alpha,i\alpha}. \tag{6.31}$$

is often suggested. The oxide cations do not necessarily have a similar electronic structure. Furthermore, the use of equation 6.31 has no formal justification other than its simplicity. However, it is important to note that the cation–cation interactions are usually small since they are not nearest neighbors.

One is tempted to take them as zero, as a first approximation, and just use the parameters computed from the end members. The problem is that many different parameter sets fit the end members properly but result in variations of properties of the mixtures of more than 100%. Without using fitting information from the mixture, it does not seem possible to predict correct mixing properties.

In the next chapter, we will further analyze these problems and suggest possible solutions.

6.5 Coding the self–consistent tight–binding method

We have implemented the self–consistent tight–binding total–energy method in a computer. A very simple description of the algorithm can be found in figure 6-3.

The two–center approximation is used to compute the Hamiltonian and overlap matrix elements. Following the procedure suggested by Sharma [199, 200], we construct the Slater–Koster integrals for arbitrary angular momentum quantum numbers. For the Hamiltonian diagonal terms, we usually assume an initial orbital occupation corresponding to their chemical formal valence. These occupations are then changed self–consistently.

The short–range electron–electron interaction is computed in the Hartree approximation. For the Madelung field and the long–range electron–electron interactions, we consider the electronic clouds and the cores as point charges. The Ewald sums are evaluated with the algorithm developed by Monkenbusch [223].

There are several possibilities to carry out the self–consistent iterations (see reference [224] and references therein). We implemented both a simple mixing procedure and the Steffensen or Aitken's δ^2 method [225]. At each iteration, the diagonalization of the Hamiltonian is performed by using the LAPACK libraries [226].

The scheme to sample the Brillouin zone is based on *special* $\vec{k}$ points. For metals, we also use the high–precision sampling technique proposed by Methfessel [227]. See appendix B.

The fitting is performed by minimizing the *merit function.* This function is defined as the sum of the squares of the differences between physical properties computed by tight binding and any first–principles method. The physical properties can range from Hamiltonian eigenvalues (bands) and equations of state, to lattice constants and bulk

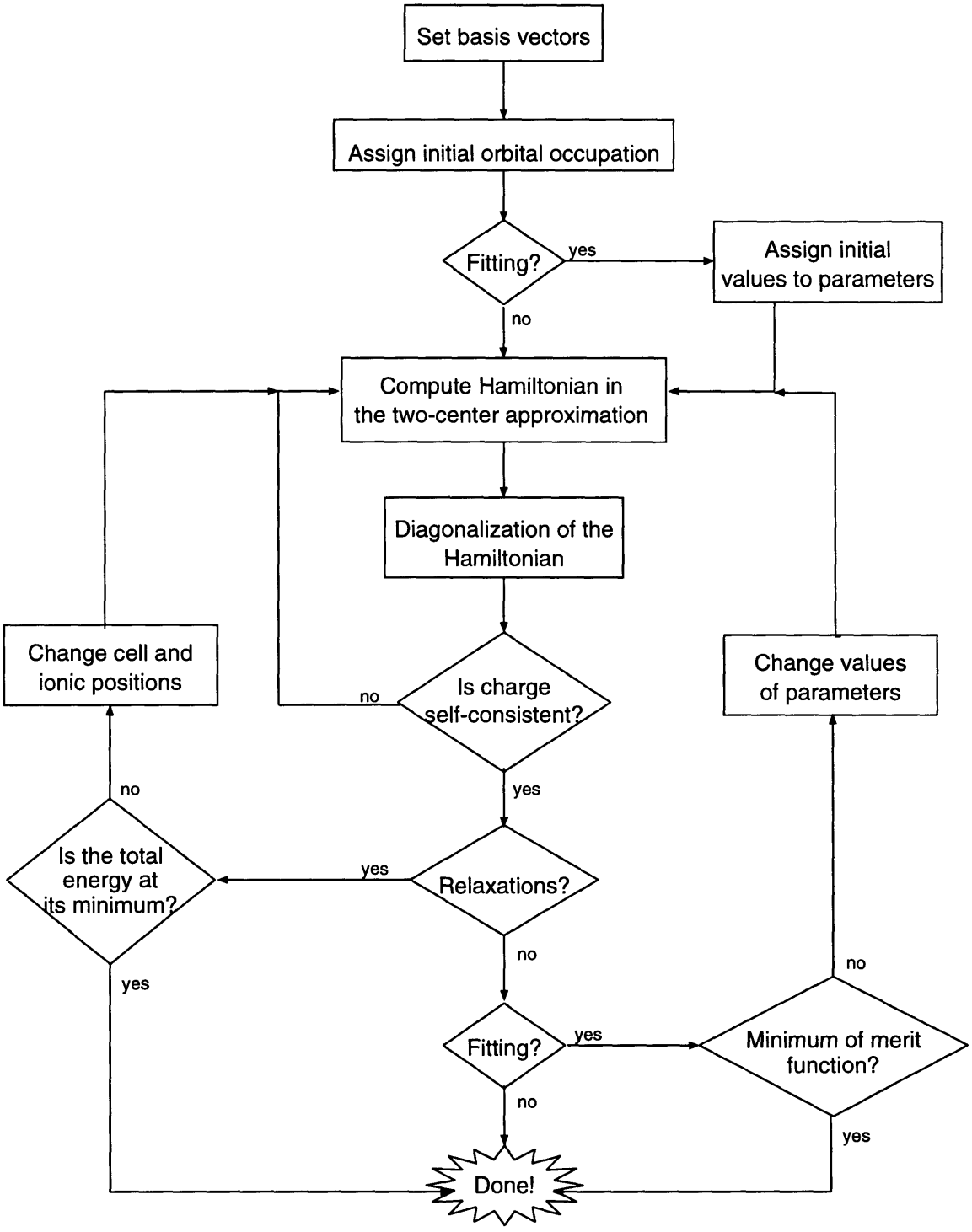

Figure 6-3: Main features of the algorithm used to implement the self-consistent tight-binding total-energy method. The merit function is defined as the sum of the squares of the differences between the properties predicted by tight binding and the *ab initio* or experimental results used in the fit.

moduli. These values can be added in the merit function with different weights. The minimization was carried out using the algorithm proposed by Marquardt [220].

This implementation of tight binding allows us not only to compute total energies and relax structures but also to obtain the adequate parametrizations of the hopping and overlap integrals.[29] In the next chapter, we will evaluate the accuracy of the self–consistent tight–binding total–energy formulation by comparing its predictions to experimental and first–principles results.

6.6 Conclusions

The tight–binding formulation presents a physically transparent picture to understand the formation of a solid from isolated atoms. The different contributions to the total energy can be clearly identified within the model. This is critical in oxides, where failure to account for mechanisms such as oxygen breathing or charge transfer can result in poor predictions of formation energy values.

In this chapter, we developed a semiempirical tight–binding Hamiltonian that is suitable for use in oxides. The Hamiltonian matrix elements were described as distance dependent parametrizations fit to several physical properties. Since some of these terms depend on the atomic charges, solutions for this model have to be found self–consistently.

The *semiempirical* approach results in significant time savings to compute materials properties. The various time–consuming integrals of the first–principles tight binding are replaced by suitable parametrizations. The name *semiempirical* can be misleading. In principle, no experimental results other than the atomic numbers are necessary as input to the method. However, the parameters of the model have to be fit to *ab initio* calculations. It is in this sense that the word *semiempirical* is used here.

Note that no radical assumptions have been made about the nature of the bonds. Our approach will deal with ionicity and covalency on equal footing. Furthermore, neither shape approximations for the potential nor artificial constraints to the amount of charge assigned to the atoms were made.

There is still the question of accuracy of this approach. The parameters of the model will be transferable as long as the correct physical effects are included in the Hamiltonian. In the next chapter, we will discuss this in detail.

[29] Different distance dependencies can be used.

Chapter 7

Applications of the tight–binding method

In chapter 6, we introduced a tight–binding model that accounts for the key mechanisms involved in studies of structural energy differences in oxides. By parametrizing the various hopping and overlap integrals, the computational time requirements of the method are greatly reduced. Now, we will assess the accuracy of this scheme to determine formation energies of mixed compounds. Our final goal is the application of the method to the calculation of phase diagrams.

We will start by revisiting the CaO–MgO system. The simplicity of the system and the abundance of theoretical and experimental results make it an ideal choice. By applying our self–consistent formalism, we will be able to extend the pseudopotential results and compute the phase diagram with an accuracy comparable to the most sophisticated LDA calculations. As far as we know, this is the most accurate calculation ever made on this system. This application clearly demonstrates the power of our approach.

The transferability of the tight–binding parameters is an important issue and CaO–MgO only represents a limited test of this property since all the structures have the same underlying lattice. We will therefore also explore the application of our model Hamiltonian to cases where the atomic arrangements are very different from the ones used during the fit. Zirconia is ideally suited for this analysis due to its polymorphic transformations from a high–temperature, highly–symmetric fluorite structure to less symmetric arrangements at lower temperatures. It is also an important test of our approach since only the most accurate LDA methods provide correct answers in this system [141, 228].

Finally, the ultimate challenge to the self–consistent tight–binding approach is a case where covalency and ionicity are both important in bonding and where charge transfer is significant. The CaO–ZrO_2 system is such a case. The formation energies and the charge transfers of many intermediate compounds will be compared to pseudopotential predictions.

Section 7.1 deals with the CaO–MgO system. The phase diagram and single–defect energies will be computed. Section 7.2 is mainly concerned with the polymorphic transitions in pure zirconia and the charge transfers and formation energies of

mixtures of CaO and ZrO_2. The chapter concludes, in section 7.3, with an evaluation of the possibility of combining parameters of single–metal oxides to predict properties of mixtures.

7.1 The CaO-MgO system

The calculation of a simple phase diagram, such as that of the CaO–MgO system, is currently at the computational time limits of the pseudopotential or FLAPW approach. It is the purpose of this section to show that the tight–binding method can reduce the computational burden of these techniques by interpolating their results for simple structures to more complex cases. As a result, a converged cluster expansion is obtained that can be used to determine the phase diagram with an accuracy comparable to the more complex LDA techniques but at a fraction of the time they would require.

In the following sections, we will assess the accuracy of the tight–binding formation energies and compute the CaO–MgO phase diagram. At the same time, we will evaluate different aspects of the model such as the distance dependence of the hopping and overlap integrals, the accuracy of universal parameters, the Hückel theory, and the fitting process.

7.1.1 Predictions of the "universal" model

As explained in section 6.2.1, "universal" coefficients and distance dependencies can be assigned to the parametrization of the hopping and overlap integrals. The advantage of using them is that no parameters need to be determined from fitting. On the other hand, since they try to reproduce the properties of many different systems their predictions are not very accurate.

We will use the same distance dependencies proposed by Harrison but the coefficients will be taken from references [192, 229]. These parameters were carefully fit to reproduce the valence and conduction bands of sp–bonded solids, as is the case of CaO–MgO. They are reproduced in table 7.1 together with the intra–atomic coefficients and orbital energies. The overlap matrix elements were computed using Hückel's theory with $K_{i\alpha,j\beta}$ (see equation 6.30) from reference [219].

The formation energies and cell parameters predicted by this model are shown in table 7.2. The same $\vec{k}$ points as in the pseudopotential calculations were used. For all structures, the solid wave function was expanded in a s–p basis. Although the results are qualitatively correct, the formation energies are well below their actual values. As suggested in reference [21], fitting to the bands is not enough to accurately compute structural energy differences. The equation of state should also be used.

In what follows, we will not use the "universal" parameters. They will only be taken as a guide to select the starting point for the fitting process.

	a–c	c–a	a–a	c–c	Ca	Mg	O
$\eta_{ss\sigma}$	-1.38	-1.38	+0.50	-0.30	—	—	—
$\eta_{pp\sigma}$	+2.20	+2.20	0.00	0.00	—	—	—
$\eta_{pp\pi}$	-0.55	-0.55	0.00	0.00	—	—	—
$\eta_{sp\sigma}$	+1.68	+1.92	0.00	0.00	—	—	—
s–orbital (eV)	—	—	—	—	-6.11	-6.88	-33.85
p–orbital (eV)	—	—	—	—	-1.46	-1.26	-17.19
$U_{i\alpha,i\beta}$ (eV)	—	—	—	—	+6.40	+7.28	+14.47

Table 7.1: Parameters used with Harrison's distance dependence. The orbital and intra–atomic parameters were taken from reference [192].

	Cell parameters (Å)	Formation energy (eV/ion)
CaO	a=4.60 (4.80)	—
MgO	a=4.38 (4.21)	—
$L1_0$	a=b=3.18 (3.24) ; c=4.49 (4.55)	0.032 (0.141)
$L1_2$ (Ca–rich)	a=4.55 (4.7)	0.024 (0.092)
$L1_2$ (Mg–rich)	a=4.33 (4.42)	0.026 (0.131)

Table 7.2: Formation energies and cell parameters of different ordered arrangements in the CaO–MgO system obtained by using the tight–binding approach with the coefficients from table 7.1. The cells were fully relaxed. The values in parenthesis are the pseudopotential predictions from table 4.2.

7.1.2 Fitting to the CaO–MgO system

The semiempirical tight–binding method was originally used to interpolate electronic band structures [230]. Consequently, the $s_{i\alpha,j\beta}$ and $t_{i\alpha,j\beta}$ matrix elements were usually fit to *ab initio* bands at selected points in $\vec{k}$ space. To study elastic properties and crystal stability, a fit to other properties such as the equation of state is also necessary. In this work, we fit to bands and equations of state of CaO, MgO, and the $L1_0$ compound (the conduction bands were assigned a lower weight in the fit than the valence bands). As expected, the resulting tight–binding parameters are very dependent on the initial guess and it is not immediately clear where the fit should be started.

In multicomponent oxides, charge transfer is one of the key mechanisms involved in the energetics. Therefore it is very important to have a good description of the charge density in order to accurately predict formation energies and make the parameters more transferable to other ordered structures. Since one of the main simplifications of this semiempirical tight–binding model is that the basis functions are not parametrized independently but as part of the $s_{i\alpha,j\beta}$ and $t_{i\alpha,j\beta}$ matrix elements, we can only check that the occupations $Q_{i\alpha}$ resemble the pseudopotential results. In figure 4-5, we showed an electronic valence density plot corresponding to the MgO (001) plane obtained from the pseudopotential calculations. From this plot, we expect the cations to transfer most of their valence electrons to the oxygen atoms. Using perturbation theory, it can be shown that by setting the hopping matrix elements between the orbitals of the anions and the cations to small values, the model will give occupation values according to the pseudopotential results for the CaO–MgO system.[1] Consequently, we choose the initial parameters to reflect this fact.

In Hückel's theory, the $s_{i\alpha,j\beta}$ and $t_{i\alpha,j\beta}$ matrix elements are assumed to be proportional. While doing this considerably reduces the number of parameters of the model, we found that for the CaO–MgO system, only a separate parametrization for **S** and the off–diagonal terms of **H** could accurately reproduce the bands and the equation of state *simultaneously*. We also found that the fit was more stable whenever a penalization function was introduced to restrict $Q_{i\alpha}$ to values close to the pseudopotential ones.

The fit tight–binding Hamiltonian reproduces the main features of the three structures used in the procedure. The lattice constants and bulk moduli are, on average, within 1% and 5% respectively of the pseudopotential values. The valence bands are also well represented, showing a RMS difference of a few hundredths of an eV. See section 7.3 for the fit parameters and a comparison of their values across different oxide systems.

We tested different distance scaling laws for the hopping integrals and the overlap matrix elements. We tried both the the usual d^{-2} distance dependence for the s–p bonded materials as well as expression 6.10. This implied a four–fold increase in the number of parameters to be determined during the fitting process and considerably

[1] The *softening of the ions* (the reduction, in absolute value, of the cation and anion charges) is proportional to $\left(\frac{H_{ij}}{H_{ii}-H_{jj}}\right)^2$ (see reference [130] for more details).

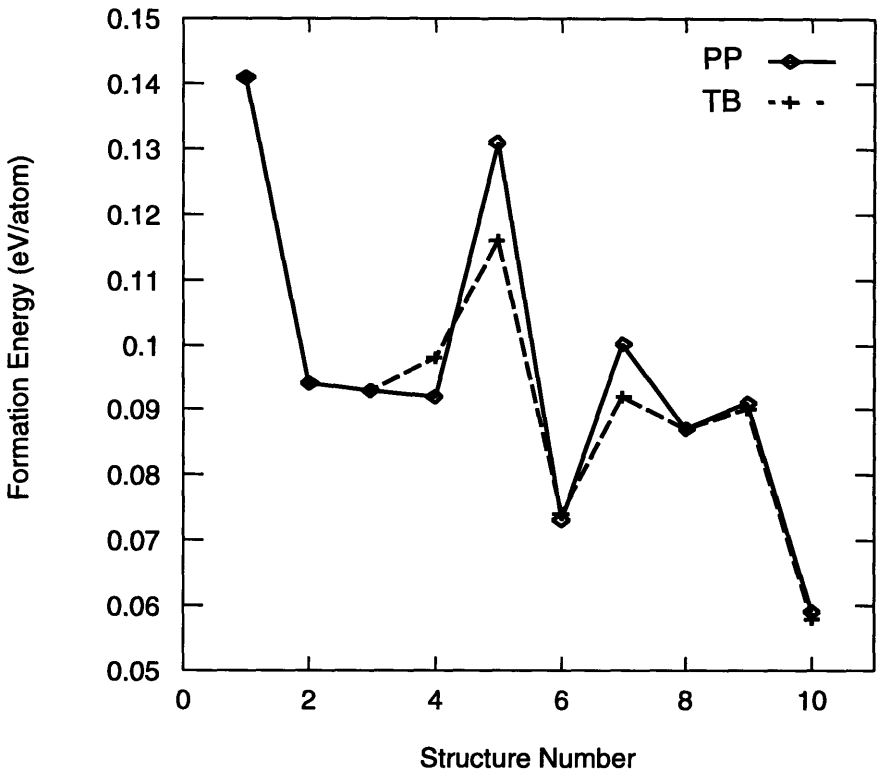

Figure 7-1: Formation energies for different ordered structures in the CaO–MgO system obtained with pseudopotentials (PP) and tight binding (TB). The number that identifies each structure corresponds to the one used in table 4.2. The tight–binding parameters were fit only to $L1_0$ (structure number 1 in the plot) and both CaO and MgO.

augmented its complexity. Although the fit to bands and total–energy curves improved, the *predicted* formation energies only changed by a few meV. Consequently, for the CaO–MgO system, the simpler d^{-2} scaling law gives enough accuracy.

7.1.3 Formation energies

With the parameters obtained in section 7.1.2, we computed the tight–binding formation energies of 21 ordered structures in the CaO–MgO system relaxing all their structural degrees of freedom compatible with their symmetry. We used 10 special Chadi–Cohen $\vec{k}$ points for Brillouin zone integrations for the rocksalt structure, resulting in a total–energy convergence better than 1meV/atom. For all the other superstructures, we took a set of $\vec{k}$ points equivalent to these 10 Chadi–Cohen points (see appendix B).

In figure 7-1, we compare the results obtained using the pseudopotential and the tight–binding methods for the ten structures listed in table 4.2. The agreement between both techniques is excellent if we note that, except for $L1_0$, none of the

structures was used in the fit. The RMS difference between the two methods is 6 meV. Consequently, we can expect the tight–binding cluster expansion obtained from these values to be very close to the actual pseudopotential expansion.

The *relative* stability of the different ordered structures is also well represented within the tight–binding model. From figure 7-1, it can be clearly seen that the *differences* between the predicted formation energies follow the same tendencies as in the pseudopotential calculations. This is important if the asymmetry of the phase diagram is to be well reproduced.

The tight–binding formation energies for the 21 ordered structures can be found in appendix A. This information will be used in the next section to compute and test the ECI's.

7.1.4 Phase diagram

The tight–binding formation energies of all the ordered structures studied in the CaO–MgO system are positive. This is consistent with the fact that the experimental phase diagram shows a miscibility gap. Two main features characterize any miscibility gap: the consolute temperature and the asymmetry of the solubility limits. Before computing the actual tight–binding phase diagram, and as a last test of the accuracy of the model we will make sure that both features are reproduced according to the pseudopotential predictions.

The consolute temperature is mainly determined by the energy scale and, as we showed in section 7.1.3, there is a very good agreement between the methods. The solubility limits depend, at low temperatures, on the energy cost of substituting a CaO(MgO) by a MgO(CaO) on an otherwise perfect CaO(MgO) lattice (see section 2.3.1). This energy corresponds to the energy necessary to invert one of the occupation variables on our lattice model from $+1(-1)$ to $-1(+1)$. Consequently, the solubility is determined, at low temperatures, by the single–defect energy, while the asymmetry is driven by the difference in this value at both end–sides of the phase diagram.

We computed the single–defect energy using a 2x2x2 fcc supercell.[2] Using a complex LDA technique on this cell is prohibitively time consuming and consequently, we compared the tight–binding results to the SSCAD calculations from table 5.3. In table 7.3, we show the single–defect energies for both a pure CaO and a pure MgO host lattice. The tight–binding defect energies are larger, in agreement with the tendency of the SSCAD to underpredict formation energies by 15–20% (see section 5.2). Note that there is an important difference between the defect energy at the MgO– and the CaO–rich sides. This translates into a lower solubility of CaO in MgO than for MgO in CaO (at the same temperature). This asymmetry is also observed experimentally (see figure 2-1).

To determine the phase diagram, we computed the ECI's from the tight–binding formation energies reported in section 7.1.3. We used pairs, triplets, and quadruplets

[2] In reference [84], we showed that a 2x2x2 supercell is big enough to avoid significant self–interactions between the defect and its images.

	Tight–binding	SCPIB
MgO *rich*	0.832	0.704
CaO *rich*	0.672	0.544
Difference:		
MgO *rich* - CaO *rich*	0.160	0.160

Table 7.3: Defect formation energies of a single MgO (CaO) on an otherwise pure CaO (MgO) lattice. The values were computed using a 2x2x2 fcc supercell and are expressed in eV. The term "rich" denotes the host lattice.

as clusters to expand the energy, and obtained a RMS difference in our cluster expansion fit of about 2 meV per atom. The computed ECI's are shown in figure 7-2. The agreement between the tight–binding input and the results reproduced by the cluster expansion is very good, as shown in figure 7-3. As a test, we left out a few structures out of the Connolly–Williams fit[3] and made sure the cluster expansion predicted their formation energy within a few meV.

The phase diagram was computed by performing a Monte Carlo simulation. The result is shown in figure 7-4. The consolute temperature is higher than the extrapolated experimental one and the one calculated with the SSCAD method in section 5.2, by approximately 20%. The tight–binding results do not include the effect of vibrational entropy. Perfect agreement with experiments should therefore not be expected.

An estimation of the effect of vibrations can be obtained from the SSCAD vibrational ECI's of table 5.4. When they are combined with the tight–binding chemical ECI's, the resulting phase diagram coincides almost perfectly with the experimental points. Although this might be somewhat fortuitous, it is a clear indication of the "corrective" effect vibrations will have.

7.2 Pure and doped zirconia

Pure zirconia undergoes two transformations from its low–temperature monoclinic phase to its high–temperature tetragonal and cubic arrangements before becoming a liquid. The high–temperature phases can be stabilized at lower temperature by the addition of dopants, such as calcia. As already mentioned in section 4.2.2, there is considerable technological interest in studying these stabilization effects. Experiments are usually difficult to perform due to the high temperatures or the presence of impurities and defects. Unfortunately, a good description of the energetics of the system with *ab initio* LDA calculations is also out of the question due to the complexity of the crystal structures of the doped zirconias.

The only known mixture of CaO and ZrO_2 that is stable at room temperature is $CaZrO_3$ (*Pcmn* structure). Although this is the simplest superstructure in the

[3]See section 2.1.4.

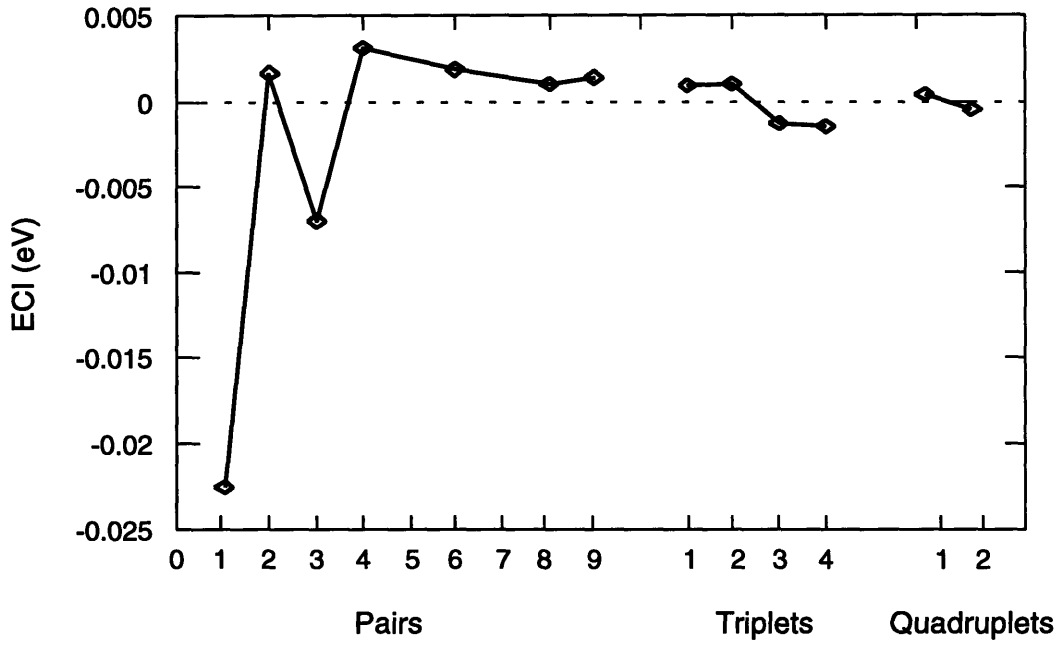

Figure 7-2: Effective cluster interactions for the CaO–MgO system computed with the tight–binding formation energies. The pairs are identified according to their length and the triplets and quadruplets according to their longest side, the other sides being nearest neighbors.

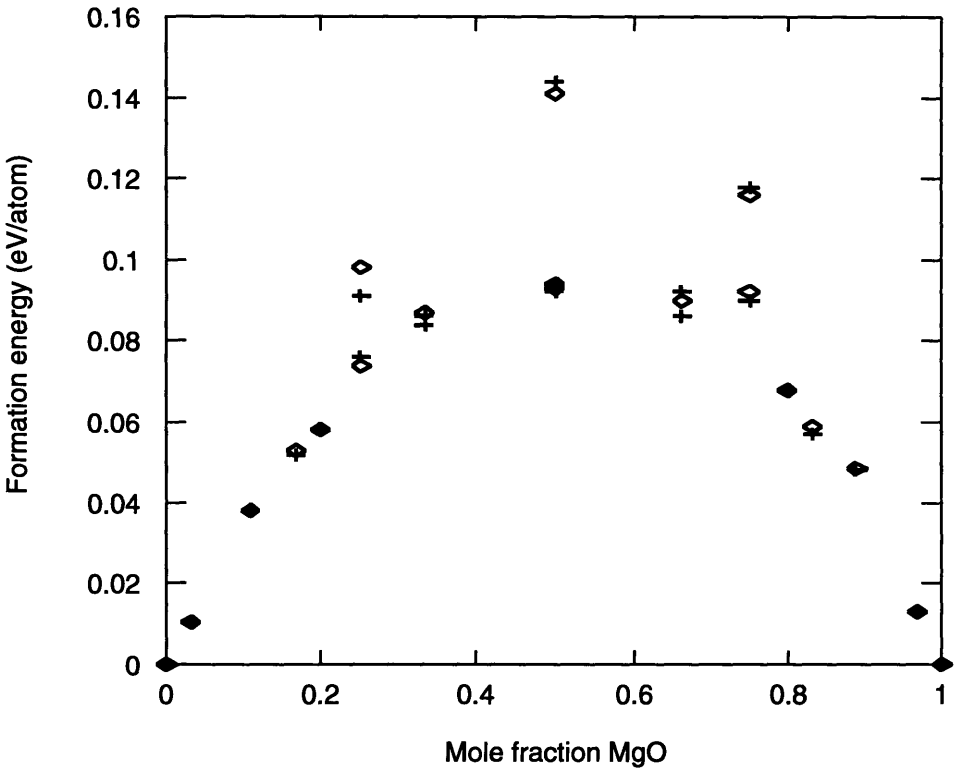

Figure 7-3: Formation energies as a function of composition for different ordered structures in the CaO–MgO system. The diamonds correspond to tight–binding results and the crosses to the cluster expansion fit.

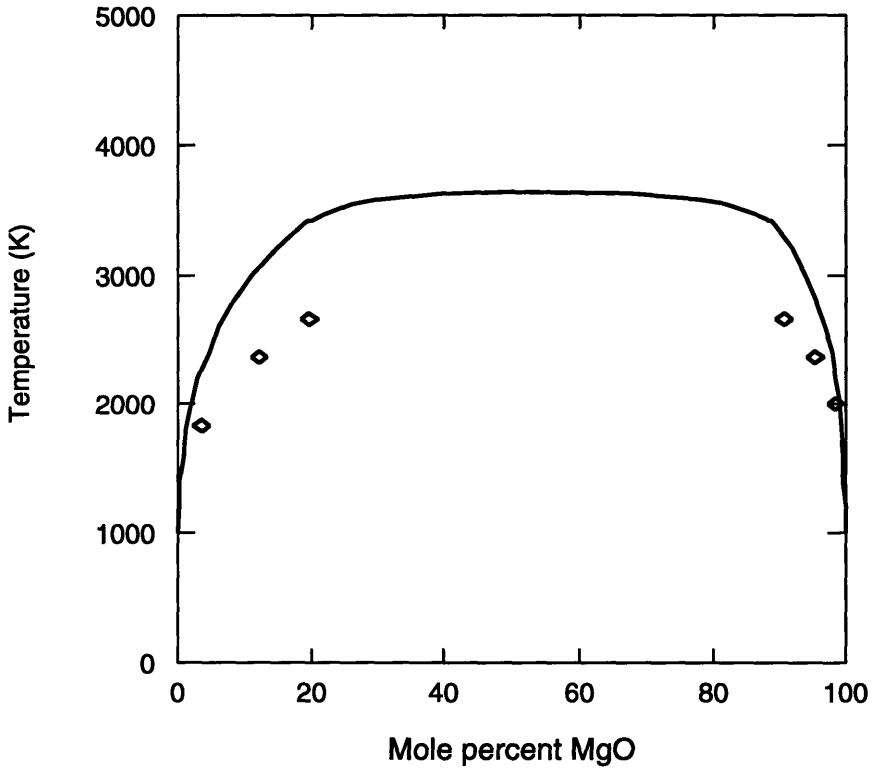

Figure 7-4: CaO–MgO phase diagram. The lines correspond to the solubility limits computed with a Monte Carlo simulation and without taking into account the effect of atomic vibrations in the free energy. The points represent experimental values [30]. Only solid phases were calculated.

system, it has a large *primitive* unit cell with 20 atoms. Other compounds, detected at high temperatures, have even larger cells (for example, $Ca_6Zr_{19}O_{44}$). Fully relaxed pseudopotential calculations for the number of compounds necessary to determine a cluster expansion[4] can not be performed in a reasonable amount of time.

The tight–binding method can be used to overcome these difficulties. We will show that accurate formation energies can be predicted by this technique in the CaO–ZrO_2 system. We will study mixtures of calcia and zirconia within the fluorite lattice so that a direct comparison with the pseudopotential results can be made. The parameters of the model will be fit to the structure S2 (see section 4.2.2) and both pure CaO and ZrO_2. The quality and transferability of their values will be tested by computing the formation energies of all the "S" structures.

Possible mechanisms for the dramatic failure of potential models in this system (see section 5.3) will also be explored. This will lead us to investigate how charge is distributed between the ions.

Before analyzing the energetics of the CaO–ZrO_2 system we will study the pure phases of zirconia. The purpose of this is to evaluate the transferability of the tight–binding parameters under lattice distortions and to assess the accuracy of these parameters when directly used in mixtures (i.e., without fitting to intermediate compounds). The last point will be discussed later, in section 7.3.

7.2.1 Pure zirconia

In section 4.2.2, we performed a detailed pseudopotential study of the tetragonal phase. Here, we will use that information to fit the tight–binding parameters. We can then *predict* the lattice constants of the fluorite (cubic) phase and compare the energy difference between these structures to the pseudopotential results. This will help us to assess the accuracy of our model Hamiltonian under lattice distortions. We will also explore the monoclinic phase though no *ab initio* calculations have been reported up to date for this structure.

Rosenbauer and Jansen performed a very accurate Slater–Koster interpolation of the tetragonal zirconia bands based on FLAPW calculations. They showed that the variation of the Slater–Koster integrals with the bond length could not be described by a simple function [231]. These problems are solved within the self–consistent formulation as demonstrated in the next section.

Fitting of pure zirconia

The elements of the overlap matrix and the hopping integrals were fit to the valence bands of pseudopotential calculations for tetragonal ZrO_2. The conduction bands were included with a smaller weight ($\frac{1}{10}$ times) than the valence bands. Significant departures from the pseudopotential lattice constants were penalized during the fit.

[4]Note that the *coupled* cluster expansion mentioned in chapter 2 should be use here. The cation and anion sublattices have two species each (Zr and Ca for the cation one and vacancies and O for the anion one).

In all the calculations, *s–p–d* and *s–p* bases were used for zirconium and oxygen respectively.

To study the problems reported by Rosenbauer and Jansen in their Slater–Koster interpolation we fit the parameters in two different ways: we either kept the cell volume constant or we changed the lattice constants in a 10% range around the energy minimum. In this last case, the distance dependence of the hopping and overlap terms was assumed to be the one proposed by Harrison (see table 6.1).

The RMS of the difference between the pseudopotential and the tight–binding bands was 6mRy per $\vec{k}$ point when the cell volume was kept constant against 1mRy per $\vec{k}$ point reported in reference [231]. Their smaller value is a consequence of the use of three–center integrals.[5]

When the cell was allowed to change volume, the difference between the tight–binding and the pseudopotential bands had a RMS value of 9mRy per $\vec{k}$ point. This is a very reasonable value, specially if we take into account that a simple distance dependence was assumed. A polynomial fit will certainly reduce this difference. On the other hand, the error incurred by neglecting charge transfer and only using the Slater–Koster formalism made a "good" fit impossible (unfortunately no numbers were given in reference [231]).

In what follows, we assume the distance dependence proposed by Harrison. For the tetragonal and cubic phases, the same $\vec{k}$ points as in the pseudopotential case were used. For the monoclinic structure, a 4x4x4 uniform grid (plus symmetry) was used. The intra–atomic zirconium parameters were obtained by applying the procedure in reference [209] (see section 6.3.2). Similar to the CaO–MgO case, the same $U_{i\alpha,i\beta}$ was assumed for all the orbitals (i.e., an average over the relevant orbitals). The value used was 11.35 eV.

Pure–zirconia results

The computed cell parameters for the different structures and the corresponding energy differences are shown in table 7.4. The experimental, pseudopotential, and pair–potential results from table 5.2 are also reproduced here for comparison. The cubic and tetragonal structures were fully relaxed. Since only the tetragonal bands were used in the fit, the energy difference between the tetragonal and cubic phases is a prediction. This prediction is in excellent agreement with the pseudopotential values. The lattice constants and internal cell parameters are also in very good agreement.

Note that the monoclinic structure has 13 crystallographic degrees of freedom. We optimized all of them except for the cell angle not fixed by symmetry which was held constant at 90°. The experimental 99° angle will place the atoms so that the integrals will have to be evaluate beyond the region of validity of the fit parameters. Furthermore, the simple Harrison distance dependence would have to be replaced by a polynomial function times an exponential decay. We decided not to pursue this fitting since we would need 4 times the number of parameters currently used and con-

[5]The typical error in the total–energy fit is much smaller than for the bands. It is usually of the order of 0.1mRy/atom.

	Expt.[a]	Pot.[b]	TB	PP
Cell Parameter				
Cubic ZrO_2				
a=b=c	5.092	5.075	5.075	5.050
Tetragonal ZrO_2				
a=b	3.571	3.588	3.607	3.575
c	5.20	5.216	5.203	5.153
z(O)	0.303	0.31	0.296	0.295
Monoclinic ZrO_2				
a	5.1505	5.241	5.03	
b	5.2116	4.898	5.22	
c	5.3173	5.578	5.39	
β	99.230	90.0	90.0[c]	
x_1(Zr)	0.2754	0.25	0.278	
y_1(Zr)	0.0395	0.0	0.036	
z_1(Zr)	0.2083	0.1899	0.203	
x_2(O)	0.0700	0.0753	0.073	
y_2(O)	0.3317	0.2818	0.344	
z_2(O)	0.3447	0.3958	0.343	
x_3(O)	0.4496	0.4247	0.445	
y_3(O)	0.7569	0.7182	0.764	
z_3(O)	0.4792	0.3958	0.474	
Energy differences:				
E_{cubic}-$E_{tetragonal}$	0.058	0.019	0.045	0.045
$E_{tetragonal}$-$E_{monoclinic}$	0.061	0.166	0.278	

Table 7.4: Cell parameters and structural energy differences for the experimentally observed phases in zirconia at zero pressure. The energies are in eV per ZrO_2 formula unit and the lattice constants are in Å. All cell parameters were fully relaxed, including the internal positions, x_i, y_i, and z_i, that are shown here according to the Wyckoff notation in reference [168]. The experimental z value for the tetragonal structure was measured at 1295 °C and the cell parameters are extrapolations to 0 °K (see chapter 4).

[a] See reference [171, 182, 183]

[b] See reference [141, 175]

[c] The β angle of the monoclinic structure was fixed. See text.

sequently more pseudopotential calculations for the tetragonal phase. However, the results are important, since the monoclinic phase, even not fully relaxed, is predicted to have a lower energy than the tetragonal phase in agreement with the experimental observations.

7.2.2 Calcia–doped zirconia

Fitting to the CaO–ZrO_2 system

The solid wave functions are expanded in atomiclike $2s$ and $2p$ orbitals localized at the oxygen ions, $4s$ and $4p$ centered at the calcium ions, and $4s$, $4p$, and $4d$ for the zirconium ions. The same $\vec{k}$ points as in the pseudopotential calculations were used here.

The initial parameters for the fitting process were taken as the CaO and ZrO_2 sets found in sections 7.1.2 and 7.2.1 (the O–O being an average of both results). For the Ca–Zr second nearest neighbors coefficients, only the $t_{sd\sigma}$ integrals were included.[6] The integrals were assumed to obey Harrison's distance dependencies of table 6.1.

We independently fit the overlap and hopping integrals (no Hückel's approximation) to the bands and lattice constants of the S2 structure and pure CaO and ZrO_2. Both the valence and the lower levels of the conduction band were used. For the latter, a much lower weight (0.01) in the merit function was given.

The root–mean square difference between the pseudopotential and the tight–binding bands was of the order of a few hundreths of an eV. On the other hand, the lattice constants differed in less than 0.5%.

Tight–binding predictions for the CaO–ZrO_2 system

In figure 7-5, the formation energies of structures S1 to S5 computed by the tight–binding approach are shown. As a reference, the pseudopotential and pair–potential predictions are also displayed. To be able to relate these results, only volume relaxations were allowed. The average difference between the pseudopotential and the tight–binding values is approximately 10%. Although the bands for the structure S2 were used in the fitting process, its formation energy can be considered as a real prediction, since neither this value nor the S2 equation of state was used in the fit.

The predicted lattice constants are also in good agreement. Table 7.5 shows the computed values for structures S1 to S5.

Note that the self–consistent calculations considerably stabilize the structures compared to the pair–potential model. The formation energies predicted by the latter are always higher. For example, for the S3 structure it is more than three times the self–consistent values. These differences are much larger than the ones previously observed in the CaO–MgO system (see section 5.3). We believe this is caused by the variation of ionic charges with different atomic environments. This *extra* degree of freedom is absent in the potential models.

The situation is clearly observed in figure 7-6 where we show the charges predicted

[6] We also tested adding s–s and s–p integrals but the results did not improve appreciably.

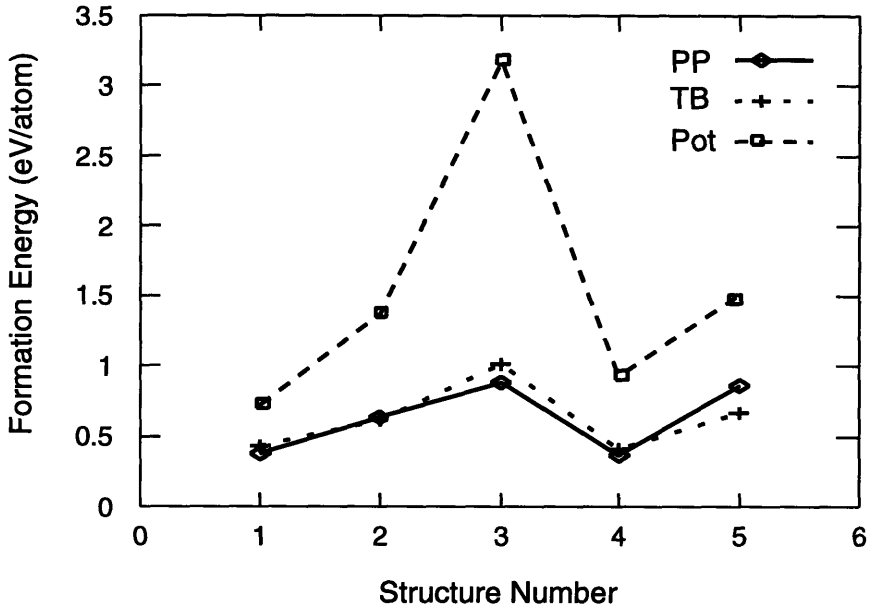

Figure 7-5: Formation energies of structures S1 to S5 computed with tight binding (TB). The pseudopotential (PP) and pair–potential (Pot) predictions computed in sections 4.2.2 and 5.3 are also shown for comparison. A description of the structures can be found in figure 4-10.

Structure	Cell Parameter (Å)		
	Pseudopotentials	Tight binding	Pair potentials
S1	5.130	5.149	5.096
S2	5.130	5.156	5.093
S3	5.136	5.189	5.134
S4	5.080	5.080	5.080
S5	5.220	5.226	5.120

Table 7.5: Cell parameter for structures S1 to S5 computed by pseudopotential, tight binding, and pair potentials. The structures are described in figure 4-10.

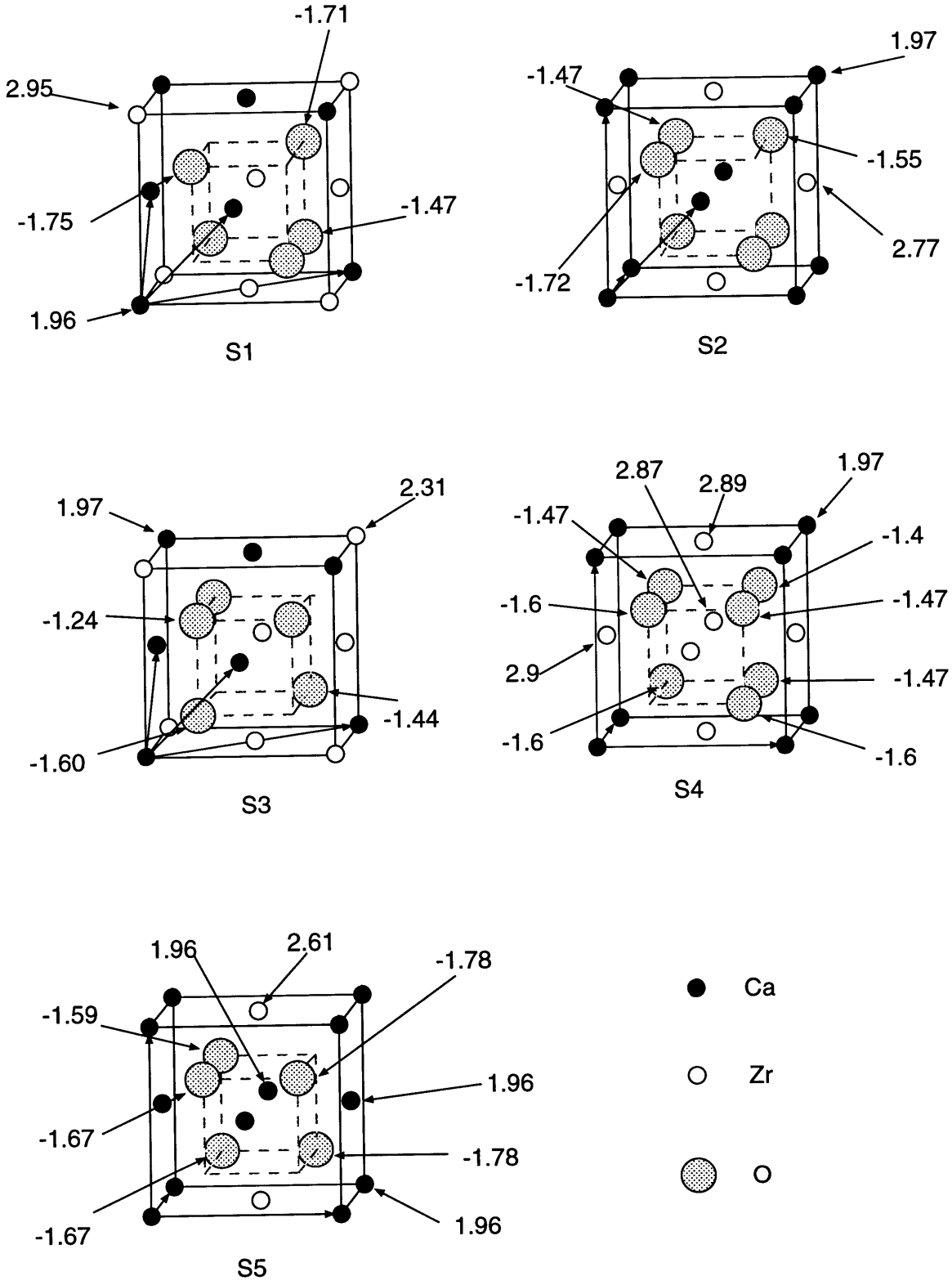

Figure 7-6: Ionic charges for structures S1 to S5 computed with tight binding.

by tight–binding for different structures in the system. In agreement with the pseudopotential results, calcium is fully ionized in all the structures. On the other hand, zirconium and oxygen considerably change their charge from one structure to another. Furthermore, within the same compound, they have different values according to the symmetry of the site.

In the CaO–MgO case, both calcium and magnesium kept their formal charge in all the different atomic arrangements in the structures. Here, oxygen and zirconium change their charges according to these arrangements. The larger the variations, the larger the errors in the pair–potential predictions. For example, structure S3 presents the worst agreement between pair potentials and the self–consistent methods. Correspondingly, the oxygen and zirconium ions have the largest charge variations within different cell sites ($\sim$0.4 electrons).

As a check of the tight–binding results we integrated the pseudopotential electronic density within spheres centered at the different oxygen sites (the sphere radii were the same in all cases). Again, significant differences were detected. The maximum variations were of the order of 0.3 electrons.

For a potential model to work properly, there is a clear need for a way of introducing charge transfer mechanisms. This will be analyzed in chapter 8.

7.3 Tight–binding parameters from fits to end members

In this section, we will determine the accuracy of tight–binding parameters fit only to physical properties of the end members. If two *binary* oxides AO_x and BO_y are mixed, all the hopping and overlap two–center integrals can be obtained from the pure oxides except for the ones involving the cations A and B. As explained in section 6.4.2, we can either disregard the missing cation–cation interaction or approximate it using different assumptions such us the one suggested in reference [222] (see equation 6.31).[7]

Here, we will focus on binary oxides mixtures. We will start by studying the effects of the different approximations in the CaO–ZrO_2 system. Four cases will be analyzed in detail:

Case 1: The parameters of the model are taken from the fits to CaO–MgO and ZrO_2 in sections 7.1.2 and 7.2.1. Since the O–O integrals are fit twice, once for each system, we use the one from CaO. No Zr–Ca overlap or hopping terms are considered.

Case 2: The same as case 1 but now the O–O parameters are taken from the ZrO_2 fit.

Case 3: The same as case 1 and case 2 but an *average* of the two available sets of O–O integrals is used.

[7] Another concern is the *transferability* to the mixtures of the anion–anion and anion–cation parameters fit to the end members.

	Universal	CaO–MgO	CaO–ZrO_2
$(p_O–p_O)_\sigma$	+0.50	+0.50	+0.41
$(s_O–s_{Ca})_\sigma$	-1.38	-0.75	-0.80
$(s_O–p_{Ca})_\sigma$	+1.68	+0.32	+0.33
$(p_O–s_{Ca})_\sigma$	+1.92	+0.46	+0.40

Table 7.6: Set of hopping integrals that were fit in both CaO–MgO and CaO–ZrO_2. The universal parameters found in reference [192] are reproduced for comparison.

Case 4: The same as case 1 except that the Zr–Ca parameters are not assumed to be zero. The *s–d* integrals are approximated by the Zr–Zr ones. We also tested the Zr *p–d* values and geometrical averages of Ca *s–s* and Zr *d–d* with similar results.

Note that cases 1 to 3 not only test the effects of absent Zr–Ca integrals but also the transferability of the O–O parameters. In a perfect situation, there should not be any difference between them. However, table 7.6 shows how the parameters change when they are fit to different systems (in this case CaO–MgO and CaO-ZrO_2). Case 4, evaluates the effect of different approximations for the Zr–Ca hopping integrals.

The results are shown in figure 7-7. The predicted formation energies are compared to the pseudopotential (PP) values. The pair–potential (Pot) estimations are also included since it is the only practical method that can be currently used to compute formation energies of *many large* cells in the system. This will provide a standard to which the tight–binding predictions can be *fairly* compared.

In all four cases, the tight–binding predictions are much closer to the pseudopotential values than the pair–potential models. In this sense, by building a table of two center integrals from fits to binary oxides, the tight–binding method can be almost as simple to use as a potential model. Fits to binary oxides are usually straightforward.

However, cases 1 to 3 also show that the transferability of the parameters is not optimum. By using the O–O integral from different fits, differences of the order of 40% are obtained. Although the difference is large, it is still of the order of the errors in the formation energies introduced by neglecting the cation–cation parameters and much better than the potential predictions. We further explored this issue by refitting both pure oxides with a *common* oxygen–oxygen set of parameters (we took the average used in case 3). This worsened the predictions of the end members by a few percent without significantly changing the results for the mixtures.

By fitting to more systems it might be possible to obtain a better set of O–O parameters. However, approximations of the tight–binding formalism, such as the use of two–center integrals, certainly *map* their effects onto the parameters during a fit. As it was shown in the previous sections, this does not constitute a problem when the fit is done to a particular system. Furthermore, only if a better description of the missing cation–cation integrals were used would it be worthy to correct these

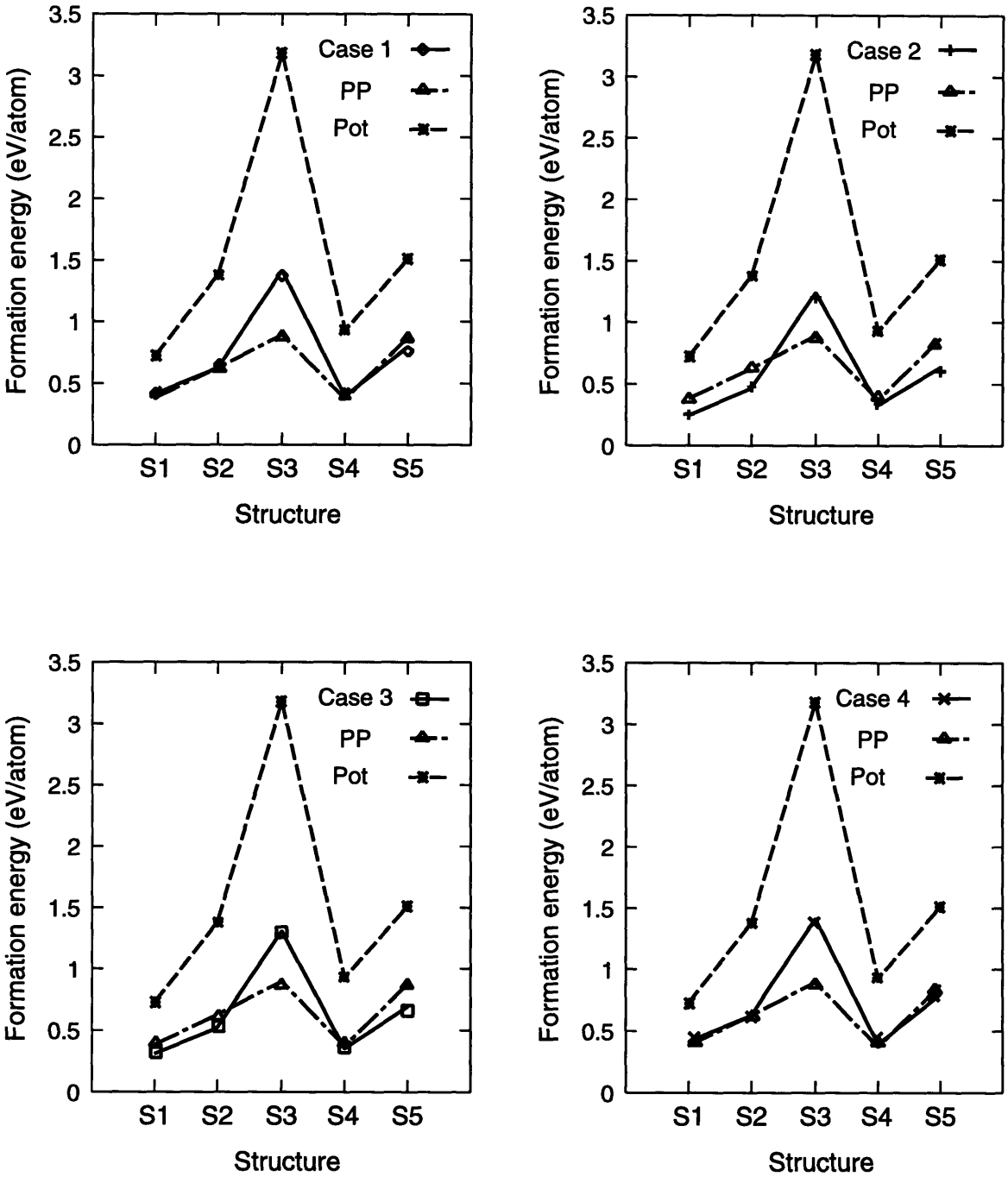

Figure 7-7: Formation energies predicted for different mixtures of CaO and ZrO_2 for the four cases explained in the text. A description of structures S1 to S5 can be found in figure 4-10.

approximations. The error introduced by not considering these integrals is still larger.

Case 4 indicates that the different estimations of the Zr–Ca integrals do not improve the results. However, our results show that their effect on the formation energies can be important. When compared to pseudopotentials, they can introduce errors of the order of 60%.

It is important to note that the parameters used in the 4 cases do not correspond to straightforward fits to the end members. The Ca–O and Ca–Ca parameters for example, were obtained from a fit to the CaO–MgO system and not just CaO. This restricted the space of possible parameters considerably. When CaO and MgO are fit independently, many different sets reproduce the pseudopotential results with similar accuracy. It is only when the $L1_0$ structure is used that one set was selected, which was the one used here. Consequently, enough "restrictions" in the fits should be used. By "restrictions" we mean either fitting to mixtures or using different deformations of the unit cell.[8]

Finally, even when a detailed fit to a given system is pursued, the combination of the end–member parameters can be used as a starting point. They have proven during the CaO–ZrO_2 fit to be much closer to the final parameters than the universal values.

7.4 Conclusions

We have shown that the semiempirical self–consistent tight–binding formalism represents an intermediate method between simple potential models and highly–accurate LDA techniques for studying the energetics of oxides. It retains the high computational speed of the former, but at the same can correctly interpolate very accurate LDA results. The computation of the CaO–MgO phase diagram is an excellent example of this. In this system, the pseudopotential results for only three structures were employed to predict formation energies of many more compounds. This information was then used to compute a converged cluster expansion from which the solubility limits of the system were obtained.

Therefore, the semiempirical tight–binding method offers a clear advantage for investigations in which the energies of many ordered structures, in the same system, have to be computed. Such is the case in the *ab initio* prediction of multicomponent oxide phase diagrams. Although a few computing–intensive LDA calculations have to be performed to fit the tight–binding parameters, the result is a transferable total–energy Hamiltonian that can be used on complex and large unit cells. This makes it an excellent extrapolation tool, considerably reducing the computational burden for phase stability calculations.

The excellent transferability properties of the tight–binding Hamiltonian were demonstrated not only in the CaO–MgO system but also in the more demanding

[8]The deformations of the unit cell do not necessarily have to be compatible with the symmetry. For example, atomic displacements that allow a sampling of many different integrals as a function of the full range of distances between ions can be used.

CaO–ZrO_2 system. Most of the approximate total–energy methods assume either covalent or ionic bonding. Consequently, systems such as CaO–ZrO_2 present an extremely difficult case for them. For example, the SSCAD and pair potentials failed to reproduce nonspherical electronic relaxations and charge transfers respectively. On the other hand, the tight–binding model predicts very accurately the energy differences between the pure tetragonal and cubic phases and the formation energies of calcia–doped zirconias. The incorporation of the relevant physical mechanisms found in chapter 5 was essential for the Hamiltonian to be transferable.

The effectiveness of the method depends critically on the fitting process. This is clearly a crucial and time–consuming step. Therefore, physical insight should be used to obtain reliable results. Fitting the end members of the system is usually simpler than dealing with the mixtures. Using just these parameters, disregarding some of the cation–cation hopping and overlap integrals, proved to be more accurate than employing pair potentials. However, the overall accuracy ($\sim$60% error) is too low to be used for *quantitative* predictions and a *full* fit should be performed.

The general accuracy of the tight–binding formalism can be improved by using a more complex distance dependence in the parametrization of the hopping and overlap terms. In all this chapter, we have just used the one–coefficient Harrison distance dependence. To deal with major distortions of the structures (with respect to the ones fit to) a more complex function should be used. This will result in a significant increase in the number of parameters to fit. In the CaO–MgO case, this produced a better description of the bands but only a marginal improvement in the formation energies. Total energies are *integrated* quantities that do not depend on the exact details of the bands. However, in cases such as the monoclinic ZrO_2 phase, using more parameters seems to be unavoidable.

Other improvements of the tight–binding formalism, such as the use of three–center integrals or a Hartree–Fock instead of a Hartree description of the electron–electron interactions, should also be considered.

The doped–zirconia results showed a significant variation of the ionic charges between and within different structures. The speed of the tight–binding formulation will let us, in the next chapter, perform large cell calculations to further understand this behavior.

Chapter 8

Charge transfer in oxides

Many *approximate* total–energy methods work with *point charges* instead of the full electronic density. Small changes in their values can have an important effect on the energy, in the scale we are interested in.

While in sophisticated quantum–mechanical techniques the electron density is computed by solving Schröedinger's equation self–consistently, a simple formulation to find the point charges within approximate methods is still lacking for oxides. Traditionally, the latter methods overcame this difficulty by simply assuming *fixed* charges for the ions, independently of their atomic environments. Unfortunately, as it was shown in this work, the above simplification can introduce large errors in the formation energy (see chapter 7).

In this chapter, we will describe how the ionic charge in an oxide changes with different atomic arrangements on a lattice. Using this information, simple rules to model the variation of the charge will be tested. We will perform these studies in calcia–doped zirconias. As shown in chapter 7, they exhibit a strong dependence of the ionic charge on the environment. The charges will be extracted from a self–consistent calculation in a large fluorite supercell. We chose this structure to maximize the number of different atomic neighborhoods in a single calculation.

In order to relate *point* charge models to actual self–consistent electronic densities, a procedure for extracting point charges from them should be defined. The electronic charge density is usually partitioned into domains of different shapes (e.g., spheres, polyhedra, etc.) and integrated within each of them to obtain the corresponding charges. This procedure is clearly not unique. However, if a *consistent* way of defining the charges is adopted, *differences* in charge transfer can be studied. Here, we will use either the muffin–tin approximation or the projection of the solid wave functions onto atomiclike basis functions to define the ionic charges as explained in the next sections.

In metallic alloys, point charges extracted from LDA calculations can be very well reproduced with a very simple analytic model [186, 187]. In this scheme, the charge on a given ion only depends on the *number of unlike* neighbors close to that ion. Here, we will explore if a similar set of rules can be applied to oxide systems, where large charge transfers and long–range interactions are present. This will involve the study of the relationship between the charge on a given site and the local environment

and Madelung field for that site. If successful, a simple formulation such as the one used in metallic alloys can considerably improve the performance of potential models, specially if they are used in conjunction with the compressible–ion model described in chapter 3 to account for the ionic breathing.

The self-consistent tight–binding method described in chapter 6 will be used to compute the charges. It is the only quantum–mechanical technique capable of handling, in a reasonable time, the large supercell calculation (more than 300 atoms) required in this study.[1] We already showed that this method accurately reproduced formation energies in doped zirconias. Since the accuracy of these predictions critically depends on the correct description of the ionic charge, it is reasonable to assume that the tight–binding model will also provide correct values for the charges.

We will start, in section 8.1, summarizing the results obtained for binary metallic alloys. Then, in section 8.2 we will use the self–consistent tight–binding formulation to study the variation of charge in oxides. Finally, in section 8.2.2, we will discuss our findings and evaluate the accuracy of simple point–charge models.

8.1 Simple charge model for metallic alloys

Mott suggested early on that the charge of an atom in a solid depends on the number of chemically similar atoms by which it is surrounded [232]. The charge is expected to have the smallest absolute value when all the neighbors of the ion are of its same species. The justification is that if the system is screened enough, an atom surrounded by like neighbors will not "know" that it is not part of a pure elemental solid but of an alloy and consequently, its charge will be close to zero.

The idea was used by Magri and collaborators to express the charge in a binary alloy as a *linear* function of the number of unlike atoms on the nearest neighbor shell [186]. This was later extended to any number of shells by Wolverton *et al.* [187]. They expressed the charge, q_i, at site i as,

$$q_i = \lambda_1 \sum_s \frac{\lambda_s}{\lambda_1} \sum_{k_s} [S_i - S_{k_s}], \tag{8.1}$$

where λ_s are constants and the first sum goes over the desired number of shells. S_i is 1(0) if an A(B) atom is located at site i and the last sum is over all sites in the shell s. Note that the latter sum counts the number of unlike neighbors in the s shell. A *generalized number of neighbors*, $\tilde{N}$ is defined so that q_i is proportional to it,

$$\tilde{N} = \sum_s \frac{\lambda_s}{\lambda_1} \sum_{k_s} [S_i - S_{k_s}]. \tag{8.2}$$

It was shown in reference [187] that the same λ_s are extracted from small– and large–

[1] Another option would be to perform *many* small cell calculations. Still, to have a similar number of different atomic neighborhoods to the one provided by a large supercell, a prohibitively large set of small structures should be used.

unit–cell (with a random distribution of the atoms) LDA calculations. This is a clear indication that similar mechanisms underlay the transfer of charge for both ordered and random alloys. These coefficients depend on the volume (and thus implicitly on the composition, for lattice mismatched alloys). See reference [187] for more details.

Expression 8.1 was tested in large supercell LDA calculations (256–432 atoms) for the $Cu_{1-x}Zn_x$ random alloy [187]. The total charge at site i was defined in terms of the muffin–tin approximation used in the evaluation of the Coulomb field,

$$q_i = 4\pi \int_0^{R^i_{MT}} \rho^i_{MT}(r) r^2 dr + \rho_0 \left[\omega_i - \frac{4\pi}{3}(R^i_{MT})^3\right] - Z_i, \tag{8.3}$$

where R^i_{MT} is the muffin–tin radius used for the atom at site i, ρ^i_{MT} is the spherically–symmetric electronic density within the muffin–tin sphere, ρ_0 is the constant electronic density in the interstitial, ω_i is the volume of the Wigner–Seitz cell surrounding each site, and Z_i is the nuclear charge.

The accuracy of equation 8.1 depends on the number of shells considered. Taking the first two (three) nearest neighbors shells was enough to reproduce the LDA results for a fcc (bcc) lattice very closely.

The supercell calculations also showed a remarkably linear relation between the charges associated with a given site and the long–range electrostatic potential at that site [233]. This behavior can be predicted from the simple charge model when enough neighboring shells are considered [187].

These results show that even for systems where small charge transfers are expected, the charges on different crystallographic sites will differ according to the atomic environment. In the next sections, we will study these mechanisms when *large* charge transfers are expected.

8.2 Charge transfer in oxides

The variation of the ionic charge in oxides within and along different structures was clearly demonstrated in calcia–doped zirconia (see section 7.2.2). Here, we will investigate if the simple model described in section 8.1 is still valid for this system, in spite of the fact that *large* charge differences are expected between dissimilar crystallographic sites.

Similar to what was described in section 8.1, we performed a large fluorite supercell calculation. The zirconia and calcium atoms were randomly distributed on the cation sublattice. Vacancies and oxygen atoms were randomly placed on the the anion sublattice. A similar number of calcium and zirconium ions was used. In this way, many different crystallographic sites and local environments could be sampled in a single calculation. The number of vacancies was selected to ensure charge neutrality when formal charges are assigned to the ions.

The point charge model, with two first neighboring shells, in equation 8.1 can be extended to this system in the following way,

$$
\begin{aligned}
q_i(\mathrm{Zr}) &= \lambda_1 N_{\mathrm{Ca}} + \lambda_2 N_{\mathrm{O}} + C_{\mathrm{Zr}}, \\
q_i(\mathrm{Ca}) &= -\lambda_1 N_{\mathrm{Zr}} + \lambda_3 N_{\mathrm{O}} + C_{\mathrm{Ca}}, \\
q_i(\mathrm{O}) &= -\lambda_2 N_{\mathrm{Zr}} - \lambda_3 N_{\mathrm{Ca}} + \lambda_4 N_{\mathrm{O}} + C_{\mathrm{O}},
\end{aligned} \tag{8.4}
$$

where λ_i and C_α are constants, and N_α is the number of α neighbors (α = Ca, Zr, or O). To preserve *charge neutrality* the coefficients C_α should be related by,

$$
x_{\mathrm{Zr}} C_{\mathrm{Zr}} + x_{\mathrm{Ca}} C_{\mathrm{Ca}} + x_{\mathrm{O}} C_{\mathrm{O}} = 0. \tag{8.5}
$$

Here, x_{Zr}, x_{Ca}, and x_{O} indicate the atomic fraction of zirconium, calcium, and oxygen ions respectively. Equations 8.4 can be written to include any number of shells.

Both a 3x3x3 (324 sites) and a 2x2x2 (96 sites) fluorite supercell were used in the study. If the charge on a given site is mostly determined by local effects the results should be similar in both cases.

The same tight–binding parameters as in section 7.2.2 were used in the calculations. For $\vec{k}$–space integrations, we tested both a 2x2x2 uniform grid and the Γ point in the 2x2x2 supercell calculation. The charges were already converged within 0.01 electrons in the latter case. Consequently, all the calculations were done with the Γ point.

The charge was defined (equation 6.26) as the projection of the electron wave function in the solid onto the basis orbitals. Note that it is the same charge used to compute the Madelung energy within the tight–binding model.

8.2.1 Charge transfer in calcia–doped zirconia

A generalized number of neighbors for each ion can be defined from equations 8.4,

$$
\begin{aligned}
q_i(\mathrm{Zr}) &= \lambda_1 \left(N_{\mathrm{Ca}} + \frac{\lambda_2}{\lambda_1} N_{\mathrm{O}} \right) + C_{\mathrm{Zr}} \\
&= \lambda_1 \tilde{N}^{Zr} + C_{\mathrm{Zr}}, \\
q_i(\mathrm{Ca}) &= -\lambda_1 \left(N_{\mathrm{Zr}} - \frac{\lambda_3}{\lambda_1} N_{\mathrm{O}} \right) + C_{\mathrm{Ca}} \\
&= -\lambda_1 \tilde{N}^{Ca} + C_{\mathrm{Ca}}, \\
q_i(\mathrm{O}) &= -\lambda_2 \left(N_{\mathrm{Zr}} + \frac{\lambda_3}{\lambda_2} N_{\mathrm{Ca}} - \frac{\lambda_4}{\lambda_2} N_{\mathrm{O}} \right) + C_{\mathrm{O}} \\
&= -\lambda_2 \tilde{N}^{O} + C_{\mathrm{O}}.
\end{aligned} \tag{8.6}
$$

The charges for the different ions can then be expressed as a function of these $\tilde{N}$.

If we do not enforce charge neutrality, each of the equations 8.6 can be fit *independently* providing the best *linear* match to the data set. The results are shown in figure 8-1 and 8-2 as a function of $\tilde{N}$ for two and four neighbor shells respectively (i.e., one cation and one anion shells in the first case, and two anion and two cation

shells in the second). Relation 8.6 predicts the straight line plot in the figures. Clearly, even by fitting the equations 8.6 independently, the dispersion in the values is very important. The variation is of the order of the change in the ionic charge reported in section 7.2.2. As we mentioned, this variation introduced large errors in the formation energies.

The fit λ parameters change from the 2x2x2 to the 3x3x3 fluorite supercell calculations, although the qualitative behavior shown in figures 8-2 and 8-1 is the same. For example, λ_4 changed from 0.18 ± 0.02 to 0.132 ± 0.007 from the smallest to the largest supercell. This is an indication that the effects that determine the charge are not entirely local or that the dependence on the local environment goes beyond simply counting the number of unlike neighbors.[2]

When the charge neutrality constraint is imposed, all the coefficients in equation 8.6 have to be determined simultaneously. The fit is clearly worse, as shown in figure 8-3.[3]

The dependence of the charge at a given site on the Coulomb potential at that site is shown in figure 8-4.

8.2.2 Discussion

The results of section 8.2.1 clearly show a strong dependence of the ionic charge on its environment. Differences of more than one electron occur in our supercells. Consequently, potential models that assume *fixed* charges are bound to fail since large errors in the Coulomb energy can be expected. The variation of charge with structure in zirconias has also been suggested by other experimental and theoretical work [141, 142].

The calcium ions are shown to be almost completely ionized, independently of the structure or the symmetry of the site that they occupy. This behavior was confirmed by the pseudopotential calculations. Electronic density plots with virtually zero electrons in the Ca ions, such us the one shown in figure 4-11, can be obtained for each of the S structures.

Unfortunately, figures 8-1 and 8-2 show that a simple description of the variation of the charge such as the one used in metallic alloys is not possible. The dispersion of the charges around a linear behavior on the number of unlike neighbors exceeds 0.4 electrons even when 4 shells of neighbors are accounted for. If the scheme were to be used to predict ionic charges within a total–energy model, large errors in the formation energies should be expected.

The charge shows a perfectly linear behavior with respect to the Coulomb potential for small values on the oxygen and zirconium ions. The calculations for the $Cu_{1-x}Zn_x$ random alloy, mentioned in section 8.1, also showed this behavior (only small charges

[2]One possible improvement is to look at the particular arrangements of the atoms around the site where the charge is computed.

[3]The predictions for the oxygen charges are closer to the actual values. This is just an artifact of the fitting process. There is more than twice the number of oxygen ions than the number of calcium or zirconium ions in the unit cell. Since equal weights were given to all data points, the oxygen data set was implicitly weighted more.

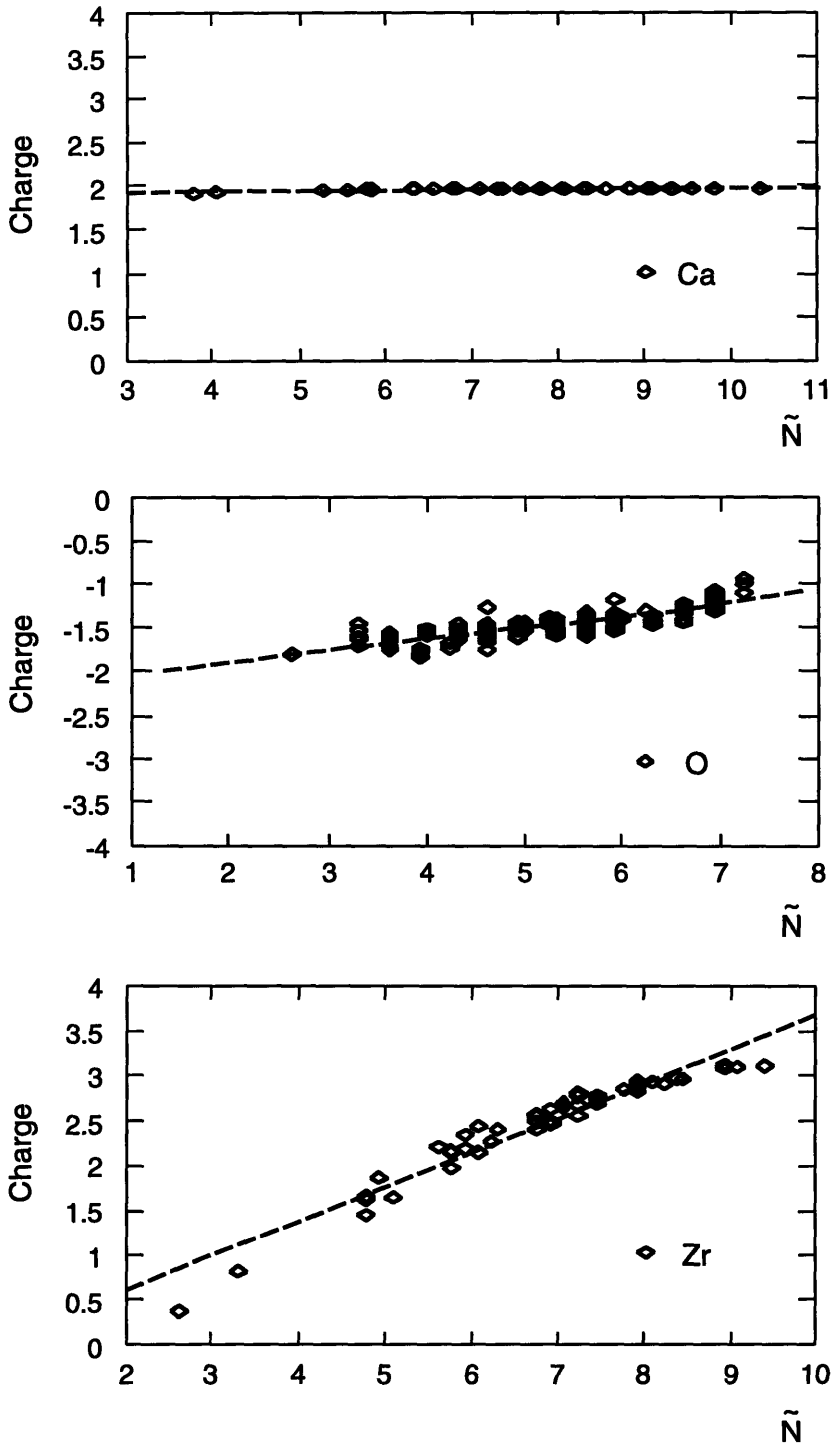

Figure 8-1: Charge (in electrons) versus generalized number of neighbors $\tilde{N}$. The straight line is the prediction of the charge model of equation 8.6 when two neighbor layers are included. The λ parameters were fit without imposing charge neutrality. The dots correspond to tight–binding large–supercell calculations.

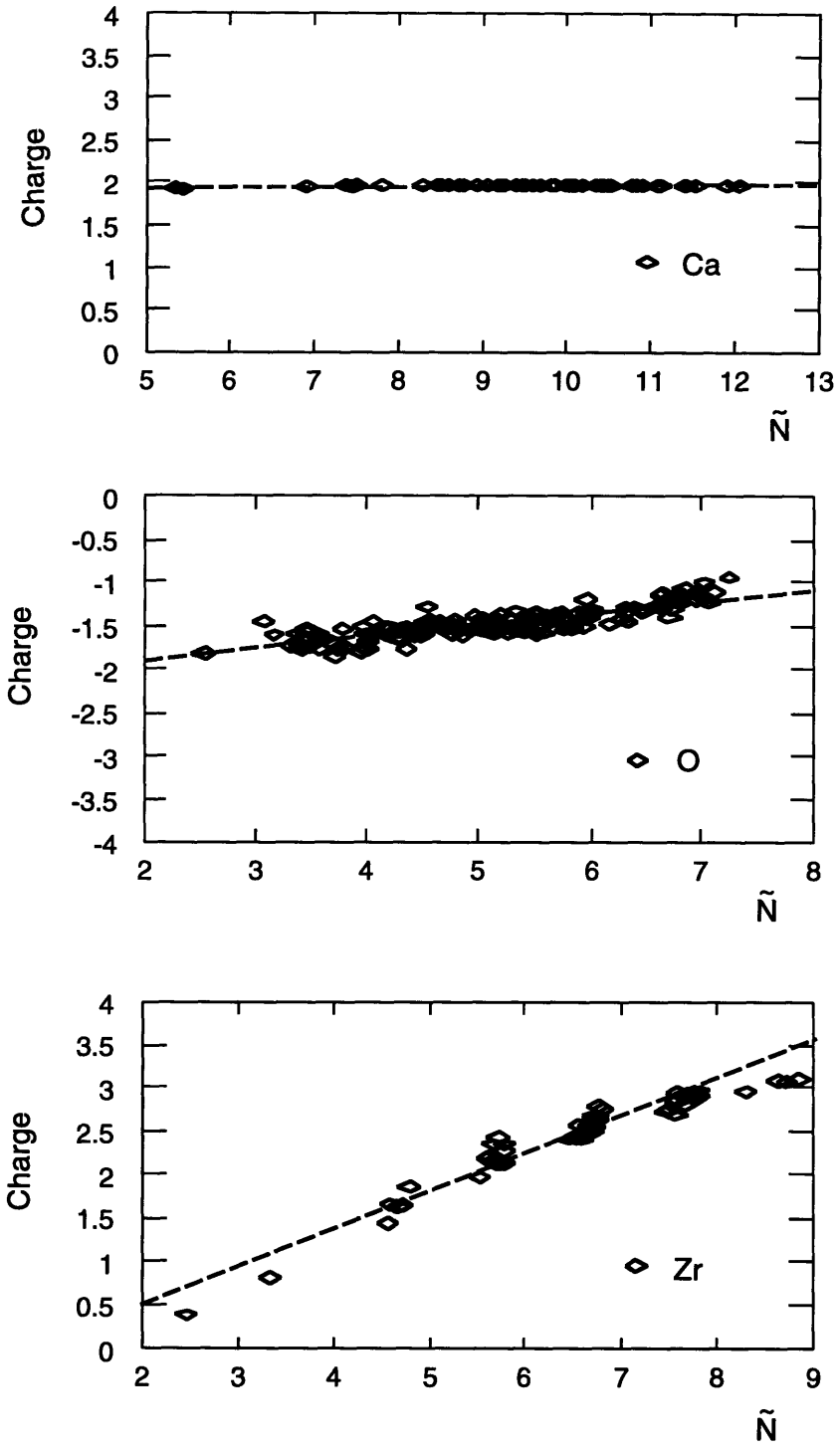

Figure 8-2: Charge (in electrons) versus generalized number of neighbors $\tilde{N}$. The straight line is the prediction of the charge model of equation 8.6 when four neighbor layers are included. The λ parameters were fit without imposing charge neutrality. The dots correspond to tight–binding large–supercell calculations.

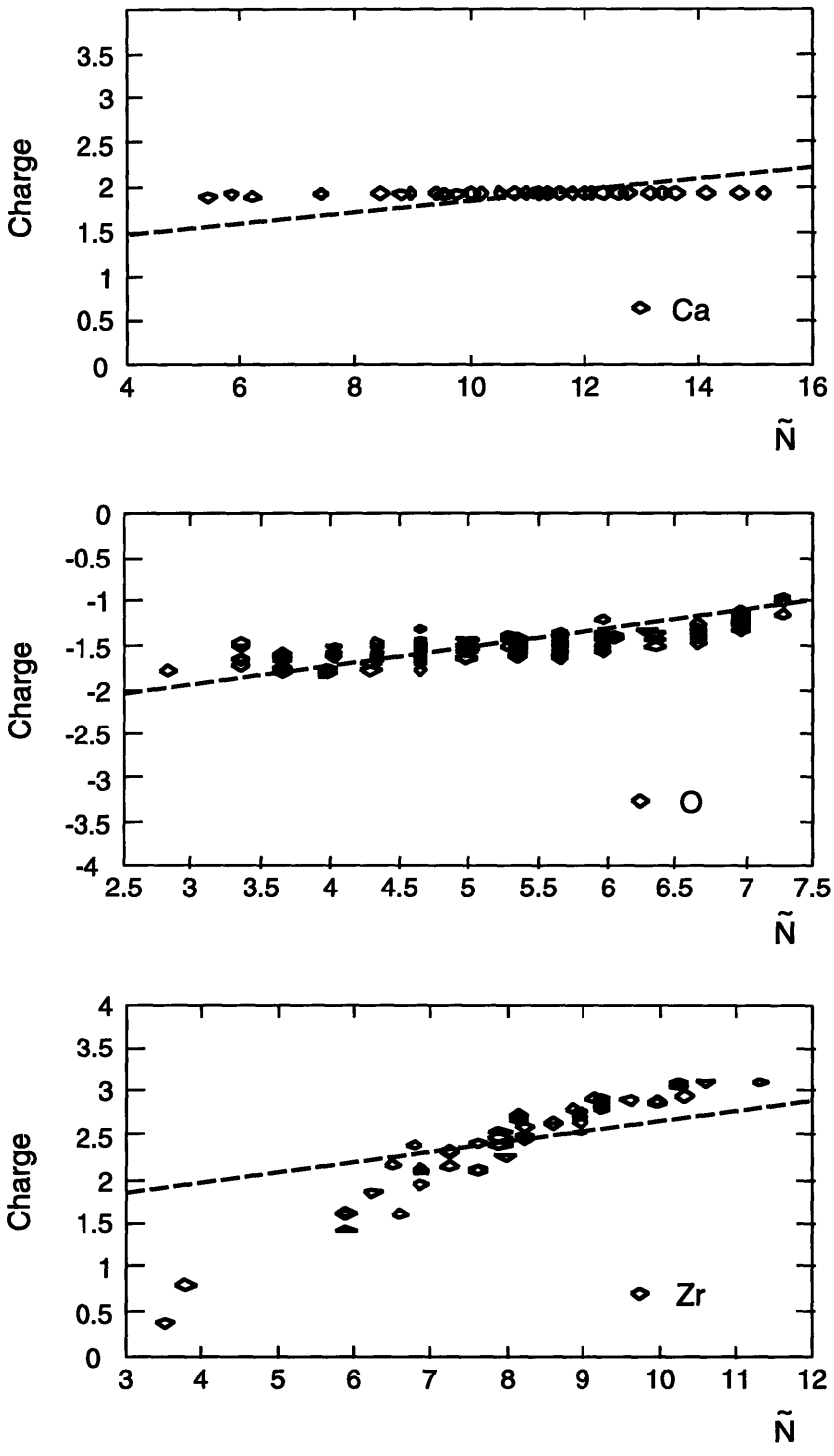

Figure 8-3: Charge (in electrons) versus generalized number of neighbors $\tilde{N}$. The straight line is the prediction of the charge model of equation 8.6 when two neighbor layers are included. The λ parameters were fit imposing charge neutrality. The dots correspond to tight–binding large–supercell calculations.

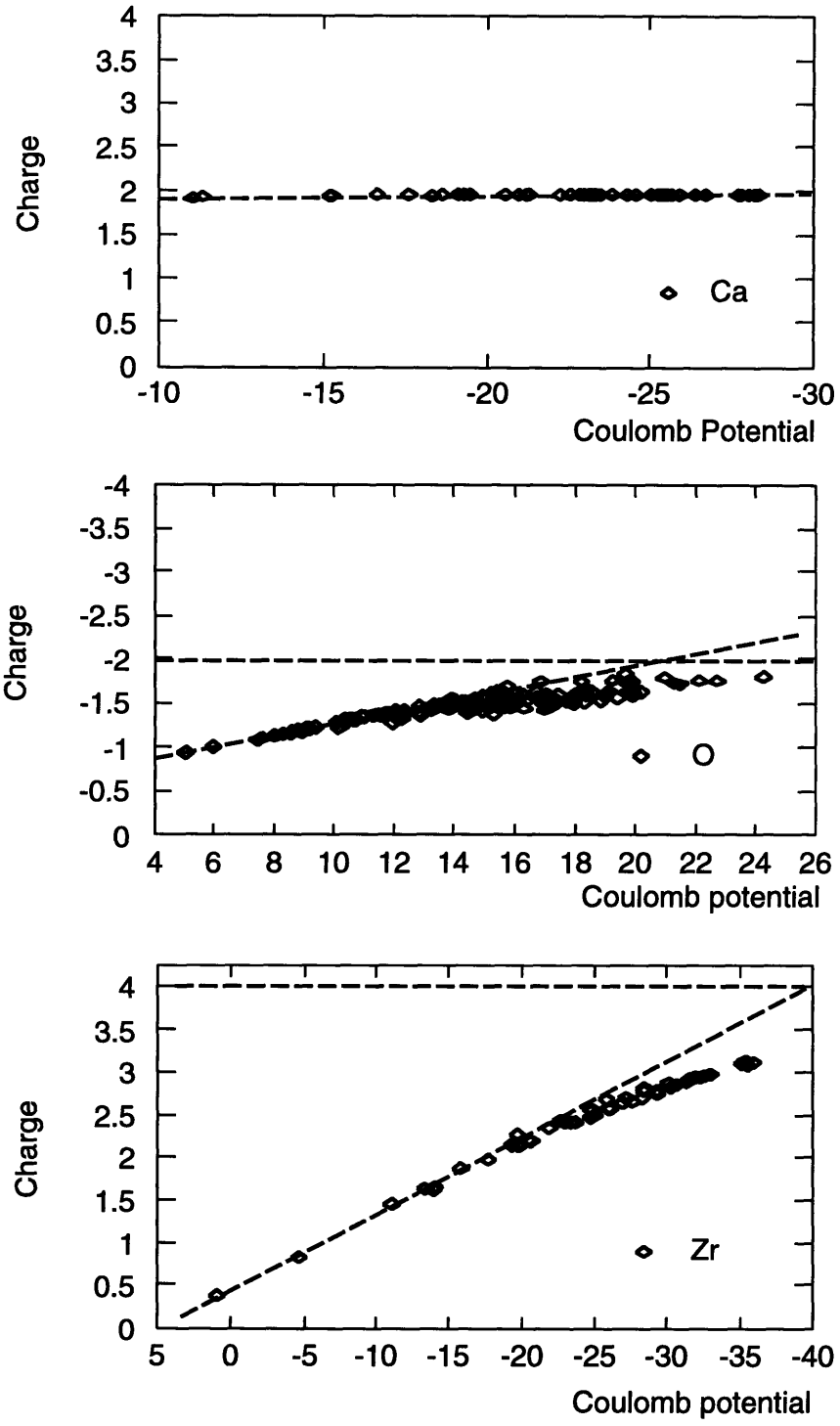

Figure 8-4: Charge (in electrons) at site i versus Coulomb potential at that site. The lines indicate the limiting behavior for small and large charge transfer.

were involved in these studies). For large fields, the charge levels off at the formal valence charge, i.e., +4 and −2 for Zr and O ions respectively. This is expected since those values correspond to electronic shell levels completely full or empty.[4]

Figure 8-4 also shows a much smaller dispersion of the ionic charge as a function of the Madelung field than as a function of $\tilde{N}$. There is almost a one–to–one correspondence between charge and Coulomb potential for the zirconium atoms. The same is true for oxygen up to an absolute charge of ∼1.4. For larger values, the dispersion starts increasing considerably. The second electron that is added to the oxygen atom is not stable if the ion is *isolated*. It is stabilized in the solid by the Madelung field. Consequently, we can expect that this loosely bounded electron will be more dependent on the particular local environment of the ions. We believe this effect is responsible for the increase in the dispersion of the values of the oxygen charges beyond the 1.4 electron absolute charge.

8.3 Conclusions

The self–consistent supercell calculations performed in this chapter clearly show the dependence of the charge of an ion on its environment. Our results indicate that the simple local rules used in metallic alloys to describe this dependence can not be *directly* applied to oxides. Even by considering four neighbor shells in the analysis, the dispersion in the predicted charges can introduce large errors if they are used to compute formation energies.

A combination of both a local and a long–range formulation may be necessary to properly describe charge variations in oxides. A more careful treatment of the local rules can also be implemented. As suggested in reference [186], the specific atomic arrangements around the ion, or nonlinear dependencies with the number of unlike neighbors can be considered.

An almost perfect one–to–one dependence between Coulomb potential and charge was found for the zirconium ions. For small charges, this relation is linear, in agreement with previous calculations in metallic alloys [233]. The same holds for the oxygen ions, though a wider dispersion in the values was found. We believe the latter effect is related to the instability of the O^{-2} ion. Calcium ions were fully ionized independently of the particular environments.

Apart from the simple point–charge model described in section 8.1, there is another non–self–consistent formalism in the literature (due to Streitz and Mintmire) that incorporates charge transfer effects. It was described in section 3.2 and is based only on the minimization of the electrostatic energy. While the point–charge model is fit to reproduce self–consistent LDA results, quantum–mechanical effects are absent in the Streitz–Mintmire approach. We have not tested this last scheme since our tight–binding formulation is more general and not much more complex to implement.

In summary, the relation between the charge of an ion and the arrangement of its

[4]The Coulomb potential would have to be increased (decreased) considerably more in order to start adding (removing) electrons to (from) the following (previous) electronic shell.

neighbor atoms can not be captured with simple local rules in oxides. The variation of the charge can be large and it is essential to incorporate these changes into any total–energy formalism. Compared to other models in the literature, the self–consistent tight–binding formalism offers the best alternative to account for these effects without using complex quantum–mechanical methods.

Chapter 9

Conclusions

The period of time we are now living will likely be recognized as the *Computer Age*. Although materials will probably no longer be used *directly* to name the ages of history, the innovations that a deeper knowledge of their properties bring, will certainly be. This shift from materials to applications is tied to the fact that we do not need to take the properties of materials as given but that we can shape them to our needs.

Actually, there is a fruitful relationship between materials and computers. Not only can more powerful computers be developed from a better control and understanding of materials properties, but also computer simulations can now help to design better materials. In this thesis, we focused on how to improve the computational techniques in order to make their predictions more reliable in oxides.

At the basis of most computational investigations lies a model to describe the energetics of the system since nearly all materials properties can be related to differences in total energies. Energy values can be determined from the solution of complex quantum–mechanical equations. In principle, the only input they require is the atomic numbers of the species that form the system to be studied. By coupling these methods to statistical–mechanical approaches, the thermodynamical properties of materials can be assessed. From these properties, essential information to process materials efficiently can be obtained.

The complexity of oxides has prevented the widespread use of state–of–the–art techniques to solve the quantum–mechanical equations. A tradition to use very simple total–energy models in these systems exists. One conclusion of this work is that these simple models do not incorporate all the relevant terms to accurately predict formation energies on the scale of thermodynamical effects (i.e., tens of meV/atom). For example, the CaO–MgO phase diagram we computed using pair–potential approaches agrees only *qualitatively* with the experimental observations. A miscibility gap with the correct asymmetry was predicted using these rudimentary models, but the solubility limits were considerably off.

On the other hand, we showed that very complex and computationally demanding methods, such as pseudopotentials or FLAPW can provide an accurate description of the energetics of oxides. We found very good agreement between their predictions and experiments whenever the local–density approximation to density–functional theory

was employed.

Still, the use of these sophisticated methods is limited to very simple cases. The computation of phase diagrams requires the determination of formation energies for many different mixtures of the end members. Some of these compounds, such as in doped zirconias, can have more than 60 atoms in a unit cell with very low symmetry. A few of these calculations can be performed with the help of supercomputers. However, the computational resources necessary to obtain all the essential energies to determine thermodynamical information are not currently available.

Even in 50 years, at the current rate of improvement in computer power, the computational simulation of many technologically relevant oxide systems will still be out of reach. Moreover, the study of surfaces or some macroscopic properties such as fracture opens a new dimension to the complexity of the problem. Unless a breakthrough is achieved in both the quantum– and statistical–mechanical models, simplifying assumptions will always have to be made in the foreseeable future.

The main conclusion of this work is that it is possible to compute formation energies in oxides very accurately without using sophisticated quantum–mechanical methods. They can be replaced by *simple* models where all the main contributions to the Hamiltonian are accounted for. However, approximations currently used in many energy techniques are not adequate to deal with the relevant effects in oxides. We showed that charge transfer mechanisms, oxygen breathing, and nonspherical relaxations of the electronic density have to be incorporated into the Hamiltonian in order to capture the essential physics of the problem.

As part of this thesis, we successfully integrated into a tight–binding formulation most of the effects mentioned above. The Hamiltonian of the model includes explicit parametrizations of these terms. The parameters are fit to the pseudopotential bands and equations of state of the end members of a specific system and one mixture of them. From this information, the formation energy of any other mixture can be computed with an accuracy comparable to the pseudopotential predictions but at a fraction of the time. Thus, the tight–binding method can be regarded as a very accurate *interpolation tool.* The predicted formation energies in the CaO–MgO and $CaO–ZrO_2$ system only differed 10% on average from the pseudopotential results.

Most of the novel terms in the tight–binding Hamiltonian depend on the charge of the ions, which is taken as variable within this model. This forces us to find the Hamiltonian eigenvalues and eigenvectors self–consistently. The procedure provides a very accurate way to treat charge transfer within highly ionic systems. We demonstrated that total energies can be considerably affected by charge transfer between the ions. The variation of the charge is easily described in metallic alloys in terms of local environments. Unfortunately, we showed that the same is not possible in oxides. Long–range interactions and local effects are needed. Tight binding was shown to be a very good option to deal with these effects.

The tight–binding formulation offers a full quantum–mechanical description of bonding and a natural way of incorporating charge transfer, oxygen breathing, and nonspherical relaxations. Even though some of these effects have recently been included within a potential or an embedded atom model, there was no simple integration of *all* of them into a single *approximate* approach. Furthermore, even if they are in-

corporated, they will still lack other quantum–mechanical effects that tight–binding provides (e.g., band effects).

The use of the tight–binding method to interpolate bands and compute total energies is not new. However, this is the first time that a *self–consistent* formulation has been used to predict formation energies in *multicomponent* oxide alloys. This approach proved to be not only fast, but very reliable.

Even when a good and fast description of the energetics of the system is provided, the evaluation of the thermodynamical properties is a very difficult task. To compute phase diagrams an effective lattice Hamiltonian is usually constructed. Monte Carlo simulations or the cluster variation method are then used to determine the phase boundaries. We showed the predictive power of this approach by computing the tight–binding CaO–MgO phase diagram. The agreement with experiments is very good. At low temperatures, equilibration times in Monte Carlo become unaffordably long and numerical instabilities can appear in the CVM. We developed a low–temperature expansion of the free energy that overcomes these difficulties. Its prediction can be smoothly joined with the other techniques at temperatures where the three approaches can be used.

As computers become more powerful and the simulation techniques more accurate, computational experiments will have a great impact in the development of novel materials. Although the scales of every day problems are still intractable in most cases, the insight computer simulations can provide is invaluable. Approximate methods, that correctly treat the relevant physical phenomena certainly extend the limits of what can be studied today.

Chapter 10

Future research

Computational experiments are a new and powerful tool in materials science and engineering. In this thesis, we have described how the combination of quantum– and statistical–mechanical techniques can be used to study phase stability in multicomponent oxides. For the predictions of the models to be more accurate, improvements in the methods are necessary.

The development of total–energy methods is a very active field of research. Work is being carried on both new and existent techniques. For example, the speed of the plane–wave approach was considerably increased by the use of ultrasoft pseudopotentials, which require a much smaller energy cutoff. Also, nonspherical relaxations of the electronic densities are being incorporated into the SSCAD model.

Novel formulations are focusing on both the speed and the accuracy of the models. Most of the calculations in this thesis have been done within the local–density approximation to density–functional theory. LDA is known to be overbinding in solids, leading to an underprediction of lattice constants (typically 1% to 2%) [97]. Errors as large as 20% are also common for elastic constants. The generalized–gradient approximation (see section 3.3.1) was proposed as a way to go beyond LDA, and is constantly being improved (see for example [234]). It tends to provide better structural energy differences but it sometimes overestimates lattice constants [235, 236]. For systems with strong Coulomb correlations, such as Mott insulators, the LDA was recently combined with a Hubbard–type model. This is the so–called LDA+U approach [237]. The LDA+U method has successfully been applied to transition–metal oxides. See reference [238] for a review of the method and its applications.

The accuracy of the calculations is not the only factor to be considered. The speed of the total–energy methods is crucial to compute the formation energies needed as input to phase diagram calculations. Massively parallel computers have started to be used. Most methods are being adapted to exploit the advantages of these computers. As mentioned in chapter 3, some techniques are also being reformulated so that they scale linearly with the number of atoms in the unit cell.

To speed up the calculations, new basis sets that provide a description of a function with spatially variable resolution have been introduced. This is ideal for oxides, since oxygen atoms have strongly peaked orbitals. In some cases, the simplicity of the plane–wave basis set is retained while generalizing it to a non–Euclidean curvi-

linear space to reduce the size of the set [157]. In other cases, the multiresolution properties of wavelets are combined with the smooth interpolation characteristics of finite element methods [158].

More accurate semiempirical approaches for oxides are also being investigated. Recently, a charge transfer scheme and a compressible ion model which includes both dipole and quadrupolar polarizability were introduced [75, 88, 89]. However, a way of integrating *all* these effects into a potential model is still lacking. On the other hand, we demonstrated that a self–consistent tight–binding formulation can easily incorporate these contributions.

A critical step in the formulation of the tight–binding Hamiltonian is the determination of an adequate set of parameters for a given system. It would be interesting to study alternative ways to perform the fitting process. One possibility is to use different atomic displacements that would independently sample different regions of the optimization space. This will also provide a more reliable determination of the distance dependence of the parametrizations. At the same time, forces can be computed and fit to. A good description of the forces is essential if vibrational ECI's will be computed.

The tight–binding Hamiltonian used in this work can be improved in many ways. Both the inter– and intra–atomic interaction can be treated more accurately. For example, a Hartree–Fock instead of a Hartree formulation can be implemented. This will be important to treat transition–metal oxides. Also, a more accurate distance dependence in the parametrizations of the hopping and overlap integrals can be used.

The computation of alloy phase diagrams needs not only a fast and accurate description of the energetics of the system but also a methodology to account for all the important contributions to the free energy. We described how the Ising lattice model can be used to accommodate both substitutional and nonsubstitutional degrees of freedom. For the latter, a coarse–graining of the alloy Hamiltonian was done. Recently, a formalism to include lattice vibrations within this model Hamiltonian in the harmonic approximation was proposed [34]. A way to accurately deal with anharmonic effects is still lacking. Electronic excitations can also be included [37].

The thermodynamic properties of *binary* alloys have been explored in many systems. However, most technologically important oxides are *multicomponent* alloys. In the CaO–MgO system, the anion sublattice is fully occupied. This allowed us to treat this problem as a binary ordering on the cation sublattice. However, in the CaO–ZrO_2 system the anion lattice accommodates not only oxygen ions but also vacancies. (The vacancies are introduced to compensate for the difference in charge between the Zr and Ca ions.) A coupled–sublattice cluster expansion is required here. It would be very interesting to use this approach, in combination with our tight–binding Hamiltonian, to compute the CaO–ZrO_2 phase diagram. The available experimental phase diagram is incomplete. There are doubts about many of its regions due to kinetic effects, the presence of defects and impurities, or just because the measurements are difficult at extreme temperatures.

If more than one type of cation dopant is added to zirconia, the system can no longer be treated as two binary problems. A ternary model seems unavoidable, and much more effort needs to be spent. It will certainly be worth developing new

approximate models to deal with the complexity of these systems.

We have investigated techniques to determine the solid portion of a phase diagram. In order to compute the full stability map, the liquid phase has to be accounted for. An accurate atomistic model for the thermodynamics of liquids is needed.

In this thesis, we have mainly been concerned with *equilibrium* properties and perfect crystalline systems. Although a great wealth of information can be obtained from these studies, *real* materials are affected by kinetic processes, grain boundaries, and other defects. The modeling of kinetic processes in oxides is very complex. It would be very interesting to apply the tight–binding approach developed in this thesis in conjunction with molecular–dynamics methods and lattice models (see for example reference [46]) to study this problem. Parallel supercomputer technology is starting to allow *ab initio* calculations on systems big enough to explore the interactions among dislocations [239]. Furthermore, combinations of first–principles approaches and simple energy models can be used to build a bridge between the different length scales of the problem.

It should be clear by now that the modeling of materials requires a combination of both sophisticated quantum–mechanical methods and simple energy models with dynamical and statistical–mechanical approaches. There is still plenty of room for improvements in all these fields. As computers become more powerful, and the methods more sophisticated the dream of designing *real* materials from first principles is turning into a *reality.*

Appendix A

Additional results for the CaO–MgO system

A.1 Introduction

In this appendix, we provide the computed formation energies for different structures in the CaO–MgO system. These values were used to fit the ECI's shown in figures 5-2 and 7-2.

A derivation of the potential used in section 5.3.3 will also be described.

A.2 Formation energies

In table A.1, we show the formation energies computed using the SSCAD, the potential in section 5.3.3, and the self–consistent tight–binding method for the CaO–MgO system.

A.3 Pair–potential model for CaO–MgO

In section 5.3.3, we used the following form for the short–range repulsive interaction in the CaO–MgO system,

$$V(r_{ij}) = \frac{A_{ij}}{r_{ij}^5}. \tag{A.1}$$

It can be directly derived from the tight–binding Hamiltonian in equation 6.23 if we assume that there is no *softening* of the ions.

The *softening of the ions* is the reduction, in absolute value, of the cation and anion charges. It is proportional to:

$$\left(\frac{H_{ij}}{H_{ii} - H_{jj}}\right)^2, \tag{A.2}$$

where H_{ij} is the hopping matrix element between the ions (i and j) that are reducing

Structure	Concentration	SSCAD	Pair Potential	Tight–Binding
Rocksalt	CaO	0.000	0.000	0.000
Rocksalt	MgO	0.000	0.000	0.000
$L1_0$	$MgCaO_2$	0.125	0.147	0.141
$L1_2$	$MgCa_3O_4$	0.085	0.100	0.098
$L1_2$	Mg_3CaO_4	0.104	0.121	0.116
A_2B_2	$MgCaO_2$	0.074	0.066	0.093
$L1_1$	$MgCaO_2$	0.075	0.090	0.094
$MoPt_2$	$MgCa_2O_3$	0.070	0.077	0.087
$MoPt_2$	Mg_2CaO_3	0.072	0.072	0.090
A_5B	$MgCa_5O_6$	0.040	0.044	0.053
A_5B	Mg_5CaO_6	0.046	0.046	0.059
Ni_4Mo	$MgCa_4O_5$	0.046	0.047	0.058
Ni_4Mo	Mg_4CaO_5	0.054	0.053	0.068
Pt_8Ti	$MgCa_8O_9$	0.032	0.034	0.038
Pt_8Ti	Mg_8CaO_9	0.041	0.043	0.048
A_4B_2	$MgCa_2O_3$	0.065	0.070	0.087
A_4B_2	Mg_2CaO_3	0.069	0.070	0.090
Do_{22}	$MgCa_3O_4$	0.060	0.060	0.074
Do_{22}	Mg_3CaO_4	0.078	0.083	0.092
S2x2x2	$MgCa_{31}O_{32}$	0.008	0.009	0.010
S2x2x2	$Mg_{31}CaO_{32}$	0.011	0.011	0.013

Table A.1: Formation energies (meV/atom) of different ordered structures in the CaO–MgO system obtained by using the SSCAD, the pair–potential in section 5.3.3, and the self–consistent tight–binding methods. All the structures were fully relaxed. A description of the structures can be found in references [45] or [66]. The S2x2x2 corresponds to the 2x2x2 supercell used in reference [84].

their charge. See reference [130] for more details.

If we assume formal values for the charges, the calcium and magnesium s orbitals have a higher energy than the oxygen p orbitals within the tight–binding model. Consequently, if all the nondiagonal terms H_{ij} are set close to zero ("hard" ions), the ionic charges will stay at those formal values. No self–consistency is needed. The Hamiltonian matrix is basically diagonal and an expression for the total energy ($E(n(\vec{r}))$) can be written directly as the sum of the Hamiltonian eigenvalues (E_{bs}) plus the Madelung energy and the corrections for the double–counting of the electron–electron interaction ($F(n(\vec{r}))$),

$$E(n(\vec{r})) = E_{bs} + F(n(\vec{r})). \tag{A.3}$$

Apart from the Coulomb terms, only $\mathcal{F}_{i\alpha}$ in E_{bs} (see equation 6.24) depends on the ionic distances. As we already mentioned, $\mathcal{F}_{i\alpha}$ is a repulsive contribution that comes from the overlap of the nonorthogonal basis. For sp–bonded materials, its distance dependence can be computed from Harrison's work (table 6.1) and the use of Hückel's theory as explained in reference [192]. The result is the $\frac{1}{d^5}$ dependence in equation A.1.

The A_{ij} values were fit to the pseudopotential lattice constant of CaO and MgO, and the formation energy and lattice constant of $CaMgO_2$ ($L1_0$ structure).

Appendix B

$\vec{k}$–space integration

B.1 Introduction

Most solid–state total–energy methods require the evaluation of integrals of periodic functions in $\vec{k}$ space to compute quantities such as the electronic density or single–particle energy sums. Since the calculation time scales linearly with the number of $\vec{k}$ points, the smallest possible number of them should be used.

Many systematic ways have been proposed to choose small sets of $\vec{k}$ points that are normally called *special points*. Usually they provide a more accurate integration, with a smaller number of points, than the ordinary tetrahedron–integration method [240].[1] Here, we will briefly review the most popular ways of choosing the special $\vec{k}$ points.

B.2 Special $\vec{k}$ points

B.2.1 Uniform mesh

A uniform grid is used in $\vec{k}$ space. The accuracy of the integrations can be improved by increasing the number of grid points. The symmetry of the crystal may be employed to eliminate those points that are equivalent. When this is done, the "weight" of the remaining $\vec{k}$ vectors has to be adjusted. (The origin of the mesh can be shifted to optimize the use of symmetry.)

B.2.2 The Chadi–Cohen scheme

The $\vec{k}$ points are chosen so that the integrals are computed exactly for those functions that contain up to a certain Fourier component. By increasing this component, a hierarchy of points can be obtained.

The point–group symmetry of the crystal is normally used to reduce the number of $\vec{k}$ points to the irreducible part of the Brillouin zone. See reference [242] for more

[1] For a comparison between the tetrahedron and the special–points integration methods see reference [241].

details.

B.2.3 The Monkhorst-Pack scheme

The method is similar in spirit to the Chadi–Cohen scheme. Again, the $\vec{k}$ points are chosen so that the integrals are computed exactly for those functions that contain up to a certain Fourier component. However, they differ on how to actually pick these points. Furthermore, a different number of special points and order of the terms canceled in the Fourier expansion is predicted. A comparison between the Chadi–Cohen and the Monkhorst-Pack scheme can be found in references [243, 244]. See reference [245] for more details.

This method was later generalized by Froyen [246].

B.3 Superstructures and "equivalent" $\vec{k}$ points

In many applications, such as the computation of formation energies or forces, it is necessary to compare results for supercells of different geometry. In order to minimize systematic errors in the evaluation of Brillouin–zone integrals, it is convenient to use an *equivalent* set of $\vec{k}$ points. By *equivalent*, we mean using the *same* points in reciprocal space.

The equivalent points can be obtained from any set of points, such as the ones in section B.2. The procedure consists in expanding all the $\vec{k}$ points used for the parent lattice by means of the symmetry of that lattice. Once all the equivalent points are identified in the first Brillouin zone, the symmetry of the supercell can be used to keep the independent ones (the weights have to be adjusted).

B.4 Brillouin–zone integrations in metals

The functions to be integrated in metals are discontinuous due to the partial filling of the energy bands. While the integrals of infinitely differentiable functions, such as the ones obtained in insulators, converge exponentially with the spacing of the grid, discontinuous functions have a very low convergence. In order to be able to perform Brillouin–zone integrations in metals with high precision but without a prohibitively large set of $\vec{k}$ points, different methods have been proposed (see reference [227] and references therein).

In one of these methods, the convergence is improved by a *smearing* of the values at each $\vec{k}$ point into Gaussians. In this way, an exponential convergence with respect to the grid spacing is recovered. However, there is no guarantee that the integral will converged to the *correct* value.

Methfessel and Paxton showed that, with a more careful choice of the broadening function, an independent control of both the $\vec{k}$ convergence (i.e., number of points) and the integral value convergence can be achieved. Thus, an exponential convergence with the number of sampling points is recovered, but without a loss in accuracy. A

hierarchy of smooth approximations to the step and δ functions was developed. See reference [227] for more details.

Appendix C

The design of lithium batteries

C.1 Introduction

The objective of this appendix is to illustrate a different application of total–energy methods. The pseudopotential formation energies will be directly linked to the voltage of a battery. *Ab initio* calculations allow the systematic investigation of the effects of chemistry and structure on the voltage. This is an excellent example of a case where *computer experiments* can help to develop materials with properties tailored to specific needs.

The voltage is one of the most important parameters when designing a battery. We will only give a brief introduction to this problem by focusing on the computation of the average voltage of lithium–transition–metal batteries. A much broader perspective and interpretation of the results can be found in references [247, 248, 249, 250].

Figure C-1 illustrates how a lithium battery works. During discharge, Li^+ ions are transferred from the anode to the cathode through the electrolyte. The charge of Li^+ is compensated in the cathode by absorbing an electron from the external circuit. By applying an external voltage the process can be reversed.[1]

The anode is usually a solution of lithium in carbon. However, for simplicity, we will assume a pure metallic lithium anode. Although different materials can be used as cathodes, we will investigate the lithium–transition–metal oxides (Li_xMO_2, where M=Ti, V, Mn, Co, Ni, Cu, or Zn).[2] Depending on the structure, the ratio of lithium to metal ions, x, can be varied between 0 and 1.

For the discharge process to proceed, the following reaction should be thermodynamically favored,

$$MO_2 + Li \longrightarrow LiMO_2. \tag{C.1}$$

Using thermodynamical arguments, it is possible to compute the **voltage** of the cell from the lithium chemical potential (μ_{Li}) on both sides of expression C.1. In general, the battery is discharged between $Li_{x_1}MO_2$ and $Li_{x_2}MO_2$. The battery voltage, V, is

[1] This is assuming that lithium can be reversibly cycled in and out of the cathode without major structural changes.

[2] Composite materials are actually used. The transition metals are combined with carbon to provide a conducting medium for the electrons.

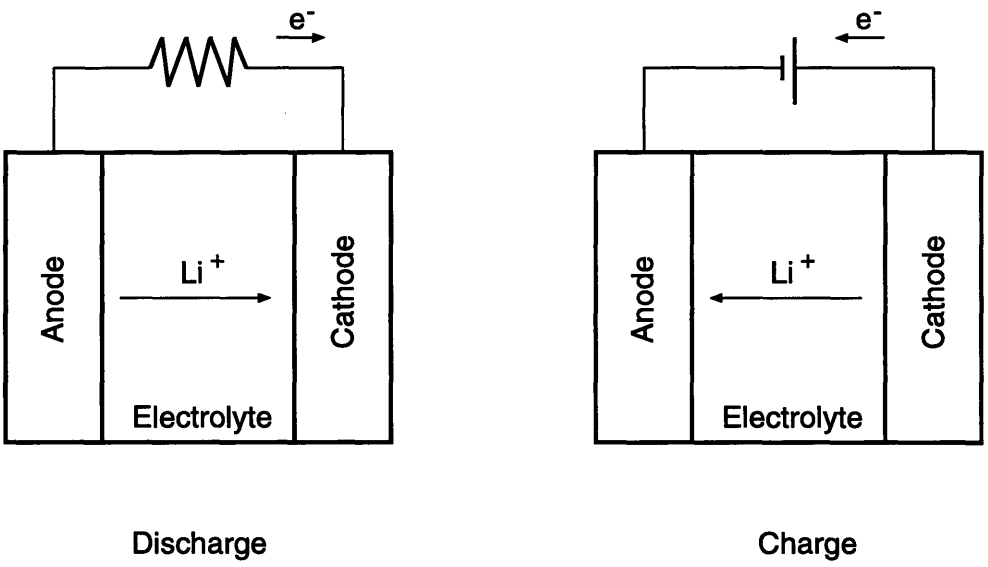

Figure C-1: Charge and discharge cycle for a lithium battery.

related to the lithium content, x, in Li_xMO_2 as [251]

$$V(x) = -\frac{\mu_{Li(x)}^{cathode} - \mu_{Li}^{anode}}{ZF}. \tag{C.2}$$

Z is the number of electrons in the external circuit for each Li ion (in our case $Z = 1$), and F is the Faraday constant.

The **average** voltage of the battery (between $x = 0$ and $x = 1$), $\langle V \rangle$, depends on the formation energy of $LiMO_2$. This can be shown by writing the total electrical energy of the battery as

$$\langle V \rangle e = e\int_0^1 V(x)dx = -e\int_0^1 \frac{\mu_{Li(x)}^{cathode} - \mu_{Li}^{anode}}{F}dx = -\frac{\Delta G}{F}e. \tag{C.3}$$

Here, ΔG is the Gibbs free energy difference (per mole) of reaction C.1 and is computed as

$$\Delta G = \Delta E + P\Delta V - T\Delta S. \tag{C.4}$$

The last two terms on the right–hand side of equation C.4 are very small compared to ΔE, which is approximated by its value at 0 °K.[3] (P, V, T, and S are the pressure, volume, temperature, and entropy respectively.) Finally,

$$\langle V \rangle = \frac{\Delta E}{F}. \tag{C.5}$$

[3]The term $P\Delta V$ is $\sim 10^{-5}$ eV, $T\Delta S$ is $\sim 10^{-2}$ eV, and ΔE is ~3–4 eV.

	Valence electron configuration	rc_s (Å)	rc_p (Å)	rc_d (Å)
Li	$2s^{0.9}2p^{0.1}$	1.16	1.16	–
Ti	$4s^{1.9}4p^{0.1}3d^{2.0}$	1.34	1.56	1.03
V	$4s^{1.9}4p^{0.1}3d^{3.0}$	1.34	1.56	1.03
Mn	$4s^{0.75}4p^{0.25}3d^{5.0}$	1.05	1.12	1.03
Co	$s^{0.75}4p^{0.25}3d^{7.0}$	1.00	1.05	1.05
Ni	$s^{0.75}4p^{0.25}3d^{8.0}$	1.11	1.16	1.05
Cu	$s^{0.5}4p^{0.25}3d^{9.25}$	1.05	1.21	1.00
Zn	$s^{0.75}4p^{0.25}3d^{10.0}$	1.21	1.32	0.96
S	$s^{1.95}3p^{4.05}$	0.95	0.95	–
Se	$s^{1.5}4p^{3.25}4d^{0.25}$	1.00	1.00	1.00

Table C.1: Valence electron configuration and core radii (rc_l) used to generate the pseudopotentials (l= s, p, d).

We would like to stress the importance of equation C.5 since it directly relates the average voltage of the battery to the formation energy of $LiMO_2$. This voltage can be simply determined by computing the total energy of $LiMO_2$, MO_2, and Li. Thus, *ab initio* approaches are particularly suited to design new cathode materials since the voltages can easily be computed. Furthermore, the effects of metal chemistry and structure on $\langle V \rangle$ can be studied independently, without being constrained to those combinations that can be actually synthesized.

We will perform two different computational experiments: We will fix the structure and change the metal or anion chemistry, and we will change the structure while keeping the identity of the elements in the cathode. For the first type of experiments, we chose to use the structure of the commercially employed $LiCoO_2$ [252]. This is the α–$NaFeO_2$ arrangement. The same structure corresponds to $LiVO_2$ [253].

C.2 Pseudopotential studies of the battery voltage

C.2.1 Pseudopotential generation

Nonlocal, optimized, Kleinman–Bylander type pseudopotentials were used. The s angular component was taken as the local potential. The atomic configurations and core radii used in the generation are shown in table C.1. There is a considerable overlap between the lithium $2s$ and $1s$ orbitals. Core corrections are needed to accurately treat the bcc lithium metal. However, they are not expected to be important in the Li^+ ion. Consequently, they will only affect the pure lithium energy, shifting all the formation energies by a fixed amount. For simplicity, we will not include these corrections here since we are primarily interested in computing the *differences* in voltages

	Ti	V	Mn	Co	Ni	Cu	Zn
Voltage	2.14	2.81 (3.1)[a]	3.13	3.75 (4.1)[b]	2.92 (3.8)[c]	3.66	4.41

Table C.2: Average voltage (in volts) computed for the $LiMO_2$ compound in the α–$NaFeO_2$ structure. The values in parenthesis are experimental. The agreement is good. The large discrepancy in the nickel case is due to the fact that the structure is unstable with respect to a Jahn–Teller distortion (not taken into account in the calculations).

[a]Experimental averaged voltage computed from reference [254]. The error in the value ~0.1 V.
[b]Experimental averaged voltage computed from reference [255]. The error in the value ~0.1 V.
[c]Experimental averaged voltage computed from reference [256]. The error in the value ~0.1 V.

	O	S	Se
Voltage	3.75	2.14	1.46

Table C.3: Average voltage (volts) for $LiCoX_2$ compounds in the α–$NaFeO_2$ structure.

between different structures and chemistries.[4]

C.2.2 Results

A 900 eV energy cutoff was used in all the calculations. The $\vec{k}$ points were chosen using the Monkhorst–Pack scheme [245]. Convergence within tens of meV in the formation energies was obtained.

In table C.2, we show the average voltages computed for different transition metals in the α–$NaFeO_2$ structure.

The voltages obtained for different anion species, X, in $LiCoX_2$ (α–$NaFeO_2$ structure) are shown in table C.3. Finally, in table C.4, we show the average voltage for $LiCoO_2$ in two different structures: α–$NaFeO_2$ (structure # 1) and a variant of this one with Pearson symbol tI16 [257] (structure # 2).[5]

C.2.3 Discussion

Table C.2 indicates that there is a strong tendency for the voltage to increase with the nuclear charge. As explained in references [249, 250], this can be qualitatively understood from the fact that the electron coming from Li populate band levels

[4]By comparing to FLAPW results we showed the effect of core corrections in the overall voltage to be small (less than 0.1 eV) [250].
[5]Here, the Co and Li ions are intermixed in the cation layers.

	structure #1	structure #2
Voltage (relaxed)	3.75	3.26
Voltage (unrelaxed)	4.22	4.14

Table C.4: Average voltage (volts) for $LiCoO_2$ compound for two different structures. For the unrelaxed case, the ideal rocksalt positions were taken.

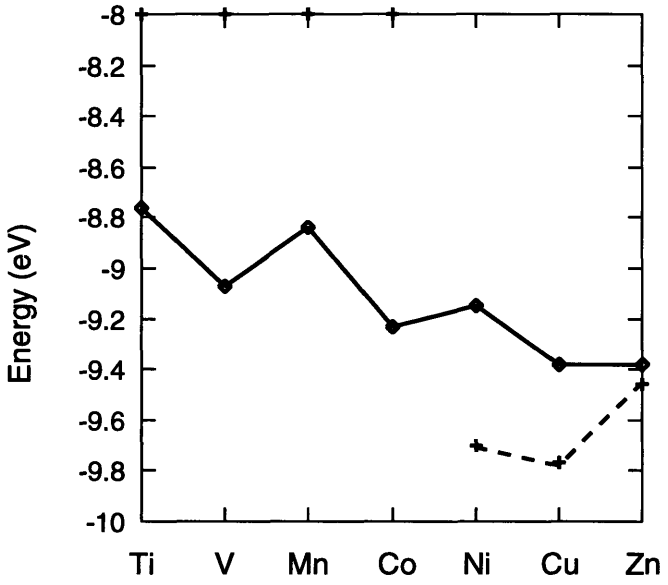

Figure C-2: Fermi energy of different $LiMO_2$ compounds in the α–$NaFeO_2$ structure (solid line). With Ni, a new band starts to be filled, producing a jump in the voltage. The highest energy point of the band that was just completely filled in Co is also shown (dashed line).

that are systematically shifted down by the increase in the nuclear charge. This is illustrated in figure C-2, where we show the decrease in Fermi energy when the nuclear charge increases. Consequently, the electron coming from the external circuit is placed at a lower energy in the transition–metal oxide, effectively raising the voltage. Note that the jump in the nickel voltage is due to the fact that the Li electron has to start populating a new band at a higher energy.

The effect of structural changes is small for the two arrangements we studied. However, the effects of relaxations are significant. They can introduce voltage changes of the order of 0.5 volts. Even more important is the effect of replacing the anion, that can change $\langle V \rangle$ by more than 2 volts.

The predicted voltages are in good agreement with the measured values whenever they can be compared. This shows the predictive power of the pseudopotential method. The advantage of performing computational experiments to determine the

voltage is clear. There is no need to synthesize new compounds. Many different possibilities can be tested without a costly and laborious processing. At the same time, the *ab initio* approach gave insight on the mechanisms that lead to the determination of voltages, which in turn provides guidance to choose new compounds.

Bibliography

[1] J. Read. *Prelude to Chemistry: An Outline of Alchemy.* The M.I.T. Press, Cambridge, 1966.

[2] B. J. Teeter Dobbs. *The Foundations of Newton's Alchemy or "The Hunting of the Greene Lyon".* Cambridge University Press, Cambridge, 1975.

[3] B. J. Teeter Dobbs. *The Janus faces of genius.* Cambridge University Press, Cambridge, 1991.

[4] M. Kranzberg and C. Stanley Smith. Materials in history and society. In M. Cohen, editor, *Materials Science and Engineering: Its Evolution, Practice and Prospects*, pages 1–39, Lausanne, 1978. Elsevier.

[5] M. L. Cohen. Predicting useful materials. *Science*, 261:307–308, 1993.

[6] G. C. Fox and P. D. Coddington. An overview of high performance computing for the physical sciences. In D. A. Browne, J. Callaway, J. P. Draayer, R. W. Haymaker, R. K. Kalia, J. E. Tohline, and P. Vashishta, editors, *High performance computing and its applications in the physical sciences : proceedings of the Mardi Gras '93 conference, February 18–20, 1993, Louisiana State University*, pages 1–21, Singapore, 1994. World Scientific.

[7] R. W. Siegel. Creating nanophase materials. *Scientific American*, 275:74–79, 1996.

[8] F. F. Abraham, D. Brodbeck, R. A. Rafey, and W. E. Rudge. Instability dynamics of fracture: A computer simulation investigation. *Physical Review Letters*, 73:272–275, 1994.

[9] J. M. Sanchez, F. Ducastelle, and D. Gratias. Generalized cluster description of multicomponent systems. *Physica*, 128A:334–50, 1984.

[10] J. W. D. Connolly and A. R. Williams. Density–functional theory applied to phase transformations in transition–metal alloys. *Physical Review B*, 27:5169–5172, 1983.

[11] Z. W. Lu, S. H. Wei, A. Zunger, S. Frota-Pessoa, and L. G. Ferreira. First–principles statistical mechanics of structural stability of intermetalic compounds. *Physical Review B*, 44:512–544, 1991.

[12] G. D. Garbulsky and G. Ceder. Linear–programming method for obtaining effective cluster interactions in alloys from total–energy calculations: Application to the fcc Pd–V system. *Physical Review B*, 51:67–72, 1995.

[13] R. Kikuchi. A theory of cooperative phenomena. *Physical Review*, 81:988–1003, 1951.

[14] K. Binder and D. W. Heermann. *Monte Carlo simulation in statistical physics.* Springer–Verlag, Berlin, 1988.

[15] P. Hohenberg and W. Kohn. Inhomogeneous electron gas. *Physical Review*, 136:864–871, 1964.

[16] W. Kohn and L. J. Sham. Self–consistent equations including exchange and correlation effects. *Physical Review*, 140:1133–1138, 1965.

[17] D. C. Langreth and M. J. Mehl. Beyond the local–density approximation in calculations of ground–state electronic properties. *Physical Review B*, 28:1809–1834, 1983.

[18] A. D. Becke. Density–functional exchange–energy approximation with correct asymptotic behavior. *Physical Review A*, 38:3098–3100, 1988.

[19] C. Pisani, R. Dovesi, and C. Roetti. *Hartree–Fock Ab Initio Treatment of Crystalline Systems.* Springer–Verlag, Berlin, 1988.

[20] J. C. Slater and G. F. Koster. Simplified LCAO method for the periodic potential problem. *Physical Review*, 94:1498–1524, 1954.

[21] M. M. Sigalas and D. A. Papaconstantopoulos. Transferable total–energy parametrizations for metals: Applications to elastic–constant determination. *Physical Review B*, 49:1574–1579, 1994.

[22] R. E. Cohen, M. J. Mehl, and D. A. Papaconstantopoulos. Tight–binding total–energy method for transition and noble metals. *Physical Review B*, 50:14694–14697, 1994.

[23] A. F. Kohan and G. Ceder. Tight–binding calculation of formation energies in multicomponent oxides: Application to the MgO–CaO phase diagram. *Physical Review B*, 54:805–811, 1996.

[24] J. G. Bednorz and K. A. Muller. Possible high T_c superconductivity in the Ba–La–Cu–O system. *Zeitschrift fur Physik B (Condensed Matter)*, 64:189–193, 1986.

[25] M. K. Wu, J. R. Ashburn, C. J. Torng, P. H. Hor, R. L. Meng, L. Gao, Z. J. Huang, Y. Q. Wang, and C. W. Chu. Superconductivity at 93 K in a new mixed-phase Y–Ba–Cu–O compound system at ambient pressure. *Physical Review Letters*, 58:908–910, 1987.

[26] D. de Fontaine, G. Ceder, and M. Asta. Low–temperature long–range oxygen order in $YBa_2Cu_3O_z$. *Nature*, 343:544–546, 1990.

[27] T. W. Eagar. The future of metals. *Welding Journal*, 70:69–72, 1991.

[28] W. D. Kingery, H. K. Bowen, and D. R. Uhlmann. *Introduction to Ceramics.* John Wiley & Sons, New York, 1975.

[29] J. L. Martin. Computer techniques for evaluating lattice constants. In C. Domb and M. S. Green, editors, *Phase Transition and Critical Phenomena*, volume 3, pages 97–112, London, 1974. Academic Press Inc.

[30] Z. Jin and Y. Du. A reassessment of the CaO–MgO system. *CALPHAD*, 16:33–36, 1992.

[31] J. F. Smith. The Pd–V (palladium vanadium) system. *Journal of Alloy Phase Diagrams*, 4:1–4, 1988.

[32] J. Cheng and A. J. Ardell. On the stability of the ordered Pd_8V phase in a proton–irradiated Pd–15 at.% V alloy. *Journal of the Less–Common Metals*, 141:45–53, 1988.

[33] M. P. Allen and D. J. Tildesley. *Computer simulation of liquids.* Oxford University Press, New York, 1987.

[34] G. D. Garbulsky. *Ground–state structures and vibrational free energy in first–principles models of substitutional–alloy thermodynamics.* PhD thesis, Massachusetts Institute of Technology, 1996.

[35] G. D. Garbulsky and G. Ceder. Contribution of the vibrational free energy to phase stability in substitutional alloys: Methods and trends. *Physical Review B*, 53:8993–9001, 1996.

[36] G. D. Garbulsky and G. Ceder. Effect of lattice vibrations on the ordering tendencies in substitutional binary alloys. *Physical Review B*, 49:6327–6330, 1994.

[37] C. Wolverton and A. Zunger. First–principles theory of short–range order, electronic excitations, and spin polarization in Ni–V and Pd–V alloys. *Physical Review B*, 52:8813–8828, 1995.

[38] H. E. Stanley. *Introduction to Phase Transitions and Critical Phenomena.* Clarendon Press, Oxford, 1971.

[39] G. Ceder, G. D. Garbulsky, and P. D. Tepesch. Convergent real–space cluster expansion for configurational disorder in ionic systems. *Physical Review B*, 51:11257–11261, 1995.

[40] D. B. Laks, L. G. Ferreira, S. Froyen, and A. Zunger. Efficient cluster expansion for substitutional systems. *Physical Review B*, 46:12587–12605, 1992.

[41] L. G. Ferreira, A. A. Mbaye, and A. Zunger. Chemical and elastic effects on isostructural phase diagrams: the $\epsilon - G$ approach. *Physical Review B*, 37:10547–10570, 1988.

[42] R. McCormack, D. de Fontaine, C. Wolverton, and G. Ceder. Nonempirical phase equilibria in the W–Mo–Cr system. *Physical Review B*, 51:15808–15822, 1995.

[43] P. D. Tepesch, G. D. Garbulsky, and G. Ceder. Model for configurational thermodynamics in ionic systems. *Physical Review Letters*, 74:2272–2275, 1995.

[44] H. Dreyssé, A. Berera, L. T. Wille, and D. de Fontaine. Determination of effective–pair interactions in random alloys by configurational averaging. *Physical Review B*, 39:2442–2452, 1989.

[45] F. Ducastelle. *Order and Phase Stability in Alloys.* North–Holland, Amsterdam, 1991.

[46] P. D. Tepesch. *Atomistic Modeling of Ceramic Materials: Predicting Crystal Structures, Thermodynamic Properties, and Diffusion Behavior.* PhD thesis, Massachusetts Institute of Technology, 1996.

[47] G. D. Garbulsky, P. D. Tepesch, and G. Ceder. Ground state analysis on the fcc lattice with four pair interactions. In J. Broughton, P. Bristowe, and J. Newsam, editors, *Materials Research Society Symposium Proceedings*, volume 291, pages 259–265, Pittsburgh, 1993. Mater. Res. Soc.

[48] K. Binder. Ordering of the face–centered–cubic lattice with nearest–neighbor interaction. *Physical Review Letters*, 45:811–814, 1980.

[49] J. A. Barker. Methods of approximation in the theory of regular mixtures. *Proceedings of the Royal Society. London*, 216:45–56, 1953.

[50] G. Ceder. *Alloy theory and its applications to long period superstructure ordering in metalic alloys and high temperature superconductors.* PhD thesis, University of California at Berkeley, 1991.

[51] C. Domb. Graph theory and embeddings. In C. Domb and M. S. Green, editors, *Phase Transitions and Critical Phenomena*, volume 3, pages 1–95, London, 1974. Academic Press Inc.

[52] C. Domb. On the theory of cooperative phenomena in crystals. *Advances in Physics*, 9:149–361, 1960.

[53] J. L. Lebowitz, M. K. Phani, and D. F. Styer. Phase diagram of Cu–Au–type alloys. *Journal of Statistical Physics*, 38:413–431, 1985.

[54] M. F. Sykes, J. W. Essam, and D. S. Gaunt. Derivation of low temperature expansions for the ising model of a ferromagnet and an antiferromagnet. *Journal of Mathematical Physics*, 6:283–298, 1965.

[55] D. de Fontaine. The cluster variation method and the calculation of alloy phase diagrams. In G. M. Stocks and A. Gonis, editors, *Alloy Phase Stability*, pages 177–203, Dordrecht, 1989. Kluwer Academic Publishers.

[56] M. Wortis. Linked cluster expansion. In C. Domb and M. S. Green, editors, *Phase Transitions and Critical Phenomena*, volume 3, pages 114–180, London, 1974. Academic Press Inc.

[57] G. Parisi. *Statistical Field Theory.* Addison Wesley, California, 1988.

[58] C. Wolverton, G. Ceder, D. de Fontaine, and H. Dreyssé. Ab–initio ground–state study with fourth–nearest–neighbor cluster interactions for fcc Pd–V alloys. *Physical Review B*, 45:13105–13108, 1992.

[59] C. Wolverton, A. Zunger, and Z. W. Lu. Long–range versus short–range order in Ni_3V and Pd_3V alloys. *Physical Review B*, 49:16058–16061, 1994.

[60] P. E. A. Turchi, G. M. Stocks, W. H. Butler, D. M. Nicholson, and A. Gonis. First–principles study of ordering properties of substitutional alloys using the generalized perturbation method. *Physical Review B*, 37:5982–5985, 1988.

[61] G. Ceder, P. D. Tepesch, C. Wolverton, and D. de Fontaine. Ab initio computation of the fcc Pd–V phase diagram. In A. Gonis, editor, *Statistics and Dynamics of Alloy Phase Transformations*, page 571, New York, 1994. Plenum Press.

[62] C. Wolverton, G. Ceder, D. de Fontaine, and H. Dreyssé. Ab–initio determination of structural stability in fcc–based transition–metal alloys. *Physical Review B*, 48:726–747, 1993.

[63] P. D. Tepesch, G. Ceder, C. Wolverton, and D. de Fontaine. An ab–initio calculation of the Pd–V fcc superstructure phase diagram with fourth nearest neighbor cluster interactions. In J. Broughton, P. Bristowe, and J. Newsam, editors, *Materials Research Society Symposium Proceedings*, volume 291, pages 129–134, Pittsburgh, 1993. Mater. Res. Soc.

[64] C. Wolverton and A. Zunger. Comparison of two cluster–expansion methods for the energetics of transition–metal alloys. *Physical Review B*, 50:10548–10560, 1994.

[65] H. L. Skriver. *The LMTO Method.* Springer, Berlin, 1984.

[66] J. Kanamori and Y. Kakehashi. Conditions for the existence of ordered structures in binary alloy systems. *Journal de Physique*, 38:C7–274, 1977.

[67] C. Cohen-Tannoudji, B. Diu, and F. Laloë. *Quantum Mechanics.* John Wiley & Sons, New York, 1977.

[68] L. I. Schiff. *Quantum Mechanics.* McGraw–Hill, New York, 1968.

[69] D. J. Singh, W. E. Pickett, and H. Krakauer. Gradient–corrected density functionals: Full–potential calculation for iron. *Physical Review B*, 43:11628–11634, 1991.

[70] D. Singh, D. P. Clougherty, J. M. MacLaren, R. C. Albers, and C. S. Wang. Influence of the local–spin–density correlation functional on the stability of bcc ferromagnetic iron. *Physical Review B*, 44:7701–7703, 1991.

[71] H. J. F. Jansen. Electronic structure calculations for magnetically ordered systems. *Physics Today*, 48:50–55, 1995.

[72] A. E. Carlsson. Beyond pair potentials in elemental transition metals and semiconductors. In H. Ehrenreich and D. Turnbull, editors, *Solid State Physics*, volume 43, pages 1–91, Boston, 1990. Academic Press.

[73] M. S. Daw, S. M. Foiles, and M. I. Baskes. The embedded–atom method: a review of theory and applications. *Materials Science Reports*, 9:251–310, 1993.

[74] T. J. Raeker and A. E. Depristo. Theory of chemical bonding based on the atom–homogeneous electron gas system. *International Reviews in Physical Chemistry*, 10:1–54, 1991.

[75] F. H. Streitz and J. W. Mintmire. Electrostatic potentials for metal–oxide surfaces and interfaces. *Physical Review B*, 50:11996–12003, 1994.

[76] M. I. Baskes. Modified embedded atom method calculations of interfaces. *Sandia Report 96–8484*, pages 1–12, 1996.

[77] B. G. Dick Jr. and A. W. Overhauser. Theory of the dielectric constants of alkali halide crystals. *Physical Review*, 112:90–103, 1958.

[78] I. M. Torrens. *Interatomic Potentials.* Academic Press, New York, 1972.

[79] G. V. Lewis and C. R. A. Catlow. Potential models for ionic oxides. *Journal of Physics C: Solid State Physics*, 18:1149–1161, 1985.

[80] V. Vitek. Pair potentials in atomistic computer simulations. *MRS Bulletin*, 21:20–23, 1996.

[81] M. Stoneham, J. Harding, and T. Harker. The shell model and interatomic potentials for ceramics. *MRS Bulletin*, 21:29–35, 1996.

[82] R. E. Watson, S. C. Parker, and A. Wall. Molecular dynamics simulation of fluoride–perovskites. *J. Phys. Condens. Matter.*, 4:2097–2108, 1992.

[83] S. C. Parker and G. D. Price. Computer modelling of phase transitions in minerals. *Adv. Solid–State Chem*, 1:295, 1989.

[84] P. D. Tepesch, A. F. Kohan, G. D. Garbulsky, G. Ceder, C. Coley, H. T. Stokes, L. L. Boyer, M. J. Mehl, B. P. Burton, K. Cho, and J. Joannopoulos. A model to compute phase diagrams in oxides with empirical or first–principles energy methods and application to the solubility limits in the CaO–MgO system. *Journal of the American Ceramic Society*, 79:2033–2040, 1996.

[85] P. P. Ewald. Die berechnung optischer und elektrostatischer gitterpotentiale. *Annalen der Physic*, 64:253–287, 1921.

[86] J. D. Gale, C. R. A. Catlow, and W. C. Mackrodt. Periodic ab initio determination of interatomic potentials for alumina. *Modelling and simulation in materials science and engineering*, 1:73–81, 1992.

[87] J. F. Nye. *Physical Properties of Crystals.* Oxford University Press, New York, 1985.

[88] M. Wilson, P. A. Madden, N. C. Pyper, and J. H. Harding. Molecular dynamics simulations of compressible ions. *Journal of Chemical Physics*, 104:8068–8081, 1996.

[89] M. Wilson, U. Schönberger, and M. Finnis. Transferable atomistic model to describe the energetics of zirconia. *Physical Review B*, 54:9147–9161, 1996.

[90] M. Wilson, M. Exner, Y. M. Huang, and M. W. Finnis. Transferable model for the atomistic simulation of Al_2O_3. *Physical Review B*, 54:15683–15689, 1996.

[91] M. S. Daw. Model of metallic cohesion: the embedded–atom method. *Physical Review B*, 39:7441–7452, 1989.

[92] F. H. Stillinger and T. A. Weber. Computer simulation of local order in condensed phases of silicon. *Physical Review B*, 31:5262–5271, 1985.

[93] M. I. Baskes. Application of the embedded–atom method to covalent materials: a semiempirical potential for silicon. *Physical Review Letters*, 59:2666–2669, 1987.

[94] M. I. Baskes. Modified embedded–atom potentials for cubic materials and impurities. *Physical Review B*, 46:2727–2742, 1992.

[95] N. W. Ashcroft and N. D. Mermin. *Solid State Physics.* Saunders College Publishing, Fort Worth, 1976.

[96] U. von Barth. Density functional theory for solids. In P. Phariseau and W. M. Temmerman, editors, *The Electronic Structure of Complex Systems*, pages 67–140, New York, 1982. Plenum Press.

[97] R. O. Jones and O. Gunnarsson. The density functional formalism, its applications and prospects. *Reviews of Modern Physics*, 61:689–746, 1989.

[98] J. F. Janak. Proof that $\frac{\delta e}{\delta n_i} = \epsilon_i$ in density–functional theory. *Physical Review B*, 18:7165–7168, 1978.

[99] J. P. Perdew and A. Zunger. Self–interaction correction to density–functional approximations for many–electron systems. *Physical Review B*, 23:5048–5079, 1981.

[100] L. Hedin and B. I. Lundqvist. Explicit local exchange–correlation potentials. *Journal of Physics C*, 4:2064–2083, 1971.

[101] J. C. Slater. Wave functions in a periodic potential. *Physical Review*, 51:846–851, 1937.

[102] O. K. Andersen. Linear methods in band theory. *Physical Review B*, 12:3060–3083, 1975.

[103] H. T. Stokes, L. L. Boyer, and M. J. Mehl. Spherical self–consistent atomic deformation model for first–principles energy calculations in ionic crystalline solids. *Physical Review B*, 54:7729–7736, 1996.

[104] E. Clementi and C. Roetti. Roothaan–Hartree–Fock atomic wavefunctions. basis functions and their coefficients for ground and certain excited states of neutral and ionized atoms, Z$\leq$ 54. *Atomic Data and Nuclear Data Tables*, 14:177–478, 1974.

[105] A. D. McLean and R. S. McLean. Roothaan–Hartree–Fock atomic wave functions Slater basis–set expansions for z=55-92. *Atomic Data and Nuclear Data Tables*, 26:197–381, 1981.

[106] R. G. Gordon and Y. S. Kim. Theory for the forces between closed–shell atoms and molecules. *The Journal of Chemical Physics*, 56:3122–3133, 1972.

[107] L. L. Boyer, M. J. Mehl, J. L. Feldman, J. R. Hardy, J. W. Flocken, and C. Y. Fong. Beyond the rigid–ion approximation with spherically symmetric ions. *Physical Review Letters*, 54:1940–1943, 1985.

[108] M. J. Mehl, R. J. Hemley, and L. L. Boyer. Potential–induced breathing model for the elastic moduli and high–pressure behavior of the cubic alkaline–earth oxides. *Physical Review B*, 33:8685–8696, 1986.

[109] R. E. Watson. Analytic Hartree–Fock solutions for $O^{=}$. *Physical Review*, 111:1108–1110, 1958.

[110] O. K. Andersen, O. Jepsen, and D. Glötzel. Canonical description of the band structures of metals. In F. Bassani, F. Fumi, and M. P. Tosi, editors, *Proceedings of the International School of Physics 'Enrico Fermi'; Course LXXXIX. Highlights of Condensed–Matter Theory*, pages 59–176, Amsterdam, 1985. North Holland.

[111] O. K. Andersen and O. Jepsen. Explicit, first–principles tight–binding theory. *Physical Review Letters*, 53:2571–2574, 1984.

[112] O. K. Andersen, O. Jepsen, and M. Sob. Linearized band structure methods. In M. Yussouff, editor, *Electronic band structure and its applications : proceedings of the International School on Electronic Band Structure and its Applications Kanpur, India, October 20–November 8, 1986*, volume 8, pages 1–57, Berlin, 1987. Springer–Verlag.

[113] A. M. Bratkovsky and S. Y. Savrasov. On the calculation of combined corrections in the LMTO method. *Journal of Computational Physics*, 88:243–249, 1990.

[114] N. E. Christensen and S. Satpathy. Pressure–induced cubic to tetragonal transition in CsI. *Physical Review Letters*, 55:600–603, 1985.

[115] K. H. Weyrich. Full–potential linear muffin–tin–orbital method. *Physical Review B*, 37:10269–10282, 1988.

[116] U. von Barth and L. Hedin. A local exchange–correlation potential for the spin polarized case. I. *Journal of Physics C*, 5:1629–1642, 1972.

[117] A. van de Walle. Private communication.

[118] E. Wimmer, H. Krakauer, M. Weinert, and A. J. Freeman. Full–potential self–consistent linearized–augmented–plane–wave method for calculating the electronic structure of molecules and surfaces: O_2 molecule. *Physical Review B*, 24:864–875, 1981.

[119] H. J. F. Jansen and A. J. Freeman. Total–energy full–potential linearized augmented–plane–wave method for bulk solids: Electronic and structural properties of tungsten. *Physical Review B*, 30:561–569, 1984.

[120] M. J. Mehl, R. E. Cohen, and H. Krakauer. Linearized augmented plane wave electronic structure calculations for MgO and CaO. *J. Geophys. Res.*, 93:8009–8022, 1988.

[121] D. J. Singh. *Planewaves, Pseudopotentials and the LAPW Method.* Kluwer Academic Publishers, Boston, 1994.

[122] P. Pulay. Ab initio calculation of force constants and equilibrium geometries in polyatomic molecules. I. Theory. *Molecular Physics*, 17:197–204, 1969.

[123] R. Car and M. Parrinello. Unified approach for molecular dynamics and density–functional theory. *Physical Review Letters*, 55:2471–2474, 1985.

[124] M. C. Payne, M. P. Teter, D. C. Allan, T. A. Arias, and J. D. Joannopoulos. Iterative minimization techniques for *ab initio* total–energy calculations: molecular dynamics and conjugate gradients. *Reviews of Modern Physics*, 64:1045–1097, 1992.

[125] A. M. Rappe, K. M. Rabe, E. Kaxiras, and J. D. Joannopoulos. Optimized pseudopotentials. *Physical Review B*, 41:1227–1330, 1990.

[126] D. Vanderbilt. Soft self–consistent pseudopotentials in a generalized eigenvalue formalism. *Physical Review B*, 41:7892–7895, 1990.

[127] W. E. Pickett. Pseudopotential methods in condensed matter applications. *Computer Physics Reports*, 9:117–197, 1989.

[128] P. J. H. Denteneer and W. van Haeringen. The pseudopotential–density–functional method in momentum space: details and test cases. *J. Phys. C.*, 18:4127–4142, 1985.

[129] J. Ihm. Total energy calculations in solid state physics. *Rep. Prog. Phys.*, 51:105–142, 1988.

[130] W. A. Harrison. *Electronic Structure and the Properties of Solids.* Dover Publications, New York, 1989.

[131] D. G. Pettifor. The tight binding approximation: Concepts and predictions. In D. G. Pettifor and A. H. Cottrell, editors, *The Electron Theory in Alloy Design*, pages 81–121, London, 1992. The Institute of Materials.

[132] F. Bloch. Über die quantenmechanik der elektronen in kristallgittern. *Z. Physik*, 52:555–600, 1928.

[133] W. Y. Ching. Theoretical studies of the electronic properties of ceramic materials. *Journal of the American Ceramic Society*, 73:3135–3160, 1990.

[134] J. A. Majewski and P. Vogl. Crystal stability and structural transition pressures of sp–bonded solids. *Physical Review Letters*, 57:1366–1369, 1986.

[135] G. Galli and M. Parrinello. Large scale electronic structure calculations. *Physical Review Letters*, 69:3547–3550, 1992.

[136] S. Baroni and P. Giannozzi. Towards very large–scale electronic–structure calculations. *Europhysics Letters*, 17:547–552, 1992.

[137] X. P. Li, R. W. Nunes, and D. Vanderbilt. Density–matrix electronic–structure method with linear system–size scaling. *Physical Review B*, 47:10891–10894, 1993.

[138] L. W. Wang and M. P. Teter. Simple quantum–mechanical model of covalent bonding using a tight–binding basis. *Physical Review B*, 46:12798–12801, 1992.

[139] S. Goedecker. Low complexity algorithms for electronic structure calculations. *Journal of Computational Physics*, 118:261–268, 1995.

[140] S. Goedecker and L. Colombo. Efficient linear scaling algorithm for tight–binding molecular dynamics. *Physical Review Letters*, 73:122–125, 1994.

[141] E. V. Stefanovich, A. L. Shluger, and C. R. A. Catlow. Theoretical study of the stabilization of cubic–phase ZrO_2 by impurities. *Physical Review B*, 49:11560–11571, 1994.

[142] R. H. French, S. J. Glass, F. S. Ohuchi, Y. N. Xu, and W. Y. Ching. Experimental and theoretical determination of the electronic structure and optical properties of three phases of ZrO_2. *Physical Review B*, 49:5133–5141, 1994.

[143] J. C. Phillips and L. Kleinman. New method for calculating wave functions in crystals and molecules. *Physical Review*, 116:287–294, 1959.

[144] M. L. Cohen, V. Heine, and J. C. Phillips. The quantum mechanics of materials. *Scientific American*, 246:82–102, 1982.

[145] W. C. Topp and J. J. Hopfield. Chemically motivated pseudopotential for sodium. *Physical Review B*, 7:1295–1303, 1974.

[146] T. Starkloff and J. D. Joannopoulos. Local pseudopotential theory for transition metals. *Physical Review B*, 16:5212–5215, 1977.

[147] D. R. Hamann, M. Schluter, and C. Chiang. Norm–conserving pseudopotentials. *Physical Review Letters*, 43:1494–1497, 1979.

[148] G. B. Bachelet, D. R. Hamann, and M. Schlüter. Pseudopotentials that work: From H to Pu. *Physical Review B*, 26:4199–4228, 1982.

[149] G. P. Kerker. Non–singular atomic pseudopotentials for solid state applications. *Journal of Physics C*, 13:L189–194, 1980.

[150] M. L. Cohen and V. Heine. The fitting of pseudopotentials to experimental data and their subsequent application. In H. Ehrenreich, F. Seitz, and D. Turnbull, editors, *Solid state physics: advances in research and applications*, volume 18, pages 37–248, London, 1970. Academic.

[151] S. G. Louie, S. Froyen, and M. L. Cohen. Nonlinear ionic pseudopotentials in spin–density–functional calculations. *Physical Review B*, 26:1738–1742, 1982.

[152] L. Kleinman and D. M. Bylander. Efficacious form for model pseudopotentials. *Physical Review Letters*, 48:1425–1428, 1982.

[153] X. Gonze, P. Käckell, and M. Scheffler. Ghost states for separable, norm–conserving, *ab initio* pseudopotentials. *Physical Review B*, 41:12264–12267, 1990.

[154] R. P. Feynman. Forces in molecules. *Physical Review*, 56:340–343, 1939.

[155] F. Gygi. Adaptive Riemannian metric for plane–wave electronic–structure calculations. *Europhysics Letters*, 19:617–622, 1992.

[156] F. Gygi. *Ab initio* molecular dynamics in adaptive coordinates. *Physical Review B*, 51:11190–11193, 1995.

[157] F. Gygi and G Galli. Real–space adaptive–coordinate electronic–structure calculations. *Physical Review B*, 52:R2229–R2232, 1995.

[158] K. Cho, T. A. Arias, and J. D. Joannopoulos. Wavelets in electronic structure calculations. *Physical Review Letters*, 71:1808–1811, 1993.

[159] A. Devenyi, K. Cho, T. A. Arias, and J. D. Joannopoulos. Adaptive Riemannian metric for all–electron calculations. *Physical Review B*, 49:13373–13376, 1994.

[160] K. J. Chang and M. L. Cohen. High–pressure behavior of MgO: Structural and electronic properties. *Physical Review B*, 30:4774–4781, 1984.

[161] A. De Vita, M. J. Gillan, J. S. Lin, M. C. Payne, I. Stich, and L. J. Clarke. Defect energetics in MgO treated by first–principles methods. *Physical Review B*, 46:12964–12973, 1992.

[162] J. F. Mammone, H. K. Mao, and P. M. Bell. Equations of state of CaO under static pressure conditions. *Geophysical Research Letters*, 8:140–142, 1981.

[163] H. K. Mao and P. M. Bell. Equations of state of MgO and epsilon Fe under static pressure conditions. *Journal of Geophysical Research*, 84:4533–4536, 1979.

[164] M. J. L. Sangster, G. Peckham, and D. H. Saunderson. Lattice dynamics of magnesium oxide. *Journal of Physics C*, 3:1026–1036, 1970.

[165] O. L. Anderson and P. Andreatch Jr. Pressure derivatives of elastic constants of single–crystal MgO at 23° and -195.8° C. *Journal of the American Ceramic Society*, 49:404–409, 1966.

[166] A. S. Rao and R. J. Kearney. Logarithmic derivative reflectance spectra of BaO and SrO. *Physica Status Solidi B*, 95:243–250, 1979.

[167] D. M. Roessler and W. C. Walker. Electronic spectrum and ultraviolet optical properties of crystalline MgO. *Physical Review*, 159:733–738, 1967.

[168] The International Union of Crystallography. *International Tables for Crystallography*. Kluwer Academic Publishers, Dordrecht, 1989.

[169] J. P. Perdew, R. G. Parr, M. Levy, and J. L. Balduz Jr. Density–functional theory for fractional particle number: derivative discontinuities of the energy. *Physical Review Letters*, 49:1691–1694, 1982.

[170] D. K. Smith and H. W. Newkirk. The crystal structure of baddeleyite (monoclinic ZrO_2) and its relation to the polymorphism of ZrO_2. *Acta Cryst.*, 18:983–991, 1965.

[171] P. Aldebert and J. P. Traverse. Structure and ionic mobility of zirconia at high temperature. *Journal of the American Ceramic Society*, 68:34–40, 1985.

[172] V. S. Stubican. Phase equilibria and metastabilities in the systems ZrO_2–MgO, ZrO_2–CaO, and ZrO_2–Y_2O_3. In S. Somiya, N. Yamamoto, and H. Yanagida, editors, *Science and technology of zirconia III*, volume 24, pages 71–82, Westerville, Ohio, 1988. The American Ceramic Society.

[173] J. R. Hellmann and V. S. Stubican. The existence and stability of $Ca_6Zr_{19}O_{44}$ compound in the system ZrO_2–CaO. *Materials Research Bulletin*, 17:459–465, 1982.

[174] H. J. A. Koopmans, G. M. H. van de Velde, and P. J. Gellings. Powder neutron diffraction study of perovskites $CaTiO_3$ and $CaZrO_3$. *Acta Crystallographica*, C39:1323–1325, 1983.

[175] A. Dwivedi and A. N. Cormak. A computer simulation study of the defect structure of calcia–stabilized zirconia. *Philosophical Magazine A*, 61:1–22, 1990.

[176] R. M. McMeeking and A. G. Evans. Mechanics of transformation–toughening in brittle materials. *Journal of the American Ceramic Society*, 65:242–246, 1982.

[177] R. Orlando, C. Pisani, C. Roetti, and E. Stefanovich. *Ab initio* Hartree–Fock study of tetragonal and cubic phases of zirconium dioxide. *Physical Review B*, 45:592–601, 1992.

[178] H. J. F. Jensen. Electronic structure of cubic and tetragonal zirconia. *Physical Review B*, 43:7267–7278, 1991.

[179] H. J. F. Jensen and J. A. Gardner. Total energy calculations for ZrO_2. *Physical Review B*, 150:10–18, 1988.

[180] F. Zandiehnadem, R. A. Murray, and W. Y. Ching. Electronic structures of three phases of zirconium oxide. *Physica B*, 150:19–24, 1988.

[181] R. E. Cohen, M. J. Mehl, and L. L. Boyer. Phase transitions and elasticity in zirconia. *Physica B*, 150:1–9, 1988.

[182] R. J. Ackermann, E. G. Rauh, and C. A. Alexander. The thermodynamic properties of ZrO_2(g). *High Temperature Science*, 7:304–316, 1975.

[183] C. J. Howard, R. J. Hill, and B. E. Reichert. Structures of the ZrO_2 polymorphs at room temperature by high–resolution neutron powder diffraction. *Acta Cryst.*, 44:116–119, 1988.

[184] H. T. Stokes. Private communication.

[185] R. Pawellek, M. Fahnle, C. Elsasser, K. M Ho, and C. T. Chan. First–principles calculation of the relaxation around a vacancy and the vacancy formation energy in bcc Li. *Journal of Physics:Condensed Matter*, 3:2451–2455, 1991.

[186] R. Magri, S. H. Wei, and A. Zunger. Ground–state structures and the random–state energy of the Madelung lattice. *Physical Review B*, 42:11388–11391, 1990.

[187] C. Wolverton, A. Zunger, S. Froyen, and S.-H.Wei. Point–charge electrostatics in disordered alloys. *Physical Review B*, 54:7843–7856, 1996.

[188] V. Heine. Electronic structure from the point of view of the local atomic environment. In H. Ehrenreich, F. Seitz, and D. Turnbull, editors, *Solid State Physics*, volume 35, pages 1–127, New York, 1980. Academic Press.

[189] D. W. Bullet. The renaissance and quantitative development of the tight–binding method. In H. Ehrenreich, F. Seitz, and D. Turnbull, editors, *Solid State Physics*, volume 35, pages 129–214, New York, 1980. Academic Press.

[190] R. Haydock. The recursive solution of the Schrödinger equation. In H. Ehrenreich, F. Seitz, and D. Turnbull, editors, *Solid State Physics*, volume 35, pages 215–294, New York, 1980. Academic Press.

[191] M. J. Kelley. Applications of the recursion method to the electronic structure from an atomic point of view. In H. Ehrenreich, F. Seitz, and D. Turnbull, editors, *Solid State Physics*, volume 35, pages 295–383, New York, 1980. Academic Press.

[192] J. A. Majewski and P. Vogl. Quantum theory of structure: Tight–binding systems. In F. R. de Boer and D. G. Pettifor, editors, *The Structure of Binary Compounds*, volume II-4, page 287, New York, 1989. North Holland.

[193] E. E. Lafon and C. C. Lin. Energy band structure of lithium by the tight–binding method. *Physical Review*, 152:579–584, 1966.

[194] J. C. Browne and R. D. Poshusta. Quantum mechanical integrals over Gaussian atomic orbitals. *Journal of Chemical Physics*, 36:1933–1937, 1962.

[195] A. T. Paxton, A. P. Sutton, and C. M. M. Nex. Structural stability of silicon in tight–binding models. *Journal of Physics C: Solid State Physics*, 20:L263–L269, 1987.

[196] D. G. Pettifor and R. Podloucky. Microscopic theory of the structural stability of pd-bonded AB compounds. *Physical Review Letters*, 53:1080–1083, 1984.

[197] M. J. Mehl and D. A. Papaconstantopoulos. Applications of a tight–binding total–energy method for transition and noble metals: Elastic constants, vacancies, and surfaces of monoatomic metals. *Physical Review B*, 54:4519–4530, 1996.

[198] P. O. Löwdin. On the non–orthogonality problem connected with the use of atomic wave functions in the theory of molecules and crystals. *The Journal of Chemical Physics*, 18:365–375, 1950.

[199] R. R. Sharma. General expressions for reducing the Slater–Koster linear combination of atomic orbitals integrals to the two center approximation. *Physical Review B*, 19:2813–2823, 1979.

[200] R. R. Sharma. Improved general expressions for the Slater–Koster integrals in the two center approximation. *Physical Review B*, 21:2647–2649, 1980.

[201] S. Froyen and W. A. Harrison. Elementary prediction of linear combination of atomic orbitals matrix elements. *Physical Review B*, 20:2420–2422, 1979.

[202] W. A. Harrison. New tight–binding parameters for covalent solids obtained using Louie peripheral states. *Physical Review B*, 24:5835–5843, 1981.

[203] W. A. Harrison and G. K. Straub. Electronic structure and properties of d– and f–shell–metal compounds. *Physical Review B*, 36:2695–2706, 1987.

[204] J. L. Mercer and M. Y. Chou. Tight–binding model with intra–atomic matrix elements. *Physical Review B*, 49:8506–8509, 1994.

[205] W. M. C. Foulkes and R. Haydock. Tight–binding models and density–functional theory. *Physical Review B*, 39:12520–12536, 1989.

[206] L. Goodwin, A. J. Skinner, and D. G. Pettifor. Generating transferable tight–binding parameters: Application to silicon. *Europhysics Letters*, 9:701–706, 1989.

[207] P. O. Löwdin. Quantum theory of cohesive properties of solids. *Advances in Physics*, 5:1–172, 1956.

[208] P. W. Anderson. Localized magnetic states in metals. *Physical Review*, 124:41–53, 1961.

[209] O. F. Sankey and J. D. Dow. Theory of tetrahedral–site interstitial s– and p–bonded impurities in Si. *Physical Review B*, 27:7641–7653, 1983.

[210] C. Huang, J. A. Moriarty, and A. Sher. Two–electron bond–orbital model. II. *Physical Review B*, 14:2539–2558, 1976.

[211] R. H. Parmenter. Effect of orbital degeneracy on the Anderson model of a localized moment in a metal. *Physical Review B*, 8:1273–1275, 1973.

[212] Walter A. Harrison. Coulomb interactions in semiconductors and insulators. *Physical Review B*, 31:2121–2132, 1985.

[213] F. Liu. Self–consistent tight–binding method. *Physical Review B*, 52:10677–10680, 1995.

[214] M. O. Robbins and L. M. Falicov. Electronic theory of ordering and segregation in transition–metal alloys. *Physical Review B*, 29:1333–1348, 1984.

[215] M. van Schilfgaarde, A. B. Chen, and A. Sher. Coulomb energy in pseudobinary alloys. *Physical Review Letters*, 57:1149–1152, 1986.

[216] J. A. Majewski and P. Vogl. Simple model for structural properties and crystal stability of *sp*-bonded solids. *Physical Review B*, 35:9666–9682, 1987.

[217] M. Kohyama, R. Yamamoto, Y. Ebata, and M. Kinoshita. Atomic forces in the self–consistent tight–binding model. *Phys. Stat. Sol. (b)*, 152:533–541, 1989.

[218] R. Hoffman. An extended Hückel theory. I. Hydrocarbons. *Journal of Chemical Physics*, 39:1397–1412, 1963.

[219] W. A. Harrison. Theory of the two–center bond. *Physical Review B*, 27:3592–3604, 1983.

[220] D. W. Marquardt. An algorithm for least–squares estimation of nonlinear parameters. *J. Soc. Ind. Appl. Math*, 11:431–441, 1963.

[221] O. K. Andersen, Z. Pawlowska, and O. Jepsen. Illustration of the linear–muffin–tin–orbital tight–binding representation: Compact orbitals and charge density in Si. *Physical Review B*, 34:5253–5269, 1986.

[222] H. Shiba. A reformulation of the coherent potential approximation and its applications. *Progress of Theoretical Physics*, 46:77–94, 1971.

[223] M. Monkenbusch. A set of routines for efficient and accurate computation of lattice sums of $1/r^n$–potentials. *Computer Physics Communications*, 67:343–355, 1991.

[224] P. H. Dederichs and R. Zeller. Self–consistency iterations in electronic–structure calculations. *Physical Review B*, 28:5462–5472, 1983.

[225] E. Issacson and H. B. Keller. *Analysis of Numerical Methods.* John Wiley & Sons, New York, 1966.

[226] E. Anderson *et. al. LAPACK Users' Guide.* Society for Industrial and Applied Mathematics, Philadelphia, 1992.

[227] M. Methfessel and A. T. Paxton. High–precision sampling for Brillouin–zone integration in metals. *Physical Review B*, 40:3616–3621, 1989.

[228] A. F. Kohan and G. Ceder. Calculation of total energies in multicomponent oxides. *Computational Materials Science*, 8, 1997, in press.

[229] P. Vogl, H. P. Hjalmarson, and J. D. Dow. A semi–empirical tight–binding theory of the electronic structure of semiconductors. *J. Phys. Chem. Solids*, 44:365–378, 1983.

[230] D. A. Papaconstantopoulos. *Handbook of the band structure of elemental solids.* Plenum Press, New York, 1986.

[231] M. Rosenbauer and H. J. F. Jansen. Slater–Koster interpolation of energy bands of complex crystal structures: Tetragonal zirconia. *Physical Review B*, 47:16148–16154, 1993.

[232] N. F. Mott. The energy of the superlattice in β brass. *The Proceedings of the Physical Society (London)*, 49:258–263, 1937.

[233] J. S. Faulkner, Y. Wang, and G. M. Stocks. Electrons in extended systems. *Physical Review B*, 52:17106–17111, 1995.

[234] J. P. Perdew, K. Burke, and M. Ernzerhof. Generalized gradient approximation made simple. *Physical Review Letters*, 77:3865–3868, 1996.

[235] D. R. Hamann. Generalized gradient theory for silica phase transitions. *Physical Review Letters*, 76:660–663, 1996.

[236] C. Filippi, D. J. Singh, and C. J. Umrigar. All–electron local–density and generalized–gradient calculations of the structural properties of semiconductors. *Physical Review B*, 50:14947–14951, 1994.

[237] V. I. Anisimov, J. Zaanen, and O. K. Andersen. Band theory and Mott insulators: Hubbard U instead of Stoner I. *Physical Review B*, 44:943–954, 1991.

[238] V. I. Anisimov, F. Aryasetiawan, and A. I. Lichtenstein. First–principles calculations of the electronic structure and spectra of strongly correlated systems: the LDA + U method. *Journal of Physics*, 9:767–808, 1997.

[239] T. A. Arias and J. D. Joannopoulos. Ab initio theory of dislocation interactions: from close–range spontaneous annihilation to the long–range continuum limit. *Physical Review Letters*, 73:680–683, 1994.

[240] J. Rath and A. J. Freeman. Generalized magnetic susceptibilities in metals: Application of the analytic tetrahedron linear energy method. *Physical Review B*, 6:2109–2117, 1975.

[241] J. Hama and M. Watanabe. General formulae for the special points and their weighting factors in k–space integration. *J. Phys.:Condens. Matter*, 4:4583–4594, 1992.

[242] D. J. Chadi and M. L. Cohen. Special points in the Brillouin zone. *Physical Review B*, 8:5747–5753, 1973.

[243] D. J. Chadi. Special points for Brillouin–zone integrations. *Physical Review B*, 16:1746–1747, 1977.

[244] J. D. Pack and H. J. Monkhorst. "Special points for Brillouin–zone integrations"–a reply. *Physical Review B*, 16:1748–1749, 1977.

[245] H. J. Monkhorst and J. D. Pack. Special points for Brillouin–zone integrations. *Physical Review B*, 13:5188–5192, 1976.

[246] S. Froyen. Brillouin–zone integration by Fourier quadrature: special points for superlattice and supercell calculations. *Physical Review B*, 39:3168–3172, 1989.

[247] M. K. Aydinol, A. F. Kohan, and G. Ceder. Ab–initio calculation of the intercalation voltage of lithium–transition–metal oxide electrodes for rechargeable batteries. *Journal of Power Sources*, 1997, in press.

[248] G. Ceder, M. K. Aydinol, and A. F. Kohan. Application of first–principles calculations to the design of rechargeable Li–Batteries. *Computational Materials Science*, 8, 1997, in press.

[249] M. K. Aydinol, G. Ceder, and A. F. Kohan. Effect of chemistry and structure on voltage of Li intercalation oxides. In A. Jacobson, P. Davies, T. Vanderah, and C. Torardi, editors, *Solid–State Chemistry of Inorganic Materials. Materials Research Society Symposium Proceedings*, volume 453, Pittsburgh, 1997. Mater. Res. Soc., in press.

[250] M. K. Aydinol, A. F. Kohan, G. Ceder, K. Cho, and J. Joannopoulos. Ab initio study of lithium intercalation in oxides and metal dichalcogenides. *Physical Review B*, 1997, in press.

[251] W. R. McKinnon. Insertion electrodes I: Atomic and electronic structure of the hosts and their insertion compounds. In P. G. Bruce, editor, *Solid state electrochemistry*, volume 16, pages 163–198, Cambridge, 1995. Cambridge University Press.

[252] K. Mizushima, P. J. Jones Wiseman, and J. B. Goodenough. Li_xCoO_2 ($0 < x \leq 1$): a new cathode material for batteries of high energy density. *Materials Research Bulletin*, 15:783–789, 1980.

[253] M. M. Thackeray, L. A. de Picciotto, W. I. F David, P. G Bruce, and J. B. Goodenough. Structural refinement of delithiated $LiVO_2$ by neutron diffraction. *Journal of Solid State Chemistry*, 67:285–290, 1987.

[254] L. A. De Picciotto, M. M. Thackeray, and G. Pistoia. An electrochemical study of the systems $Li_{1\pm x}V_2O_4$ and $Li_{1-x}VO_2$ ($0 \leq x \leq 1$). *Solid State Ionics*, 28–30:1364–1370, 1988.

[255] T. Ohzuku and A. Ueda. Solid–state redox reactions of $LiCoO_2$ ($R\bar{3}m$) for 4 volt secondary lithium cells. *Journal of the Electrochemical Society*, 141:2972–2977, 1994.

[256] T. Ohzuku, A. Ueda, and M. Nagayama. Electrochemistry and structural chemistry of $LiNiO_2$ ($R\bar{3}m$) for 4 volt secondary lithium cells. *Journal of the Electrochemical Society*, 140:1862–1870, 1993.

[257] W. B. Pearson, P Villars, and L. D. Calvert. *Pearson's Handbook of Crystallographic data for intermetallic phases.* American Society for Metals, Metals Park, Ohio, 1985.